INTERNATIONAL JOURNAL OF
IJCOE
COASTAL, OFFSHORE AND ENVIRONMENTAL ENGINEERING

Experimental study of gas flow regime criterions in underwater gas-saturated liquid blowouts
Maryam Bafandeh, Abbas-Ali Ali Akbari Bidokhti, Mojtaba Ezam, Majid Ghodsi Hasanabad, Sara Allahyari Beyk

Changes of Physical Parameters of the Water Column from the Indian Ocean to the Persian Gulf
Parvaneh Sobhani *, Mahyar Majidi Nik

Hybrid Intelligence for Coastal Pattern Recognition: ANFIS-Based Prediction of Multi -Level Beach Cusp Spacing
Azadeh Valipour, Hossein Shirgahi

Numerical simulation of bottom outlet valve openings and reverse slope transition to control downstream pressure drop in pipeline of effluent discharge to sea
Saeed Madadyari, Mehdi Nezhadnaderi, Babak Fazli Malidareh

Data-Driven Assessment and Forecasting of Port Services Demand: A Case Study of Shahid Rajaee Por
Pouria Rafati, Seyede Masoome Sadaghi, Ali Fakher

A Critical Review of Challenges and opportunities in Using Remote Sensing and Image Processing for Rip Current Studies
Azadeh Valipour

The failure probability of reinforced concrete marine structures and cost optimization of maintenance
Abdolhossein Mohammadrahimi, Afshin Ghasri, Mesbah Sayebani, Akbar Esfandiari

The Role of Standards in Maritime-Based Development: An Analysis of Challenges in Iran's Maritime Industry
Amir Nezam Barati, Ali Sheykh Bahaei , Meysam Bali, Ali Alimohamadpour

Volume 11 | Isssue 3| JUNE 2026

www.ijcoe.org

International Journal of Coastal, Offshore and Environmental Engineering (IJCOE) Vol.11/Issue 3/ JUNE 2026

International Journal of Coastal, Offshore & Environmental Engineering

IJCOE

International Journal of Coastal, Offshore & Environmental Engineering
Since 2015
ISSN: 2980-8721 (online)

In The Name of God

Message from the Editor-in-Chief

The IJCOE journal office was established in 2015,and its first issue was published in 2016. TheIJCOE covers a wide range of research in thefields of oceanography & ocean technology, aswell as marine industries & marine engineering.The editorial board of IJCOE consists of nearly130 of the greatest scientists and researchersfrom over 30 countries worldwide, and thejournal's review board comprises 1,000 membersfrom all five continents. The membership andapplication process for joining the editorial andreview boards of this journal is ongoing. IJCOE isa research-academic quarterly journal that haspublication and distribution permissions fromthe Press Organization and permission topublish scientific-research articles from theMinistry of Science, Research, and Technology(MSRT) with an "A" rating. It also holds a "Q1"rating from the ISC institute with an impactfactor (IF) of approximately 0.43 and isconsidered a "core journal" (prestigious andoutstanding journal). IJCOE is an open-accessjournal and allows the download and receipt ofaccepted articles in full text for free. It respectsand adheres to copyright and COPE regulations.The journal's office operates 24/7, providingservices to researchers. In addition to publishinga regular quarterly journal, IJCOE has 16 specialissues on specific topics in preparation. It alsoprovides conditions for publishing specializedbooks, references, and handbooks. Moreover, itis ready to cooperate with the secretariats ofreputable international conferences to publishtheir selected and outstanding articles. IJCOEevaluates, appraises, and publishes books,articles, and the scientific achievements andfindings of esteemed researchers and scientistsworldwide who are innovating and conductingin-depth research in the "important and strategicfield of the maritime technology & Oceanengineering." It welcomes any form of jointcooperation with universities, research institutes,and related research centers at the national,regional, and international levels, and extends ahand for collaboration.

Classification of Editorial Board in IJCOE

- Editor-in-Chief
- Director-in-Chief
- Deputy Editor
- Executive Managers
- English Text Editor
- Technical Editor
- International Editorial Board
- National Editorial Board
- Editorial Board Associate
- Editorial Board Assistant
- Guest Editorial Board
- Advisory Board
- Administrative Coordinator
- Honorary Board Member
- Methodology Advisor

Author Benefits

- Open Access
- Rapid Publication
- Thorough Peer-Review
- No Copyright Constraints
- Coverage by Leading Indexing Services
- Discounts On Article Processing Charges (APC)
- No Space Constraints, No restriction on the maximum length of the papers, number of figures or colors

INTERNATIONAL JOURNAL OF IJCOE COASTAL, OFFSHORE & ENVIRONMENTAL ENGINEERING

Aims of IJCOE

Hydrodynamics

Marine equipment

Structural mechanics

Ocean environmental predictions

Stochastic calculations Experimental

Automatic Control of Marine Systems

Scope of IJCOE

Marine Hazards

Ocean Acoustics

Naval Architecture

Ocean Engineering

Coastal Engineering

Marine Meteorology

Marine Earth Sciences

Underwater Technology

Marine Renewable Energy

Polar & Arctic Engineering

Marine Renewable Energy

Marine Geography & Geodesy

Marine Environmental Engineering

Automatic Control of Marine Systems

Hydro Physics & Physical Oceanography

Type of papers

- Case Studies
- Book Reviews
- Review Article
- Letters to the Editor
- Methodology Papers
- Editorials and Commentaries
- Response or Rejoinder Papers
- Perspective or Opinion Papers
- Conceptual or Theoretical Papers
- Meta-Analysis and Systematic Reviews
- Short Communications or Brief Reports
- Research Articles (Original Research Papers)

Scientific Research Journal

Ministry of Science, Research And Technology (MSRT)

Jurnal Ranking 2023: A

Ministry Of Science, Research And Technology (ISC)

Citation Impact 2022: 0.429

Quartile 2022 : Q1

Core Collection



IJCOE is a Member of



Cantact Us

Office 1 | Research Institute of Meteorology and Atmospheric Science

Address | Tehran, Shahid Kharrazi Highway, Pajoohesh Blvd, Research Institute of Meteorology and Atmospheric Science, Sand and Dust Storm International Research Center (SDS-IRC), No. 13, 1st floor.

Phone | +982144787652

Postal code | 13611-14977

website | www.rimac.ac.ir

Office 2 | Iranian National Institute for Oceanography and Atmospheric Science

Address | Tehran, Dr. Fatemi Gharbi St., Shahid Etemadzade St., No. 3, third floor.

Phone | +982166944873

Postal code | 13389 – 14118

website | www.inio.ac.ir

Email | Info@ijcoe.org

Website | www.ijcoe.org

Follow Us

www.ijcoe.org

INTERNATIONAL JOURNAL OF IJCOE COASTAL, OFFSHORE & ENVIRONMENTAL ENGINEERING

Volume & Issue:

Volume 11, Issue 3, JUNE 2026

Number of Articles: 8

Content

Experimental study of gas flow regime criteria in underwater gas-saturated liquid blowouts Maryam Bafandeh, Abbas-Ali Ali Akbari Bidokhti, Mojtaba Ezam, Majid Ghodsi Hasanabad, Sara Allahyari Beyk	1
Changes of Physical Parameters of the Water Column from the Indian Ocean to the Persian Gulf Parvaneh Sobhani *, Mahyar Majidi Nik	17
Hybrid Intelligence for Coastal Pattern Recognition: ANFIS-Based Prediction of Multi -Level Beach Cusp Spacing Azadeh Valipour, Hossein Shirgahi	34
Numerical simulation of bottom outlet valve openings and reverse slope transition to control downstream pressure drop in pipeline of effluent discharge to sea Saeed Madadyari, Mehdi Nezhadnaderi, Babak Fazli Malidareh	48
Data-Driven Assessment and Forecasting of Port Services Demand: A Case Study of Shahid Rajaee Por Pouria Rafati, Seyede Masoome Sadaghi, Ali Fakher	56
A Critical Review of Challenges and opportunities in Using Remote Sensing and Image Processing for Rip Current Studies Azadeh Valipour	69
The failure probability of reinforced concrete marine structures and cost optimization of maintenance Abdolhossein Mohammadrahimi, Afshin Ghasri, Mesbah Sayebani, Akbar Esfandiari	86
The Role of Standards in Maritime-Based Development: An Analysis of Challenges in Iran's Maritime Industry Amir Nezam Barati, Ali Sheykh Bahaei , Meysam Bali, Ali Alimohamadpour	98

INTERNATIONAL JOURNAL OF IJCOE COASTAL, OFFSHORE & ENVIRONMENTAL ENGINEERING

INTERNATIONAL JOURNAL OF
COASTAL, OFFSHORE & ENVIRONMENTAL ENGINEERING IJCOE Vol.11/No. 3/Summer 2026(1-16)

Available online at: www. Ijcoe.org

Experimental study of gas flow regime criteria in underwater gas-saturated liquid blowouts

Maryam Bafandeh[1], Abbas-Ali Ali Akbari Bidokhti[2], Mojtaba Ezam[3], Majid Ghodsi Hasanabad[4], Sara Allahyari Beyk[5]

[1]Department of Physical Oceanography, Tehran Science and Research Branch, Islamic Azad University, Tehran, Iran, maryam.bafandeh88@gmail.com
[2]Professor, Institute of Geophysics, University of Tehran, Tehran, Iran, bidokhti@ut.ac.ir
[3]Associate Professor, Department of Physical Oceanography, Tehran Science and Research Branch, Islamic Azad University, Tehran, Iran, ezam@srbiau.ac.ir
[4]Associate Professor, Department of Mechanical Engineering, Tehran Science and Research Branch, Islamic Azad University, Tehran, 1477893855, Iran
[5]Department of Physical Oceanography, Tehran Science and Research Branch, Islamic Azad University, Tehran, Iran, s.allahyaribeik@gmail.com

ARTICLE INFO

Article History:
Received 12 Jan 2026
Accepted 8 June 2026
Available online ….

Keywords:
Bubbly Jet
Multiphase Flow
Underwater Blowout
Oil and Gas blowout
Underwater Waste Disposal

ABSTRACT

In a series of laboratory experiments, CO_2-saturated freshwater at different volumetric gas to liquid ratios (GLR) and different flow momentums was injected at the bottom of square cross-section open-top basins filled with homogeneous saltwater as well as stratified saltwater. Flow visualization of the experiments and comparison of different criteria for discerning the gas flow regimes showed that Wallis (1969) critical velocity criterion and Payne and Prince (1975) modified Froude number criterion are more suitable to distinguish the gas flow regimes in gas-saturated liquid blowouts. The other evaluated criteria of modified Froude number, Reynolds number, and modified Weber number, overestimate the ratio of inertia and bubble destructive forces to breakup resisting forces in gas-saturated liquid blowouts. It seems that off-source rapid formation of a huge number concentration of minute bubbles in the zone of flow establishment and momentum-driven region decreases the inertia and bubble destructive forces in gas-saturated liquid blowouts when compared to bubbly jets of similar GLR and flow rates.

1- INTRODUCTION

Discerning the gas flow regime in liquid basins has significant implications in the industry. Jet instabilities and dispersed phase break-up processes have been widely studied in different aspects of science and applications, including (but not limited to) water treatment, metallurgy, chemical engineering, and environmental engineering (Oguz & Prosperetti, 1993). In liquid-gas systems, fluid dynamics of the dispersed phase, the liquid-gas force coupling, and the mass transfer rate depend on the bubble size and the amount of contact surface between two immiscible fluids; as such, the core of numerical models simulating such processes is the flow regime and breakup processes of the dispersed phase in the basin (Sun, Cao, Liang, & Bian, 2020).

One of the implications areas of jet instability studies is in marine applications such as CO_2 sequestration in oceans as well as marine accidental underwater oil and gas blowouts. Generally, in live-oil underwater blowouts from offshore facilities, some amount of gas partitions from the live oil. Meanwhile, stratification in the water column may cause the pollutant plume to peel and trap at finite heights. In stratified plumes, the volumetric ratio of gas phase to liquid phase (GLR) and the slip velocity of bubbles, which in turn is a function of bubble size, can significantly affect the dynamics of the pollutant plume.

Zhao et al. (2016) used the numerical model VDROP-J (L. Zhao et al., 2014) to simulate the processes of gas separation, bubble formation, dissolution, expansion, and fate of bubbles in underwater oil blowouts. They showed that minute bubbles would dissolve in seawater bulk while the bubbles that are bigger than a certain estimable size would reach the sea surface. Encountering different physical-chemical processes they argued that bubble size is the key factor in determining the bubbles fate, whether they reach the surface, dissolve in liquid phase or form hydrates.

Fate of bubbles in gas-liquid plumes directly affects plume peeling and trapping heights and consequently plays a crucial role in plume surfacing time, surfacing location and the pollutant distribution on sea surface. As such determining the gas phase break-up processes in accidental underwater oil and gas blowouts is important for predicting the environmental impact of the accident, risk assessment and response planning.

Contrary to deepwater blowouts where the contaminant plume most likely would trap below sea surface (Johansen, Brandvik, & Farooq, 2013) the effect of bubble size on increasing the plume peeling and trapping heights is more significant in moderate and shallow waters. As such a proper estimation of gas phase flow regime and bubble size distribution is crucial for realistic oil and gas plume fate prediction and estimating the extent of contaminant distribution on the sea surface.

Different criterions for the prediction of gas flow regimes (jetting, transitional, or bubbling) in gas-saturated liquid blowouts in stagnant waters are evaluated in this research, using a series of laboratory experiments. Based on the findings of this research, it is possible to predict the gas flow regimes in underwater live oil blowouts and conduct a pre-assessment. Knowledge about the qualitative behavior of the pollutant plume and quantitative estimation of oil and gas surfacing time, surfacing distance from the blowout point, and the extent of pollutant distribution on the sea surface are important for safety-related and environmentally-related applications.

The innovative approach of the present study lies within the experimental method where gas-saturated liquid is released in the basin to qualitatively investigate the effect of off-source bubble formation on gas flow regime during gas-saturated liquid blowouts (Brandvik et al., 2015) the majority of previous experimental studies were conducted by simultaneous gas pumping and liquid pumping aiming to inject the gas in liquid pipeline downstream to release point for mixing the gas flow with the liquid flow.

1-1 The effect of Bubble sie distribution on plume dynamics

Flow properties, geometry of the blowout opening, seawater density, viscosity, and surface tension are some of the major variables that cause a certain plume GLR to produce different sizes of gas bubbles. The effect of changes in these criterions on dynamic parameters of single-phase gas plumes and two-phase gas-liquid plumes in liquid basins has been the subject of several experimental and numerical research (Bafandeh, Bidokhti, Lari, & Ezam, 2022; Brandvik et al., 2015; Socolofsky & Adams, 2005; Sun et al., 2020; L. Zhao et al., 2017; L. Zhao et al., 2014).

In stratified two-phase gas-liquid plumes, gas bubbles separate from the entrained seawater plume and tend to lift the liquid phase further upward in the water column than the level of neutral buoyancy (trapping height). That is due to the imparted energy from gas bubbles to the liquid phase as a function of bubble slip velocity. Thereafter, the plume will continue to rise above the trapping height until it reaches a peeling height, where dispersed phase buoyancy can no longer lift the entrained seawater (Socolofsky, Adams, & Sherwood, 2011).

In two-phase gas-liquid blowouts, the size of bubbles directly affects the slip velocity of the bubbles relative to the rest of the plume fluids. Momentum exchange between gas phase and liquid phase per unit volume Φ is the opposite of the sum of the momentum transfer rate of forces exerted by liquid on bubbles present in unit volume (Eq. 1). The exerted forces can be listed as drag force, D, lift force, L, virtual mass force, VM, Basset history, H, and the gravity and far-field pressure contributions, $F_G + F_P$ (Delnoij, Kuipers, & van Swaaij, 1997).

$$\Phi V_{cell} = \sum_i (F_{Di} + F_{VMi} + F_{Li} + F_{Hi} + F_G + F_P) \quad (1)$$

The forces acting from bubbles to the liquid are attributed to bubble size, either directly or through the bubble slip velocity (U_{si}), which in turn is also related to the size of bubbles (Delnoij et al., 1997).

Lift force and Basset history force are of several orders of magnitude smaller than drag force and other applied forces in Eq.1 and can be neglected in calculations of bubbly plumes dynamics (Delnoij et al., 1997; L. Zhao et al., 2017). Accordingly, Zhao et al. (2017) formulated the impact of bubbles on the mixing energy of the jet/plume systems (Eqs. 2 and 3).

$$\varepsilon_i = \frac{F_{imposed} U_{si} N_i}{\rho_c} \quad (2)$$

$$F_{imposed} = \frac{1}{2} C_D A_b \rho_C |U_b - U_c|(U_b - U_c) + \frac{1}{2} m_c \left(\frac{dU_b}{dt} - \frac{dU_c}{dt}\right) \quad (3)$$

Here N_i $(number\ of\ bubbles/m^3)$ is the number concentration of bubbles with a specific size d_i in the volume of water in concern. ε_i is the energy dissipation rate generated from the rise of this group of bubbles, C_D is the drag coefficient, and A_b is the projected area of the bubble (m^2). U_b and U_c are the velocity of bubbles and continues phase respectively (m/s), m_c is the added mass of the liquid which in the absence of bubbles is accelerated and ρ_c is the density of the continues phase.

One of the major influential factors on number concentration of bubbles and size of bubbles in gas-saturated liquid blowouts is the gas flow regime of the blowout. Bubbling gas flow regime may produce large bubbles with lower number concentration of bubbles while jetting regime develops small bubbles with higher number concentration of bubbles.

1-2 Gas flow regime criterions in Gas-saturated liquid blowouts in stagnant water

Blowout flow specifications and ambient conditions (pressure, temperature, cross flows, etc.) have major effects on the bubbling regime of plumes, while the shape, surface roughness, and size of the opening also play significant roles in bubble size and number concentration of bubbles (Goda, Iguchi, Sasaki, & Kiuchi, 2005; Kubasch, 2001; Tsuge, Tezuka, & Mitsudani, 2006).

Irrgang et al (2012) classified the gas flow regimes in liquid basins into three main categories of static bubbling, dynamic bubbling, and jetting regimes. They studied Payne and Prince (1975) and Hoefele and Brimacombe (1978) correlations of gas flow regime transition in liquid basins as two of the most commonly accepted correlations. They argued that in the static bubbling regime, the equality between surface tension and bubble buoyancy forces plays a significant role in the bubble formation process and also stated that bubble volume is governed by the orifice diameter and surface roughness, independent from the gas flow rate.

Oguz and Prosperetti (1993) introduced a critical value for gas flow rate (Q_{cr}) above which the gas bubble radius at detachment is proportional to $Q^{2/5}$ where Q is the gas flow rate, D_0 is the nozzle internal diameter, σ is the liquid surface tension, ρ is the liquid density, and g is the gravitational acceleration (Eq.4).

$$Q_{cr} = \pi \left(\frac{16}{3g^2}\right)^{\frac{1}{6}} \left(\frac{\sigma D_o}{\rho}\right)^{\frac{5}{6}} \quad (4)$$

In Oguz and Prosperetti (1993) correlation, for $Q < Q_{cr}$ the bubble radius can be as small as Fritz radius R_F (Eq. 5) where the buoyancy and surface tension forces are in balance. Oguz and Prosperetti (1993) argued that for static bubbling regime, R_F is the smallest possible bubble radius in quiescent water detached from a nozzle with a given internal diameter of D_0.

In a dynamic bubbling regime, both bubble volume and frequency of bubble formation increase with increasing the gas flow rate. For $Q > Q_{cr}$ Oguz and Prosperreti correlation for radius of the bubbles is proportional to gas flow rate (Eq.6),

$$R_F = \left(\frac{3}{2}\frac{\sigma D_o}{\rho g}\right)^{\frac{1}{3}} \quad (5)$$

$$\bar{R} = \left(\frac{9}{8\pi^2}\frac{Q^2}{g}\right)^{\frac{1}{5}} \quad (6)$$

Payne and Prince (1975) correlation (Eqs. 7 and 8) is based on the relation between the

modified Froude number Fr^* and the ratio of basin liquid height H to the orifice diameter D_o, above which jetting regime will occur.

$$\frac{H}{D_o} = 1.5Fr^* \quad (7)$$

$$Fr^* = U_0\sqrt{\rho_g/(D_o g(\rho_l - \rho_g))} \quad (8)$$

Hoefele (1978) criterion is based on the correlation between Mach number $M' = U_0/C$ and density ratio of liquid and gas phases above which jetting regime occurs (Eq.9). Here C is the speed of sound in air

$$M'\left(\frac{\rho_g}{\rho_l}\right)^{0.5} = 0.009 \quad (9)$$

Bubbling process in gas-saturated liquid blowouts starts at pressure drop points and the amount of released gas is relative to the gas solubility in liquid at initial pressure and decreased pressure (Gros, Reddy, Nelson, Socolofsky, & Arey, 2016). In underwater blowouts, pressure drop may happen during pipeline transfer (due to pipe internal friction, change of cross section area, fittings, etc) and across the plume source nozzle (due to orifice effect). Additionally, since neither water nor bubbles are clean even in laboratory (L. Zhao et al., 2017) another form of gas separation commences after the release in ambient water (off-source bubble formation). This form can be considered similar to formation of bubbles with phase change which involves an initial state of a gas dissolved in liquid and later stage of bubble formation (nucleation), similar to boiling or cavitation processes (Clift, Grace, & Weber, 2005). The radius of bubbles formed in bubble nucleation can be estimated by surface tension of ambient fluid and the internal pressure of bubbles at local pressure (Eq.10). In off-source bubble formation, internal pressure of bubbles compensates the surface tension (σ) of the ambient liquid (Clift et al., 2005).

$$d_{eq} = 4\sigma/(P_v + P_g - P_l) \quad (10)$$

Here d_{eq} is the bubble's equivalent diameter, P_g is the partial pressure of non-condensable gas, P_v is the vapor pressure of the liquid at a given temperature, and P_l is the local pressure.

Off-source bubble formation is a time, pressure, and temperature dependent process and happens after the release of gas-saturated fluid from the nozzle (Gros et al., 2016) at the bubbly jet region ($z > 0.1l_M$) and bubbly plume region ($z > 5l_M$).

Here $l_M = M_0^{0.75}/F_0^{0.5}$ is the characteristic plume length, z represents the axial distance from the plume source, and M_0 and F_0 are the kinematic momentum and buoyancy flux of the blowout at the source, respectively (Lima Neto, 2012) Contrary to off-source bubble formation, pressure drop through the pipeline and bubble formation due to pressure drop across the plume source nozzle will cause the plume flow to become effervescent at the blowout nozzle. Based on flow and ambient parameters, there can be three different flow regimes of bubbling (static), transitional (dynamic bubbling), or jetting (atomization) release. Wallis (1969), Payne and Prince (1975), Hoefele and Brimacombe (1979) and Zhao and Iron (1990) criterions are each cited in different occasions by different researchers as the correlations commonly accepted for discerning the gas flow regime in underwater blowouts (Bie, Ye, & Hao, 2016; Cai, Shen, Shen, & Dai, 2010; Irrgang, Hinrichsen, & Lau, 2012; Kubasch, 2001; Miao et al., 2018). While each of the criterions are applicable in certain flow and ambient conditions, there might be cases that none of the criterions can define changes of flow patterns from bubbling to jetting regime (Kubasch, 2001).

Wallis (1969) has pointed on a critical gas flow velocity from the nozzle tip ($U_{0critical}$) above which jetting regime occurs (Eq.11).

$$U_{0critical} = 1.25\left[\frac{4\sigma}{g(\rho_{liq}-\rho_{gas})D_0^2}\right]^{0.5}\left[\frac{g\sigma(\rho_{liq}-\rho_{gas})}{\rho_{gas}^2}\right]^{0.25} \quad (11)$$

Here σ is the surface tension of the ambient liquid and D_o is the nozzle tip diameter.

When the flow velocity at the plume source nozzle is low, the interface of the gas phase with ambient water is smooth, and the flow falls in a bubbling regime. Zhao and Iron (1990) showed that when the flow Weber

number exceeds the critical Weber number ($We_{critical}$), the bubbles' surface starts to ripple and bubbles start to break into small gas particles. Small gas particles are then pushed into the liquid phase, while the liquid is also pushed into the gas phase. The small droplets pushed into the gas phase are easily accelerated, and thus the gas momentum is transferred to the liquid droplets. This momentum can elongate the bubble and disrupt the interface of gas bubbles with liquid even further. The mixture of gas and liquid droplets can then push deeply into the liquid. Therefore, discrete bubble release transforms to continuous gas flow and consequently the flow falls into the jetting regime. The critical Weber number above which the jetting regime starts is given in Eq.12 (Y.-F. Zhao & Irons, 1990):

$$We_{critical} = \frac{\rho_{gas}\, U_0^2\, D_0}{\sigma} \geq 10.5 \sqrt{\frac{\rho_{liq}}{\rho_{gas}}} \qquad (12)$$

Martinez-Bazan et al. (1999) suggest that high values of Ohnesorge number ($Oh = \mu/(\rho\sigma D)^{1/2}$) and Reynolds number ($Re = \rho UD/\mu$) are required for jetting (atomization) regime. Johanson et al (2013) plotted the result of Neto et al. (2008) experiments of bubbly water jets on Ohnesorge vs. Reynolds number diagram and found that it is promising that the transition lines of constant Weber number derived from single liquid flows, also applies to bubbly jets and the mean bubble size. Johansen et al. (2013), after Tang and Masutani (2003) used boundaries of constant Weber numbers $We = c^2$ between laminar and transitional breakup regimes ($c = 5.5$) and between transitional and turbulent (atomization) breakup regimes ($c = 18$) in liquid-liquid jet blowouts ($We = \rho_{jet\ fluid}\, U_0^2\, D_0/\sigma$). Here, c is a constant of proportionality.

Hoeffel and Brimacombe (1979) used the correlation of Mach number with gas to liquid density ratio (Eq.9) and developed a bubble-jet behavior diagram based on the gas to liquid density ratio and the modified Froude number. Using the density ratio of the gas phase to the liquid phase on the diagram and delineating the modified Froude number of a gas flow in a liquid basin, one can easily find out whether the flow falls in the bubbling, transitional or jetting regime. The modified Froude number as used in Hoefele and Brimacombe (1979) criterion is given in Eq.13.

$$F_{rm} = \frac{\rho_{gas} U_0^2}{g(\rho_{liq} - \rho_{gas}) D_0} \qquad (13)$$

Krishnapisharodi and Iron (2013) suggested that the modified Froude number, as a function of gas flow rate (Eq.14), would also be a comprehensive characteristic for underwater gas jets.

$$F_{rm} = \frac{\rho_{gas} Q^2}{g(\rho_{liq} - \rho_{gas}) D_0^5} \qquad (14)$$

They also argued that the modified Froude number is not an appropriate characteristic for use in buoyancy driven plumes where the injected momentum is dissipated within a very short distance from the nozzle (Krishnapisharody & Irons, 2013).

The above criterions have been widely used in several industrial applications and research. Most of the previous researches were conducted based on single-phase gas flow injection at the bottom of the liquid basin, or as mentioned earlier in the present report, two-phase experiments were based on producing bubbly jets by combining gas pumping with liquid pumping within the pipeline. In the experiments of the present research, first of all, the liquid was saturated with different pre-defined gas concentration ratios, and then the gas-saturated liquids were injected at different flow rates at the bottom of the liquid basin. Laboratory experiments were visually analyzed for qualitative evaluation of gas flow regime criterions in gas-saturated liquid blowouts.

2- MATERIAL AND METHODS

A series of laboratory tests was conducted in a transparent plexiglass square cross-section open-top basin of 1.20×0.45×0.45 m dimensions, which was filled with homogenous or stratified saltwater up to the level of 1.05 m height (height to width aspect ratio = 2.33).

Plume flow was produced by a 12-liter pressurized vessel filled with tap water ($\rho = 998.5\, kg/m^3$ at $T = 20$ ℃), colored by food-

grade colors and pressurized with CO_2 gas (99% purity). The laboratory experiment setup is schematically shown in Fig. 1.

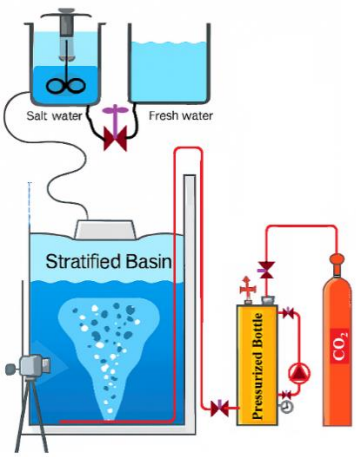


Fig.1 Schematic diagram of the setup for laboratory experiments.

After saturation of water with CO_2 at a pressure of 5 kg/cm^2 in the pressurized vessel, the pressure of the vessel was decreased to 1 kg/cm^2, 2 kg/cm^2 and 3 kg/cm^2 for different test groups of 1bar, 2bar, and 3bar, respectively. The pressure of the vessel was maintained constant at the desired pressures with an adjustable pressure relief and an adjustable pressure regulating valve.

The constant vessel's internal pressures were used to pump out the colored and CO_2-saturated water through a series of hoses and copper tubes to the bottom of the stratified basin, where a circular hole of 3.5 mm in diameter was prepared in a vertical upward direction. The photo of experimental setup in the laboratory is shown in Fig 2.



Fig.2 Experimental setup for gas flow visualization in the laboratory.

3- RESULTS AND

A total number of 30 experimental tests were conducted. The experiments were recorded with ~10 frames per second photography (596 fpm), and images were analyzed visually on a mesh grid of 2.5 mm resolution. Bubbles diameter in laboratory experiments was roughly measured using a 2.5 mm mesh grid, as a precise bubble diameter was not required to investigate the gas flow regimes. The list of different groups of experiments is given in Table 1, and samples of flow visualizations of gas-saturated liquid blowouts in stratified basins are shown in Fig. 3. The bubble formation in the test setup is shown in Fig. 4.

Table 1. list of laboratory experiments

Test Group	Test No.	Flow rate (m^3/s)	CO_2 saturation pressure (Kg/cm^2)	Density of the plume fluid (Kg/m^3)	Reynolds number	Plume GLR at nozzle tip	Temperature (°C)	Basin's bottom layer salinity (ppt)	Buoyancy frequency of the basin (s^{-1})
1bar	T-5	0.0000429	1	1001	15603	0.131	15.4	15	0.283
1bar	T-6	0.0000429	1	1001	15603	0.131	18	25	0.323

1bar	T-7	0.0000429	1	1001	15603	0.131	12.8	36	0.395
1bar	T-8	0.0000429	1	1001	15603	0.131	21	45	0.437
1bar	T-9	0.0000429	1	1001	15603	0.131	16.7	45	0.441
1bar	T-10	0.0000429	1	1001	15603	0.131	18	55	0.460
1bar	T-12	0.0000429	1	1001	15603	0.131	20	35	0
1bar	T-13	0.0000429	1	1001	15603	0.131	20	35	0
2bar	T-17	0.0000645	2	1001	23459	0.235	14	35	0
2bar	T-18	0.0000645	2	1001	23459	0.235	14	35	0
2bar	T-19	0.0000645	2	1001	23459	0.235	20	35	0
2bar	T-20	0.0000645	2	1001	23459	0.235	15.6	25	0.332
2bar	T-21	0.0000645	2	1001	23459	0.235	12	36	0.438
2bar	T-23	0.0000645	2	1001	23459	0.235	18.2	45	0.433
3bar	T-26	0.0000811	3	1001	29498	0.335	12	35	0
3bar	T-27	0.0000811	3	1001	29498	0.335	12	35	0
3bar	T-30	0.0000811	3	1001	29498	0.335	13	36	0.431

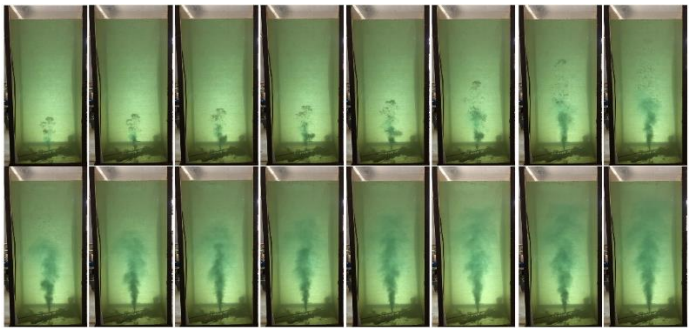


Fig.3 Sample flow visualization of gas-saturated in stratified basin

Flow visualization of 1bar test group experiments clearly depicts the presence of small bubbles of order of $10^{-4}m$ or less in diameter, along with large bubbles of order of $10^{-3}m$ in diameter within the plume. Large bubbles were continually generated from effervescent flow due to gas separation from liquid through the pipeline and across the nozzle.

These bubbles were ascending and separating from the liquid plume during the whole test duration. However, only in the initial frames of 2bar and 3bar test groups some large bubbles of order of $10^{-3}m$ in diameter were seen.

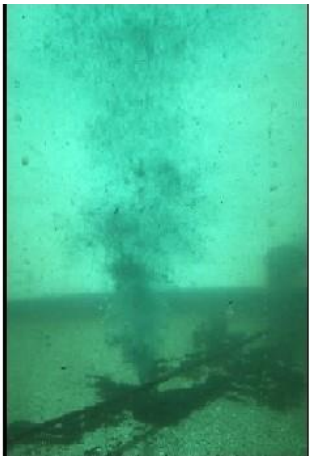


Fig.4 Bubble formation from effervescent flow in stratified water column

In 2bar and 3bar test groups, the large bubbles that were ascending to the surface disappeared after a few seconds (5 to 6 seconds), and the rest of the bubbles generated in these test groups were of order of $10^{-4}m$ or less in diameter, as the experiments were continued. The initial large bubbles of 2bar and 3bar test groups can be considered as the result of some amount of air that might had been trapped in the pipeline prior the initiation of each experiment. Presence of these few bubbles for a short duration of time can be eliminated from the experimental results. Flow visualization of the experiments and presence of almost irregular sizes of bubbles in 1bar test group suggest that this test group falls in dynamic (transitional) gas flow regime while

2bar and 3bar test groups with relatively uniform minute bubbles fall in jetting (atomizing) regime (Lima Neto, 2012).

For the case of two phase gas-liquid blowouts, Johansen et al. (2013) findings imply that a situation with a gas volume fraction (n) and a liquid volume flow (Q_L) might be represented by a liquid only experiment with an adjusted equivalent liquid volume flow $Q_E = Q_L/(1-n)^{1/2}$ and equivalent liquid only velocity $U_E = U_L/(1-n)^{1/2}$. Here gas volume fraction (n) is defined as the ratio of the gas flow rate (Q_G) to the total gas–liquid mixture flow rate at the nozzle, $n = Q_G/(Q_L + Q_G)$, and U_L is the liquid only velocity. In gas-saturated liquid blowouts of present experiments, the amount of the gas released through the pipeline and across the plume source nozzle was originally dissolved in the liquid. Assuming that in an effervescent liquid flow, the contribution of the gas phase to the momentum flux (due to the much smaller density of the gas) is negligible (Brandvik et al. 2014) we can consider the gas volume fraction (n) equal to the plume GLR at nozzle tip (Table 1).

Zhao et al. (2017) developed an expression based on the work of Johansen et al. (2013), for the equivalent liquid only exit velocity $U_{E,LO}$ and equivalent liquid only exit flow rate $Q_{E,LO}$ (Eq.15 and 16)

$$U_{E,LO} = (U_L + U_G)(1 - n\left(1 - \frac{\rho_G}{\rho_L}\right))^{1/2} \quad (15)$$

$$Q_{E,LO} = (Q_L + Q_G)(1 - n\left(1 - \frac{\rho_G}{\rho_L}\right))^{1/2} \quad (16)$$

Where U_L and U_G are the velocity of liquid phase and gas phase in the mixture respectively (m/s), $U_L = \frac{Q_L}{A_{Exit}}$, $U_G = \frac{Q_G}{A_{Exit}}$, $Q_L$and Q_G are the liquid and gas flow rates (m^3/s) respectively, ρ_L and ρ_G are the liquid and gas densities (kg/m^3) respectively and A_{Exit} is the cross section area of exit nozzle. Using Eqs. 15 and 16 the equivalent liquid only velocity of 1bar, 2bar and 3bar test groups are 4.701 (m/s), 7.243 (m/s) and 9.181 (m/s) respectively and the equivalent liquid only flow rates are 0.00004523 (m^3/s), 0.00006969 (m^3/s) and 0.00008833 (m^3/s) respectively.

To compare the application of mostly accepted flow regime criterions for discerning the flow regimes in gas-saturated liquid blowouts of present experiments, the criterions were applied to flow specifications of present laboratory experiments. The results of the flow regime criterions on underwater gas-saturated liquid blowouts of present research are summarized in Table 2. Table 2 shows the outputs of the correlations when equivalent liquid only flow specifications are considered as the dispersed phase characteristics in the correlations (eg. velocity, flow rate, density, etc.).

Table 2. Gas flow regime criterions in experimental results using equivalent liquid only velocities and flow rates.

salinity ppt	Characteristic	Criterion	Lower limit for Jetting regime	1bar test group	2bar test group	3bar test group
25	Critical Velocity	Wallis Critical Velocity criterion	7.121	4.701	7.243	9.181
25	Mach number	Hoefele and Brimacombe nominal Mach number criterion	0.00907	0.0137	0.0211	0.0267
25	Weber number	Zhao and Iron critical Weber number criterion	238.025	1063.91	2525.17	4056.50
25	Weber number	Tang and Masutani modified Weber number criterion	324	1063.91	2525.17	4056.50
25	Modified Froude number	Hoefele and Brimacombe velocity based modified Froude number criterion	185	39061	92711	148934
25	Modified Froude number	Hoefele and Brimacombe flow rate based modified Froude number criterion	185	390.7	927.3	1489.7
25	Modified Froude number	Payne and Prince modified Froude number criterion	200	197.6	304.4	385.9
35	Critical Velocity	Wallis Critical Velocity criterion	7.159	4.701	7.243	9.181
35	Mach number	Hoefele and Brimacombe nominal Mach number criterion	0.00910	0.0137	0.0211	0.0267
35	Weber number	Zhao and Iron critical Weber number criterion	238.78	1054.10	2501.90	4019.12
35	Weber number	Tang and Masutani modified Weber number criterion	324	1054.10	2501.90	4019.12
35	Modified Froude number	Hoefele and Brimacombe velocity based modified Froude number criterion	185	28022	66510	106844
35	Modified Froude number	Hoefele and Brimacombe flow rate based modified Froude number criterion	185	388.2	921.5	1480.3

35	Modified Froude number	Payne and Prince modified Froude number criterion	200	167.3	257.8	326.87
45	Critical Velocity	Wallis Critical Velocity criterion	7.376	4.701	7.243	9.181
45	Mach number	Hoefele and Brimacombe nominal Mach number criterion	0.00913	0.0137	0.0211	0.0267
45	Weber number	Zhao and Iron critical Weber number criterion	239.71	1010.22	2397.74	3851.79
45	Weber number	Tang and Masutani modified Weber number criterion	324	1010.22	2397.74	3851.79
45	Modified Froude number	Hoefele and Brimacombe velocity based modified Froude number criterion	185	20790	49346	79271
45	Modified Froude number	Hoefele and Brimacombe flow rate based modified Froude number criterion	185	385.9	916.1	1471.6
45	Modified Froude number	Payne and Prince modified Froude number criterion	200	144.1	222.1	281.5
55	Critical Velocity	Wallis Critical Velocity criterion	7.458	4.701	7.243	9.181
55	Mach number	Hoefele and Brimacombe nominal Mach number criterion	0.00917	0.0137	0.0211	0.0267
55	Weber number	Zhao and Iron critical Weber number criterion	240.64	992.98	2356.82	3786.07
55	Weber number	Tang and Masutani modified Weber number criterion	324	992.98	2356.82	3786.07
55	Froude number	Hoefele and Brimacombe velocity based modified Froude number criterion	185	16525	39224	63010
55	Froude number	Hoefele and Brimacombe flow rate based modified Froude number criterion	185	383.0	909.05	1460.3
55	Froude number	Payne and Prince modified Froude number criterion	200	128.5	198.05	251.01

Using the equivalent liquid only velocities and flow rates, Wallis (1969) criterion for critical velocity discerns the gas flow regimes of all test groups in stratified basins filled with saltwater of salinity of 25 ppt and 35 ppt at bottom layer. However, in stratified basins filled with saltwater of salinity of 45 ppt and 55 ppt at bottom layer, although the criterion discerns the flow regimes of 1bar and 3bar test group experiments, it does not distinguish the change of flow regime from 1bar to 2bar test group.

Modified Weber number in Zhao and Iron (1990) as well as Tang and Masutani (2003) criterions, determine all test groups in fully developed jetting regime. The modified Weber number in these criterions are of order of 10^3 which is well above the expected limits to distinguish the change of flow regime from 1bar test group to 2bar test group (ranging between 238.78 and 324 for different experiments).

Modified Froude number as introduced by Hoefele and Brimacombe (1979) as well as nominal Mach number criterion (Hoefele & Brimacombe, 1979) predict all test groups in jetting regime. Use of velocity based modified Froude number correlation results in figures of order of 10^4 against the expected limit of ~ 185 (non-dimensional) to distinguish the change of flow regime. However the modified Froude number correlation based on flow rate, results in figures of order of 10^2. The range of resulted modified Froude numbers from the correlations based on jet flow rate are more acceptable than the velocity based modified Froude number.

Payne and Prince (2003) criterion of modified Froude number results in close discerning of gas flow regimes in all test groups with the basin bottom layers of 25 ppt, 35 ppt and 45 ppt. However, with the basin bottom layer of 55 ppt, although it discerns the flow regimes of 1bar and 3bar test groups experiments, it could not distinguish the change of flow regime from 1bar to 2bar test groups.

The above results were obtained by using the equivalent liquid only flow as the dispersed phase characteristics in the subjected correlations. In Table 3 the correlations output by using the equivalent gas only flow rates and velocities are listed. To obtain the equivalent gas only flow rates and velocities, the momentum exerted by liquid part of the flow is replaced with the equivalent momentum of gas if the only flowing fluid in jet was the gas phase. The following correlation (Eqs. 17 and 18) are derived from the principle of conservation of momentum flux. In the following, M_g and M_l are the exit momentum flux of gas phase and liquid phase in the bubbly water jet respectively and $M_{E,GO}$ is the momentum flux of an equivalent gas only jet. The equivalent gas only velocity is then defined as the velocity of a pure gas jet producing the same momentum flux as the bubbly water jet:

$$M_{E,GO} = M_l + M_g = \rho_l(1-n)AU^2 + \rho_g nAU^2 \quad (17)$$

$$U_{E,GO} = U\left(n + (1-n)\frac{\rho_l}{\rho_g}\right)^{\frac{1}{2}} \quad (18)$$

Here $U_{E,GO}$ is the equivalent gas only flow velocity and A is the nozzle cross section area. Using Eqs. 17 and 18 the equivalent gas only velocity of 1bar, 2bar and 3bar test groups are 93.642 (m/s), 132.116 (m/s) and 155.500 (m/s) respectively and the equivalent gas only flow rates for test groups are 0.000901 (m^3/s), 0.001271 (m^3/s) and 0.001496 (m^3/s) respectively.

Table 3. Gas flow regime criterions in experimental results using equivalent gas only velocities and flow rates.

salinity ppt	Characteristic	Criterion	lower limit for Jetting regime	1bar test group	2bar test group	3bar test group
25	Critical Velocity	Wallis Critical Velocity criterion	7.063	93.642	132.116	155.5
25	Mach number	Hoefele and Brimacombe nominal Mach number criterion	0.2040	0.2730	0.3851	0.4533
25	Weber number	Zhao and Iron critical Weber number criterion	238.02	844.0162	1680.0269	2327.376

25	Weber number	Tang and Masutani modified Weber number criterion	324	844.0162	1680.0269	2327.376
25	Modified Froude number	Hoefele and Brimacombe velocity based modified Froude number criterion	185	497.954	991.186	1373.110
25	Modified Froude number	Hoefele and Brimacombe flow rate based modified Froude number criterion	185	307.163	611.413	847.003
25	Modified Froude number	Payne and Prince modified Froude number criterion	200	22.314	31.4831	37.055
35	Critical Velocity	Wallis Critical Velocity criterion	7.159	93.642	132.116	155.5
35	Mach number	Hoefele and Brimacombe nominal Mach number criterion	0.2046	0.2730	0.3851	0.4533
35	Weber number	Zhao and Iron critical Weber number criterion	238.78	827.050	1646.255	2280.592
35	Weber number	Tang and Masutani modified Weber number criterion	324	827.050	1646.255	2280.592
35	Modified Froude number	Hoefele and Brimacombe velocity based modified Froude number criterion	185	494.787	984.882	1364.377
35	Modified Froude number	Hoefele and Brimacombe flow rate based modified Froude number criterion	185	305.209	607.524	841.616
35	Modified Froude number	Payne and Prince modified Froude number criterion	200	22.243	31.382	36.937
45	Critical Velocity	Wallis Critical Velocity criterion	7.376	93.642	132.116	155.5
45	Mach number	Hoefele and Brimacombe nominal Mach number criterion	0.2054	0.2730	0.3851	0.4533
45	Weber number	Zhao and Iron critical Weber number criterion	239.71	792.617	1577.716	2185.643
45	Weber number	Tang and Masutani modified Weber number criterion	324	792.617	1577.716	2185.643
45	Modified Froude number	Hoefele and Brimacombe velocity based modified Froude number criterion	185	490.944	977.232	1353.780
45	Modified Froude number	Hoefele and Brimacombe flow rate based modified Froude number criterion	185	302.839	602.806	835.080
45	Modified Froude number	Payne and Prince modified Froude number criterion	200	22.157	31.260	36.793
55	Critical Velocity	Wallis Critical Velocity criterion	7.458	93.642	132.116	155.5
55	Mach number	Hoefele and Brimacombe nominal Mach number criterion	0.2062	0.2730	0.3851	0.4533
55	Weber number	Zhao and Iron critical Weber number criterion	240.64	779.091	1550.794	2148.347

55	Weber number	Tang and Masutani modified Weber number criterion	324	779.091	1550.794	2148.347
55	Froude number	Hoefele and Brimacombe velocity based modified Froude number criterion	185	487.160	969.701	1343.347
55	Froude number	Hoefele and Brimacombe flow rate based modified Froude number criterion	185	300.505	598.160	828.644
55	Froude number	Payne and Prince modified Froude number criterion	200	22.071	31.140	36.651

Table 3 shows that the critical velocity criterion of Wallis (1969) predicts all the present experiments in fully developed jetting regime and Payne and Prince (1975) modified Froude number criterion with noticeable underestimation predicts all the experiments in bubbling regime. The results suggest that, using the equivalent gas only flow velocity is not applicable to Wallis critical velocity and Payne and Prince modified Froude number criterions, while by using the equivalent liquid only flow velocity, these two criterions showed to be suitable for discerning the flow regimes of present experiments

Hoefele and Brimacombe nominal Mach number criterion, velocity based modified Froude number criterion and flow rate based modified Froude number criterion as well as Zhao and Iron critical Weber number criterion and Tang and Masutani modified Weber number criterion, predict the flow regime of present research experiments in fully developed jetting regime. The resulted from these correlations when using the equivalent gas only velocities seem to be closer to the lowe limits expected from the criterions when compared with using the equivalent liquid only velocities in the correlations. Although these criterions also fail to predict the flow regimes in present experiments but contrary to Wallis critical velocity criterion and Payne and Prince modified Froude number criterion, the results of these correlations are in justifiable ranges.

4- DISCUSSION

Flow visualization of the experiments showed that the gas flow regime in 1bar test group was in transition from bubbling regime to jetting regime, containing both large bubbles and minute bubbles while in 2bar and 3bar test groups, the flow was in form of jetting (atomization) regime.

The formation process of gas bubbles is affected by surface tension, viscosity, inertia and buoyancy forces while the mechanism of bubble breakup and atomization are based on the concept that the destructive forces due to inertia and turbulence prevail over the resistance forces due to surface tension and viscosity (L. Zhao et al., 2014). Martinez-Bazan et al. (1999) suggest that for the case of submerged bubbles in turbulence water flow, the Ohnesorge number which is the ratio of viscose forces to surface tension forces is very small ($Oh < 10^{-2}$) and internal viscose deformation forces are negligible compared to surface tension forces.

Some researchers suggest that the Reynolds number ($Re > 11000$) which is the ratio of inertial forces to viscous forces is preferred to identify bubbling-

criterion for discerning the transition from bubbling to jetting regime.

Table 2 suggests that by using the equivalent liquid only velocity, Wallis (1969) critical velocity and Payne and Prince (2003) velocity based modified Froude number criterions are more suitable to predict the gas flow regime for the case of gas-saturated liquid blowouts. These two criterions distinguish the change of flow regime from 1bar test group to 2bar test group in experiments with lower bottom layer density ($1017\,kg/m^3$ and $1024\ kg/m^3$), better than

jetting regime (Cai et al., 2010). Also Neto et al. (2008) propose that a minimum value of Re = 8000 is necessary to produce bubbles of approximately uniform sizes, independent from gas to liquid volume fraction in bubbly jets. Presence of irregular bubble sizes consisting of both larger bubbles (with diameters of order of $10^{-3}\ m$) and minute bubbles (with diameters of order of $10^{-4}m$ or less) in 1bar test group experiments ($Re = 15600$) suggests that Reynolds number is not an unconditional

the other experiments with higher density at basin bottom layer (1032 kg/m^3 and 1040 kg/m^3). This is consistent with the observations of Mirsandi et al. (2019) which showed that when the liquid density is increased the buoyancy force, which aids the bubble detachment increases therefore the bubble volume and bubble detachment time decrease in favor of leaning the flow regime towards bubbling form.

Experimental results show that the modified Weber number criterion and the majority of modified Froude number criterions, which are based on inertia forces, predict 1bar test group of present research in fully developed jetting (atomizing) regime. Failure of these criterions to discern the change of flow regime from 1bar test group to 2bar test group, suggests that the overestimation of destructive forces might be a reason of this discrepancy when compared with bubbly jets produced by combining liquid pumping with gas pumping.

The lesser than expected destructive forces in gas-saturated liquid blowouts can be explained by sudden separation of gas from the liquid phase at zone of flow establishment, which happens due to sudden pressure drop at nozzle tip. Sudden gas separation from the gas-saturated liquid, forms part of the minute bubbles observed in the plume and reduces the buoyancy of the continues-phase control volume, which consequently reduces the inertia forces. It seems that off-source buoyancy enhancement caused by bubble formation in zone of flow establishment ($z < 0.1l_M$) hampers flow instabilities (Bhat and Narasimha, 1996 and Narasimha et al. 2002). Formation of tiny bubbles will continue further to zone of bubbly jet ($z > 0.1l_M$) and bubbly plume zone ($z > 5l_M$) and disrupts the turbulence and coherent eddy structures in these zones as well, whereas the role of the disrupted turbulences was to provide the lacking amount of energy to obtain the breakup of pre-deformed bubbles (Lima Neto, 2012).

Furthermore, Brandvik et al (2019) reported unexpectedly higher interfacial tensions measured from their live-oil samples that were treated with dispersants. They suggest that the unexpected high interfacial tensions were caused by emulsification due to gas expansion and surfactant interaction with the live oil during depressurization during sampling (Brandvik et al., 2015). The effect of emulsification due to sudden depressurizing and formation of a huge number of tiny bubbles in the zone of flow establishment on the resisting forces (e.g. viscosity and surface tension) requires further investigation. It is worth to note that surface-active agents are usually present in all waters even in laboratory, unless extreme care has been taken specifically to exclude them (Motarjemi & Jameson, 1978).

5- CONCLUSION

More than thirty experimental gas-saturated liquid blowouts tests were visually studied with imaging technique. The most accepted gas flow regime criterions found in literature were employed to predict the gas flow regimes of the experiments. Non-dimensional forms of the criterions for continues-phase flow specifications were defined, using both equivalent liquid only velocities and equivalent gas only velocities.

The results obtained from the criterions suggest that Wallis (1969) and Payne and Prince (1979) criterions are more suitable for discerning the gas flow regimes in gas-saturated liquid blowouts when the equivalent liquid only flow characteristics are applied.

The majority of studied criterions overestimate the ratio of bubble destructive forces (e.g., inertia force) to breakup resisting force (e.g., surface tension and viscosity) in gas-saturated liquid blowouts. The lesser destructive forces in gas-saturated liquid blowouts, when compared to the bubbly jets produced by combining gas pumping with liquid pumping, seem to be due to the effect of off-source bubble formation in the zone of flow establishment. Formation of a huge number concentration of tiny bubbles in the zone of flow establishment and bubbly jet zone causes off-source bouncy enhancement. Off-source buoyancy enhancement disrupts the instabilities, which are the destructive forces in the criterions. Furthermore, the off-source bubble formation process is continued in the bubbly jet zone (momentum-dominated region) and the bubbly plume zone (buoyancy-dominated region), which hampers the turbulence and coherent eddy structures that are the source of providing the lacking energy to obtain the breakup of pre-deformed bubbles.

A reliable estimation of gas flow regimes in live oil blowouts contributes in determining the plume dynamic behavior of pollutants in stratified seawater and can support reasonable

pollutant fate prediction and risk evaluation in offshore oil and gas leakage accidents. The results of this work can be useful for users of numerical models in real-world underwater oil and gas blowout fate prediction.

REFERENCES

[1] Bafandeh, B., Bidokhti, A., Lari, K., & Ezam, M. (2022). Experimental and numerical study of gas to liquid ratio in stratified gas-saturated liquid blowouts' plumes. *International Journal of Environmental Science and Technology, 19*(4), 2365-2378. doi:https://doi.org/10.1007/s13762-021-03343-w

[2] Bie, H.-Y., Ye, J.-J., & Hao, Z.-R. (2016). Effect of nozzle geometry on characteristics of submerged gas jet and bubble noise. *Journal of laboratory automation, 21*(5), 652-659. doi:https://doi.org/10.1177/2211068215584902

[3] Brandvik, P. J., Johansen, Ø., Farooq, U., Davies, E., Krause, D., & Leirvik, F. (2015). Subsurface oil releases–Experimental study of droplet size distributions Phase-II. *Environmental Technology, 2015*, 04-04.

[4] Cai, Q., Shen, X., Shen, C., & Dai, G. (2010). A simple method for identifying bubbling/jetting regimes transition from large submerged orifices using electrical capacitance tomography (ECT). *The Canadian Journal of Chemical Engineering, 88*(3), 340-349. doi:https://doi.org/10.1002/cjce.20295

[5] Clift, R., Grace, J. R., & Weber, M. E. (2005). Bubbles, drops, and particles.

[6] Delnoij, E., Kuipers, J., & van Swaaij, W. P. M. (1997). Dynamic simulation of gas-liquid two-phase flow: effect of column aspect ratio on the flow structure. *Chemical engineering science, 52*(21-22), 3759-3772. doi:https://doi.org/10.1016/S0009-2509(97)00222-4

[7] Goda, T., Iguchi, M., Sasaki, Y., & Kiuchi, H. (2005). Empirical equations for bubble formation frequency from downward-facing nozzle with and without rotating flow effects. *Materials transactions, 46*(11), 2461-2466. doi:https://doi.org/10.2320/matertrans.46.2461

[8] Gros, J., Reddy, C. M., Nelson, R. K., Socolofsky, S. A., & Arey, J. S. (2016). Simulating gas–liquid– water partitioning and fluid properties of petroleum under pressure: implications for deep-sea blowouts. *Environmental science & technology, 50*(14), 7397-7408. doi:https://doi.org/10.1021/acs.est.5b04617

[9] Hoefele, E., & Brimacombe, J. (1979). Flow regimes in submerged gas injection. *Metallurgical Transactions B, 10*(4), 631-648.

[10] Irrgang, C., Hinrichsen, O., & Lau, R. (2012). Effects of orifice angle and surface roughness on the bubbling-to-jetting regime transition in a bubble column. *Industrial & engineering chemistry research, 51*(11), 4445-4451. doi:https://doi.org/10.1021/ie202890u

[11] Johansen, Ø., Brandvik, P. J., & Farooq, U. (2013). Droplet breakup in subsea oil releases–Part 2: Predictions of droplet size distributions with and without injection of chemical dispersants. *Marine Pollution Bulletin, 73*(1), 327-335. doi:https://doi.org/10.1016/j.marpolbul.2013.04.012

[12] Krishnapisharody, K., & Irons, G. (2013). A critical review of the modified Froude number in ladle metallurgy. *Metallurgical and Materials Transactions B, 44*(6), 1486-1498. doi:https://doi.org/10.1007/s11663-013-9943-4

[13] Kubasch, J. H. (2001). *Bubble hydrodynamics in large pools.* ETH Zurich,

[14] Lima Neto, I. E. (2012). Modeling the liquid volume flux in bubbly jets using a simple integral approach. *Journal of hydraulic engineering, 138*(2), 210-215. doi:https://doi.org/10.1061/(ASCE)HY.1943-7900.0000499

[15] Miao, T., Liu, J., Qin, S., Chu, N., Wu, D., & Wang, L. (2018). The flow and acoustic characteristics of underwater gas jets from large vertical exhaust nozzles. *Journal of Low Frequency Noise, Vibration and Active Control, 37*(1), 74-89. doi:https://doi.org/10.1177/1461348418761688

[16] Motarjemi, M., & Jameson, G. (1978). Mass transfer from very small bubbles—the optimum bubble size for aeration. *Chemical engineering science, 33*(11), 1415-1423.

[17] Oguz, H. N., & Prosperetti, A. (1993). Dynamics of bubble growth and detachment from a needle. *Journal of Fluid Mechanics, 257*, 111-145. doi:https://doi.org/10.1017/S002211209300301

[18] Socolofsky, S. A., & Adams, E. E. (2005). Role of slip velocity in the behavior of stratified multiphase plumes. *Journal of hydraulic engineering, 131*(4), 273-282. doi:https://doi.org/10.1061/(ASCE)0733-9429(2005)131:4(273)

[19] Socolofsky, S. A., Adams, E. E., & Sherwood, C. R. (2011). Formation dynamics of subsurface hydrocarbon intrusions following the Deepwater Horizon blowout. *Geophysical Research Letters, 38*(9). doi:https://doi.org/10.1029/2011GL047174

[20] Sun, Y., Cao, X., Liang, F., & Bian, J. (2020). Investigation on underwater gas leakage and dispersion behaviors based on coupled Eulerian-Lagrangian CFD model. *Process safety and environmental protection, 136*, 268-279. doi:https://doi.org/10.1016/j.psep.2020.01.034

[21] Tsuge, H., Tezuka, Y., & Mitsudani, M. (2006). Bubble formation mechanism from downward nozzle—Effect of nozzle shape and operating parameters. *Chemical engineering science, 61*(10), 3290-3298. doi:https://doi.org/10.1016/j.ces.2005.12.002

[22] Zhao, L., Boufadel, M. C., King, T., Robinson, B., Gao, F., Socolofsky, S. A., & Lee, K. (2017). Droplet and bubble formation of combined oil and gas releases in subsea blowouts. *Marine Pollution Bulletin, 120*(1-2), 203-216. doi:https://doi.org/10.1016/j.marpolbul.2017.05.010

[23] Zhao, L., Boufadel, M. C., Socolofsky, S. A., Adams, E., King, T., & Lee, K. (2014). Evolution of droplets in subsea oil and gas blowouts: Development and validation of the numerical model VDROP-J. *Marine Pollution Bulletin, 83*(1), 58-69. doi:https://doi.org/10.1016/j.marpolbul.2014.04.020

[24] Zhao, Y.-F., & Irons, G. A. (1990). The breakup of bubbles into jets during submerged gas injection. *Metallurgical Transactions B, 21*(6), 997-1003. doi:https://doi.org/10.1007/BF02670270

INTERNATIONAL JOURNAL OF
COASTAL, OFFSHORE & ENVIRONMENTAL ENGINEERING IJCOE Vol.11/No. 3/Summer 2026 (17-33)

Available online at: www. Ijcoe.org

Changes of Physical Parameters of the Water Column from the Indian Ocean to the Persian Gulf

Mahyar Majidi Nik[1], Parvaneh Sobhani[*2]

[1] *Ph.D. student of oceanography, Researcher of the Department of Environmental Geography Studies, Madde Danesh Studies Center;majidynik@yahoo.com*
[2*] *Corresponding author, Department of Environmental Science, Natural Resources Faculty, Lorestan University, Khorramabad, Iran;sobhani.pa@lu.ac.ir.*

ARTICLE INFO

Article History:
Received 29 Jan 2026
Accepted 16 June 2026
Available online ….

Keywords:
Speed of sound propagation, Persian Gulf, Strait of Hormuz, Sea of Oman, North Indian, WOA

ABSTRACT

A comprehensive and complete understanding of how physical parameters and sound wave propagation change in different places and times is essential and inevitable. The present study examined and evaluated vertical and horizontal changes in temperature, salinity, and sound velocity parameters in the seas surrounding the country's south, including the Persian Gulf, the Strait of Hormuz, the Sea of Oman, and the northern Indian Ocean. The physical parameters of the water column in the two cold and warm seasons of the region have been monitored and analyzed at selected stations in the aforementioned seas from the surface to the bed using the international data of the World Ocean Atlas 2018. The results of the studies indicate the existence of a permanent thermocline layer in the deep regions of the Oman Sea and the northern Indian Ocean, due to which the propagation of sound waves is reduced by more than 30 units. In the Persian Gulf and the Strait of Hormuz, due to the shallowness of the region, the thermocline layer is created only in the warm season of the region, and as a result, a weak sound channel is formed at depths near the bed. It should be noted that in all the studied regions, the propagation speed of sound waves is strongly dependent on the temperature parameter and its resulting changes in the water column are similar to vertical temperature changes. Also, two-dimensional sections indicate the penetration of salty waters of the Persian Gulf into the Oman Sea in layers near the bed throughout the year.

1. Introduction

As it is known, on average, 72% of the Earth's surface is covered by water, of which more than 97% is made up of seas and oceans. There are huge mineral resources and oil in these areas, which are now being used by humans for extraction and exploitation with the advancements in science and technology [4]. The science of sound wave propagation, or sonar for short, has numerous and abundant applications in marine activities. Among its applications are remote control systems in exploration equipment, collection and reception of information obtained by autonomous submarines, establishing voice communication between divers, studies and measurements of physical and chemical parameters of water, mapping of sea and ocean beds, tracking and navigation of subsurface floating systems, and real-time notification of some natural disasters such as tsunamis [4]. Therefore, accurate modeling of sound wave propagation and investigation of environmental effects is the first step in designing and building advanced industrial and military marine systems and estimating the efficiency of equipment used at sea.

Radio waves are highly attenuated in water and have a short effective range. Therefore, to send and receive information via radio waves over long distances, carriers with very low operating frequencies are required, which in turn requires very large antennas with very high transmission power [13]. This leads to the use of wireless communications underwater based on the use of sound waves in subsurface sound channels. Sound waves have received more attention and use than other common methods of communication due to their sufficient transmission and coverage of

data transfer rates in the subsurface. Therefore, sound wave communications in the subsurface have made it possible to establish highly reliable communication over distances on the scale of several hundred kilometers [4]. The use and application of sound waves in marine topics and sciences is very effective and fruitful. However, the use of acoustic equipment in water bodies has several limitations and technical bottlenecks, including the following:

1. Information loss in the propagation path of sound waves;
2. Limitations in bandwidth selection;
3. Fading due to multipath propagation, due to multiple collisions with the surface and seabed;
4. Dependence of propagation and transmission of information on the frequency of sound waves;
5. Unknowingness' of sound channels at different times and places;
6. Delay in the propagation of sound waves due to the low speed of sound propagation compared to radio waves.

The underwater sound channel is one of the most challenging communication interfaces. Among the challenges of this environment are the low speed of sound propagation, distance and frequency dependent attenuation, noise caused by sea state and wind speed, reflection from the surface and seabed, and Doppler effects. These phenomena vary depending on the geographical conditions of the underwater environment, such as temperature, salinity, depth, etc. [10].

Many phenomena affect the propagation of sound waves underwater. The wave sent from the transmitter in this environment is subject to more severe attenuation, which depends not only on the distance but also on the frequency, and increases with increasing frequency. Part of this attenuation is due to the conversion of sound energy into heat and the other part is due to the absorption of sound energy by water molecules. On the other hand, sound waves sent underwater are combined with a lot of noise. Among these noises, we can mention noise caused by ship traffic, noise caused by sea surface turbulence, noise caused by marine organisms, and thermal noise. The effect of these phenomena is different at different frequencies. Another very important phenomenon, especially in shallow waters, is the reflection of sound waves from the surface and seabed, which causes wave multipathing. The amount of wave reflection from the seabed depends on the frequency and type of sediment. The amount of wave reflection from the sea surface also depends on atmospheric conditions, including wind speed and sea turbulence. In addition to the above, due to the low speed of sound underwater, the Doppler effect also has a significant effect on sound propagation [10].

The theory of sound wave propagation in an elastic medium can be described by solving the wave equation with respect to boundary conditions, and these waves can be evaluated as plane and spherical sound waves according to the propagation of waves in the medium. A plane wave does not exist in practice because it requires an infinite source to produce it. However, if we move far enough away from the source, the wave front (constant phase surface) becomes almost spherical, and a very small part of the surface of a large sphere is very close to a plane. The characteristics of plane waves have a certain simplicity and their study is important from a theoretical and practical point of view. Cartesian coordinates are used to study plane waves, and spherical coordinates are used for spherical sound waves [11]. The spatial and temporal characteristics of hydrophysical parameters in Dabob Bay were evaluated by Jinshan et al. (2008) using measured data. In this study, the effects of tides, temporal changes in sound velocity, and substrate material on sound transmission loss have been investigated and analyzed by presenting the MITgcm hydrophysical model [8]. Hareesh et al. (2010) studied the sound transmission loss caused by the effects of supereruption and suberuption on the southern coast of India using the parabolic method. The first step of this study included identifying and investigating the way supereruption and suberuption are created, and then modeling sound propagation using the parabolic wave equation at a frequency of 3 KHz in the presence of these phenomena has been studied [3]. Sridevi et al. (2010) also evaluated the effect of internal waves on sound propagation on the eastern coast of India using the beam method by placing the sound source at different depths in two modes: range-independent and range-dependent. According to their research results, the presence of internal waves causes a change in the transmission loss in the range of 2.86 dB and 15.59 dB in the water column [14]. In another study conducted by Hareesh et al. (2007), the effects of the cold and warm cores of the Arabian Sea in the range of 67.5 degrees East to 75 degrees East on the propagation of sound waves with a frequency of 100 kHz were investigated [6]. In this study, the cold and warm cores of the Arabian Sea were identified and the propagation of sound waves dependent on the presence of these cores was

evaluated. The results of this study indicate that the sound transmission loss changes almost significantly in the presence of these cores [6].

Xun et al. (1999), in a project affiliated with the Institute of Acoustic Studies of the Chinese University of Sciences, studied the dispersion and scattering of signals in places with underwater turbulence and fast ocean currents [18]. A study on sound propagation and detection of targets and obstacles in shallow and deep basins was conducted by Clary and Medwin in 1977. In this study, it was determined through sampling and measurements of sound speed, sound signals and the formation of sound channels that sound channels with the sea surface and seabed as their boundaries are formed in shallow places [3].

The variability of the mixed layer in the North Arabian Sea was investigated using measurements taken by the Argo floats in 2007 by Bhaskar et al. In line with the international Argo project, more than 5000 unmanned surface and subsurface vessels of various types are active in waters around the world to create a complete archive of observations of physical and chemical parameters since 2000 [2]. Ohno et al. (2004), also investigated and analyzed the depth of the mixed layer in the winter season using data from the Argo float in the North Pacific Ocean. They also continued their studies in 2006 to investigate the distribution of mixed layer characteristics in the Pacific Ocean [19]. The depth of acoustic channels and their relationship with other physical parameters and the depth of the surface mixed layer in different oceans was evaluated by Helber et al. in 2007. According to their results, the depth of the acoustic layer and the depth of the surface mixed layer often coincide [7].

Ross and Lavery conducted experiments on the scattering behavior of sound waves in the presence of dual-scattering microstructures in 2007. After creating a dual-scattering structure in a laboratory glass tank, they investigated the scattering of sound signals through these structures at two frequencies, 250 kHz and 500 kHz.

2. Materials and methods

2.1 Methodology

The physical parameters studied in the present study include temperature, salinity, and sound velocity. Changes in the aforementioned physical parameters in the water column are variable and depend on factors such as the location of the region, latitude, season, water depth, time of day, and so on. Therefore, in the present study, the changes in the mentioned parameters in the cold and warm seasons of the northern Indian Ocean, the Sea of Oman, the Strait of Hormuz and the Persian Gulf in different layers of the water column have been investigated and evaluated. This study aims to determine the changes in each of the parameters in the water column for different marine areas in the cold and warm seasons of the region to comprehensively and completely understand the physical parameters, especially the speed of sound propagation in different layers of the water column. The vertical structure of the water column can be divided as follows [15].

1. Surface layer: The waters located at the sea surface are referred to as the surface layer and the changes in the speed of sound in this layer change with daily changes in water level, temperature and atmospheric conditions. Due to relatively high-speed winds, the waters in this layer mix with the underlying layers and create a mixed layer.

2. Seasonal thermal layer: By passing through the mixed layer, we will face a sharp drop in temperature. This layer is formed in shallow areas and mid-latitudes in the warm season and weakens in the cold season. In this layer, the speed of sound usually decreases with a relatively steep slope.

3. Main layer: In this layer, which is also known as the main thermocline layer, the temperature of the water layers always decreases with increasing depth. As a result of this decrease, the speed of sound propagation in this layer also decreases with increasing depth.

4. Deep isothermal layer: This layer, which is usually formed at depths of more than 1000 meters, has the same temperature and temperature changes do not occur with increasing depth. In this layer, the speed of sound propagation usually increases with increasing depth due to the increase in the density of the water layers.

Among the factors affecting the propagation of sound waves in marine environments is the change in the sound velocity profile. According to ray theory, if the change in the sound velocity is negative, the rays bend in the direction where the sound velocity is reduced; but if the change in the sound velocity is positive, the rays bend upward. The areas of the sea where sound waves do not penetrate are called the dark zone (Figure 1).

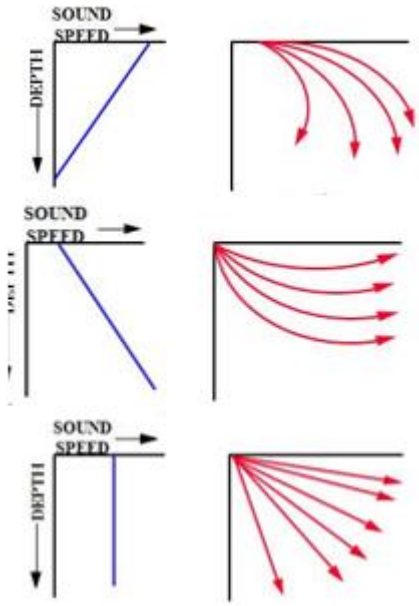


Figure 1. How sound propagates based on the sound velocity profile [15]

2.2 Data collection

In this project, monthly averaged data from the international World Ocean Atlas 2018 project in the northern Indian Ocean, the Sea of Oman, the Strait of Hormuz, and the Persian Gulf with a spatial accuracy of 0.25 degrees have been used to obtain vertical profiles of temperature, salinity, and sound velocity parameters. The World Ocean Atlas is a collection of averages of temperature, salinity, oxygen, phosphate, silicate, and nitrate that have been obtained through measurement data and analyzed after accurate and reliable quality control based on the World Ocean Database data. These data can be used to establish boundaries and initial conditions for various ocean models, or to validate and verify the results of numerical modeling, as well as to confirm the accuracy and precision of satellite data [16]. It is worth noting that WOA2018 used the latest seasonal data updates for the aforementioned parameters. Figure 3 shows the areas studied in terms of vertical profiles of temperature, salinity, and sound speed in the northern Indian Ocean, the Sea of Oman, the Strait of Hormuz, and the Persian Gulf. The evaluated stations are indicated in this figure by black dotted dots.

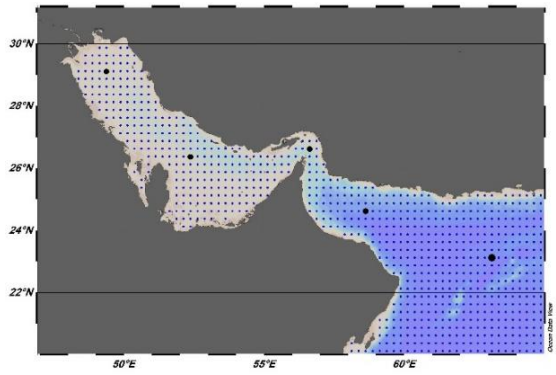
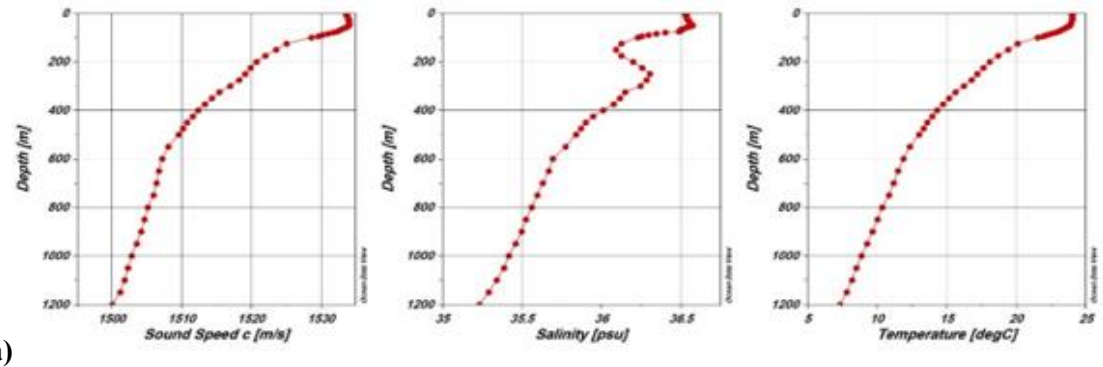


Figure 2. Surveyed stations in target areas [17]

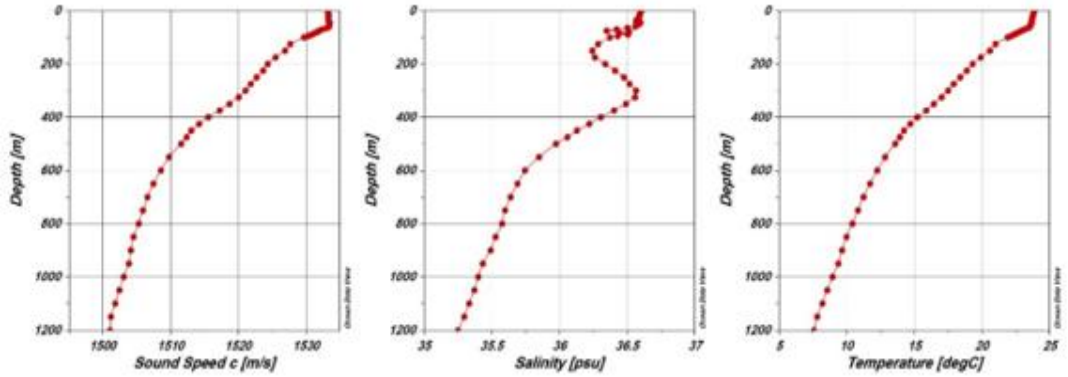
Considering the climate of the region and the location of the studied areas at latitudes of 20 to 30 degrees north, the mentioned areas have only two cold and hot seasons throughout the year. Accordingly, in the present project, the physical parameters of the water column in the two cold and hot seasons of the region, in January and July, respectively, have been investigated. The data at the same depths from the surface to the bed and averaged in January and July have been used to determine the different layers of the column and the way the vertical profiles of the physical parameters change.

3. Results and Discussion

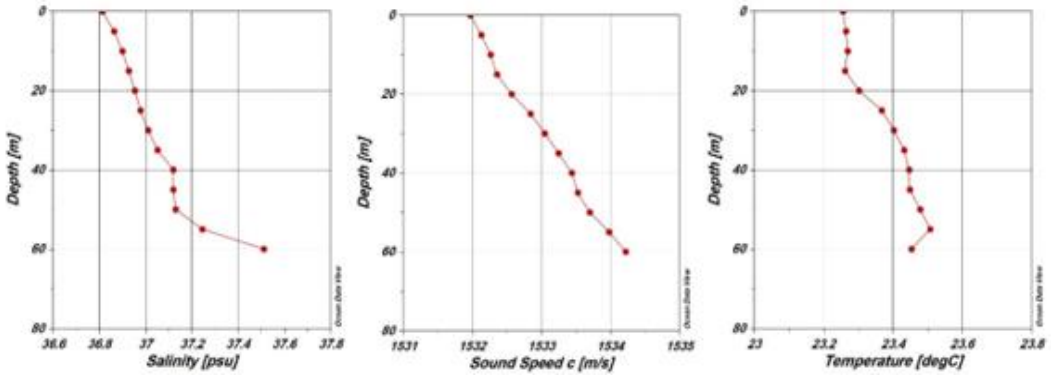
In this section, the vertical profiles of the physical parameters of temperature, salinity and sound speed of the studied stations are shown (Figure 3). In the following figures, the vertical changes of the physical parameters of the stations of the northern Indian Ocean, the central Oman Sea, the central Strait of Hormuz, the central Persian Gulf and the northwestern Persian Gulf are presented in the cold season and then in the warm season of the region. Considering the bathymetric conditions and the presence of shallow areas in the Persian Gulf and the Strait of Hormuz and deep oceanic areas in the Oman Sea and the Indian Ocean; the vertical changes in the stations have been evaluated in proportion to the depth of the station in question.


Depth [m]
Sound Speed c [m/s]
Salinity [psu]
Temperature [degC]

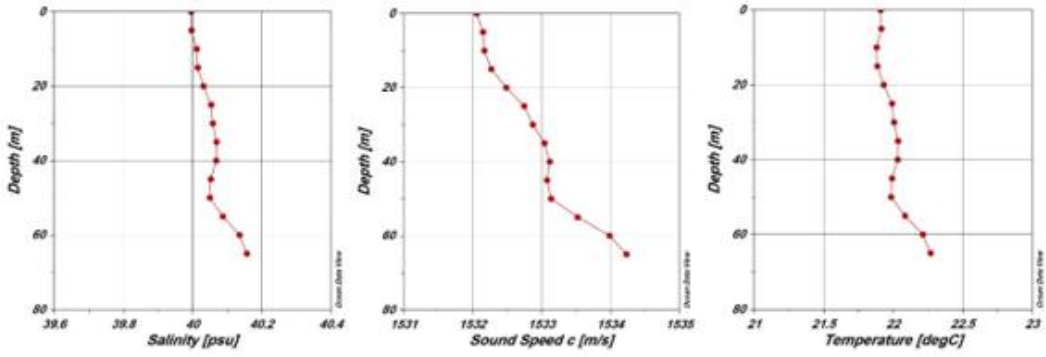
a)


Depth [m]
Sound Speed c [m/s]
Salinity [psu]
Temperature [degC]

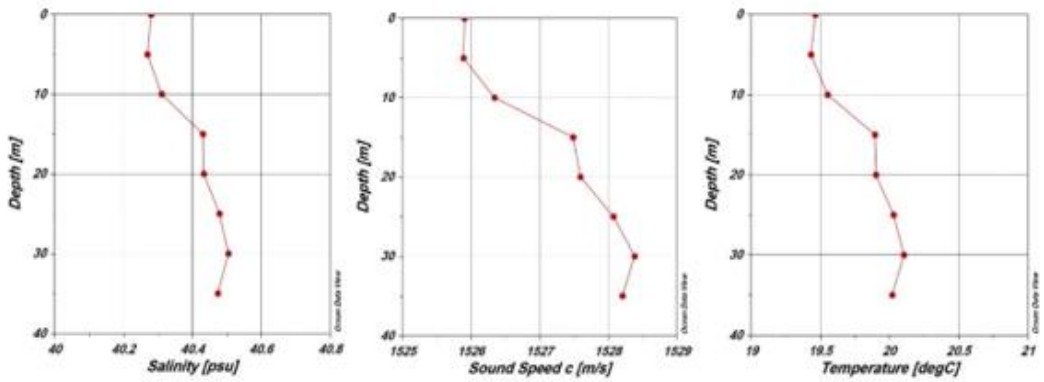
b)


Depth [m]
Salinity [psu]
Sound Speed c [m/s]
Temperature [degC]

c)


Depth [m]
Salinity [psu]
Sound Speed c [m/s]
Temperature [degC]

d)



e)

Figure 4. Right profile (temperature), middle profile (salinity), left profile (speed of sound) (January) in cold season: a) North Indian Ocean, b) Central Sea of Oman, c) Central Strait of Hormuz, d) Central Persian Gulf, e) Northwestern Persian Gulf

Given the presence of depths of more than 1000 m in the northern Indian Ocean and the central regions of the Sea of Oman, vertical changes in physical parameters indicate the presence of a permanent thermocline layer (slope) in these areas. Accordingly, in the first 100 m of the depth of the aforementioned areas, a homogeneous layer is formed and changes in temperature, salinity and sound speed at these depths are very insignificant. Due to the presence of winter monsoon winds (left diagram of Figure 4) in the northern parts of the Indian Ocean, which blow from the northeast and move parallel to the eastern coast of Africa towards the southwest, the surface homogeneous layer has a relatively large depth compared to the warm months of the region.

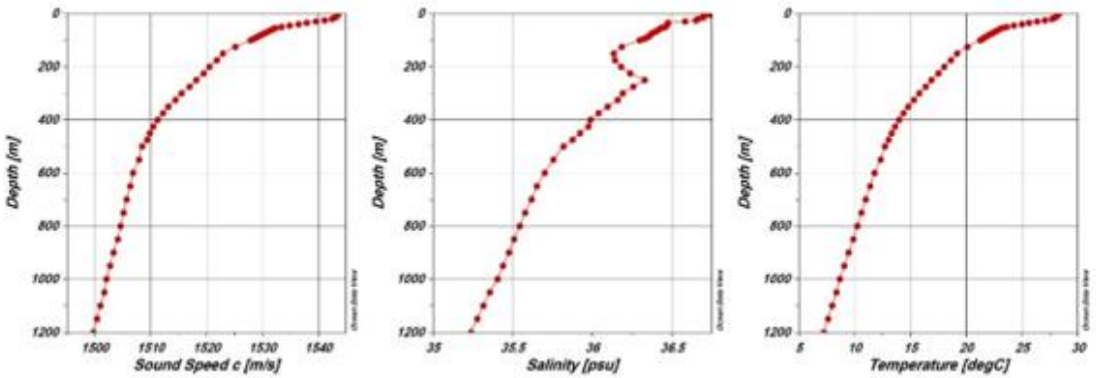
Upon passing through the surface homogeneous layer, the thermocline layer begins with a relatively steep slope and continues to depths of more than 1000 m and a temperature of 6 degrees Celsius. This sharp decrease in temperature also affected the speed of sound waves, causing a decrease of more than 30 m/s in the thermocline layer. Vertical changes in the speed of sound in the vertical direction indicate the existence of a deep sound channel in the northern Indian Ocean and the Sea of Oman. Accordingly, if there is a sound source at depths of more than 100 meters, sound waves will be able to travel long distances without colliding with the surface layer of water with minimal loss.

Salinity changes in the deep regions of the Indian Ocean and the Sea of Oman are such that the depth range of 200 to 400 meters has an increase of 0.5 psu. This increase in the aforementioned depths in the middle of the Sea of Oman and the northern Indian Ocean can be attributed to the penetration of dense outflow currents (with relatively high salinity) deep subsurface of the Persian Gulf. This is also clearly evident in the vertical salinity profile in the center of the Strait of Hormuz. Salinity changes in the Strait of Hormuz indicate an increase of more than 1 unit of salinity from the surface to the bed of this region, which indicates a subsurface flow near the bed in this region.

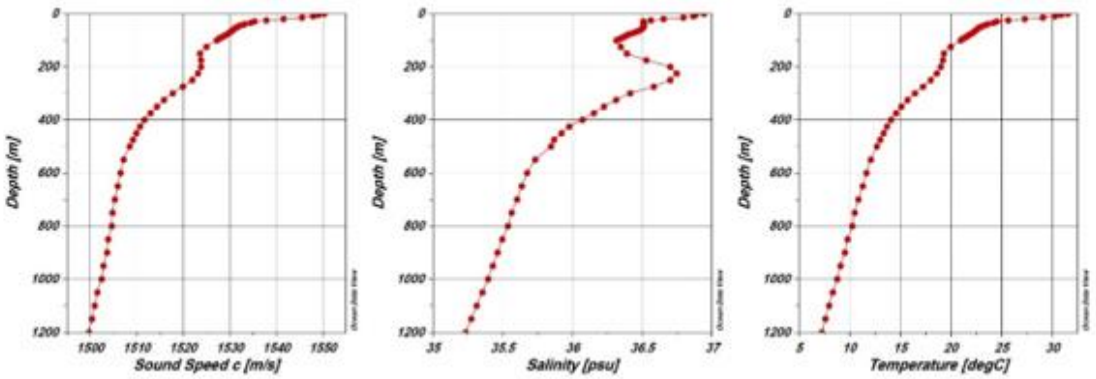
Temperature changes in this cold season of the region from the surface to the bed are very insignificant and the entire water column can be considered almost isothermal. This is due to the increase in surface wind speed in the region and especially the prevailing atmospheric conditions in the cold season, which causes the water mass to become thermally homogeneous. Due to the insignificant temperature changes, changes in the speed of sound are not a function of temperature, and therefore, due to the increase in salinity with depth and the increase in water column pressure, we witness a 2-unit increase in the

speed of sound from the surface to the bed in this region.

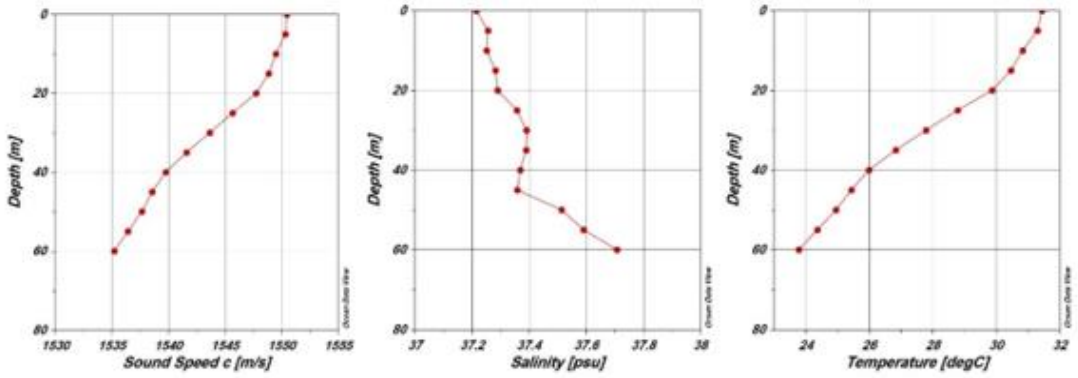
Due to depths of less than 100 in most of the Persian Gulf, and especially in the shallow areas of the northwest Persian Gulf; this water body has almost homogeneous waters from the surface to the bed in the cold season, and we witness very limited vertical changes in the parameters of temperature, salinity, and sound speed. This has caused the changes in the speed of sound from the surface to the bed to be more a function of the water column pressure than temperature changes. Hence, a 2-unit increase in the speed of sound has been recorded in the water column of the central and northwest Persian Gulf. This slight increase in the speed of sound relative to the water surface has created a relatively weak surface sound channel, and due to this, sound waves will have successive collisions with the water surface in their propagation path.



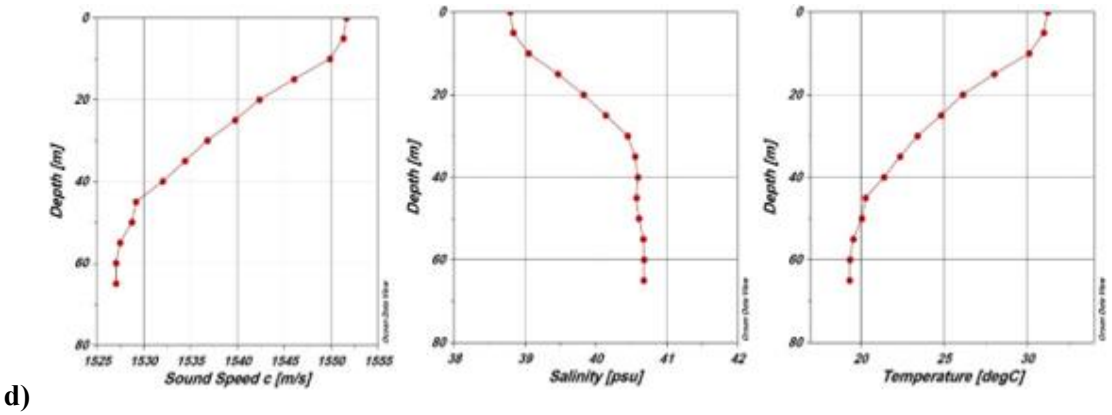
a)



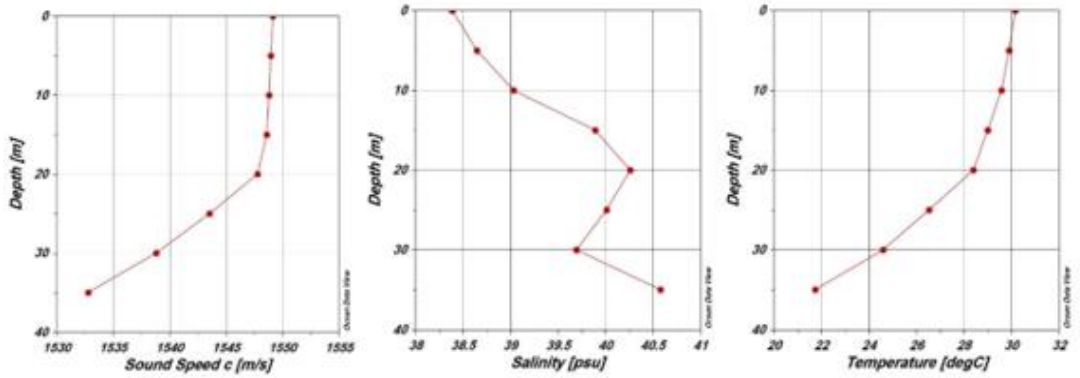
b)



c)



d)



e)

Figure 5. Right profile (temperature), middle profile (salinity), left profile (speed of sound) in warm season (July): a) North Indian Ocean, b) Central Sea of Oman, c) Central Strait of Hormuz, d) Central Persian Gulf, e) Northwestern Persian Gulf

As mentioned earlier, the summer monsoon is the dominant weather system in the warm months of the year in the northern Indian Ocean and the Sea of Oman. During monsoon times (right-hand diagram in Figure 6), relatively strong winds blow from the southwest along the east coast of Africa to the north of the Indian Ocean in a northeasterly direction. This creates surface currents and waves towards the northern Indian Ocean and, in some cases, the central Sea of Oman.

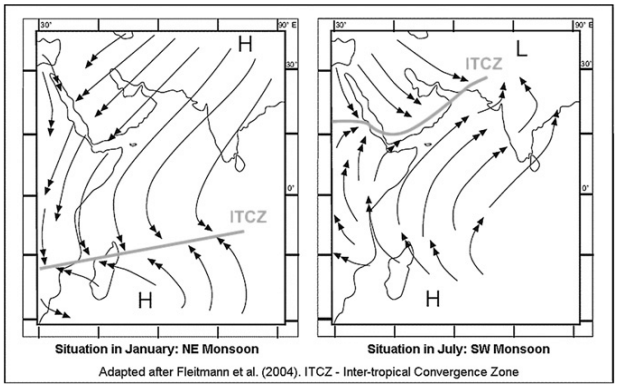


Figure 6. The path of the winter (left) and summer (right) monsoon atmospheric system in the North Indian Ocean [12]

The homogeneous surface layer in the warm months of the region is shallower than in the cold season due to the decrease in surface wind speed and is limited to a few tens of meters at the beginning of the water column in the northern Indian Ocean and the Sea of Oman stations. In this season, a strong permanent thermocline layer is still visible in the deep waters of these regions with a decrease of 20 units in water temperature and 50 units in the speed of sound propagation. This has created a stable water mass in terms of density in these regions, to the extent that even the penetration of salty waters of the Persian Gulf at depths of 200 to 250 meters is not able to destabilize the water column of these regions. By passing through the deep regions of the Sea of Oman and reaching the shallow parts of the Strait of Hormuz and the Persian Gulf, due to the decrease in wind speed in the warm season and the increase in air temperature at a height of 2 m above sea level, we witness the creation of seasonal thermoclines in these regions. There is a relatively weak homogeneous layer in the first few meters of the

surface layer, and immediately after passing the first few meters, the thermocline layer begins and continues to the bed. In this layer, the temperature of the water column has decreased by more than 10 units, and due to this, the speed of sound propagation also shows a decrease of 15 units.

Vertical changes in salinity in the Strait of Hormuz have continued to witness an increase in depths near the bed; this increase in salinity, like the cold season, indicates the outflow of dense currents with high salinity compared to the surface layer from this region. This outflow exists at all times of the year and only has increases and decreases in the salinity of the outflow during different seasons. Shallow waters along the southern coasts of the Persian Gulf, between Qatar and the Emirates, which have depths of less than 30 m, among the areas forming waters with salinity exceeding 40 psu are the Persian Gulf.

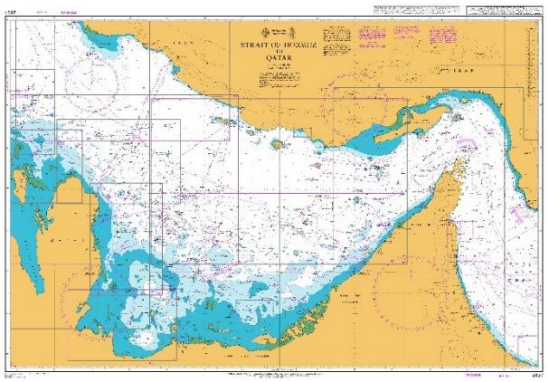


Figure 6. Nautical chart 2837, southern coast of the Persian Gulf [16]

Vertical changes in the speed of sound in shallow areas of the Persian Gulf indicate a decrease in the speed of sound with increasing depth in these areas. Therefore, if there is a sound source at depths of more than 20 m, it causes sound propagation in these areas to encounter multiple collisions with the bed and, as a result, high transmission loss. The 20-unit decrease in the speed of sound observed has created a sound channel near the bed in the warm season of the region, which, due to the shallowness of the region, causes sound waves to interact more with the bed. The changes in the physical parameters of the water column have been analyzed and investigated in the form of two-dimensional profiles over a length of more than 2000 km from the northern Indian Ocean to the northwest of the Persian Gulf. In this regard, the characteristics of the physical parameters of the water column along the center of the target areas from the surface to the bed are presented in the figures below. It is necessary to explain that, considering the shallowness of the Persian Gulf and the Strait of Hormuz regions, as well as the depth of the central parts of the Sea of Oman and the northern Indian Ocean, two-dimensional profiles have been evaluated in two sections: the Persian Gulf to the Sea of Oman and then the Sea of Oman to the northern Indian Ocean.

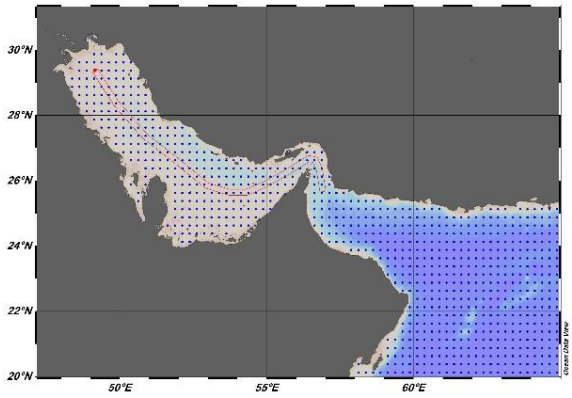


Figure 7. Assessed section of the Persian Gulf to the Sea of Oman

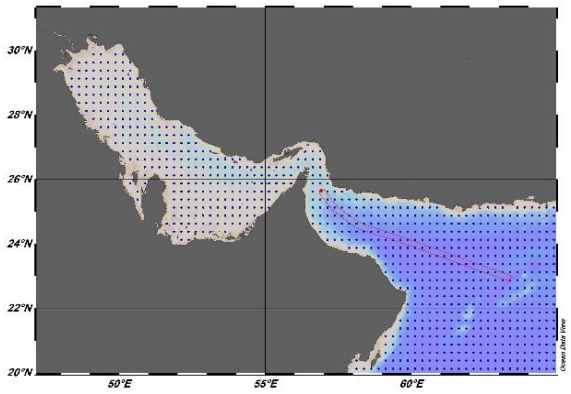


Figure 8. Assessed section of the Sea of Oman to the northern Indian Ocean

Figures 9, 10, and 11 respectively show two-dimensional cross-sections of temperature, salinity, and sound velocity parameters from the northwestern parts of the Persian Gulf to the west of the Strait of Hormuz (corresponding to the cross-section in Figure

6) in the cold season of the region. Considering the vertical changes in the aforementioned parameters, it is possible to observe the homogeneity of temperature and salinity of water from the surface to the bed in most areas. This issue, which was also observed in the cold season temperature and salinity indexes of the Persian Gulf and the Strait of Hormuz, is due to the increase in local wind speed, especially the north wind, in the cold season of the year and the creation of vertical mixing of the water column, resulting in the homogenization of temperature and salinity parameters.

Only in the areas close to the Strait of Hormuz (800 to 1000 km in the figures below) do we witness an increase in salinity at depths near the bed, which indicates the penetration of permanent subsurface currents of Persian Gulf salt into the Sea of Oman in these areas. Moving from the northwestern parts of the Persian Gulf towards the Strait of Hormuz; the water temperature in the same depth layers has increased and the salinity in these layers shows a significant decrease.

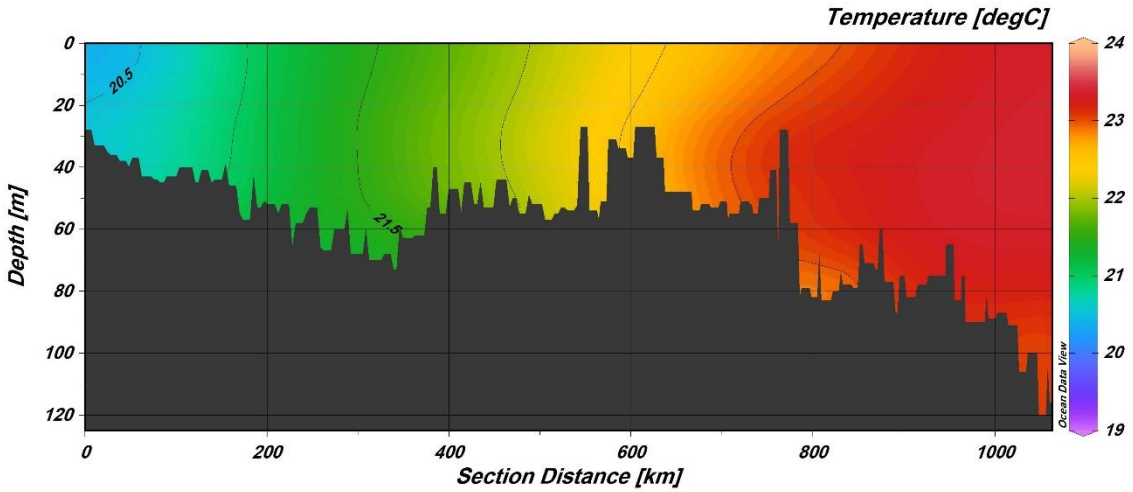


Figure 9. Two-dimensional cross-section of temperature changes from the northwest of the Persian Gulf to the Sea of Oman (along the cross-section path of Figure 6) in the cold season (January)

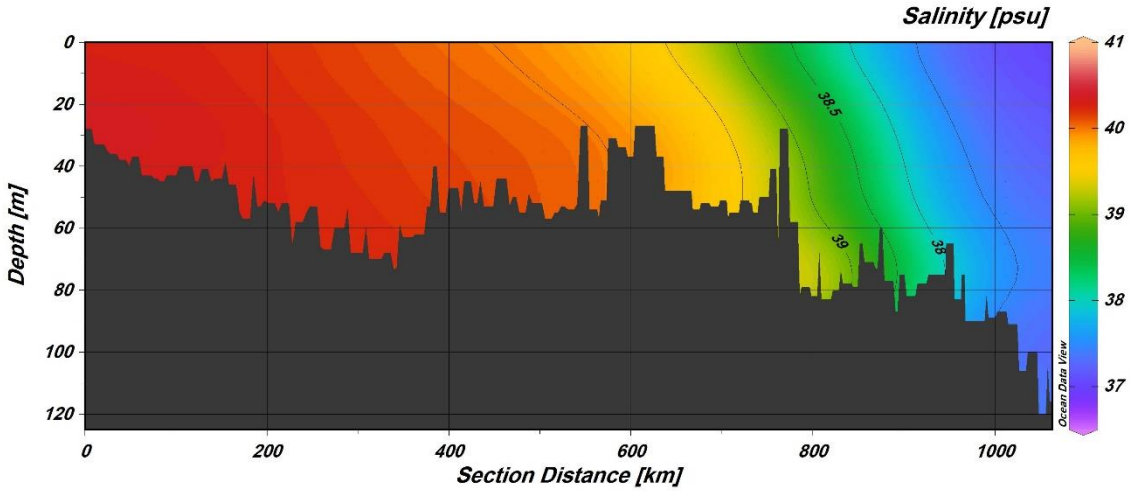


Figure 10. Two-dimensional cross-section of salinity changes from the northwest of the Persian Gulf to the Sea of Oman (along the cross-section path of Figure 6) in the cold season (January)

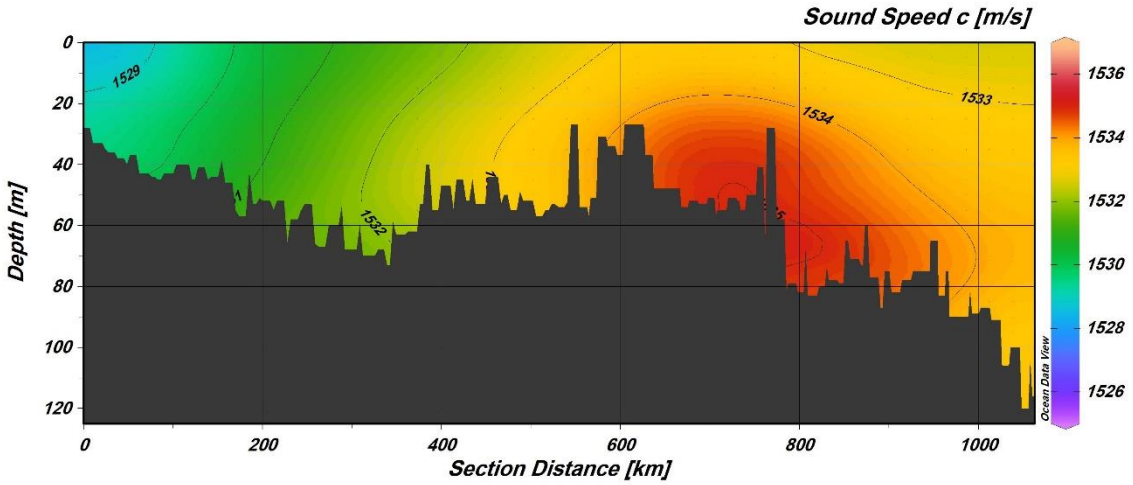


Figure 11. Two-dimensional cross-section of sound velocity changes from the northwest of the Persian Gulf to the Sea of Oman (along the cross-section path of Figure 13) in the cold season (January)

The two-dimensional changes in the cross-section of the Sea of Oman to the northern Indian Ocean are presented in Figures 12, 13 and 14, respectively, for the temperature, salinity and speed of sound parameters. In these areas, due to the great depth, a permanent thermocline has formed in all areas. This causes the surface homogeneous layer to be separated from the deep homogeneous layer by the thermocline layer. It is worth noting that in these areas there is a relatively strong sound channel at depths of more than 500 m due to the reduction in the speed of propagation of sound waves from the surface to the bed during the cold season of the region.

The penetration of dense (high salinity) waters from the layers near the bed of the Strait of Hormuz into the Sea of Oman can be clearly seen up to the first 200 km in Figure 13. Due to their high density, these water masses penetrate up to 100 km into the Sea of Oman until they gradually mix with the adjacent waters and overflow into the Indian Ocean. Also, when moving from the central parts of the Oman Sea towards the northern Indian Ocean in layers of the same depth, no significant changes occur in any of the physical parameters.

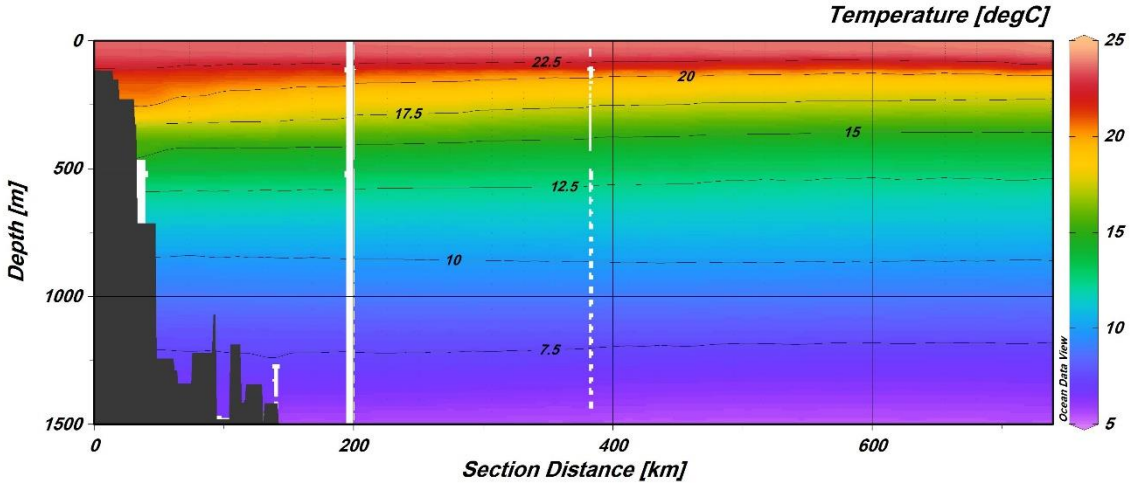


Figure 12. Two-dimensional cross-section of temperature changes from the center of the Oman Sea to the northern Indian Ocean (along the cross-section path of Figure 8) in the cold season (January)

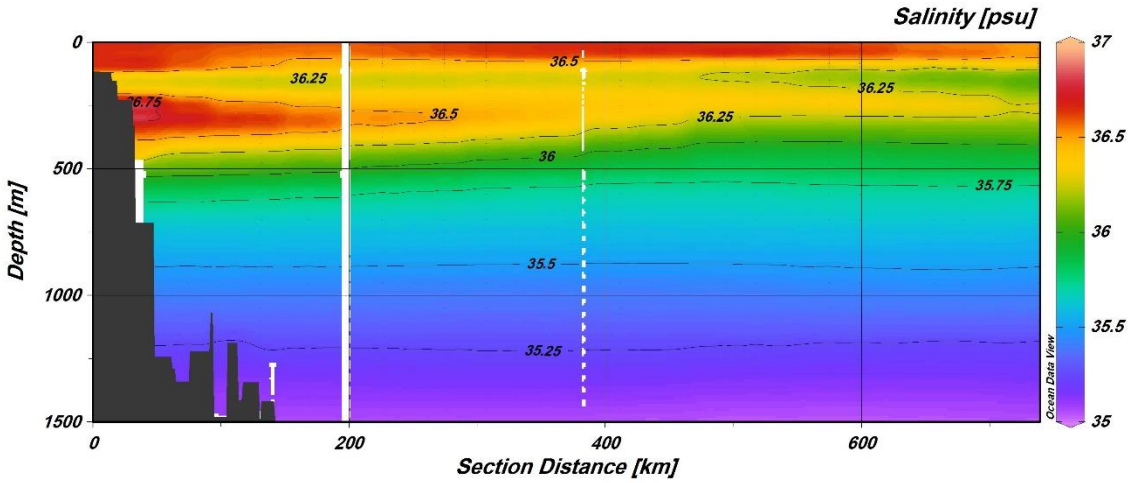


Figure 13. Two-dimensional cross-section of salinity changes from the center of the Oman Sea to the northern Indian Ocean (along the cross-section path of Figure 8) in the cold season (January)

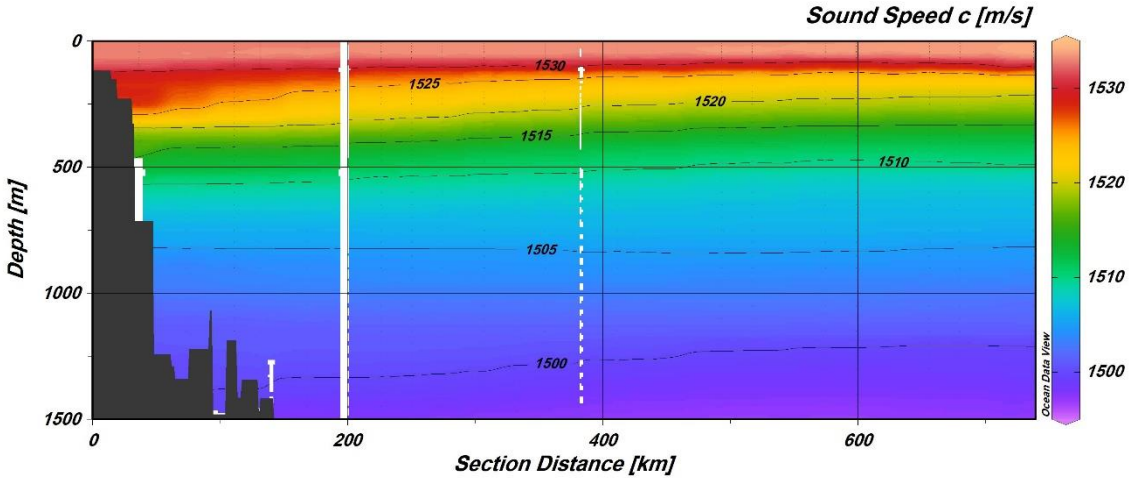


Figure 14. Two-dimensional cross-section of sound velocity changes from the center of the Oman Sea to the northern Indian Ocean (along the cross-section path of Figure 8) in the cold season (January)

Two-dimensional cross-sections of changes in physical parameters in the warm season are shown in Figures 15, 16, and 17 of the cross-sections of Figure 8. The results of the study indicate the formation of a seasonal thermocline layer in most areas, especially in the deeper areas of the Persian Gulf. Accordingly, temperature changes of more than 15 units have been recorded in some areas, which indicates the formation of a relatively strong thermocline layer at depths of less than 100 meters in the Persian Gulf. In this season, we also observe the highest salinity values (more than 40 units) in the shallow northwestern parts. The northwestern regions along with the shallow southern parts of the Persian Gulf have always had higher salinities than other regions of the Persian Gulf and are considered to be the main factors in creating dense subsurface currents from the Persian Gulf to the Sea of Oman. A relatively weak sound channel has formed in the deep parts and near the bed of the Persian Gulf and the Strait of Hormuz due to a reduction of more than 20 units in the speed of sound from the surface to the bed in the deep areas of the Persian Gulf and the Strait of Hormuz. This causes sound rays to have multiple collisions with the bed in their propagation path and increases the loss due to transmission.

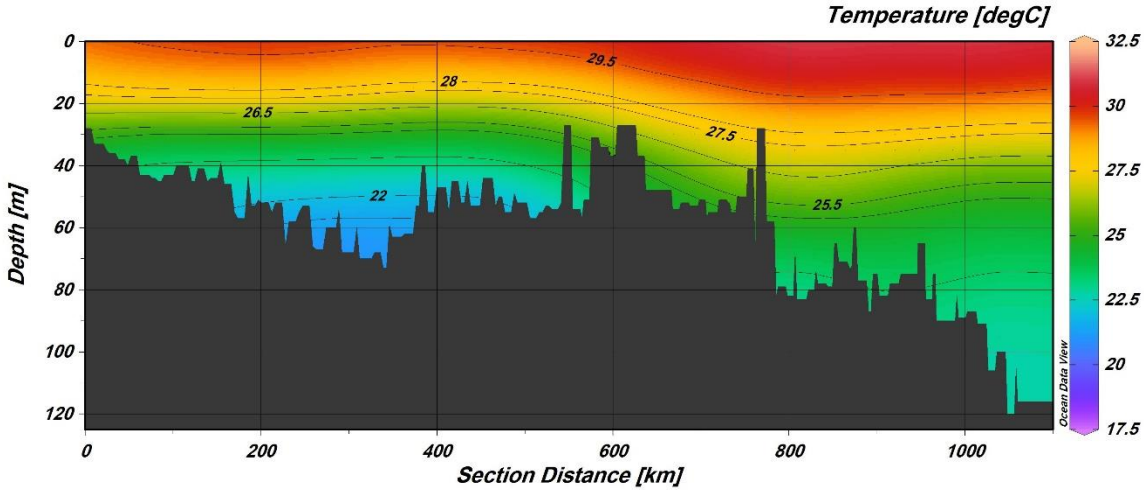


Figure 15. Two-dimensional cross-section of temperature changes from the northwest of the Persian Gulf to the Sea of Oman (along the cross-section path of Figure 8) in the warm season (July)

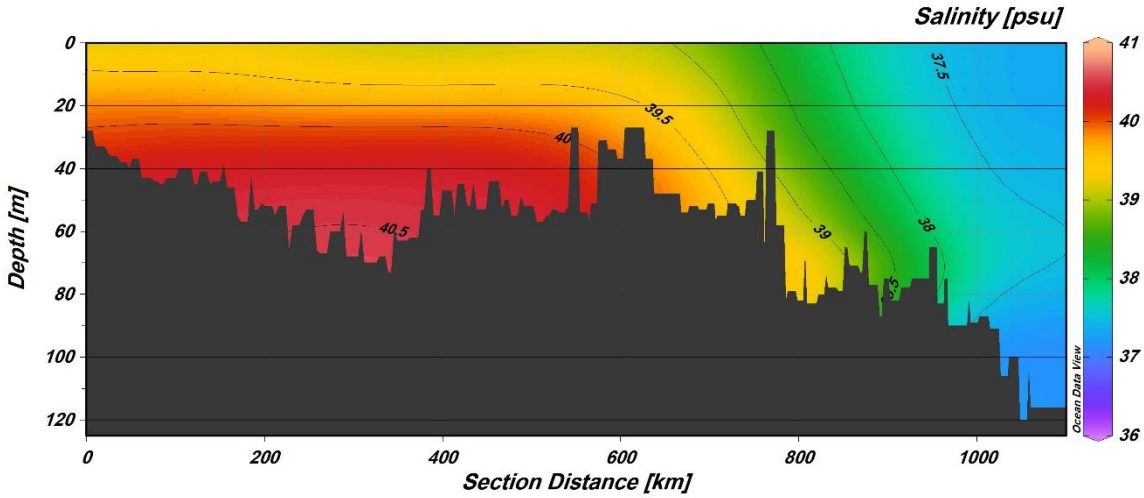


Figure 16. Two-dimensional cross-section of salinity changes from the northwest of the Persian Gulf to the Sea of Oman (along the cross-section path of Figure 8) in the warm season (July)

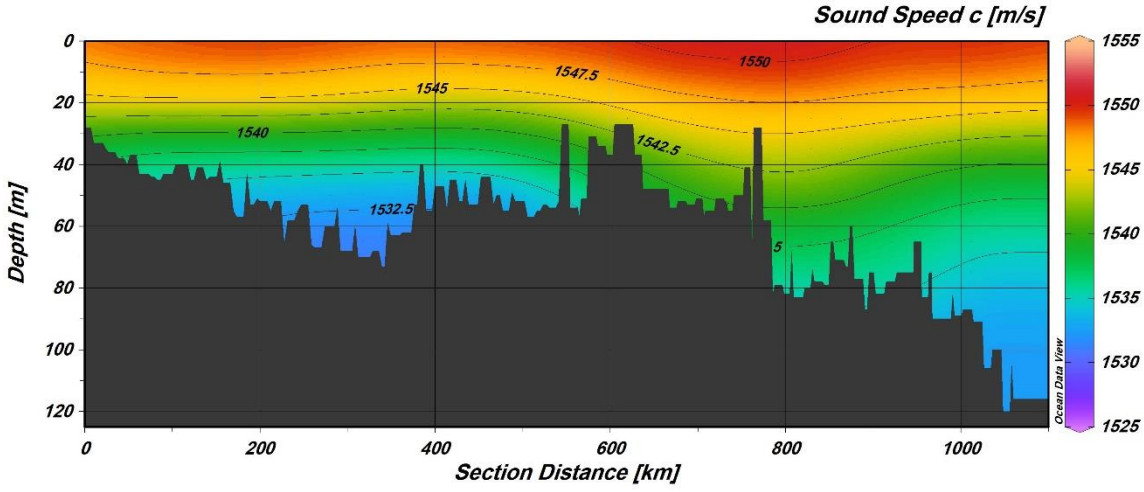


Figure 17. Two-dimensional cross-section of sound speed changes from the northwest of the Persian Gulf to the Sea of Oman (along the cross-section path of Figure 8) in the warm season (July)

Figures 18, 19 and 20 show two-dimensional variations in temperature, salinity and sound velocity from the Sea of Oman to the northern Indian Ocean over a distance of more than 700 km during the warm season of the region. In this season, as in the cold season of the region, there is a strong permanent thermocline due to the presence of depths of more than 1500 meters. Due to the increase in the surface air temperature, the water surface temperature has reached more than 30 degrees Celsius, causing the temperature to decrease by more than 25 units from the surface to the bottom. This significant decrease in temperature has caused a sharp decrease in the speed of sound, and due to this, a deep sound channel with speeds of 1500 to 1505 m per second has formed at depths of nearly 1000 m.

Like in the cold season, in this season, the intrusion of salty waters from the Persian Gulf into the Sea of Oman (Figure 19) is also visible. The intrusion of saltwater in this season affects fewer areas than in the cold season and mixes more rapidly with the surrounding waters. Other changes in the same depth layers are almost the same and no significant changes are observed in the layers.

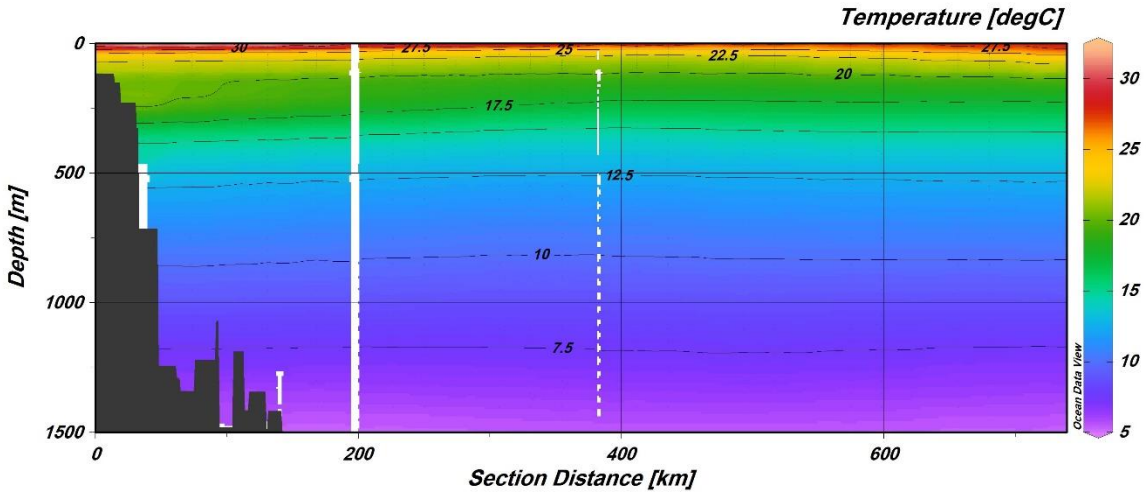


Figure 18. Two-dimensional cross-section of temperature changes from the center of the Oman Sea to the northern Indian Ocean (along the cross-section path of Figure 9) in the warm season (July)

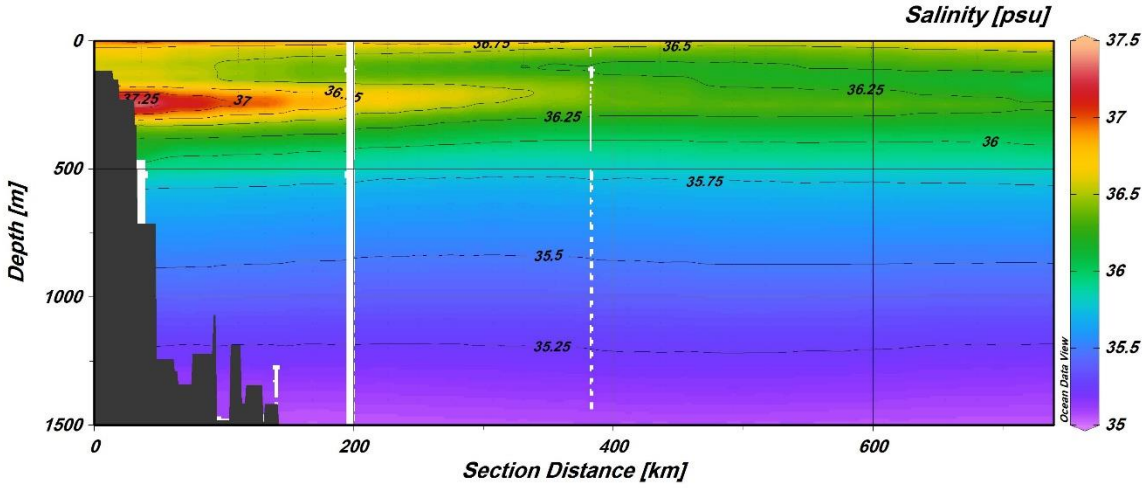


Figure 19. Two-dimensional cross-section of salinity changes from the center of the Oman Sea to the northern Indian Ocean (along the cross-section path of Figure 9) in the warm season (July)

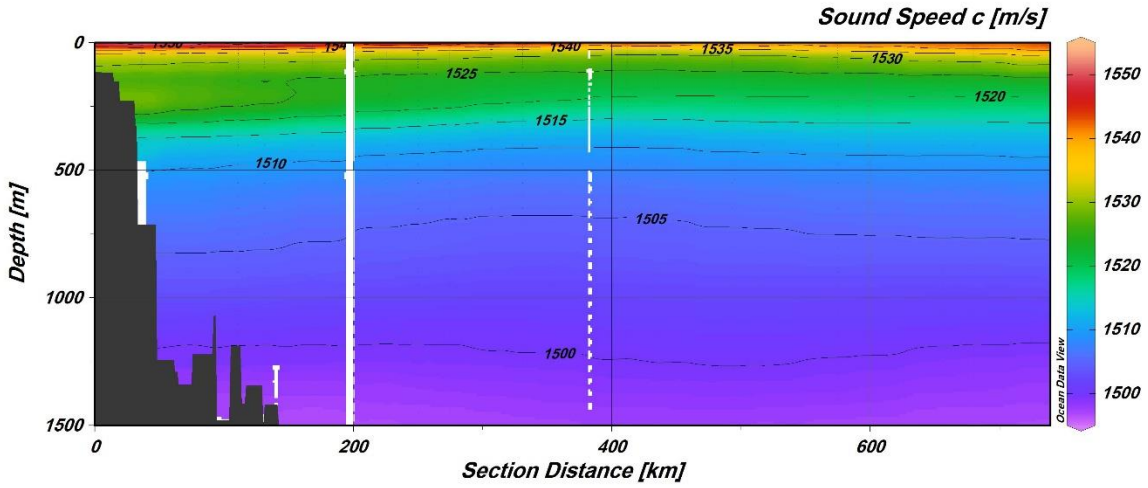


Figure 20. Two-dimensional cross-section of sound speed changes from the center of the Oman Sea to the northern Indian Ocean (along the cross-section path of Figure 9) in the warm season (July)

4. Conclusion

The main objectives of the present project have been to investigate the vertical changes in the physical parameters of the water column, including the speed of sound propagation in the seas adjacent to the south of the country and the northern regions of the Indian Ocean. In this regard, the temperature, salinity and speed of sound indices have been evaluated at 5 stations in the northern Indian Ocean, the central Oman Sea, the central Strait of Hormuz, the central Persian Gulf and the northwestern Persian Gulf in the two cold and warm seasons of the region. The results indicate the existence of a permanent thermocline in the deep parts of the Oman Sea and the northern Indian Ocean, as well as a seasonal thermocline in the shallow areas of the Strait of Hormuz and the Persian Gulf. Due to the sharp decrease in the speed of sound with increasing depth in the deep regions of the Oman Sea and the Indian Ocean, a deep acoustic channel exists throughout the year. The only seasonal difference in these areas is related to the depth of the surface homogeneous layer. In the cold season, the depth of the mixed layer is more than 100 m, while this depth reaches less than 50 m in the warm season of the region. This difference is due to different weather conditions resulting from prevailing systems in different seasons, especially unstable weather conditions caused by the winter and summer monsoons.

In the shallow parts of the studied areas, including the Strait of Hormuz and the Persian Gulf, due to the shallowness of the area and unstable atmospheric conditions in the cold season, the water mass is almost homogeneous, which is lost in the warm season and the relative stability of atmospheric conditions, and with the warming of the air temperature at a height of 2 meters, a relatively strong seasonal thermocline layer is created in these areas. Changes in the speed of sound propagation in the warm season of the Persian Gulf have caused the creation of a sound channel near the bed, which causes sound rays to collide with the bed multiple times along their propagation path due to the shallowness of the area and the conditions of vertical changes in the speed of sound propagation. Since the use of acoustic equipment in marine subsurface activities is necessary and inevitable, the environmental conditions of the area should be examined and monitored before any action is taken. Therefore, in the first step, a comprehensive and complete understanding of how the speed of sound waves changes as the most effective factor in the use of sound equipment at different times and places should

be obtained. Therefore, what has been evaluated and studied in the present plan can be a useful step in this field so that its results can be used for secondary activities such as the applications mentioned at the beginning of this document. The two-dimensional changes in various parameters, which have been evaluated in the form of cross-sections along the Persian Gulf to the northern Indian Ocean, well indicate how physical parameters change along the region and different seasons. The two-dimensional diagrams obtained in this section show how changes occur in the horizontal direction and over a length of more than 2000 kilometers of the study area. Accordingly, the intrusion of salty waters of the Persian Gulf in the deep parts of the Sea of Oman has existed at all times and can be traced well up to the middle of the Sea of Oman. The permanent thermocline is visible in the deep areas of the Sea of Oman and the Indian Ocean throughout the year, and its difference in different seasons is only in the thickness of the surface homogeneous layer and the beginning of the thermocline layer. Also, considering the changes in the speed of sound in different seasons of the Persian Gulf section, it can be concluded that the propagation of sound waves in these shallow areas will face a very high loss due to multiple collisions with the surface and the bed. Based on the data used in the present design and also known numerical models of sound propagation and adding several parameters such as the depth of the sound source, the frequency of the sound source, the type of bed, the way of vertical changes in density, the location of the receiver and the distance between the transmitter and the receiver, it is possible to achieve the propagation of sound waves in different areas. These results will be able to identify the main paths of sound wave propagation at different frequencies and depths of sound sources, along with complete information about the loss caused by the transmission of sound waves. Also, from the results of these issues, dark spots (shadows) can be identified for the use of different detection and tracking systems in different regions and seasonal conditions to maximize their use.

5. References

[1] Akbari Nasab, M., Sadri Nasab, M., & Ali Akbari Bidokhti, A. (2012). The effect of horizontal and vertical heterogeneity on the propagation of acoustic waves in the Oman Sea (Strait of Hormuz area). PhD thesis in Oceanography, Khorramshahr University of Marine Sciences and Technology.

[2] Bhaskar, T. V. S. U., Swain, D., & Ravichandran, M. (2007). "Mixed layer variability in Northern Arabian Sea as detected by an Argo float," Ocean Science Journal 42, 241-246.

[3] Clay, C. S., & Medwin, H. (1977). Acoustical Oceanography: Principles and Applications. New York: John Wiley and Sons.

[4] Dosti Aref, A., & Ebrahimzadeh, A. (2017). Cooperative subsurface acoustic communications in the Persian Gulf Channel. PhD thesis in Electrical Engineering, System Communications, Noshirvani University of Technology, Babol.

[5] Hareesh Kumar, P.V. and Radhakrishnan, K.G. (2010). Transmission Loss Variability Associated with Upwelling and Downwelling Off the Southwest Coast of India. Defence Science Journal, 60 (5), 476-482.

[6] Hareesh Kumar, P.V., Sanilkuma, K.V. R., & Prasada Rao, C.V.K. (2007). Arabian Sea Mini Warm Pool and its Influence on Acoustic Propagation, Defense Science Journal, 57, 115-121.

[7] Helber, C. N., Barron, M. R. Carnes, & Zingarelli, R. A. (2008). "Evaluating the sonic layer epth relative to the mixed layer depth," Geophysical research 113.

[8] Jinshan, X.U., Pierre, F. L., Patrick, J. H. J., Wayne, G. L., & Oleg G. L. (2008). Spatial and Temporal Variations in Acoustic propagation during the

PLUSNet'07 Exercise in Dabob Bay. Acoustical Society of America, 4.

[9] Ohno, Y., Kobayashi, T., Iwasaka, N & Suga., T. (2004). "The mixed layer depth in the North pacific as detected by the Argo floats," geophys. Res. Lett 31.

[10] Rafati Sokhango, F., & Sherbaf Tabrizi, S. (2013). Modeling the Persian Gulf acoustic channel and improving system efficiency using cooperative communications. Master's thesis in Electrical Engineering, Telecommunication Systems, Imam Reza University.

[11] Sam Daliri, H., & Mehdizadeh, M. (2012). Modeling the propagation of sound waves in the Sea of Oman using the beam theory method. Master's thesis in Marine Physics, University of Hormozgan.

[12] Scholte, P., & De Geest, P. (2010). The climate of Socotra Island (Yemen): A first-time assessment of the timing of the monsoon wind reversal and its influence on precipitation and vegetation patterns.

[13] Siegel, M., & King, R. (1973). "Electromagnetic propagation between antennas submerged in the ocean," IEEE Trans. Antennas Propag., vol. 21, no. 4, pp. 507-513.

[14] Sridevi, B., Ramana Murty, T.V., Sadhuram,Y., Rao, M.M.M., Maneesha., K., Sujith Kumar, S., & Prasanna, P.L. (2010). Impact of internal waves on sound propagation off Bhimilipatnam, east coast of India. Estuarine, coastal and Shelf Science, 88, 249-259.

[15] Urick, J. "Principles of underwater sound," McGraw-Hill, 1983.

[16] www.admiralty.co.uk

[17] www.ncei.noaa.gov

www.odv.awi.de

[18] Xun, Z., Xue,Z. Z., Martin. J. S., & Berthelot, Y. H. (1999). Sound diffraction by an underwater ridge with soft finite impedance. J. Acoust. Soc. Am, 109: 2266-2269.

INTERNATIONAL JOURNAL OF
COASTAL, OFFSHORE & ENVIRONMENTAL ENGINEERING IJCOE Vol.11/No. 3/Summer 2026 (34-47)

Available online at: www. Ijcoe.org

Hybrid Intelligence for Coastal Pattern Recognition: ANFIS-Based Prediction of Multi-Level Beach Cusp Spacing

Azadeh Valipour[1*], Hossein Shirgahi[2]

[1*] *Assistant Professor,Department of Marine Science and Technology, Jo.C., Islamic Azad University, Jouybar, Iran; azadeh.valipour@iau.ac.ir*
[2] *Assistant Professor,Department of Computer Engineering, Jo.C., Islamic Azad University, Jouybar, Iran; hossein.shirgahi@iau.ac.ir*

ARTICLE INFO

Article History:
Received: 24 Feb 2026
Accepted: 24 June 2026

Keywords:
Adaptive Neuro-Fuzzy Inference System
Machine learning
Coastal management
Membership functions
Neural network

ABSTRACT

Given the necessity of understanding coastal dynamics and predicting erosion in coastal areas, this research employs the Adaptive Neuro-Fuzzy Inference System as a machine learning model for predicting beach cusp spacing and subsequently optimizing coastal management. ANFIS has the advantage over other techniques to model the more complex nonlinear relationships involved in beach cusp formation. It learns from existing data, adapts to new information varying with coastal hydrodynamic conditions, and gives back to the user interpretability by showing underlying rules dictating cusp dynamics. This paper discusses implementing ANFIS to predict beach cusp spacing and examines its performance against a neural network. In this way, different ANFIS configurations were tested, and the effect of membership functions on the performance of the fuzzy system was investigated. The main outcomes of this research indicate that even though optimized Artificial Neural Network (ANN) models perform reasonably well for the upper beach face, the optimized ANFIS (trimf) model performs better in accuracy and stability for the middle and lower beach faces. This study effectively highlights the importance of selecting the optimal model tailored to each beach section's specific conditions and characteristics.

1. Introduction

Beach cusps are rhythmic features that form on the beach face after complex interactions between wind, waves, and currents with beach sediments. It is found that these shore-parallel features are more abundant at medium-energy, reflective beaches which have steeper beaches with coarser sediments [1].

Single- level beach cusps form as only one level of cusps on the beach face (Figure 1a); on the other hand, beach cusp systems can also occur at different levels on the beach face. When there are different levels of cusps lining a beach, this system would be called multi-level beach cusps (Figure 1b).

The levels may be lower, middle, and upper parts of the beach [2]. Lower beach cusps are more dynamic because these shift from one point to another as a result of a tidal cycle, while middle and upper beach cusps are fairly static and can be retained between tidal cycles [3]. Thus, beach cusps be classified into various groups according to their formation conditions and position on the beach profile [2]. Types of these features include Swash cusps, Storm cusps, and Low tide cusps, and each type has its peculiar features and formation processes (Figure 1c).

To investigate the morphodynamic behavior of these coastal features, familiarity with the definitions of relevant beach cusp parameters is essential. The most significant parameter for this type of coastal formation is the cusp spacing (C_s), defined as the horizontal distance along the shoreline between the apexes of two adjacent beach cusp horns.

Cusp elevation (C_e) is the vertical distance from the highest point on the beach cusp horn to the Mean Sea Level (MSL). Cusp depth (C_d) represents the vertical distance from the highest point on the beach cusp horn to the wave swash limit in the cusp bay. Lastly, cusp amplitude (C_a) is defined as the maximum vertical difference between the beach cusp horn and the cusp bay (Figure 1d).

To date, numerous theories have been proposed by various researchers to explain the formation and evolution of beach cusps (Table 1).

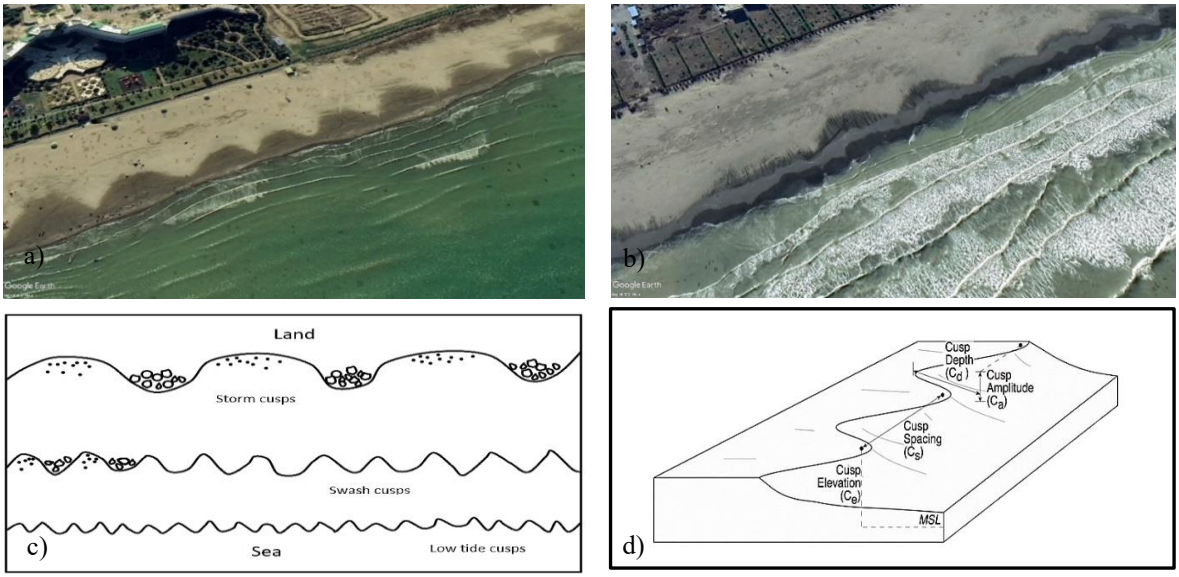


Figure 1. Google Earth view of the a) single-level beach cusps b) multi-level beach cusps c) Different types of beach cusps d) Schematic design of the definition of beach cusp parameters [4].

Some of these studies make it possible to estimate the spacing of beach cusps based on the hydrodynamic and morphodynamic conditions of the coast [5][6][7][8][9]. However, the variable hydrodynamic conditions of the coast and the difficulties in determining sediment grain size due to the increasing use of mixed sand and gravel in recent coastal engineering projects [10] render the application of these theories for reliably estimating cusp spacing challenging and unreliable. According to the information recorded in Table 1, the methods employed in studies related to beach cusps include field observations, numerical modeling, sediment analysis, and laboratory investigations, each possessing distinct disadvantages despite their considerable advantages.

Table 1. Some of the most important theories about the formation and evolution of beach cusps

#	Theory	Researchers	Mechanism of cusp formation	Cusp Spacing Formula	Methods Used
1	Standing Edge Wave Theory	Guza and Inman (1975)	Cusps form due to the interaction between incoming waves and standing edge waves. The spacing is proportional to the wavelength of the edge waves	$\lambda_c = \frac{mg}{\pi} T^2 \sin\beta$ m is equal to 1 and 0.5 for subharmonic and synchronous edge waves, β is the beach slope, g is the acceleration due to gravity, and T is the wave period	Field Surveys, Numerical Modeling
2	Self-Organization Theory	Werner and Fink (1993)	Cusps emerge through a feedback mechanism involving sediment transport and wave run-up	$\lambda_c = fS_c$ S_c is the swash excursion across the beach and f is equal to 1.7	Field Surveys, Theoretical Modeling
3	Sanamura's Theory	Sanamura (2004)	Cusps form based on the relationship between the path of divergent uprush flow on horns and the cusp spacing, influenced by grain size of sediments.	$\lambda_c = A\varphi T\sqrt{gh}$ λ_c is cusp spacing, H is the nearshore wave height, T is the wave period, φ is a dimensionless quantity that shows the effect of the sediment grain size, and A is a constant estimated to be equal to 1.35	Field Surveys, Numerical Modeling, Sediment Analysis
4	Resonance Theory	Guza and Bowen (1976)	Beach cusps form when incoming wave frequencies resonate with natural modes of the beach morphology.	–	Field Surveys, Theoretical Analysis
5	Hydrodynamic Instability Theory	Coco, Huntley & O'Hare (2000)	Beach cusps result from instabilities in the wave and current interactions on the beach face, leading to rhythmic sedimentation patterns.	–	Numerical Modeling, Laboratory Experiments, Field Surveys

Field observations through direct method application, like GPS and terrestrial vehicles for measuring the characteristics of beach cusps entail a lot of profiles to adequately capture their morphology. Because these features are typically rhythmic, fieldwork takes a lot of time and labor [11][12][13][14][4]. In the same way, even with several hydrodynamic parameters estimated and changes in coastal morphology possible to study, numerical methods will still impose constraints on results being dependent on assumptions of the model. Such results would also have to be calibrated with computational resources drawn from field observations [8]. On the other hand, simplifications of some coastal processes are made by a researcher when it comes to numerical applications, yet modeling it truly in actuality is much complicated [15][16]. This method has also been used by researchers in studying the formation mechanisms of beach cusps [17][18].

The controlled conditions of laboratory methods provide accurate manipulation of variables affecting cusp spacing; however, results obtained from such methods do not hold in larger scales or extrapolate well into varying heterogeneous scales. While the monitoring of parameters related to beach cusps using remote sensing tools such as drones allows for the survey of a wide expanse of the beach face, offering significant advantages like spatial resolution, accuracy, and repeatability in monitoring compared to traditional

methods [19], they are also employed as supplementary methods and are costly [20][21].Therefore, in the investigation of features like beach cusps, due to their highly dynamic behavior and the absence of a cost-effective method, the utilization of tools such as various Artificial Intelligence (AI) models in conjunction with video-based techniques for observing morphological changes in the beach face and predicting the behavior of beach cusp systems can be highly efficient. Among different AI techniques, Artificial Neural Networks (ANNs), through their ability to estimate various quantities without the need for their direct measurement, are capable of solving a large number of scientific and engineering problems, including those related to coastal/ocean engineering [22].

To date, various studies have been conducted by researchers in this field to investigate coastal features using neural networks. Among these, the long-term prediction of sandbar behavior on coastlines using neural networks stands out [23]. Additionally, the most recent research undertaken by the authors of this paper focused on predicting beach cusp spacing based on neural network analysis, the results of which are used in the present study for comparison [24]. Several key factors motivated the authors' choice of the Adaptive Neuro-Fuzzy Inference System (ANFIS) for predicting beach cusp spacing. One key advantage is the combination of the capabilities of neural networks and fuzzy logic. As ANFIS is a unique hybrid technique integrating both Fuzzy Inference Systems (FIS) and Artificial Neural Networks (ANNs), it can simultaneously leverage the strengths of both systems [25][26]. Therefore, given that coastal phenomena such as the formation of multi-barred crescentic beach cusps often involve data with ambiguity, noise, or sometimes uncertainty, ANFIS, with its fuzzy rules and learning ability, can manage these complexities more effectively than purely neural models. Another rationale for having chosen the ANFIS for the prediction of beach cusp spacing lies in the non-linear and intricate behavior of beach cusps. ANFIS is capable of good performance when modeling nonlinear relationships and extracting fuzzy rules from data, and therefore it can better model the hidden relationships between input-output features.

The Adaptive Neuro-Fuzzy Inference System (ANFIS) further stands out for its enhanced interpretability when compared to 'pure' neural network systems. While classical neural models such as the Multilayer Perceptron (MLP) are commonly regarded as black, ANFIS is characterized by a high level of transparency and interpretability due to its usage of IF-THEN fuzzy rules; this is a distinct advantage for coastal analysts in analyzing geomorphological processes.

Furthermore, prior studies have demonstrated the considerable success of ANFIS in modeling marine phenomena and coastal morphological features [27][28][29][30]. Successful applications of this technique include predictions related to sea wave characteristics [28][31][32], wave run-up [33] , sea level forecasting [30][34][35][36][37], estimation of suspended sediment [38][39], and prediction of sediment transport rates [40]. Moreover, it is well-established that accessing large datasets can be challenging in coastal geomorphology studies, and ANFIS can effectively model even with limited but high-quality datasets. Consequently, the shortcomings of the aforementioned methods in studying coastal features, alongside the reasons outlined for choosing the ANFIS model, have prompted the authors to utilize ANFIS to smooth and bridge gaps in our overall understanding of cusp systems by estimating inter-cusp spacing and determining the morphological effects of swash on the beach face. The objectives of the present paper are as follows:

(a) Develop a robust ANFIS paradigm to estimate beach cusp spacing with a large dataset.

(b) Investigate this method with famous assessment methods regarding prediction quality.

(c) Compare the model performance with other soft computing methods, such as ANN, so the conclusion ends up with which of them gives better accuracy in prediction.

(d) Comparison of accuracy and performance for the best models in different sections of beach face. The remaining structure of this research has section 2 introducing materials and methods onto a discussion of the study area, datasets, and neuro-fuzzy model. This is followed by section 3 which discusses results obtained in ANFIS and neural network methods and analyzes those results. Finally, section 4 briefly summarizes all findings of this research.

2. Materials and Methods

This study developed an ANFIS architecture to obtain predictions for beach cusp spacing using morphodynamic datasets as input to the model. Initially, field observations made by Nuyts et al. (2021) were drawn out over different months as morphodynamic characteristics of the beach cusp system in different levels of the beach face [2][41].

Configurations concerning different ANFIS models are presented in Table 2. Then, statistical metrics relevant to each step were calculated, thus providing comparison grounds for the accuracy of the optimum configuration among competing membership functions at each elevation of the beach cusp system. Accordingly, sections of the coastline yielded the most acceptable output results. MATLAB Software (2019) was utilized in this study for the simulation of various models. With the help of an extensive toolbox, the software facilitates design and appraisal of models for the systems under investigation in this study. In the last phase, a comparison between results and numerical outputs published by Nuyts et al. (2021) also occurred.

Table 2. Different configurations of the ANFIS architectures

Type of Input MF	Number of MF	Number of Hidden Neurons	Type of Output MF	Number of Epochs	Learning Method
Pimf	3-3-3-3-3	-	Linear	50	hybrid
gauss2mf	3-3-3-3-3	-	Linear	50	hybrid
gaussmf	3-3-3-3-3	-	Linear	50	hybrid
trapmf	3-3-3-3-3	-	Linear	50	hybrid
psigmf	3-3-3-3-3	-	Linear	50	hybrid
gbellmf	3-3-3-3-3	-	Linear	50	hybrid
dsigmf	3-3-3-3-3	-	Linear	50	hybrid
trimf	3-3-3-3-3	-	Linear	50	hybrid

2.1. Description of the Study Area

Set against a shoreline of natural beauty and largely left undeveloped, Long Strand in Rosscarbery Bay is located in County Cork in the southwest of Ireland. Because of its unique geographical location to the North Atlantic Ocean, the area is being studied by specialists in coastal geomorphology, bed dynamics, and modeling of natural processes for its high dynamism concerning hydrodynamic conditions, geomorphological features, and oceanographic characteristics.

These coasts are associated with high-energy waves and strong littoral currents where the annual average significant wave height offshore is approximately 1.33m, with an annual mean period per wave of about 9.98 seconds. The prevailing winds also come from the southwest, by the way. In its natural biome morphologic characteristics, beach sand is darker and coarse-grained, median grain size (D_{50}) = 0.673 mm [42]. For Long Strand, as regards neap tide, it varies between 1.75m minimum and 1.7m standard maximum for spring tide, based on the Irish Transverse Mercator (ITM) grid, classifying it as a mesotidal beach.

Powerful ocean waves exposed this coast to highly dynamic sedimentary processes, rendering it an important site for investigating erosion and deposition. With beach cusps, features found between the high-water mark and the low-water mark, and bars below water level, this particular shoreline is typical among other sites along this coast [43][2] (Figure 2).

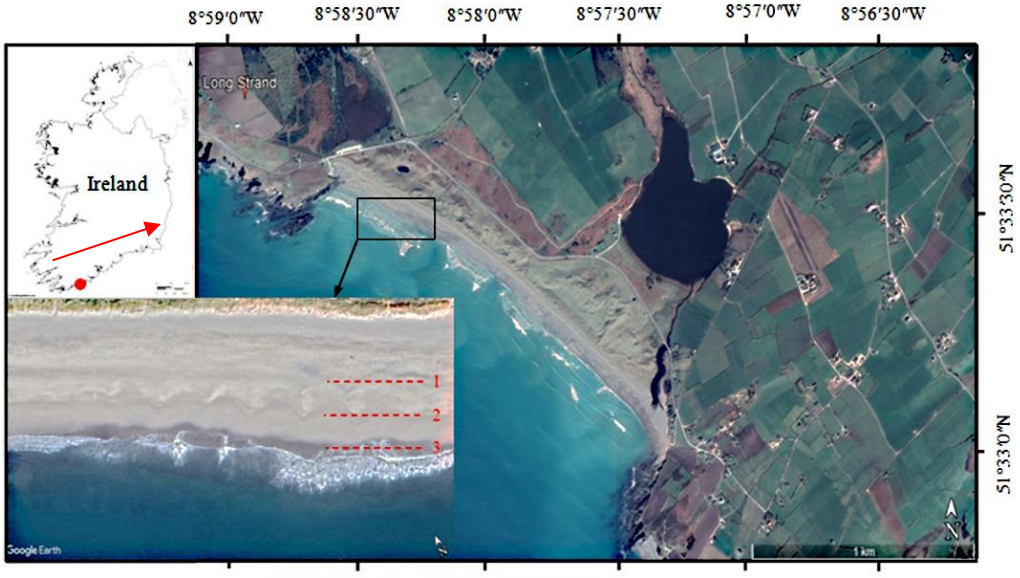


Figure 2. Satellite image of the study area (from Google Earth) (1) Upper level, (2) Middle level, and (3) Lower level of beach cusps [2]

2.2. Dataset

The surveys of a multi-level beach cusps system were employed during a field campaign using an Unmanned Aerial Vehicle (UAV) along the southwestern coast of Ireland between March and September 2019 [4]. Morphodynamic characteristics of the beach cusps system were recorded on 23 different days in a year, producing 61 morphodynamic datasets at various beach levels. These datasets were divided into four: cusp spacing (C_s), cusp elevation (C_e), cusp depth (C_d), and cusp amplitude (C_a). With regard to running ANFIS models, 80% of the data was allocated for training, while the rest 20% of the data was reserved for validating the predicted outcome [44]. Table 3 is a chart of some of the parameters of observed recorded beach cusps from field observations; Table 4 offers many statistical parameters related to the recorded data.

Table 3. Sample field observation data [2]

	Date	Level	Spacing(m)	Amplitude(m)	Elevation	Depth(m)
1	26 March	Upper Beach	39.5	0.86	5.41	16.91
		Mid Beach	38.5	0.58	3.14	16.57
		Low Beach	-	-	-	-
2	10 April	Upper Beach	40.3	0.83	5.46	15.01
		Mid Beach	24.6	0.34	2.81	12.31
		Low Beach	11.5	0.25	1.91	9.87
3	11 April	Upper Beach	39.2	0.87	5.62	14.98
		Mid Beach	25.0	0.43	2.76	12.69
		Low Beach	-	-	-	-
4	01 May	Upper Beach	38.9	1.05	4.87	15.67
		Mid Beach	14.9	0.21	2.33	9.06
		Low Beach	11.6	0.32	2.08	6.01
5	03 May	Upper Beach	37.7	0.81	5.69	13.24
		Mid Beach	12.8	0.23	2.42	8.81
		Low Beach	12.3	0.04	1.03	2.73
6	10 May	Upper Beach	37.9	0.79	5.68	12.32
		Mid Beach	19.9	0.29	2.96	8.55
		Low Beach	16.5	0.18	1.82	8.97

Table 4. Statistical parameters of recorded data [2]

Statistical properties	Upper Beach	Mid Beach	Low Beach
Max (m)	40.9	38.5	16.7
Min (m)	37.7	11.1	6.5
Mean (m)	40.26	18.17	11.09
Standard Deviation (m)	0.95	5.48	2.91
Coefficient of Variation	0.02	0.30	0.26

2.3. ANFIS Neuro-Fuzzy Model

The ANFIS neuro-fuzzy system is an intelligent hybrid model that is structured like a multilayer perceptron feedforward neural network designed by integrating artificial neural network learning algorithms with fuzzy inference systems. The first introduction was made by Jang (1993), and the proposed model is based on the Takagi-Sugeno fuzzy system rules. [25].

Within the architecture of this network, the nonlinear mapping of the input space into the output space is established through IF-THEN rules. Each rule output is designed as a linear combination of the input variables plus one constant, and the final output is the weighted average of the outputs of all the rules. Relations for the IF-THEN rules of a Takagi-Sugeno system with three inputs are given as follows:

Rule 1: IF x is A_1 and y is B_1 and z is C_1 THEN $f_1 = p_1x + q_1y + r_1z + s_1$ (1)

Rule 2: IF x is A_2 and y is B_2 and z is C_2 THEN $f_2 = p_2x + q_2y + r_2z + s_2$ (2)

Rule 3: IF x is A_3 and y is B_3 and z is C_3 THEN $f_3 = p_3x + q_3y + r_3z + s_3$ (3)

B_i, A_i, and C_i would be the membership functions for inputs x, y, and z, respectively, while p_i, q_i, and r_i would be the parameters of the output function, and s_i would be a constant. This output value y* would be inferred by some relations.

$$y^* = f = \frac{(w_1f_1+w_2f_2+w_3f_3)}{w_1+w_2+w_3} = \overline{w_1}f_1 + \overline{w_2}f_2 + \overline{w_3}f_3 \quad (4)$$

The ANFIS architecture consists of five layers, each of which has specific functions (Figure 3). The first and the fuzzification layer transforms x, y, and z into membership degrees via A_1, B_1, and C_1 for the first fuzzy rule, A_2, B_2, and C_2 for the second fuzzy rule, and A_3, B_3, and C_3 for the third fuzzy rule. The second layer is the rule layer, which combines the membership values in the antecedent part to obtain the weight of each rule. The third layer, known as the weight's normalization layer, calculates the normalized weight by dividing the weight of each rule by the sum of the weights of all possible rules, denoted as w_1, w_2, and w3 for rules 1, 2, and 3, respectively. The output of each rule that is obtained by multiplying the weight and the output defined in the consequent part of the fuzzy rule is calculated in the fourth layer or the defuzzification layer. The overall output in this part (output layer) is determined and recorded as the sum of all outputs from the fuzzy rules [28].

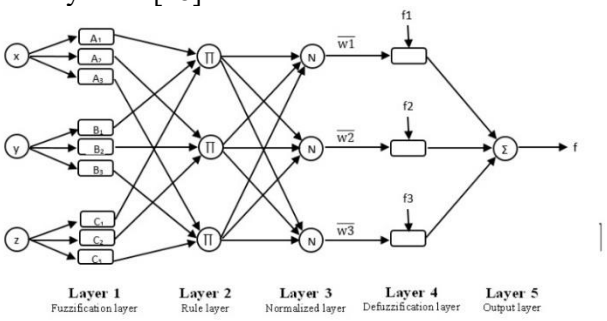


Figure 3. The structure of ANFIS model.

2.4. Evaluation Criteria

Different models are ordinarily assessed by calculating the discrepancies between the predicted and the observed values based on five statistical parameters. These parameters include the Coefficient of Efficiency (CE), Correlation Coefficient (R), Root Mean Square Error (RMSE), the Scatter Index (SI), and Mean Square Error (MSE), defined in Equations 5-9.

$$CE = 1 - \frac{\sum_{i=1}^{N}(O_i - P_i)^2}{\sum_{i=1}^{N}(O_i - \bar{O}_m)^2} \quad (5)$$

$$R = \frac{\sum_{i=1}^{N}(O_i - \bar{O}_m)\sum_{i=1}^{N}((P_i - \bar{P}_m)}{\sqrt{\sum_{i=1}^{N}(O_i - \bar{O}_m)^2}\sqrt{\sum_{i=1}^{N}(P_i - \bar{P}_m)^2}} \quad (6)$$

$$RMSE = \sqrt{\frac{1}{N}\sum_{i=1}^{N}(P_i - O_i)^2} \quad (7)$$

$$SI = \frac{RMSE}{\text{avrage observed value}} \quad (8)$$

$$MSE = \frac{1}{N}\sum_{i=1}^{N}(P_i - O_i)^2 \quad (9)$$

Here, N represents the total number of data points, O_i is the observed value obtained from field studies, $P_i$is the predicted value from the model results, $\overline{O}_m$ denotes the mean of the observed values from field studies, and $\overline{P}_m$is the mean of the predicted values calculated from the model results.

The range of Coefficient of Efficiency (CE) is one of the evaluation criteria by which values closer to one are regarded as a more ideal model [42]. The value of Correlation Coefficient (R) lies always between -1 and 1; the value 1 indicates zero error in prediction. RMSE usually is a popular parameter used to evaluate models that assume the errors follow a normal distribution. The RMSE value coming closer toward zero would indicate a higher accuracy in prediction [43]. The Scatter Index (SI) is also the percentage of the predicted data from the actual data in terms of dispersion, wherein 0 would mean that there is no dispersion in the model's prediction output. Another evaluation parameter is the range of the Coefficient of Efficiency (CE); a value of this metric closest to one will then indicate an ideal model [44].

3. Discussion and Conclusion

3.1. ANFIS Model Results

In this study, ANFIS was employed with the aim of accurately and interpretably modeling the relationships among geometric parameters. The results obtained from implementing this model demonstrated that selecting an appropriate structure for fuzzy rules and membership functions plays a key role in enhancing the model's accuracy and generalizability. Visual evaluation of the model through the Rule Viewer and analysis of the initial membership functions provided greater transparency regarding the model's operation and sensitivity to input variations. Figure 4 presents a view of the ANFIS Rule Viewer, illustrating the performance of 27 fuzzy rules in response to three input parameters- cusp depth (C_d), cusp elevation (C_e), and cusp amplitude (C_a)-and one output (Cusp spacing). Each column represents one of the input parameters, and the yellow lines indicate the activation level of each rule for the current input value (shown by the red line). The final column displays the output of each rule using blue rectangles.

As shown in this figure, for the current input values (Depth=9.05, Elevation=3.38, Amplitude=0.445), the highest activation corresponds to the intermediate rules, which match the "Medium" levels of the input membership functions. This indicates that the model assigns greater weight to the intermediate rules, and the final output (Cusp spacing=33) is determined accordingly. Such behavior demonstrates the model's accuracy and efficiency in appropriately identifying and weighting fuzzy rules under real data conditions.

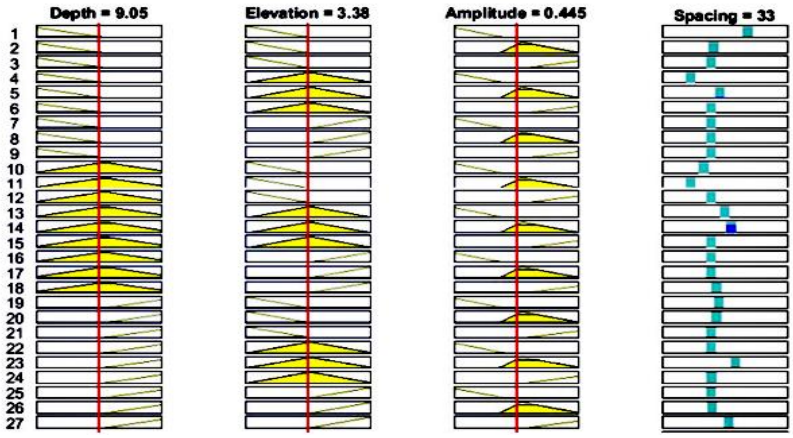
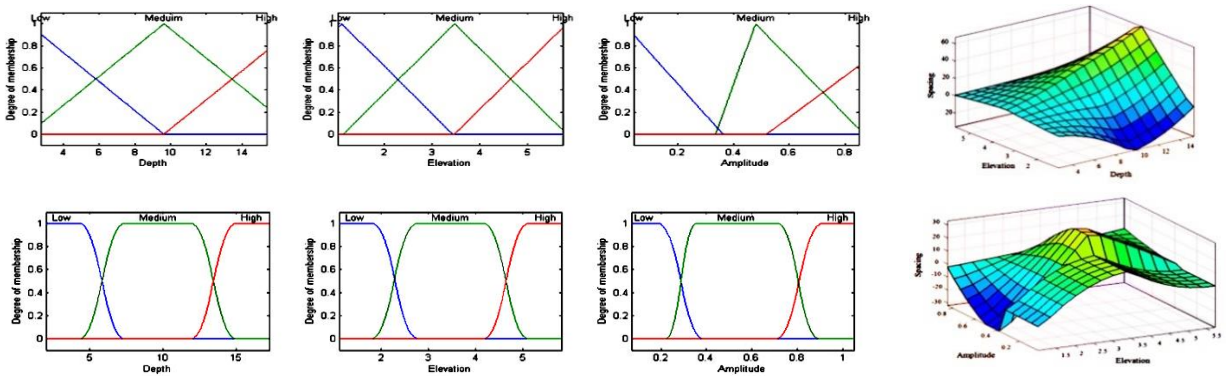


Figure 4. Rule viewer of designed fuzzy model.

The functional structure of ANFIS model for two types of input initial membership functions for input parameters (depth, elevation, and amplitude) is depicted in Figure 5. Upper sections (a, b, c) show the model using trimf membership function; lower sections illustrate the functional operation of the model under the pimf membership function. Each input parameter is divided into three fuzzy sets labeled "Low," "Medium," and "High," which each decide the degree of membership for the input value. Within (d), a 3D illustration depicts the relationships between the input variables (Elevation vs Depth shown in the upper graph; Amplitude vs Elevation shown in the lower graph) and the output variable (Cusp spacing). The three-dimensional surfaces therefore denote the complex non-linear interdependencies between input and output parameters; thus, proving ANFIS's strength in identifying hidden patterns within the data. Trimf and pimf membership functions differ in transition behavior; trimf has clear boundaries and linear transition, while pimf transition is smooth and floored with overlapping characteristics, increasing model

flexibility in dealing with real-life data. The different slopes observed in the 3D surfaces indicate the response of the model output to changes in input parameters, which is important for further analyses and finding critical points in the system.



(a) (b) (c) (d)

Figure 5. Two examples of the initial membership functions (trimf and pimf) of X-axis input parameters for the ANFIS model: (a) Depth (b) Elevation, (c) Amplitude (d) 3D surface visualization of the relationship between the input and spacing cusps.

The ANFIS model performances are listed in the tables of statistical metrics achieved for all the phases of identification (Table 5). Since Model (VIII) stated in the table provides better accuracy from training and testing phases compared to the other models as shown by various metrics, therefore, this model is found to be better in fitting the data. R is the metric that indicates how well the predicted values correlate with the actual values; the closer R is to 1, the better the model has performed, exhibiting a high degree of consistency in prediction with the actual data.

From the bar chart shown in Figure (6a), R for the model with 'trimf' membership functions is significantly higher for both training and testing, therefore, indicating that the data was fit more by this model. The RMSE signifies the absolute error in prediction, with lower values implying higher model fitness. The model with the 'trimf' function has shown the lowest RMSE in both training and testing phases as shown in the bar chart in Figure (6b). So, this contributes to lower errors and more accurate predictions when compared with other models. The combination of these two ranges hence would argue that the ANFIS with the 'trimf' function achieved a robust trade-off between accuracy and error in predicting the data. This becomes very important as in practical scenarios the models that are less erroneous as well as highly correlated to the actual data are more acceptable. In addition, the difference between the performances of the models during training and testing suggests generalization strength of the model 'trimf' one is a good performer even in testing and hence is free from overfitting and predicting fresh data.

The main outcome of Figure 6 suggests the ANFIS model with the 'trimf' membership function to be excellent for prediction for this study, as it had the highest R value (very close to 1) in conjunction with the lowest RMSE value during both testing and training phases. Hence, implying the highest prediction accuracy and stability for new data. The 'dsigmf' and 'psigmf' models, on the contrary, got low ratings and high RMSE, which means they were not capable of learning and generalizing to new data. Further, variations in model performance between training and testing in some instances indicate their sensitivity and instability against the input data.

Table 5. Results of different models of ANFIS

Archite-cture. no	Type of MFs		Phases	RMSE	MSE	SI	CE	R	Overall (MSE)
	Input	Output							
I	pimf	Linear	Training	0.047321	0.002239	0.001782	0.999987	0.997739	0.001881
			Testing	0.020456	4.18E-04	0.001177	0.999994	0.99916	
II	gauss2mf	Linear	Training	0.05265	0.002772	0.001983	0.999984	0.998475	0.002298
			Testing	0.019052	3.63E-04	0.001096	0.999995	0.998209	
III	gaussmf	Linear	Training	0.077447	0.005998	0.002917	0.999965	0.996026	0.004932
			Testing	0.024149	5.83E-04	0.00139	0.999992	0.99948	
IV	trapmf	Linear	Training	0.052437	0.00275	0.001975	0.999984	0.998714	0.002302
			Testing	0.02179	4.75E-04	0.001254	0.999993	0.998719	
V	psigmf	Linear	Training	0.06841	0.00468	0.002577	0.999973	0.997655	0.003954
			Testing	0.031501	9.92E-04	0.001813	0.999986	0.999859	
VI	gbellmf	Linear	Training	0.052679	0.002775	0.001984	0.999984	0.998773	0.002314
			Testing	0.020873	4.36E-04	0.001201	0.999994	0.999591	
VII	dsigmf	Linear	Training	0.068128	0.004641	0.002566	0.999973	0.998809	0.004037
			Testing	0.039644	0.001572	0.002282	0.999978	0.998488	
VIII	trimf	Linear	Training	0.037968	0.001442	0.00143	0.999992	0.9999	0.001192
			Testing	0.013254	1.76E-04	7.63E-04	0.999998	0.9999	

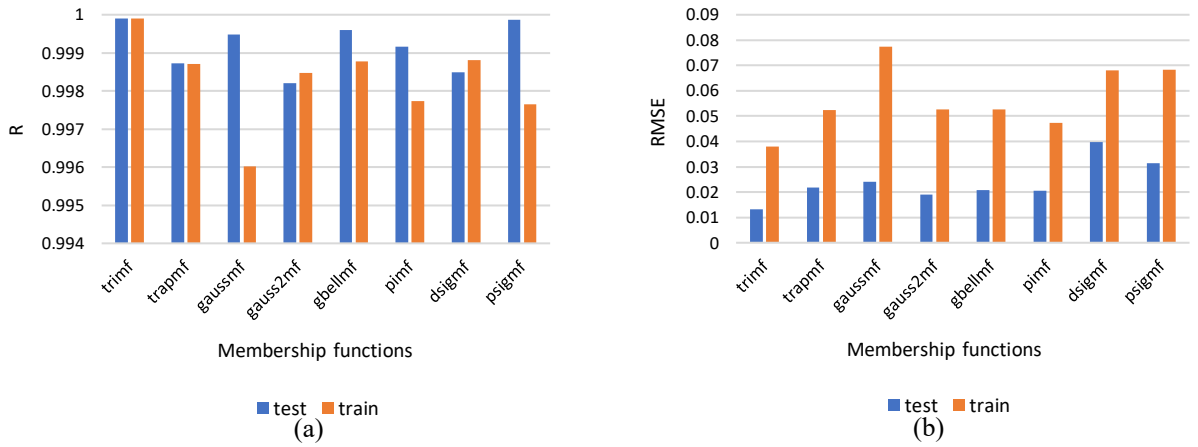


Figure 6. Variation of (a) R and (b) RMSE for ANFIS models

Figure 7 presents box plots concerning percentage error for different ANFIS models in two phases: testing (Figure 7a) and training (Figure 7b). The examination of these plots tells us that the line within each box indicates the median value (second quartile); the cross symbol indicates the mean of the data; and the box width indicates the interval between the first and third quartiles, that is, the IQR. The purpose of this figure, aside from rating the models' accuracies, is to rate their stability and sensitivity to input data.

A comparison of the box plots validates that in the testing phase, the error percentage is quite variable for the dsigmf model, exhibiting the largest IQR, signifying the model is input data-sensitive and unstable. In addition, the model possesses outliers, suggesting instances where error values are dramatically larger than normal. During the training phase, the gbellmf, dsigmf, and psigmf models also show high IQRs, which means their errors are also very dispersed. In contrast, the models with the smallest IQRs during both the testing and training phase are the trimf, which indicates a very limited range of variability in percentage error, and is one in which most of the errors are near its central value. This model also has the least median and mean error values as compared to all other tested models, and its box plot is nearly symmetrical, with median and mean being almost coincident. There are no significant amounts of outliers in this model and it shows the most consistent and reliable performance across all data instances.

The ANFIS model with the trimf membership function is the best among all membership functions examined in terms of error magnitude, error dispersion and the presence of outliers, which figure 7 demonstrates very well. This overarching superiority suggests that the trimf model is both stable and accurate in prediction compared to others.

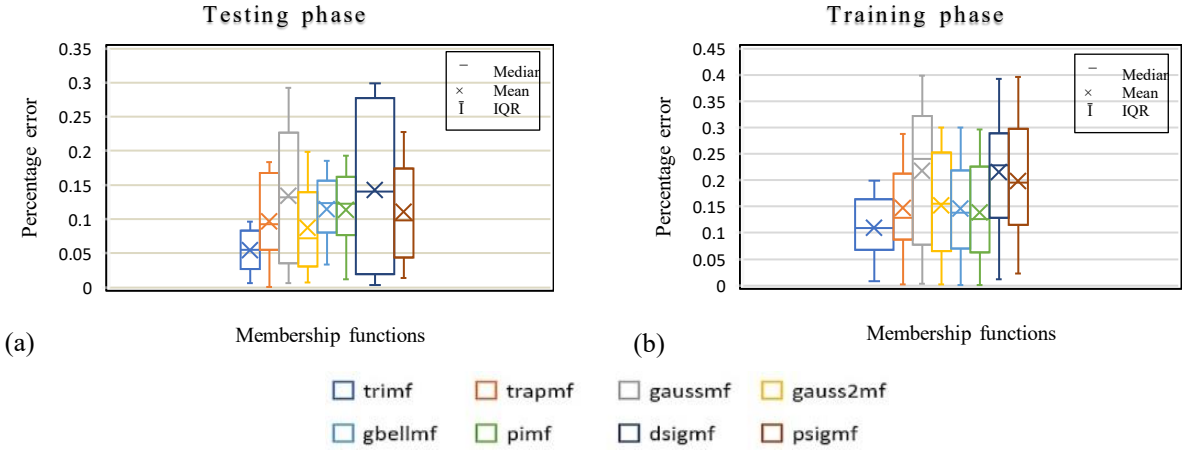


Figure 7. Box plots of percentage error for ANFIS models (a) testing and (b) training stage.

The evaluated ANFIS model with the trimf membership function presents a comparison between the observed and predicted data of beach cusp spacing in training (a) and testing (b) (Figure 8). The blue dotted lines represent actual data, while red dotted lines are predicted data. The close agreement of both data sets in both phases considered with even lower MSE values (0.0014416 in training and 0.00017567 in testing) indicates a very high accuracy of the model in reproducing and predicting the complex trends of cusp spacing. This, thus, confirms the generalization capability and reliable performance in real-world conditions and unseen data for ANFIS (trimf) model.

Radar plots (spider plots) are made on the five statistical measures called the correlation coefficient (R), the root mean squared error (RMSE) and the mean square error (MSE), the index of agreement (SI), and the efficiency coefficient (CE) to evaluate the performance of ANFIS in the model with different membership functions for their predictions on cusp spacing in training (a) and testing (b) phases. Such plots can facilitate easy comparisons of model performance across different facets.

In the stage of training (Figure 9a), gaussmf is the membership function for which the model gives the worst performance among these models; in most of the metrics, this model's values were less favorable than those of every other model. This is quite extreme in the RMSE and MSE metrics, where this model indicated a higher value. Meanwhile, the trimf model had exhibited better performance through most of the metrics, issuing favorable values.

In the testing phase (Figure 9b), the dsigmf model exhibits the lowest accuracy in most of the statistical measures clearly deviating from the other models. It then has higher values in RMSE and MSE but shows poor performance in CE and R metrics. Hence, it indicates high sensitivity and instability of the dsigmf model when faced with new and unseen data.

As observed in Figure 9, ANFIS model used with the trimf membership function revealed superior performance values in the majority of statistical metrics during both the training and the testing phases. It is important to note that in the final evaluation and selection of the best model, the criteria of the correlation coefficient (R) and the mean square error (MSE) were emphasized the most, as these two metrics really represent the accuracy and generalization capability of the model. Hence, best performance was given to the trimf model, which finally gets selected as the best model.

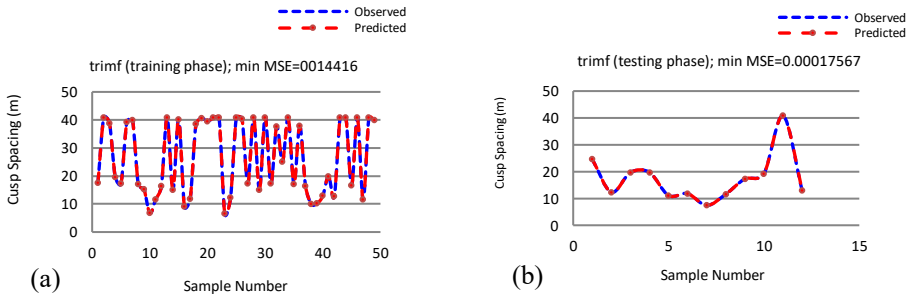
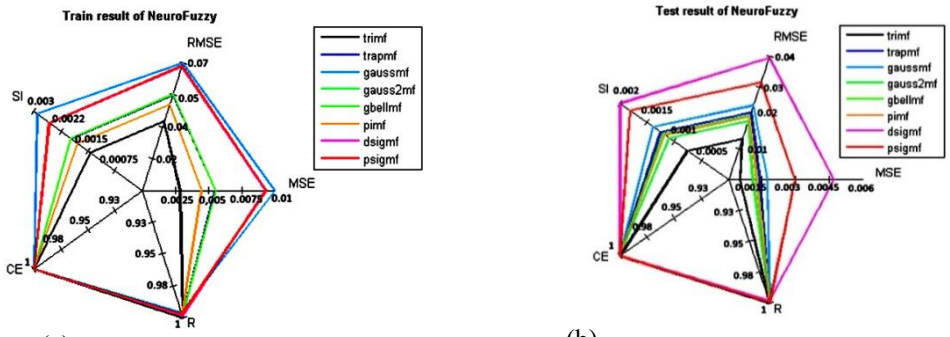


Figure 8. Compare the observed cusp spacing and the best predicted performance of optimal model-ANFIS (trimf), a) Training phase b) Testing stage.

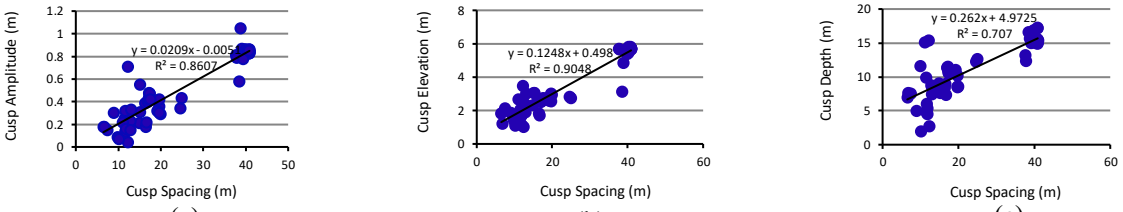


(a) (b)

Figure 9. Spider plots of five performance criteria for prediction of cusp spacing in a) training and b) testing stages.

Figure 10 consists of three scatter plots showing the relationship between predicted cusp spacing by the optimized ANFIS model with the trimf membership function and the beach cusps' three primary morphological parameters: Amplitude, Elevation, and Depth. All plots show the relationship between the parameters investigated, including the linear regression line and coefficient of determination (R^2) reflecting the strength of correlation between the variables.

Plot (a) considers the relationship between cusp spacing and cusp amplitude. The R^2 value of 0.86 confirms a strong correlation between these two parameters, signifying that changes in cusp spacing are significantly associated with changes in their amplitude. The slope of the regression line (0.0209) further asserts that an increase in cusp spacing results in an increase in amplitude in direct proportion to it. In plot (b), the focus is on the relationship between cusp spacing and cusp elevation. The R^2 value for this plot is calculated to be 0.90, signifying a very high and significant correlation between these two parameters. This is the highest coefficient of determination among the three plots and infers that cusp spacing greatly influences the elevation of cusps. The slope of the line of regression is 0.1248, indicating that with an increase in cusp spacing, elevation also increases greatly. Plot (c) gives the relationship between cusp spacing and depth. The R^2 value for this plot is 0.70, indicating a moderate correlation between these two parameters. Though a positive and linear correlation exists with a slope of 0.262 for cusp spacing to depth, the data points here show greater dispersion compared to the previous two plots, indicating that some other factors may also influence the depth of cusps. These three plots together affirm that the ANFIS model with the trimf membership function successfully drew reasonably strong linear correlations between cusp spacing and their primary morphological parameters. More significantly, the higher R^2 value in the elevation plot, compared with that of amplitude and depth, puts additional emphasis on the importance of elevation with respect to cusp spacing. Equally, the positive slopes of the regression lines trending in all three plots assist in inferring that in addition to cusp spacing, other morphological parameters also tend to increase in direct proportion with it.



(a) (b) (c)

Figure 10. Scatter plots of the predicted cusp spacing versus other parameters of the cusps, based on the ANFIS (trimf) model, (a)cusp amplitude, (b) cusp elevation, and (c) cusp depth

3.2. Comparison Between ANN and ANFIS

Figure 11 shows box plots of relative error in the beach face for three sections - Upper, Mid, and Low sections of the beach face with respect to the ANFIS (trimf) model. Obviously, the central line in the box will represent the median error in that box, while the symbol × indicates the value of the mean error. Furthermore, a boxwidth indicates the interquartile range (IQR) of the data. It is evident that the lowest mean relative error occurs in the Mid Beach section of the ANFIS (trimf) model. The lowest median relative error was recorded in the Low section; this implies that these two zones exhibit the same behavior with respect to beach cusp spacing prediction, in which the model's performance

is better and more consistent than in most Upper beach sections. Furthermore, the dispersions of errors occurring in the Low section of the beach face are smaller compared with other sections, which indicates a higher stability and robustness of the model in that area. This will become practically important, as the model has actually been performing more reliably for those parts of the beach face experiencing considerable morphological adjustment.

Taking into account that the authors have employed artificial neural networks in some studies to assess the variations that happen in cusp spacings [24], this study will therefore aim at assessing the ANFIS model's performance through comparing the obtained MSE values from both methods and in turn improve on the investigation into the predictive metrics of each of the models as well as the groundworks for providing better discussions on the performances and generalization capabilities of the various models in predicting morphodynamic patterns throughout some regions of the beach face.

Figure 12 provides the MSE values of various ANN and ANFIS models in bar chart form, as well as in tabular format, across the beach face sections. These values are compared and it was found that the ANFIS (trimf) model always gave the lowest MSE as compared with the three fished out ANN models (ANN with CFBP, FFBP, and EBP algorithms) across the entire beach face sections. Specifically, the least MSE among all sections and models was recorded for the ANFIS model in the Low Beach Face section, scoring a net value of 0.0001. On the flip side, the least MSE values for the ANN types are predominantly seen under the Upper Beach Face section (specifically under ANN (EBP) model with a value of 0.06).

It is worth noting that ANFIS (trimf) model performs very well in all other sections and not just in Low Beach Face section, with MSE scores greatly lower than those recorded by ANN models. Hence, this buttresses the claim that the ANFIS model has a higher competence in simulating and forecasting spacings between beach cusps in Low Beach Face region, which usually has more complex conditions from morphodynamics.

In summary, the conclusion derived from this is that artificial neural network models were quite acceptable for application on the Upper Beach Face section, while there was a clear difference between the two models with the ANFIS (trimf) being much preferable in terms of accuracy and stability, primarily in Mid Beach Face and Low Beach Face. Consequently, the ANFIS (trimf) model is recommended for more precise simulation and prediction of morphodynamic features in lower beach face areas, while ANN models could be more suitable for upper beach face areas. This critical comparison indicates the preference for selecting the finest model for the conditions or characteristics of each section of beach face.

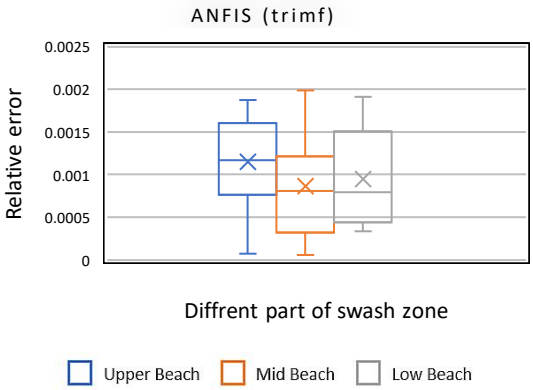
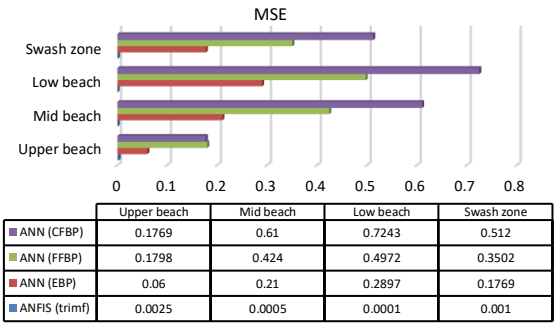


Figure 11. Box plots of relative error in different parts of the beach face in ANFIS (timf) model.



	Upper beach	Mid beach	Low beach	Swash zone
ANN (CFBP)	0.1769	0.61	0.7243	0.512
ANN (FFBP)	0.1798	0.424	0.4972	0.3502
ANN (EBP)	0.06	0.21	0.2897	0.1769
ANFIS (trimf)	0.0025	0.0005	0.0001	0.001

Figure 12. The magnitudes of MSE of optimal models in different parts of the beach and different models.

4. Results

The study adopted the Adaptive Neuro-Fuzzy Inference System (ANFIS) model for the prediction of the spacing of multi-barred crescentic beach cusps. The results obtained from this model showed that correctly choosing a fuzzy rule structure and membership functions was instrumental in enhancing the model's accuracy and interpretability. The analysis of the model performance using the Rule Viewer and initial membership function examination added much transparency related to the way model output varies concerning input changes.

The ANFIS model using the triangular membership function (trimf) performed best in this study compared to other models tested in both training and test phases. The model exhibited a high correlation coefficient (R close to 1); low values for Root Mean Square Error (RMSE) and Mean Square Error (MSE); and very low dispersion of errors (low IQR). Moreover, the absence of outliers in the trimf model output indicates the stability and reliability of this model in the face of new data.

The results from the comparison made between the ANFIS model and optimal ANN models considered for this study also indicated that the ANFIS (trimf) achieved higher prediction accuracy and significantly lower error values than the ANN models in all the different beach face zones (Upper Beach Face, Mid

Beach Face, and Low Beach Face). In particular, in the Low Beach Face area, the ANFIS model exhibited superior performance by recording the lowest MSE value.

When the relationships between the beach cusp spacing and three morphological parameters-amplitude, elevation, and depth of the beach cusps-were examined, strong and significant ones were extracted by the model, with the highest correlation being found between the spacing and the elevation of the beach cusps (R^2=0.9).

In summary, the current study concluded high spatial accuracy, good generalization capability, stability, and enhanced interpretability of the proposed ANFIS with trimf membership function as a promising technique for predicting the spacing of multi-barred crescentic beach cusps, thus placing it in the front line when compared to optimal ANN models.

5. References

[1] Ribas, F., Falqués, A., Deèswart, H. E., Dodd, N., Garnier, R., & Calvete, D. (2015). Understanding coastal morphodynamic patterns from depth-averaged sediment concentration. *Reviews of Geophysics*, *53*(2), 362–410. https://doi.org/10.1002/2014RG000457

[2] Nuyts, S., Li, Z., Hickey, K., & Murphy, J. (2021). Field observations of a multilevel beach cusp system and their swash zone dynamics. *Geosciences (Switzerland)*, *11*(4), 1–24. https://doi.org/10.3390/geosciences11040148

[3] Vousdoukas, M. I. (2012). Characteristics and interactions of multiple beach cusp systems on a meso-tidal, steeply-sloping beach. *Proceedings of the International Offshore and Polar Engineering Conference*, *4*, 1475–1481.

[4] Nolan, T. J., Kirk, R. M., & Shulmeister, J. (1999). Beach cusp morphology on sand and mixed sand and gravel beaches, South Island, New Zealand. *Marine Geology*, *157*(3–4), 185–198. https://doi.org/10.1016/S0025-3227(98)00150-9

[5] Guza, R.T. and Inman, D. (1975). Edge Waves and Beach Cusps. *Journal of Geophysical Research*, *80*(21), 2997–3012. https://doi.org/10.9753/icce.v16.81

[6] Guza, R. T., & Bowen, A. J. (1976). Finite Amplitude Edge Waves. *Journal of Marine Research*, *34*(2), 269–293.

[7] Werner, B. T., & Fink, T. M. (1993). Beach cusps as self-organized patterns. *Science*, *260*(5110), 968–971. https://doi.org/10.1126/science.260.5110.968

[8] Sunamura, T. (2004). A predictive relationship for the spacing of beach cusps in nature. *Coastal Engineering*, *51*(8–9), 697–711. https://doi.org/10.1016/j.coastaleng.2004.07.004

[9] Coco, G., D. A. Huntley, and T. J. O. (2000). Investigation of a self-organisation model for beach cusp formation and development. *J. Geophys. Res*, *105–21*(1), 991– 22,002.

[10] Guest, T. B., & Hay, A. E. (2019). Timescales of beach cusp evolution on a steep, megatidal, mixed sand-gravel beach. *Marine Geology*, *416*(September 2018), 105984.

[11] Ali, S., Darsan, J., & Wilson, M. (2017). Cusp morphodynamics in a micro-tidal exposed beach. *Journal of Coastal Conservation*, *21*(6), 777–788. https://doi.org/10.1007/s11852-017-0536-2

[12] Shiea-Ali, M., & Valipour, A. (2021). Impact of Hydrodynamic Forces on Morphodynamic Classification of Beaches in some parts of the Iranian coasts. International Journal of Coastal and Offshore Engineering, 5(3), 26–39. https://doi.org/10.52547/ijcoe.5.3.26

[13] Masselink, G. (1999). Alongshore variation in beach cusp morphology in a coastal embayment. *Earth Surface Processes and Landforms*, *24*(4), 335–347. https://doi.org/10.1002/(sici)1096-9837(199904)24:4<335::aid-esp968>3.3.co;2-8

[14] Pitman, S. J., Hart, D. E., & Katurji, M. H. (2019). Application of UAV techniques to expand beach research possibilities: A case study of coarse clastic beach cusps. *Continental Shelf Research*, *184*(July), 44–53. https://doi.org/10.1016/j.csr.2019.07.008

[15] Sathish, S., Kankara, R. S., & Rasheed, K. (2018). Morphometric and sediment analysis of beach cusp in correlation to rip currents: a case study from tropical coast, West coast of India. *Environmental Earth Sciences*, *77*(16), 0. https://doi.org/10.1007/s12665-018-7754-2

[16] Daly, C. J., Floc'h, F., Almeida, L. P. M., Almar, R., & Jaud, M. (2021). Morphodynamic modelling of beach cusp formation: The role of wave forcing and sediment composition. *Geomorphology*, *389*, 107798. https://doi.org/10.1016/j.geomorph.2021.107798

[17] Kaneko, A. (1985). Formation of beach cusps in a wave tank. *Coastal Engineering*, *9*(1), 81–98. https://doi.org/10.1016/0378-3839(85)90028-6

[18] Aoki, H., & Sunamura, T. (2000). A laboratory experiment on the formation and morphology of beach cusps. *Chikei*, *21*(3), 291–306.

[19] Pitman, S. J., Coco, G., Hart, D. E., & Shulmeister, J. (2024). Observations of beach cusp morphodynamics on a composite beach. *Geomorphology, 447*, 109026. https://doi.org/10.1016/j.geomorph.2023.109026

[20] Masselink, G., Hegge, B. J., & Pattiaratchi, C. B. (1997). Beach cusp morphodynamics. *Earth Surface Processes and Landforms, 22*(12), 1139–1155. https://doi.org/10.1002/(SICI)1096-9837(199712)22:12<1139::AID-ESP766>3.0.CO;2-1

[21] Van Gaalen, J. F., Kruse, S. E., Coco, G., Collins, L., & Doering, T. (2011). Observations of beach cusp evolution at Melbourne Beach, Florida, USA. *Geomorphology, 129*(1–2), 131–140. https://doi.org/10.1016/j.geomorph.2011.01.019

[22] Alexandridis, A. (2013). Evolving RBF neural networks for adaptive soft-sensor design. *International*

Journal of Neural Systems, 23(6), 1–14. https://doi.org/10.1142/S0129065713500299
[23] Pape, L., Ruessink, B. G., Wiering, M. A., & Turner, I. L. (2007). Recurrent neural network modeling of nearshore sandbar behavior. *Neural Networks, 20*(4), 509–518. https://doi.org/10.1016/j.neunet.2007.04.007
[24] Valipour, A., & Shirgahi, H. (2024). Prediction of the multi-level beach cusp spacing using artificial neural networks. *Iranian Journal of Geophysics, 17*(5), 1–18. https://doi.org/10.30499/IJG.2023.387044.1500
[25] Jang, J. S. R. (1993). ANFIS: Adaptive-network-based fuzzy inference system. *IEEE Transactions on Systems, Man, and Cybernetics, 23*(3), 665–685. https://doi.org/10.1109/21.256541
[26] Brown, M., & Harris, C. (1995). *Neurofuzzy adaptive modeling and control*. Englewood Cliffs, NJ: Prentice-Hall.
[27] Kisi, O. (2005). Suspended sediment estimation using neuro-fuzzy and neural network approaches. *Hydrological Sciences Journal, 50*(4), 683–696. https://doi.org/10.1623/hysj.2005.50.4.683
[28] Kazeminezhad, M. H., Etemad-Shahidi, A., & Mousavi, S. J. (2005). Application of fuzzy inference system in the prediction of wave parameters. *Ocean Engineering, 32*(14–15), 1709–1725. https://doi.org/10.1016/j.oceaneng.2005.02.001
[29] Hong, Y. S. T., & White, P. A. (2009). Hydrological modeling using a dynamic neuro-fuzzy system with on-line and local learning algorithm. *Advances in Water Resources, 32*(1), 110–119. https://doi.org/10.1016/j.advwatres.2008.10.006
[30] Shiri, J., Makarynskyy, O., Kisi, O., Dierickx, W., & Fard, A. F. (2011). Prediction of short-term operational water levels using an adaptive neuro-fuzzy inference system. *Journal of Waterway, Port, Coastal, and Ocean Engineering, 137*(6), 344–354. https://doi.org/10.1061/(ASCE)WW.1943-5460.0000097
[31] Özger, M. (2009). Neuro-fuzzy approach for the spatial estimation of ocean wave characteristics. *Advances in Engineering Software, 40*(9), 759–765. https://doi.org/10.1016/j.advengsoft.2009.02.004
[32] Bozorgzadeh, L., Bakhtiari, M., Shani Karam Zadeh, N., & Esmaeeldoust, M. (2019). Forecasting of wind-wave height by using adaptive neuro-fuzzy inference system and decision tree. *Journal of Soft Computing in Civil Engineering, 3*(3), 22–36. https://doi.org/10.22115/scce.2019.199291.1125
[33] Bakhtyar, R., Yeganeh Bakhtiary, A., & Ghaheri, A. (2008). Application of neuro-fuzzy approach in prediction of runup in swash zone. *Applied Ocean Research, 30*(1), 17–27. https://doi.org/10.1016/j.apor.2008.02.004
[34] Lin, L. C., & Chang, H. K. (2008). An adaptive neuro-fuzzy inference system for sea level prediction considering tide-generating forces and oceanic thermal expansion. *Terrestrial, Atmospheric and Oceanic Sciences, 19*(1–2), 163–172. https://doi.org/10.3319/TAO.2008.19.1-2.163(SA)
[35] Karimi, S., Kisi, O., Shiri, J., & Makarynskyy, O. (2013). Neuro-fuzzy and neural network techniques for forecasting sea level in Darwin Harbor, Australia. *Computers & Geosciences, 52*, 50–59. https://doi.org/10.1016/j.cageo.2012.09.015
[36] Kaloop, M. R., El-Diasty, M., & Hu, J. W. (2017). Real-time prediction of water level change using adaptive neuro-fuzzy inference system. *Geomatics, Natural Hazards and Risk, 8*(2), 1320–1332. https://doi.org/10.1080/19475705.2017.1327464
[37] Wang, B., Wang, B., Wu, W., Xi, C., & Wang, J. (2020). Sea-water-level prediction via combined wavelet decomposition, neuro-fuzzy and neural networks using SLA and wind information. *Acta Oceanologica Sinica, 39*(5), 157–167. https://doi.org/10.1007/s13131-020-1569-1
[38] Kisi, O., Haktanir, T., Ardiclioglu, M., Ozturk, O., Yalcin, E., & Uludag, S. (2009). Adaptive neuro-fuzzy computing technique for suspended sediment estimation. *Advances in Engineering Software, 40*(6), 438–444. https://doi.org/10.1016/j.advengsoft.2008.06.004
[39] Shamaei, E., & Kaedi, M. (2016). Suspended sediment concentration estimation by stacking the genetic programming and neuro-fuzzy predictions. *Applied Soft Computing, 45*, 187–196. https://doi.org/10.1016/j.asoc.2016.03.009
[40] Sadeghifar, T., & Barati, R. (2018). Application of adaptive neuro-fuzzy inference system to estimate alongshore sediment transport rate (a real case study: Southern shorelines of Caspian Sea). *Journal of Soft Computing in Civil Engineering, 2*(4), 72–85. https://doi.org/10.22115/SCCE.2018.135975.1074
[41] Nuyts, S., Murphy, J., Li, Z., & Hickey, K. (2020). A methodology to assess the morphological change of a multilevel beach cusp system and their hydrodynamics: Case study of Long Strand, Ireland. *Journal of Coastal Research, 95*(sp1), 593–598. https://doi.org/10.2112/SI95-116.1
[42] Ruz, M. H. (1989). Recent evolution of the southeast barrier coast of Ireland. *Journal of Coastal Research, 5*(3), 523–539.
[43] Malvarez, G. C., Cooper, J. A. G., & Jackson, D. W. T. (2001). Relationships between wave-induced currents and sediment grain size on a sandy tidal-flat. *Journal of Sedimentary Research, 71*, 705–712. https://doi.org/10.1306/d4268d74-2b26-11d7-8648000102c1865d
[44] Mandal, S., & Prabaharan, N. (2006). Ocean wave forecasting using recurrent neural networks. *Ocean Engineering, 33*(10), 1401–1410. https://doi.org/10.1016/j.oceaneng.2005.08.007
[45] McCuen, R. H., Knight, Z., & Cutter, A. G. (2006). Evaluation of the Nash–Sutcliffe efficiency index. *Journal of Hydrologic Engineering, 11*(6), 597–602. https://doi.org/10.1061/(ASCE)1084-0699(2006)11:6(597)

[46] Chai, T., & Draxler, R. R. (2014). Root mean square error (RMSE) or mean absolute error (MAE)? Arguments against avoiding RMSE in the literature. *Geoscientific Model Development, 7*(3), 1247–1250. https://doi.org/10.5194/gmd-7-1247-2014

[47] Valipour, A., & Shirgahi, H. (2022). Estimation of rip density on intermediate beaches using an extreme learning machine model. *Regional Studies in Marine Science, 52*, 102332. https://doi.org/10.1016/j.rsma.2022.102332

INTERNATIONAL JOURNAL OF
COASTAL, OFFSHORE & ENVIRONMENTAL ENGINEERING IJCOE Vol.11/No. 3/Summer 2026 (48-55)

Available online at: www. Ijcoe.org

Numerical simulation of bottom outlet valve openings and reverse slope transition to control downstream pressure drop in pipeline of effluent discharge to sea

Saeed Madadyari[1], Mehdi Nezhadnaderi[2]*, Babak Fazli Malidareh[3]

[1]*Department of Civil Engineering, Na.C., Islamic Azad University, Najafabad, Iran; 2219791505@iau.ir*
[2*] *Associate Professor, Department of Civil Engineering, To.C., Islamic Azad University, Tonekabon, Iran. (Corresponding Author); mehdi.nezhadnaderi@iau.ac.ir*
[3] *Associate Professor, Department of Civil Engineering, BaB.C., Islamic Azad University, Babol, Iran; fazli.babak@iau.ac.ir*

ARTICLE INFO

Article History:
Received 27 Feb 2026
Accepted 30 June 2026
Available online ….

Keywords:
Negative pressure, Bottom outlet valve, Hydraulic model, effluent discharge to sea, Cavitation.

ABSTRACT

Bottom outlets are a set of structures used to transfer water from the dam reservoir to the downstream. Therefore, due to the importance of this part of the dam, the study of the cavitation phenomenon is particularly sensitive. In the downstream bottom outlets, the flow is transferred at high speed, and due to the separation of the flow and its sudden transformation from a pressurized state to a free state, a sharp drop in the pressure values downstream of the valve occurs. The flow passing under the valve creates a swirling flow downstream of it, the main characteristic of which is a sharp pressure drop. The drop created is a function of the valve opening, the water head behind the valve, and the geometry of the channel. On the other hand, severe pressure fluctuations cause a decrease in local pressure in that area, and due to the high flow velocity, the potential for cavitation increases. How to minimize the negative pressures created downstream of the valve is one of the important issues that are raised in the case of valves. The negative pressures created will ultimately lead to damage to the downstream structure and the valve itself. Cavitation is one of the most unpleasant hydrodynamic phenomena that occurs as a result of such negative pressures created downstream of the valve. In this paper, the governing equations of flow in the two-dimensional case in the physical model of the bottom outlet of the Narmashir dam were solved using appropriate turbulence models to calculate the flow and turbulence pattern. The pressure values were obtained from the numerical solution and then the pressure values on the bottom outlet and the surface in front of the bottom outlets were investigated for 30, 50, and 80 percent opening. The results show that the pressure values obtained from the numerical model follow a similar pattern as the results of physical model. With greater opening, the pressures on the bottom and top of the bottom outlet decrease. In this study, by installing a reverse slope transition after the valves and a larger diameter pipe after the transition, the negative pressure at the end of the pipe after the valve can be reduced. By opening the valve up to 50%, this negative pressure is reduced and the possibility of wastewater returning to the pipe is reduced. Also, the risk of cavitation due to direct impact of the jet with the seabed is reduced. A very strong jet may cause: sediment erosion, local mud, pollution, bed

erosion and damage to benthic habitats near the seabed. Therefore, installing a reverse slope transition and an end pipe with a larger diameter than the transfer pipe can be a good idea to reduce the risk of the jet impacting the seabed.

1. Introduction

In many cases, when floods enter dam reservoirs, muddy flows are created at the bottom of the reservoir. This flow is one of the factors that causes sedimentation and reduces the water capacity of the reservoirs and the useful life of the dams. Opening the lower gates of the dam is the common method of draining these flows and maintaining the useful volume of the reservoir.

Ariaei and Lashkara (2023) evaluated of the effect of the lower discharger on the behavior of the muddy flow entering the Dez dam reservoir [1].

In this research, in order to pass the incoming sediments to the Dez dam reservoir, the construction of a channel to discharge the flow containing sediment was proposed as a remedial solution. Also, the behavior of the muddy flow entering the reservoir of the dam and its effectiveness in passing the sediments were investigated using numerical simulation. First, in order to calibrate the model, the thick flow pattern formed inside the tank was simulated using different models with different wall roughness heights, as well as RNG and LES turbulence models, and the results of depth and flow velocity were compared with field measurements. In the next step, the lower discharge channel was added to the model in the proposed position and the impact of the construction of this discharger on the behavior of the thick flow entering the tank was evaluated. Investigations showed that the amount of sediments released from the dam tank is directly related to the input concentration and the opening percentage of the lower discharger. In such a way that by averaging the results in different input concentrations, the sediment discharge efficiency in openings of 25%, 50% and 100% was calculated as 15.4%, 20.8% and 25.1% respectively. In the following, profiles of the flow velocity in the upstream sections of the discharger were taken in order to evaluate the intensity of mixing and the amount of deviation of the flow lines. In general, as the flow approaches the inlet opening of the discharge valve, the values of the maximum velocity and also the intensity of the mixing of the surrounding fluid into the concentrated flow increase. Also, with the increase in the opening percentage of the valve, the effect of the discharge channel on the deviation and acceleration of the flow lines becomes wider.

Daryaei et al. (2023) investigated of Flow Pattern Changes Caused by Installing Diagonal Plates Upstream of the Lower Discharge Valve Using Numerical Simulation [2].

In the present study, the effect of installing diagonal plates on changes in the flow pattern upstream of the orifice was investigated using the Flow3D numerical model. The variables studied in this study are the width of the plates, the angle of installation of the plates, and the distance from the plates to the orifice. A total of 5 scenarios (considering the control condition (without installation of plates)) were defined for the numerical model. The numerical model was calibrated using experimental results and the RNG turbulence model was selected for simulation. The results showed that installing diagonal plates in front of the orifice led to the creation of vortices and also the development of a low-pressure zone upstream, which led to an increase in the volume of outgoing sediments. Also, reducing the width of the plates, increasing the installation angle and increasing the distance between the plates will lead to a decrease in the intensity of the vortices and a decrease in the area of the low-pressure zone, which reduces the effect of installing diagonal plates to increase the volume of outgoing sediments.

Rasouli et al. (2021) evaluated the effect of the dimensions of the bottom outlet on the amount of sediment behind the dam in pressure leaching by Laboratory investigation [3].

The exploitation of reservoir dams has so far been carried out with an emphasis on the goals of meeting water needs, controlling flood energy, and improving environmental conditions, and the issue of sediment discharge from the dam reservoir has received less attention. In this study, in order to determine a method for improving sediment discharge, a hemispherical structure was tested in front of the bottom outlet. The tests were conducted by building 16 physical models with different gap lengths and widths at four water heights, three hemispherical diameters, and a total of 208 tests. The results of the experiments showed that by installing a half-cylinder structure in front of the lower discharger, the volume of sediment washing

increases. In other words, a pair of rotating vortices are created inside the half-cylinder structure on both sides of the central axis of the valve, in which case installing half-cylinders with different diameters increases the volume and length of sediment washing several times compared to the model without a cylinder. So that by increasing the gap height four times, the volume and length of sediment washing increase by 101.3 and 27.2 percent. The results of this study showed that installing half-cylinders with diameters of 12.7, 15.2 and 19.2 will result in an average increase of 587, 732 and 829 percent in the volume of sediment washing, respectively, compared to the model without a cylinder. Also, installing half-cylinders with diameters of 12.7, 15.2, and 19.2 will result in an average increase in sediment washing length of 94, 106, and 111 percent, respectively, compared to the model without a cylinder.

Jamali Roshet and Manafpour (2019) studied numerical of the flow pattern through the bottom outlet of Seymareh dam [4].
bottom outlet, as one of the hydraulic structures dependent on the dam, have the important task of withdrawing the required water from the reservoir and delivering it to the downstream of the dam. These structures face some problems during operation, such as the occurrence of local eddy currents, severe pressure fluctuations, etc. To identify and deal with these factors, we need a correct understanding of the flow pattern in the channel. In the present study, a numerical study of the flow pattern in the bottom outlet of the Seymareh Dam, in the pressurized and free states, has been carried out using FLOW3D software and the turbulence model (RNG (k-ε)) for different service valve and full emergency valve openings. The results indicate an increase in flow velocity and a decrease in pressure with advancing in the flow direction; so that at full service of valve opening and normal head of 100 meters, the maximum flow velocity was 6.45 m/s and the minimum pressure was 1.4 kPa. In addition, with a gradual decrease in valve opening, the difference in average velocity values and also the bottom pressure immediately upstream and downstream of the valve increases. By comparing the free surface flow profiles, it was observed that the presence of a flow separating ramp at the end of the channel causes an increase in the water level in small valve openings, and with increasing opening, its effect is not significant.

Nemati and Ahmadi (2017) investigated numerical models of the effect of channel curvature before the service gate of the bottom outlet on the hydraulic flow [5].
Bottom outlets are known as lateral hydraulic structures in dams that are responsible for flood control, sediment discharge and flow transfer. In this study, the numerical solution of the flow in a sloping bottom outlet, consisting of multiple geometric sections and with channel curvature before the service gate has been investigated using FLOW-3D software as a computational fluid dynamics (CFD) model. The k–ε model was used as a turbulence model to solve the supercritical flow. The objectives of this paper were to determine and propose a suitable geometric structure of the flow channel to eliminate the downstream swirling flow pattern and to predict the effect of changing the channel geometry on the flow characteristics at the gate location and downstream of the flow. The numerical modeling results were compared with the experimental results. The results showed that by choosing a 25-meter straight length before the gates, the values of turbulence energy and flow pressure after the gates were reduced by 27.86% and 26.17%, respectively.

Manafpour and Jamali Roshet (2016) investigated the possibility of cavitation phenomenon in the bottom outlet of the Seymareh dam [6].

Bottom outlets are used as one of the hydraulic structures of the dam to control the initial water intake of the reservoir, discharge the reservoir in necessary situations, and help with the overflow discharge capacity in floods. By examining damaged bottom outlets in the world, problems caused by cavitation and valve vibration have been identified as the most important causes of bottom outlet failure. In the above phenomena, parameters such as flow velocity, hydrodynamic pressure of water, and flow rate are effective. Increasing the flow velocity in the bottom outlet and subsequently reducing the local pressure leads to a phenomenon called cavitation, which is one of the important and noteworthy issues in bottom outlets. The basic indicator of this evaluation is the cavitation index. It is a function of local pressure and fluid velocity. The critical value of this index is 0.2-0.25 along the channels and 0.2 inside the grooves. For this purpose, the present study investigates the phenomenon of cavitation in the bottom outlet of the Seymour Dam at different service valve openings with the RNG turbulence model using the FLOW3D software, so that if this phenomenon occurs, solutions can be provided to remedy it.

Hosseini Nezhad (2012) studid hydraulic simulation of flow in the bottom outlet of Siazakh dam with FLOW3D software [7].
The bottom outlet of dams is one of the important components of these structures that are exposed to numerous hydraulic problems. Pressure fluctuations are a design consideration for a wide range of hydraulic structures. In addition, the performance of the structure is affected by pressure fluctuations. This phenomenon mainly occurs in hydraulic structures where flow separation occurs at high velocities and low pressures. This research was conducted using Flow-3D software

on the service valve and at different openings of 60, 80, and 100% at three different water heights of 4, 5, and 6 meters in a cylindrical tank. The results obtained from this simulation are consistent with the experimental results. The comparison was made and it is in good agreement. The results show that at lower openings the pressure on the service valve decreases and air injection is a suitable way to solve this problem.

The Narmashir Reservoir Dam is a concrete-core gravel dam that is being constructed 97 km southwest of Bam city on the Narmashir River in Kerman Province to meet downstream water needs. Geographically, the dam is located at latitude 29-30 and 28° and longitude 40-58° and 57°.
The type of dam is a concrete-core gravel dam with a height of 116 meters from the bottom and a crest length of 600 meters. The crest level of the dam is 1465 meters above sea level, the maximum water level in the reservoir is 1465 meters above sea level, and the minimum water level in the reservoir is 1414 meters above sea level.
The type of bottom outlet is an overpass type and the crest level of the bottom outlet is 1460 cubic meters per second. The bottom level of the channel at the gate location is 1364 meters above sea level and the number of gates is 2 service and emergency gates and the type of gate is sliding. The deep bottom outlet consists of a channel with a rectangular cross-section of 2×2.5 and approximately 30 meters long, which is connected to a funnel-shaped opening. Upstream of this opening, there is the main tunnel, at the beginning of which is the dam's inlet intake opening, which is shaped like a funnel. The intake opening leads the flow behind the dam into an elbow, and from there the flow is directed into a 240-meter-long tunnel with a diameter of 6 meters, which ultimately ends at the gates. In the middle of the tunnel, the control system includes a sliding gate and an emergency gate. Downstream of the gates, the flow enters a long tunnel 240 meters long with a circular cross section of 6 meters in diameter (larger than the dimensions of the gate), and therefore the flow downstream of the service gate is assumed to be free.
Due to the high flow velocity in the bottom outlet, which is approximately equal to $V = \sqrt{2gH}$, cavitation, corrosion, and flow aeration are important hydraulic issues in these structures. Therefore, in order to ensure proper performance of the bottom outlet against problems and limitations such as cavitation, hydrodynamic forces, vibration, and structural wear, as well as to examine the ability to completely discharge the tank, the bottom discharger must be carefully designed so that it works well under all desired conditions [8].

2. Methods

In this paper, Gambit software version 16.3.2 is used to generate the geometry and mesh. The mesh pattern is Quad element and map type is used for the surfaces. The existing boundary conditions are velocity input from the left and the pressure output boundary condition is at the outlet from the right. Fluent software uses continuity and Navier-Stokes equations in flow analysis. If the flow is turbulent, then the governing equations are transformed into Reynolds equations and one-equation, two-equation, five- or six-equation models are used to determine the eddy viscosity, with the user specifying the type of model. The flow field is solved based on the separation of equations by the finite volume method and different methods of separation of the transfer terms of the equations such as upstream, second-order upstream, power and Quick can be selected by the user. In order to couple the velocity field and the pressure field, the Simple, Simple C and Piezo methods are available in the program. In this article, Fluent software version 6.3.26 has been used to simulate the flow field.
To solve the flow using computational fluid dynamics, the following steps must be performed (Shojaifard and Noorpour Hashtroodi, 1995) [9].
- Selecting the Gambit model to create the geometry
- Selecting the computational model
- Selecting the calculation solution method in the model
- Selecting the basic equations to solve
- Determining the physical characteristics of the materials
- Determining the boundary conditions
- Specifying the problem solving parameters
- Making an initial guess in the entire solution field
- Performing the solution and outputting the calculations.

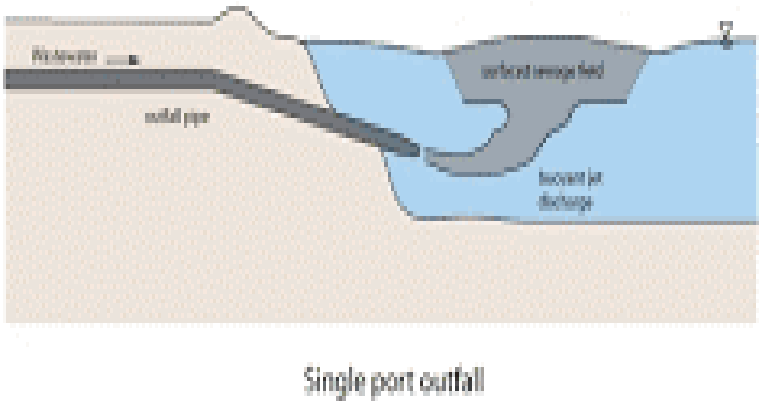


Figure 1- A very strong jet system discharging effluent into the sea may cause: Sediment erosion, Localized siltation, Bed erosion and Damage to benthic habitats near the seabed.

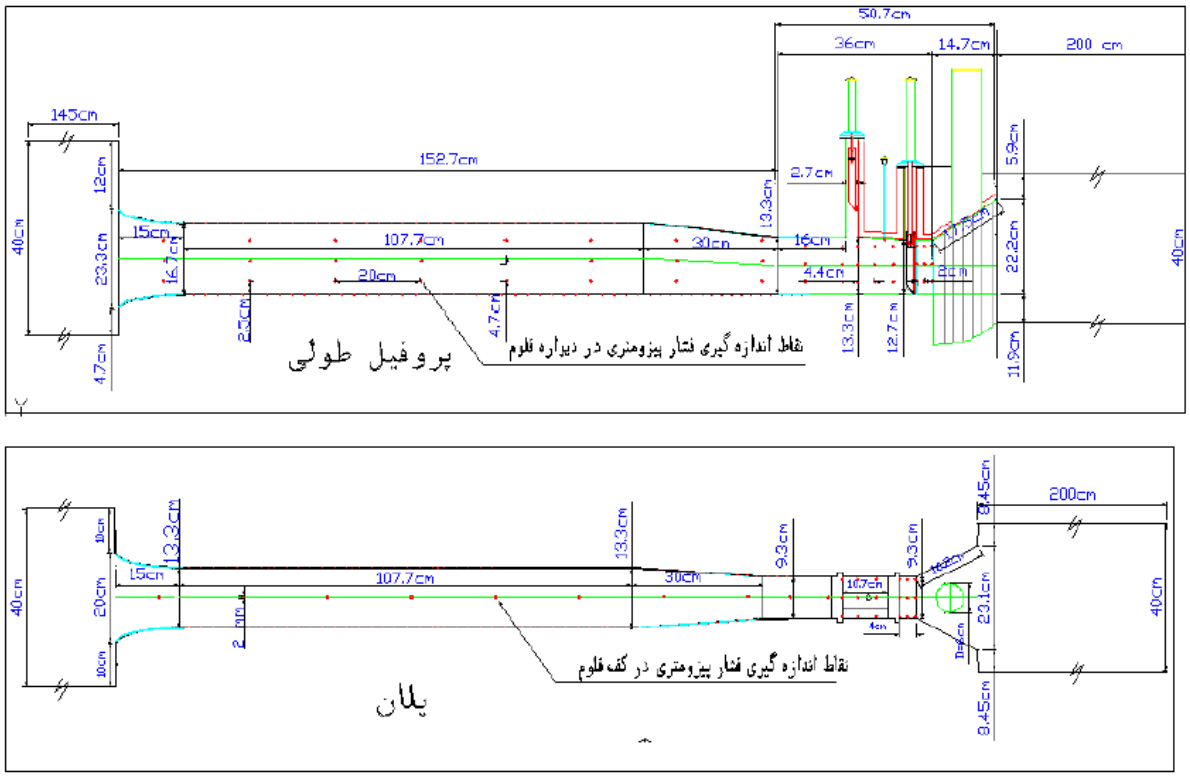


Figure 1- Geometric dimensions of the channel, gates, etc. Physical model of the Narmashir Dam [8].

Table 1 - Horizontal and vertical forces acting on the service valve at normal head (Hosseini et al., 2008) [8].

Service Gate opening	P/γ (top)	P/γ (bottom)	A_{top}	A bottom	Ft (KN)	F_b (KN)	F_{dp} (KN)	F_h (KN)
90	258.4	54.94	0.42	0.448	108.5	241.5	-132.9	1081.0
80	273.11	46.69	0.42	0.448	114.7	205.2	-90.5	1213.0
70	371.7	42.79	0.42	0.448	156.1	188.1	-31.9	1317.3
60	449.69	37.84	0.42	0.448	188.9	166.3	22.6	1619.0
50	493.84	36.34	0.42	0.448	207.4	159.7	47.7	1765.0
40	571.82	38.89	0.42	0.448	240.2	170.9	69.2	1843.0
30	608.61	45.79	0.42	0.448	255.6	201.2	54.4	2020.9
20	661.59	56.14	0.42	0.448	277.9	246.7	31.1	2134.1
10	677.77	73.24	0.42	0.448	284.7	321.9	-37.2	2334.4
5	705.73	83.89	0.42	0.448	296.4	368.7	-72.3	2404.0
2	726.33	91.01	0.42	0.448	305.1	400.0	-94.92	2410.9

3. Results and Discussions

In this study, Gambit software version 3.3.2 was used to generate the geometry and mesh it. The mesh pattern was Quad element and map type was used for the surfaces. The existing boundary conditions are velocity input from the left side from the top of the arc and pressure output boundary condition at the bottom of the arc outlet. The simulation results from Fluent software are seen in Figures 2 to 4.

The first and second stages of the solution process require a geometry and mesh generator. The GAMBIT preprocessor or one of the CAD/CAE software can be used to generate the geometry and mesh. The Tgrid preprocessor can also be used to generate a mesh with volume elements from an existing surface mesh. In the third stage, the two-dimensional FLUENT software must be run.

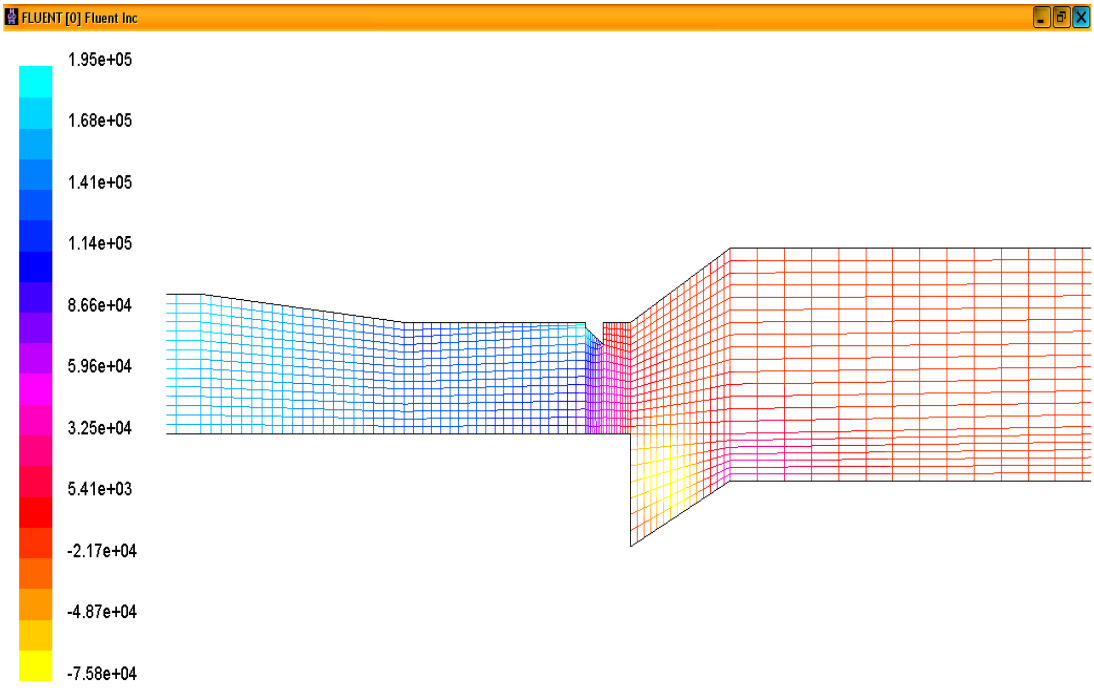


Figure 2- The isopressure curve in Pascals, in the bottom outlet with 80% opening of the lower valve and using the K-ε turbulence model. The results show that the pressure values obtained from the numerical model follow a similar pattern as the results of Hosseini et al. (2008), Table (1). [8].

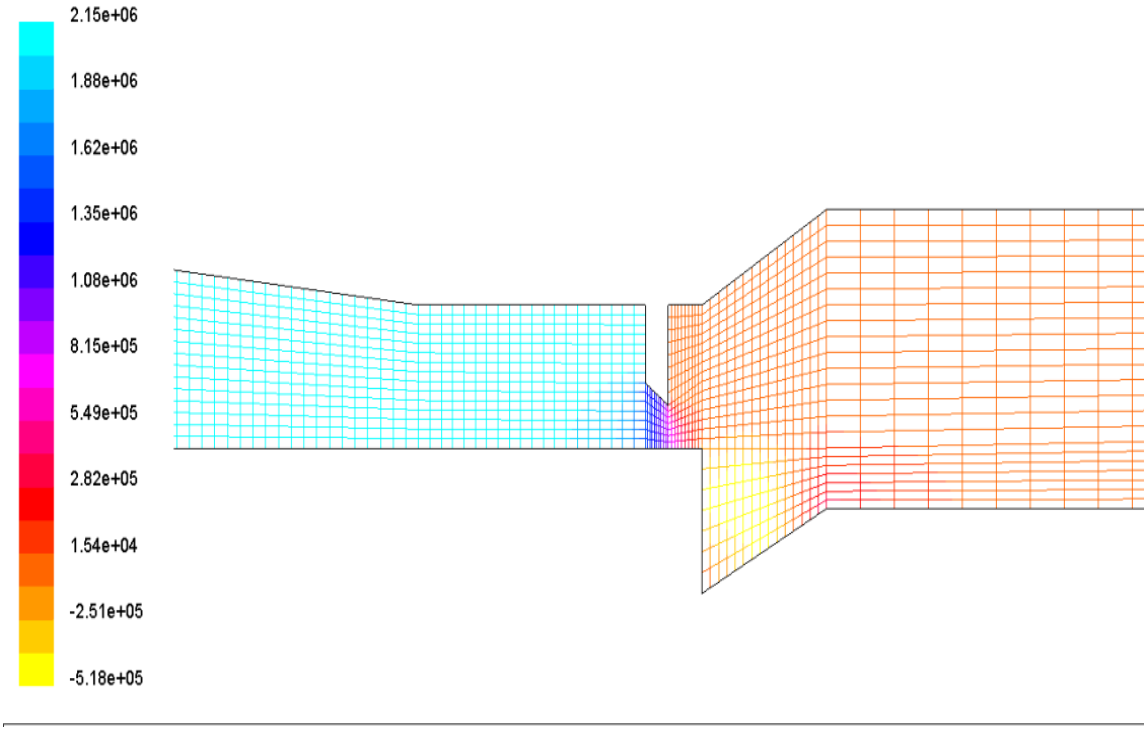


Figure 3- The isopressure curve in Pascals, in the bottom outlet with 30% opening of the lower valve and using the K-ε turbulence model. The results show that the pressure values obtained from the numerical model follow a similar pattern as the results of Hosseini et al. (2008), Table (1). [8].

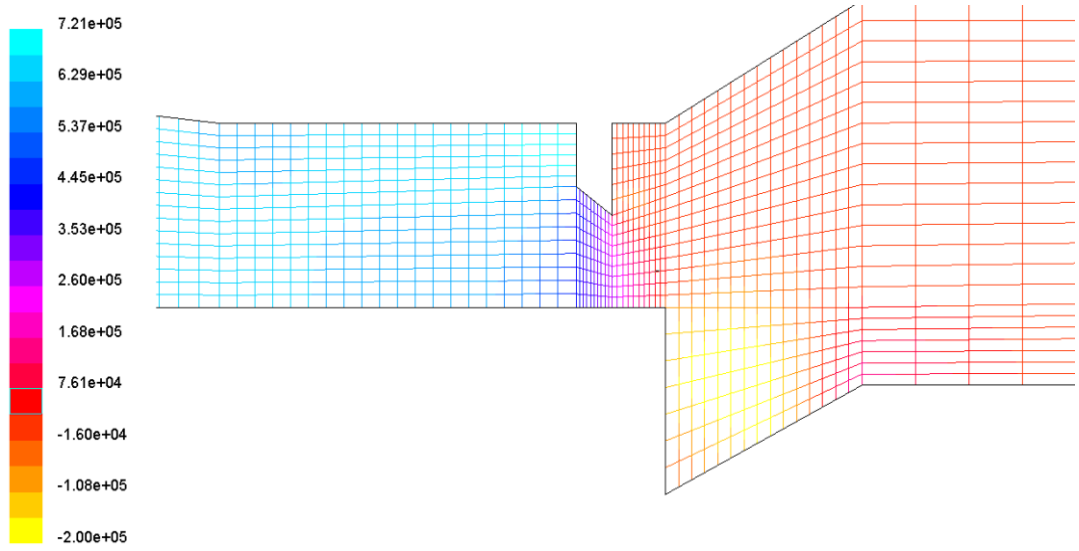


Figure 4- The isopressure curve in Pascals, in the bottom outlet with 50% opening of the lower valve and using the K-ε turbulence model. The results show that the pressure values obtained from the numerical model follow a similar pattern as the results of Hosseini et al. (2008), Table (1). [8].

4. Conclusion

Bottom outlets are structures used to regulate the transfer of water from the dam lake to the downstream discharge point. The present study was conducted to calculate the pressure and velocity at

different service gate openings. In this paper, the governing equations of flow in the two-dimensional case in the physical model of the bottom outlet of the Narmashir Dam were solved using appropriate turbulence models to calculate the flow and turbulence pattern. The velocity and pressure values were obtained from the numerical solution and then the pressure values on the bottom outlet and the surface in front of the bottom outlet were investigated for 30, 50, and 80 percent opening. The results show that the pressure values obtained from the numerical model follow a similar pattern as the results of Hosseini et al. (2008). With greater opening, the pressures on the bottom and top of the bottom outlet decrease. Based on the results obtained from the combined operation of the valves, an aerator is required immediately after the emergency valve to prevent cavitation. In this study, by installing a reverse slope transition after the valves and a larger diameter pipe after the transition, the negative pressure at the end of the pipe after the valve can be reduced. By opening the valve up to 50%, this negative pressure is reduced and the possibility of wastewater returning to the pipe is reduced. Also, the risk of cavitation due to direct impact of the jet with the seabed is reduced. A very strong jet may cause: sediment erosion, local mud, pollution, bed erosion and damage to benthic habitats near the seabed. Therefore, installing a reverse slope transition and an end pipe with a larger diameter than the transfer pipe can be a good idea to reduce the risk of the jet impacting the seabed.

5. References

[1] Hossein Ariaei, Babak Lashkara. 2023. Evaluation of the effect of the lower discharger on the behavior of the muddy flow entering the Dez Dam reservoir. Journal of Advanced Technologies in Water Efficiency » Volume 3, Issue 3 (Fall 2023).

[2] Daryaei, M., Naderi, S., Kashfipour, M. and Najafi, N. 2023. Investigation of Flow Pattern Changes Caused by Installing Diagonal Plates Upstream of the Lower Discharge Valve Using Numerical Simulation. Journal of Advanced Technologies in Water Efficiency » Volume 3, Issue 3 (Fall 2023).

[3] Ali Akbar Rasouli, A.A., Kaman-Basted, A., Ansari Qojaqar, M., Salajqeh, A. and Parsi, E. 2021. Laboratory investigation of the effect of the dimensions of the bottom outlet on the amount of sediment behind the dam in pressure leaching. Journal of Water and Irrigation Management » Volume 11, Number 1 (Spring 2021).

[4] Jamali Roshet, T. and Manafpour, M. 2019. Numerical study of the flow pattern through the bottom outlet of Seymareh dam. Iranian Water Research Journal » Spring 2019 Issue 32.

[5] Nemati, M. and Ahmadi, H. (2017). Numerical investigation of the effect of channel curvature before the service gate of the bottom outlet on the hydraulic flow. Hydraulic Journal » Volume 12, Issue 3 (Fall 2017).

[6] Manafpour,M. and Jamali Roshet, T. 2016. Investigation of the possibility of cavitation phenomenon in the lower discharge of the Seymareh Dam. 15th National Hydraulic Conference of Iran.

[7] Hosseini Nezhad, E. 2012. Hydraulic simulation of flow in the bottom outlet of Siazakh Dam with FLOW3D Software. The 9th International Seminar on River Engineering.

[8] Hosseini, S. A., and Sanei, M., and Parekar, M., and Habibi, M., and Davoudi, M. M., and Ghafouri, A. (2008). "Hydraulic model of the lower discharge system of Narmashir Dam", Soil Conservation and Watershed Management Research Institute Project, Tehran.

[9] Shojaei-fard, M. J., and Noorpour Hashtroodi, A. (Translators). Versteeg, H.K. and Malalaskara, V. (1995). "Introduction to Computational Fluid Dynamics", Iran University of Science and Technology Press, Tehran, 1379.

INTERNATIONAL JOURNAL OF
COASTAL, OFFSHORE & ENVIRONMENTAL ENGINEERING IJCOE Vol.11/No. 3/Summer 2026 (56-68)

Available online at: www. Ijcoe.org

Data-Driven Assessment and Forecasting of Port Services Demand: A Case Study of Shahid Rajaee Port

Pouria Rafati[1], Seyede Masoome Sadaghi[2*], Ali Fakher[3]

[1] *M.Sc. in Coastal, Ports and Marine Structures Engineering, University of Tehran, Tehran, Iran; rafati.pouria@ut.ac.ir*
[2*] *Assistant Professor, Road, Housing & Urban Development Research Center, Tehran, Iran; S.sadaghi@bhrc.ac.ir*
[3] *Professor, School of Civil Engineering, University of Tehran, Tehran, Iran; afakher@ut.ac.ir*

ARTICLE INFO

Article History:
Received 18 March 2026
Accepted 6 July 2026
Available online

Keywords:
Port Services
Service Demand Forecasting
Port Management
Data assessment
Shahid Rajaee Port

ABSTRACT

Ports play a vital role in maritime transport and international trade, and port services—as a critical component of the maritime supply chain—significantly influence overall port efficiency. Accordingly, accurately forecasting port service demand in relation to economic fluctuations, trade constraints, and infrastructural conditions is essential for operational planning and infrastructure development. This study aims to analyze various categories of port services and to forecast service demand, with a specific focus on Shahid Rajaee Port. For this purpose, real operational data—including maritime and land-side traffic information and key performance indicators—were collected, refined, and analyzed using regression, time-series and moving-average models. The results indicate that variables such as cargo handling volume, number of incoming vessels, duration of marine service operations, truck and rail flows, economic and political conditions have a decisive impact on port service demand. The findings of this research provide valuable guidance for managers in resource allocation, capacity development, congestion management, and enhancing port operations in line with sustainable development objectives.

1. Introduction

Ports, as key nodes within logistics networks and commercial transport systems, play a vital role in cargo flow, supply chain support, and the facilitation of international trade. With the continuous growth of cargo and passenger movements, the need to expand port infrastructure and provide diverse port services has become increasingly important. These services include a range of operational and support activities such as tugging, berthing, loading and unloading, warehousing, and customs-related services, each of which has a direct impact on the speed and quality of port performance. Despite their importance, port performance evaluations have often focused primarily on the volume of cargo handled, while port services have received comparatively less attention, an issue that can lead to an inaccurate understanding of a port's actual operational status and limit the ability to identify weaknesses and improvement opportunities. Moreover, the fundamental differences between goods and services further complicate the assessment and forecasting of port services. Goods are physical and measurable, whereas services are intangible, activity-based, and lack a standardized unit of measurement. This distinction necessitates more comprehensive and multi-dimensional analytical approaches for evaluating and forecasting port services.

In this study, focusing on Shahid Rajaee Port—the largest commercial port in Iran—a set of port service data has been extracted and analyzed using a data-driven modeling approach. This paper aims to provide a reliable picture of future port service behavior by presenting a clear conceptual framework, conducting detailed trend analysis, and applying quantitative forecasting models.

2. Research Background and Literature

The research related to forecasting port demand and analyzing maritime port services indicates that accurate modeling in this field requires a combination of economic, operational, and statistical approaches. A review of key studies shows that the literature can generally be categorized into economic and trade-based models, port operational models, and statistical and time-series models.

In the domain of economic approaches to port demand forecasting, classical studies such as the work of Miklius and Wu (1988) demonstrate that demand for

port services is primarily a function of projected foreign trade and cargo volume. Their study forecasted demand for a new port through a multi-stage process involving national trade projection based on economic indicators, commodity-based demand estimation, and cargo allocation among ports using the PTA[1] model. In these models, national trade is first forecasted, then assigned to commodity groups, and finally allocated to individual ports.

In the study by Tongzon (1991), the future supply of shipping services was estimated through a model that examines the relationship between trade volume, global shipbuilding trends, and the physical limitations of the port. The model forecasts the number of future vessel trips as well as the characteristics of the incoming fleet. The findings indicate that the port's commercial demand plays the most significant role in determining the supply of shipping services, while the influence of global technological developments is assessed to be limited in the short term.

In the thesis by Joharianzadeh (2012), which is based on port operations models, future cargo volumes were forecasted using statistical methods such as trend analysis and regression. The forecasted cargo was then distributed among various ports using the PTA model, based on minimizing inter-port transportation costs, then an optimization model was employed for berth allocation. The results indicate that integrating cargo forecasting with berth allocation and vessel scheduling can reduce waiting times and lead to more efficient utilization of port capacity.

Joharianzadeh and Babazadeh (2012) reported in their article that the future demand of Kish Port was estimated using four approaches: historical trend analysis, macroeconomic indicators, induced demand arising from development projects, and the gravity model. Past data, regional capacities, and development plans were modeled under multiple scenarios. A comparison of scenario outputs with actual performance showed that the combined approach of historical trends and macroeconomic indicators produced the highest level of alignment and was identified as the most reliable estimation method.

Studies using statistical and data-driven approaches—such as those by Jugović, Hess, and Poletan Jugović (2011) and Lättilä and Hilmola (2012) demonstrate that statistical models including ARIMA [2], multivariate regression, and system dynamics perform strongly in long-term demand forecasting, particularly when uncertainties and structural changes are present in the data.

The study by Jugović et al. (2011) tested several time-series models—including linear trend, quadratic trend, moving average, and exponential smoothing—to forecast demand for the Port of Rijeka. Methods based on economic indicators were also examined to compare. The results showed that the linear-trend model yielded the lowest deviation from actual long-term data and was therefore identified as the most suitable method. In the study by Lättilä and Hilmola (2012), long-term port demand forecasting was conducted using a combination of multivariate regression, ARIMA, system dynamics, and Monte Carlo simulation. Instigators such as industrial production, GDP [3], and Russian oil exports were incorporated into the model, and multiple future scenarios were defined. The findings indicated that industrial production is the primary determinant of demand trends for Finnish ports, and that system-dynamics-based approaches provide greater accuracy in representing uncertainty.

In the field of machine learning, studies such as those by Sadaghi, Shivafar, and Rastad (2024) and Sadaghi and Shivafar (2024b) have shown that deep learning networks are capable of capturing nonlinear patterns present in port operations and can provide higher predictive accuracy compared to traditional models. In the study by Sadaghi and Shivafar (2024b), the demand for empty containers at Shahid Rajaee Port was forecasted using deep learning networks. Operational data from empty-container terminals, temporal patterns, and storage capacities were introduced into the model, and the nonlinear relationships among variables were extracted by the network. The results indicated a significant improvement in forecasting accuracy compared with conventional methods, enabling more optimal planning for the allocation and distribution of empty containers. Another study by Sadaghi and Shivafar (2024a) utilized operational data and simulation techniques to optimize container-handling processes at Shahid Rajaee Port. From this perspective, the study provides a practical framework for evaluating the efficiency and quality of port services based on statistical and operational data.

3. Methodology

For this study, data were extracted from the official statistics of the Ports and Maritime Organization (PMO), consisting of two main categories: traffic information (number of vessels, berth calls, truck and train movements) and operational data (cargo volume, vessel waiting time, berth utilization rate, and equipment capacities). These monthly data were obtained from the PMO portal and, assuming their accuracy, were used as the basis for the analysis. The dataset was consolidated in Excel, variable trends were plotted, and four analytical methods were applied: linear and nonlinear regression, descriptive–analytical assessment, moving-average analysis, and time-series forecasting.

[1] Port Traffic Allocations

[2] Autoregressive Integrated Moving Average

[3] Gross domestic product

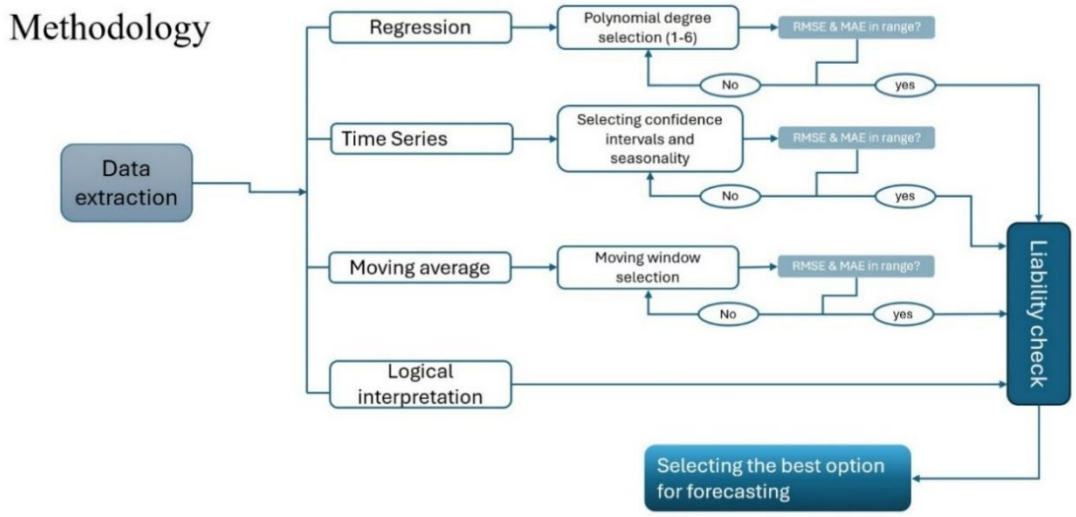


Figure 1. Methodology Diagram

In the regression analysis, polynomial equations of degrees 1 through 6 were fitted, and the model with the lowest RMSE[4] and MAE[5] was selected. It should also be noted that certain nonlinear functions—such as exponential, logarithmic, and trigonometric forms—are often unsuitable for empirical port data due to characteristics such as unbounded behavior, undefined domains, or periodic patterns, which may lead to unrealistic forecasts. For this reason, polynomial models generally provide more reliable results.

In the descriptive analytical assessment, upward or downward trends in the plotted data were interpreted in light of the port's economic, political, and operational conditions. In the moving-average method, an appropriate window was chosen to smooth short-term fluctuations and extract the underlying trend. Time-series forecasting was conducted using the Forecast Sheet tool in Excel, which allowed adjustment of confidence intervals and identification of potential seasonality to generate future estimates. Finally, the accuracy of the models was compared, and the most suitable forecasting method for each variable was selected (Figure 1).

4. The Port Under Study

The data used in this study were obtained from Shahid Rajaee Port (Figure 2), located in Iran, near the city of Bandar Abbas. Shahid Rajaee Port is the largest commercial port in the country, situated 15 kilometers west of Bandar Abbas along major international transit corridors, and handles more than one-third of Iran's maritime trade. The port is equipped with 30 gantry cranes, including Super Post-Panamax units, enabling it to accommodate seventh-generation container vessels. Its current annual handling capacity is 6 million TEU[6], which will increase to 8 million TEU upon completion of Phase 3 development.

5. Data Under Study (Rafati, 1403)

The extracted data is categorized into several fields which are shown in figure 3.



Figure 2. Aerial view of Shahid Rajaee Port

[4] Root Mean Square Error
[5] Mean Absolute Error
[6] Twenty-foot equivalent unit

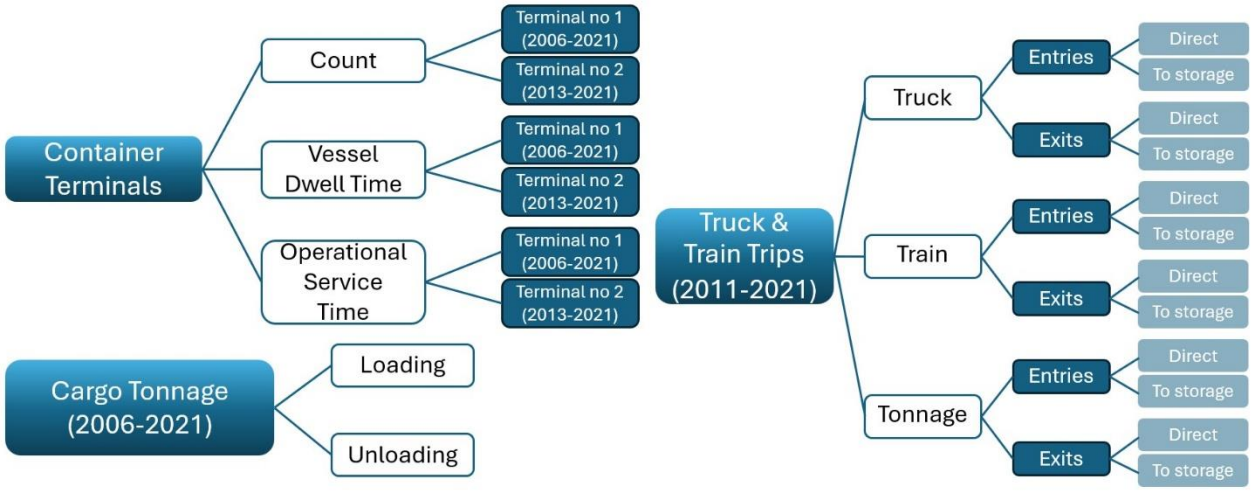


Figure 3. Extracted data categories

5.1. Container Vessel and Its Dwell and Service Times

The container terminals No. 1 and 2 of Shahid Rajaee Port, as the main hubs of container operations, play a significant role in Iran's maritime supply chain. Terminal No.1 has been operational since 1997, and Terminal No. 2 since 2013. Equipped with Super Post-Panamax cranes and modern infrastructure, Terminal No. 2 enables the accommodation of larger vessels and increases operational capacity, marking a major milestone in the port's development. In this analysis, the data are examined based on the number of arriving container vessels and the average dwell and service times. Accordingly, the results reflect the mean behavior of vessels and may differ for smaller or larger ships.

5.1.1. Temporal Pattern and Vessel Count in Terminal No. 1

As shown in Figure 4, in Terminal No. 1 the average vessel service time remained nearly constant throughout the statistical period, while the average dwell time increased significantly after 2013, coinciding with the intensification of sanctions and the commencement of operations at Terminal No. 2. During the same period, the number of vessels calling at Terminal No. 1 (Figure 5) declined, which can be attributed to the relocation of larger vessels to Terminal No. 2, the reduction in trade volumes caused by sanctions, decreased revenue and workforce among contractors, lower operational pressure and congestion, and limitations in equipment maintenance and spare parts supply. Consequently, after 2013 Terminal No. 1 experienced a reduction in vessel calls alongside a relative increase in dwell time, while service time remained almost unchanged.

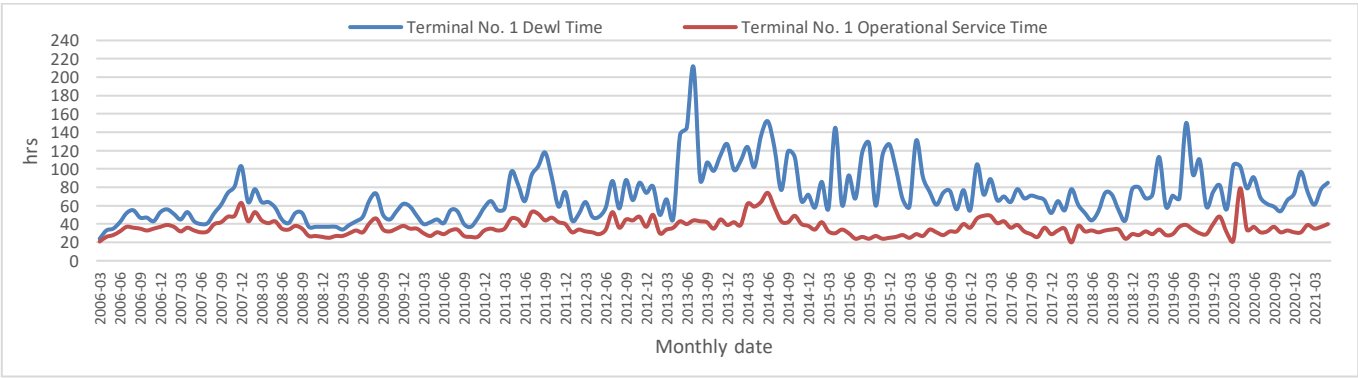


Figure 4. Vessel Dwell Time and Service Time at Container Terminal No. 1

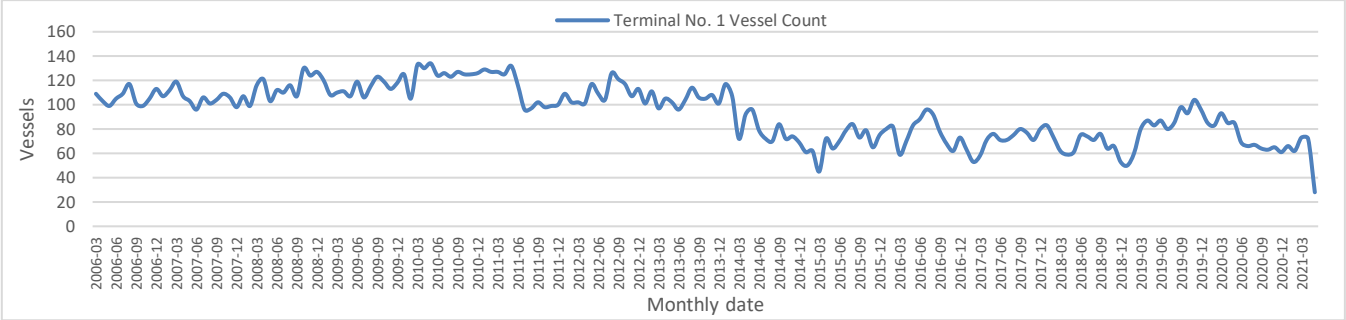


Figure 5. Vessel Count in Container Terminal No. 1

5.1.2. Temporal Pattern and Vessel Count in Terminal No. 2

Data for Terminal No. 2 begin in 2013 and show an upward trend in the number of arriving vessels (Figure 6), while the average service time remains nearly constant and the average dwell time exhibits fluctuations (Figure 7). Modern equipment such as high-capacity Super Post-Panamax cranes along with updated design and operational practices and improved management processes, have contributed to greater efficiency in berthing and cargo-handling operations, thus attracting a significant portion of container traffic. Consequently, Terminal No. 2 has gradually gained a prominent role in accommodating larger vessels and enhancing the port's overall operational capacity.

5.1.3. Forecasting the Number of Incoming Vessels to the Terminals

To forecast the number of vessels entering Terminals 1 and 2, a combination of linear and polynomial regression, moving-average analysis, and time-series models was applied, and the most suitable curves were selected based on RMSE and MAE indicators. In Terminal No. 1, although a third-degree polynomial provides a better fit over the historical dataset, simpler models and time-series forecasting (Figure 8) were found to be more realistic for future projections. For Terminal No. 2, the linear model (Figure 9) offers an appropriate representation of the trend. By integrating the results of the models and considering economic and political conditions, the number of incoming vessels for each terminal is estimated to be approximately 60 to 80 vessels per month over the next three years. This value is approximate and should be revised if underlying conditions change.

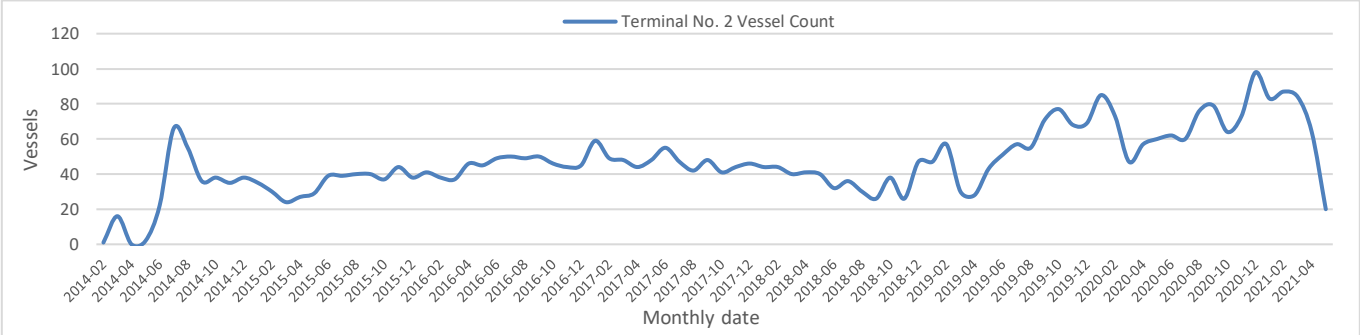


Figure 6. Vessel Count in Container Terminal No. 2

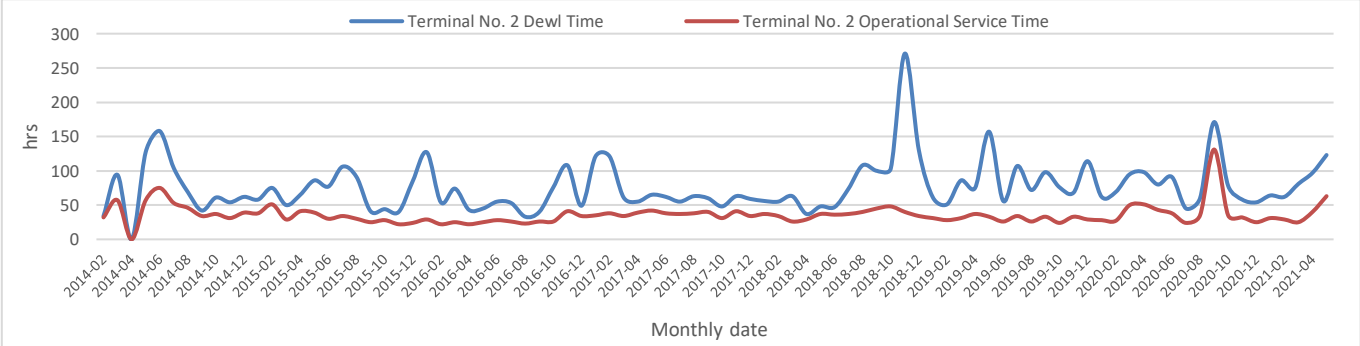


Figure 7. Vessel Dwell Time and Service Time at Container Terminal No. 2

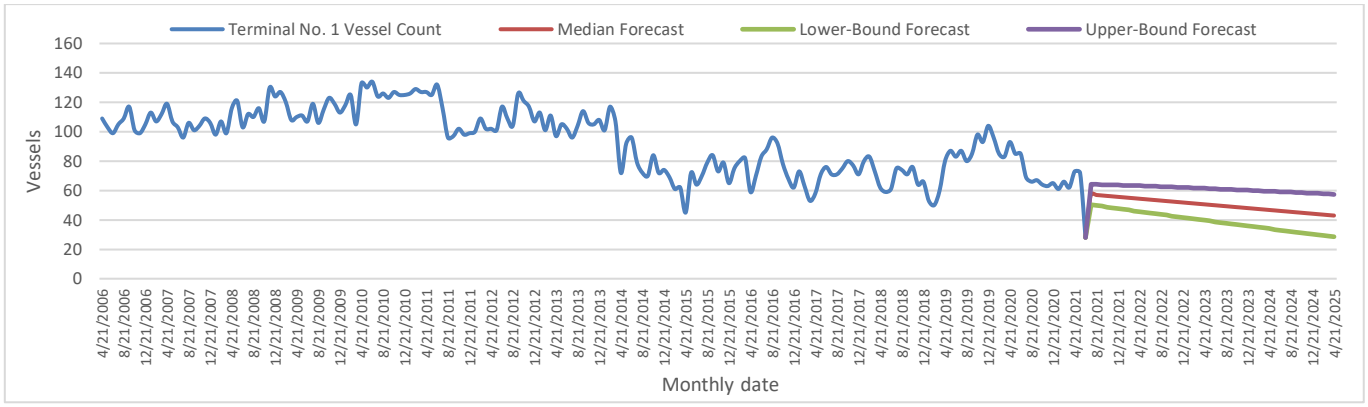


Figure 8. Three-Year Time-Series Forecast of Incoming Container Vessels at Terminal No. 1

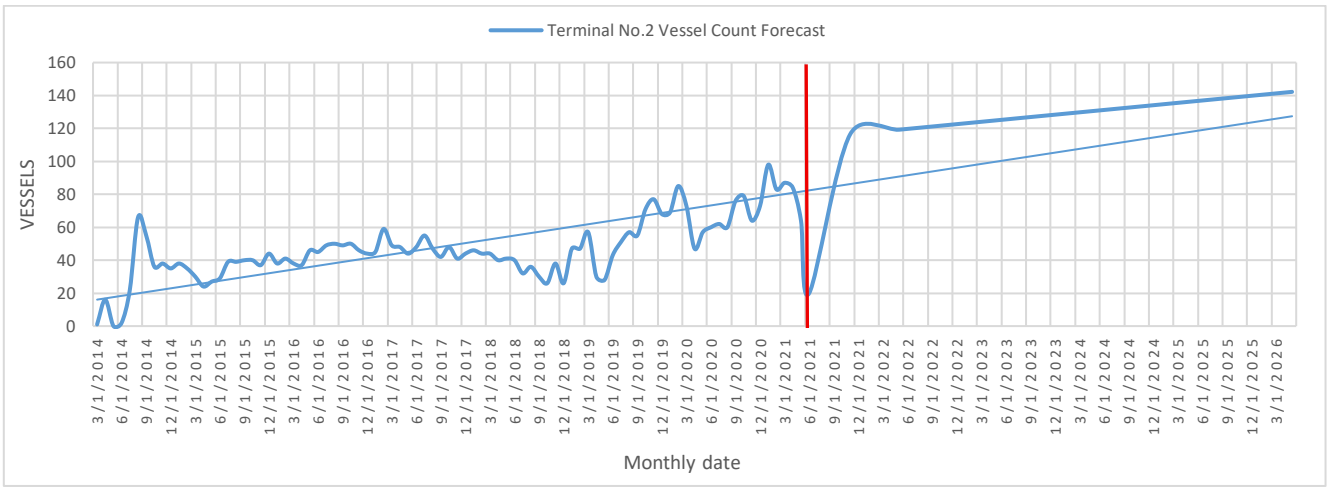


Figure 9. Regression Forecast of Incoming Container Vessels—Terminal No. 2

5.1.4. Forecasting the Average Vessel Dwell Time at Berth

To analyze and forecast the average vessel dwell time at each terminal, regression, moving-average analysis, and time-series modeling were employed. In Terminal No. 1, the 30-month moving average shows that dwell time increased by approximately 40% from 2011 to 2015, decreased by about 30% between 2015 and 2019, and then rose gradually by around 15% until 2021, reaching a relatively stable level thereafter. In Terminal No. 2, the 20-month moving average indicates an initial increase of about 60% up to 2018, followed by a 20% decline in 2020, and then stabilization. The time-series models (Figures 10 and 11) produced reasonable results consistent with the moving-average trends. Based on these findings, the average vessel dwell time for both terminals is estimated to be approximately 80 to 100 hours over the next three years.

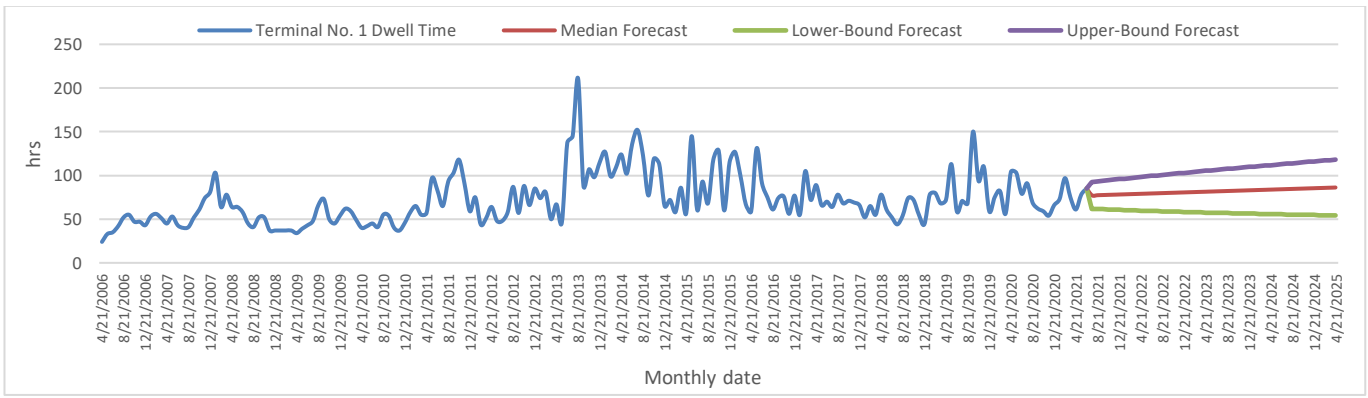


Figure 10. Three-Year Time-Series Forecast of Average Vessel Dwell Time—Terminal No. 1

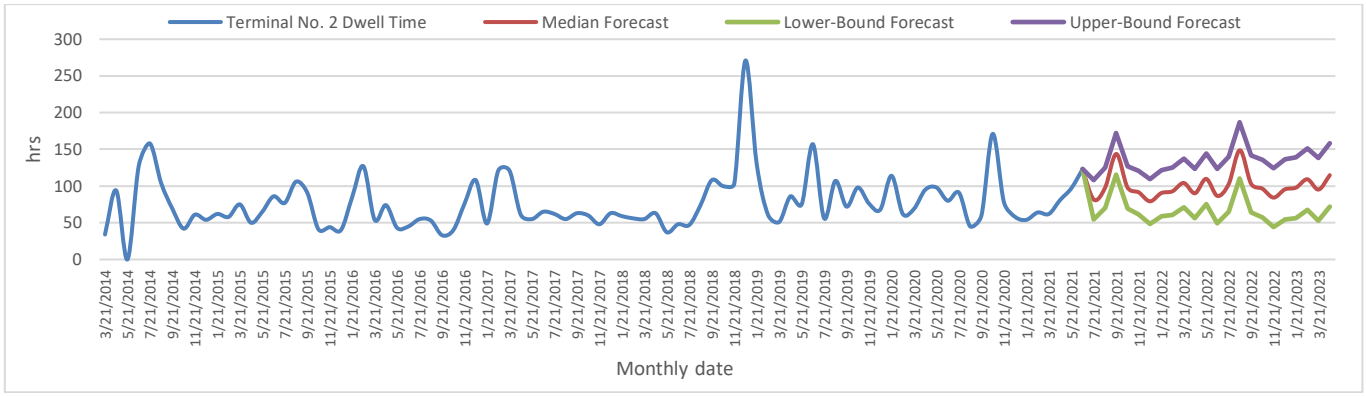


Figure 11. Three-Year Time-Series Forecast of Average Vessel Dwell Time—Terminal No. 2

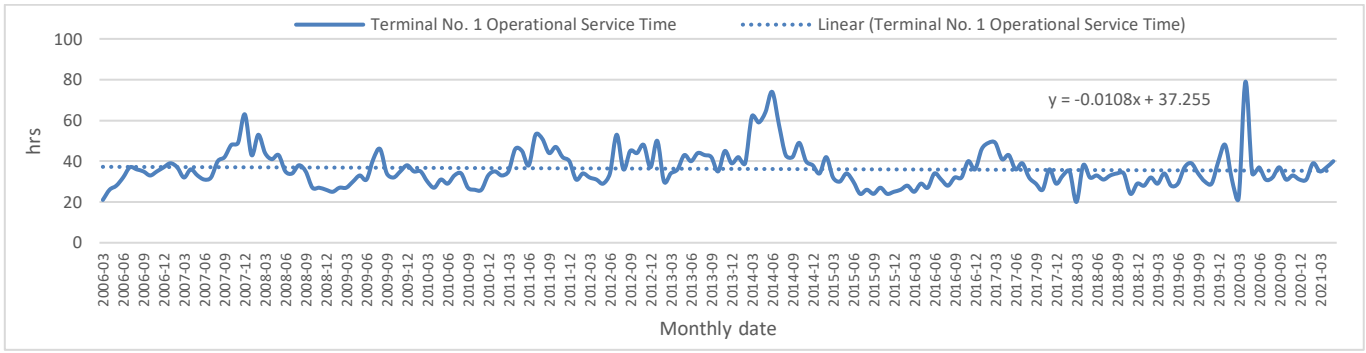


Figure 12. Average Vessel Service Time at Terminal No. 1

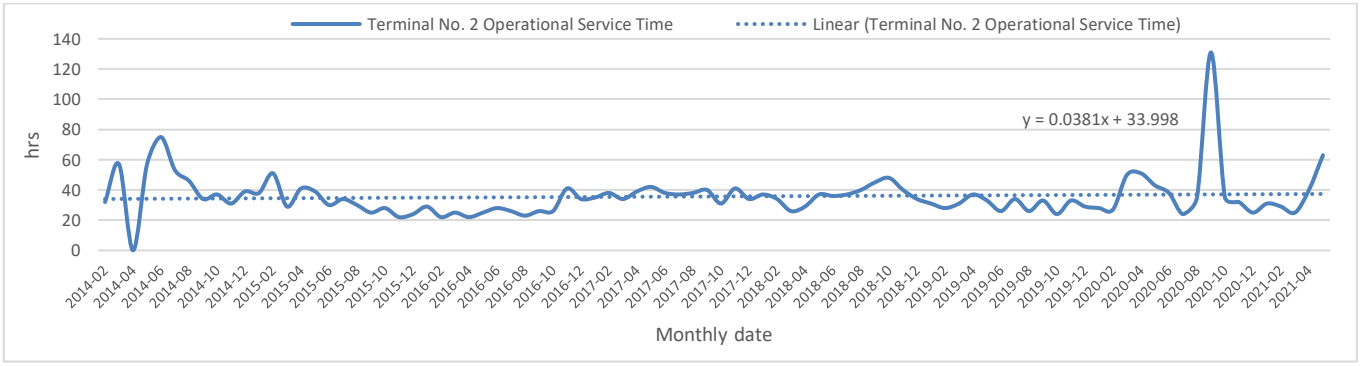


Figure 13. Average Vessel Service Time at Terminal No. 2

5.1.5. Forecasting the Average Vessel Service Time

The plots of average vessel service time in both terminals indicate a generally stable pattern with limited fluctuations. Polynomial regression analysis combined with RMSE and MAE evaluation shows that the linear (first-degree) model yields the lowest error in both terminals and is therefore suitable for approximate estimation. In Terminal No. 1 (Figure 12), despite fluctuations, the mean service time has remained nearly constant over the study period, reflecting relatively stable operational management, reasonably efficient equipment utilization, and a steady level of activity. A similar trend is observed in Terminal No. 2 (Figure 13), where service time fluctuates within a narrow and stable range. Based on this analysis, the average vessel service time in both terminals is projected to be approximately 30 to 40 hours over the next three years, provided that current operational and equipment conditions do not undergo major changes.

5.2. Truck and Wagon Movements and Cargo Tonnage

5.2.1. Truck Entries Forecasting

Incoming trucks to the port consist of two categories: direct-entry (ship-side) trucks and storage-entry trucks. At the beginning of the study period (2011), the number of trucks in both categories was nearly the same; however, since 2013, storage-entry traffic has sharply declined while direct-entry traffic has increased. This shift is attributed to improved port space utilization, higher warehousing costs, the mechanization of loading and unloading operations, changes in cargo characteristics (notably the rise of

containerized and bulk cargo), and the growing share of time-sensitive goods. However, certain types of cargo—such as oversized or heavy items, shipments facing administrative delays, and some transit goods—still require mandatory entry into storage areas. The trend over recent years shows that storage-entry truck traffic has approached nearly zero, and future forecasts confirm this pattern; therefore, the need for major warehouse expansion is minimal. For direct-entry trucks, polynomial regression models were unsuitable and produced unrealistic results. Consequently, qualitative assessment, moving-average analysis (Figure 14), and time-series forecasting (Figure 15) were applied. Based on these methods and assuming current operational conditions remain unchanged, it can be said that over the next three years approximately 40,000 to 50,000 direct-entry trucks and 3,000 to 3,500 storage-entry trucks will arrive annually.

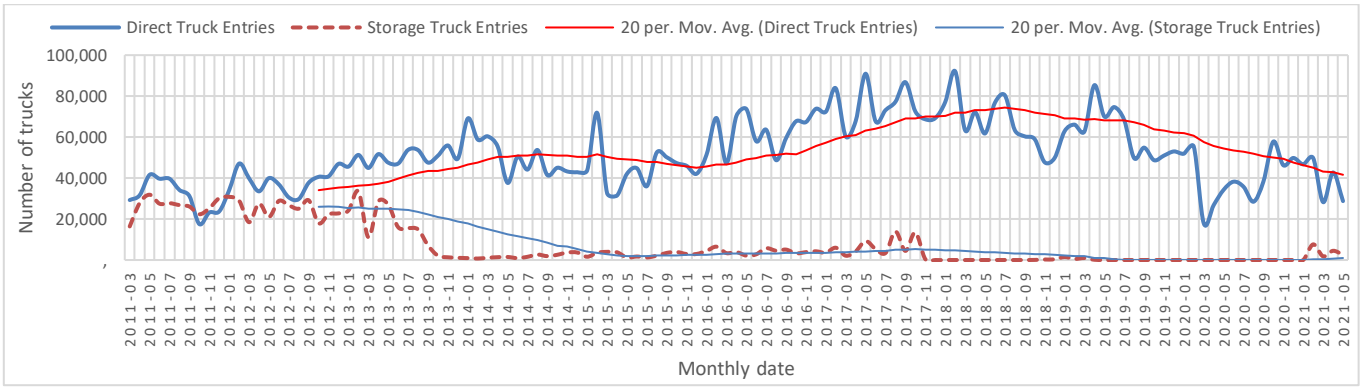


Figure 14. Incoming Truck Count with Fitted Moving-Average Curve

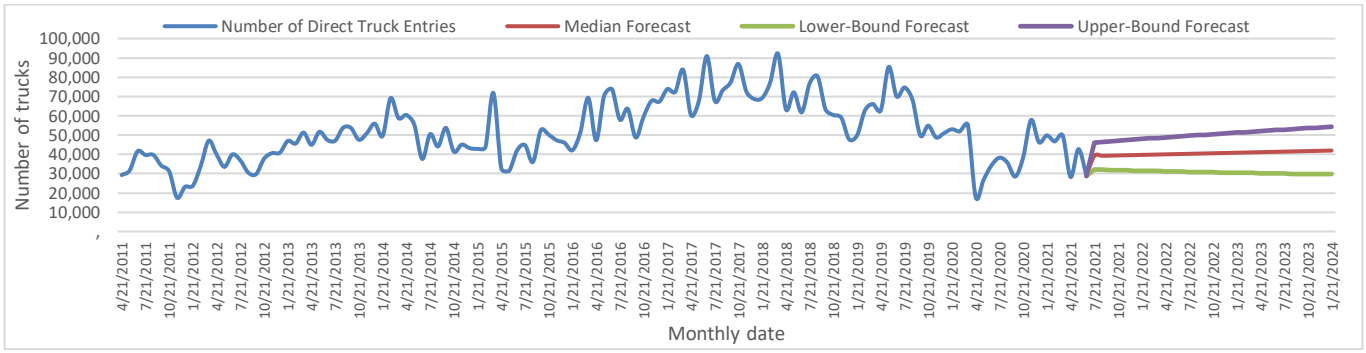


Figure 15. Three-Year Time-Series Forecast of Direct Entry Trucks

5.2.2. Trucks Exits and Forecasting

The pattern of outgoing trucks is similar to that of incoming traffic. Warehouse-based dispatches decreased to nearly zero by 2015, and after a period of decline (2015–2019), the total number of outgoing trucks began to rise from 2019 onward before stabilizing at a steady level. Using moving-average analysis (Figure 16) and time-series forecasting (Figure 17), it is estimated that over the next three years direct (ship-side) dispatches will range between 8,000 and 9,000 trucks per year, while warehouse-based dispatches will range from 1,500 to 2,000 trucks per year.

5.2.3. Incoming and Outgoing Wagons and Forecasting

Inbound rail transport to the port has nearly ceased in recent years, approaching zero (Figures 18 and 19). This decline is primarily due to the higher cost of rail transport, the complexity of loading and unloading processes, and the longer transit time associated with rail shipments. Although rail infrastructure is available, its practical utilization has significantly decreased. Based on this trend, the number of inbound wagons (both direct-entry and storage-entry) is projected to remain within the range of 0 to 200 units per year over the next three years. Similarly, the number of outgoing wagons has gradually declined and has almost reached zero. The influencing factors mirror those affecting inbound rail traffic, including economic and operational challenges associated with railway transport. Accordingly, future forecasts align with the inbound pattern, and the number of outbound wagons (direct and storage-based) is estimated to remain within 0 to 200 units per year.

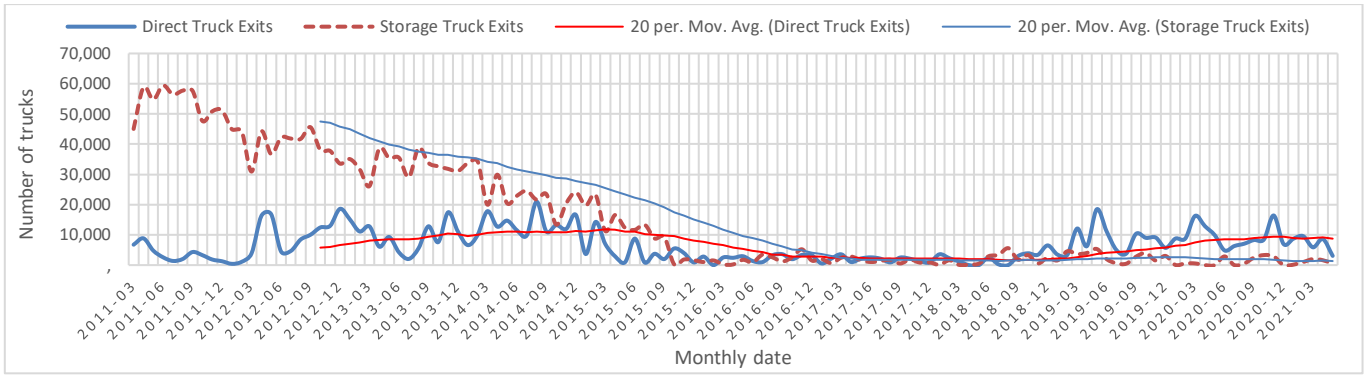


Figure 16. Outgoing Truck Count with Fitted Moving-Average Curve

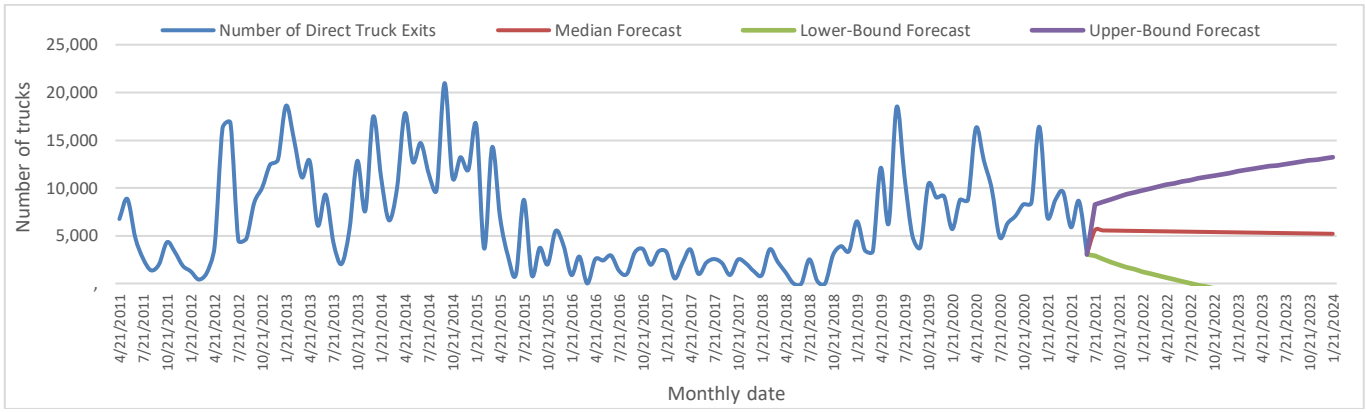


Figure 17. Three-Year Time-Series Forecast of Direct Exit Truck Numbers

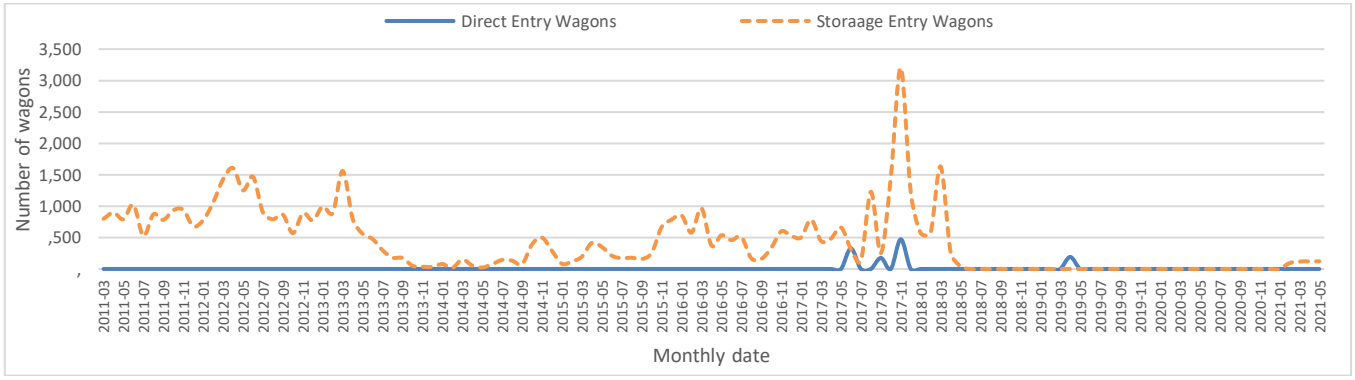


Figure 18. Number of Incoming Wagons to the Port

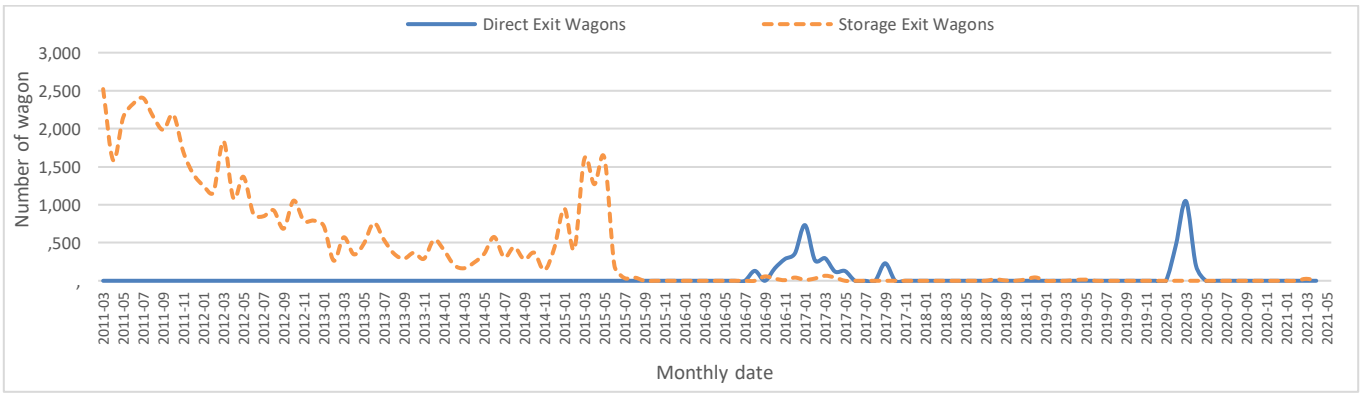


Figure 19. Number of Outgoing Wagons from the Port

5.2.4. Cargo Tonnage of Inbound and Outbound Shipments by Trucks and Wagons, and Forecasting

The inbound and outbound cargo tonnage of the port is primarily driven by truck operations, as the share of rail wagons is negligible; therefore, tonnage charts essentially reflect truck-traffic behavior. The inbound and outbound tonnage (both direct and to storage) follows a pattern similar to that of truck counts, confirming earlier trends. The moving-average analysis (Figures 20 and 21) shows that warehouse-related inbound and outbound tonnage has approached nearly zero in recent years, a condition that is expected the future. Direct outbound tonnage remains stable and is likely to continue this trend, while direct inbound tonnage despite fluctuations has become to a stable average over the past two years, making it a suitable basis for forecasting. Using moving-average analysis, time-series forecasting, and mean values from the final period, the three-year outlook suggests the following annual estimates:

- Direct inbound tonnage: approximately 2.5 to 3 million tons
- Inbound warehouse tonnage: 100,000 to 120,000 tons
- Direct outbound tonnage: approximately 1.5 to 1.7 million tons
- Outbound warehouse tonnage: about 190,000 to 200,000 tons

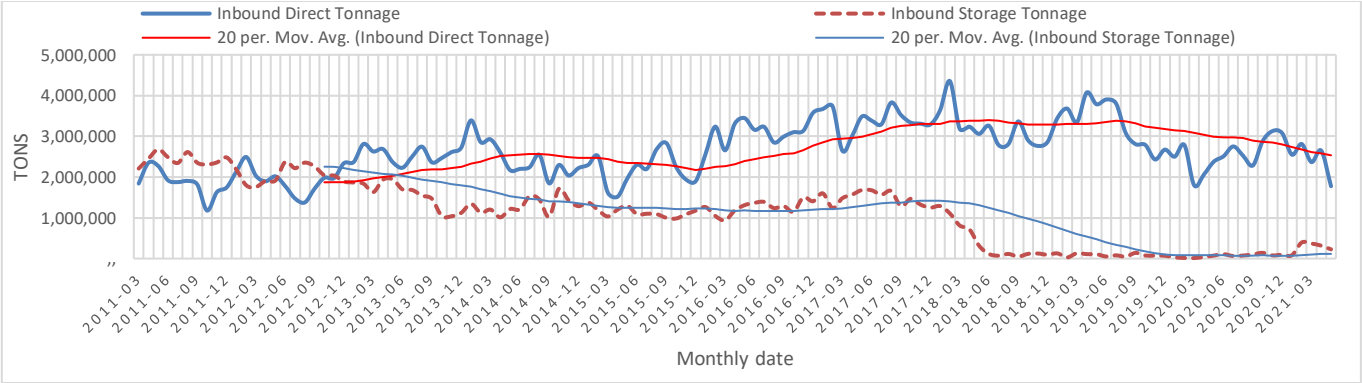


Figure 20. Inbound Cargo Tonnage by Trucks and Wagons with Fitted Moving-Average Curve

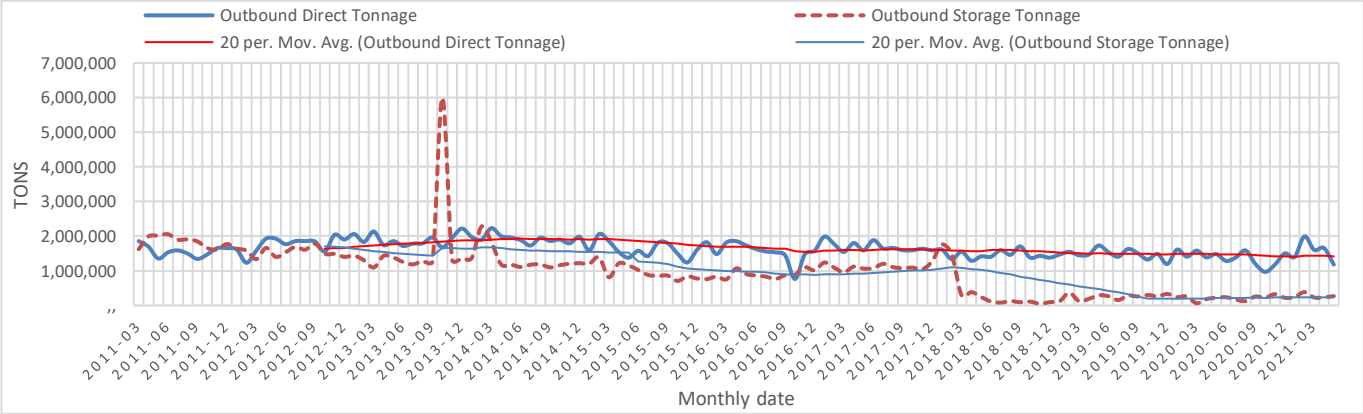


Figure 21. Outbound Cargo Tonnage by Trucks and Wagons with Fitted Moving-Average Curve

5.3. Total Port Cargo (Loading and Unloading)

5.3.1 Trend Analysis and Forecasting of Loading Tonnage

The port's loading data include the total volume of petroleum and non-petroleum commodities. The loading tonnage increased up to 2013, but with the imposition of sanctions by U.S. and EU—particularly those targeting oil and petrochemical exports—the trend shifted downward. Following the JCPOA agreement in 2015, a partial lifting of sanctions led to an increase in exports and a subsequent rise in loading tonnage. However, after the U.S. withdrawal from the JCPOA in 2018 and the reinstatement of sanctions, the downward trend resumed and continued through the end of the study period. Thus, fluctuations in this category are clearly driven by political and trade conditions. Based on error metrics (RMSE and MAE), the third-degree polynomial model (Figure 22) provided the best fit and was adopted for forecasting. The model output indicates that the forecast is reliable for approximately three years. Assuming current conditions remain unchanged, the loading tonnage over the next three years is estimated to be between

3.5 and 4 million tons per month. The 20-month moving-average curve shows a downward trend in the later months, suggesting that loading tonnage could fall below 3.5 million tons. In contrast, the time-series forecast (Figure 23) exhibits a slightly upward trend and suggests marginally higher values. Therefore, the actual amount is likely to fall somewhere between the ranges suggested by these three methods.

5.3.2. Trend Analysis and Forecasting of Unloading Tonnage

The unloading tonnage, representing the country's imports, exhibits a pattern similar to loading volumes and has been strongly influenced by economic conditions and trade restrictions. After an initial period of growth, a downward trend began in the mid-2010s, primarily driven by banking limitations, currency instability, and a decline in import volumes. In this section as well, based on RMSE and MAE metrics, the third-degree polynomial model (Figure 24) provided the best fit, and its three-year forecast aligns with the recent trend. Given the relative stabilization observed over the last three years, the unloading tonnage is estimated to range between 2 and 2.5 million tons per month over the next three years. The moving-average analysis confirms this range, while the time-series model (Figure 25) suggests slightly lower values. Therefore, a confident estimate for future unloading tonnage lies within 2 to 2.5 million tons per month.

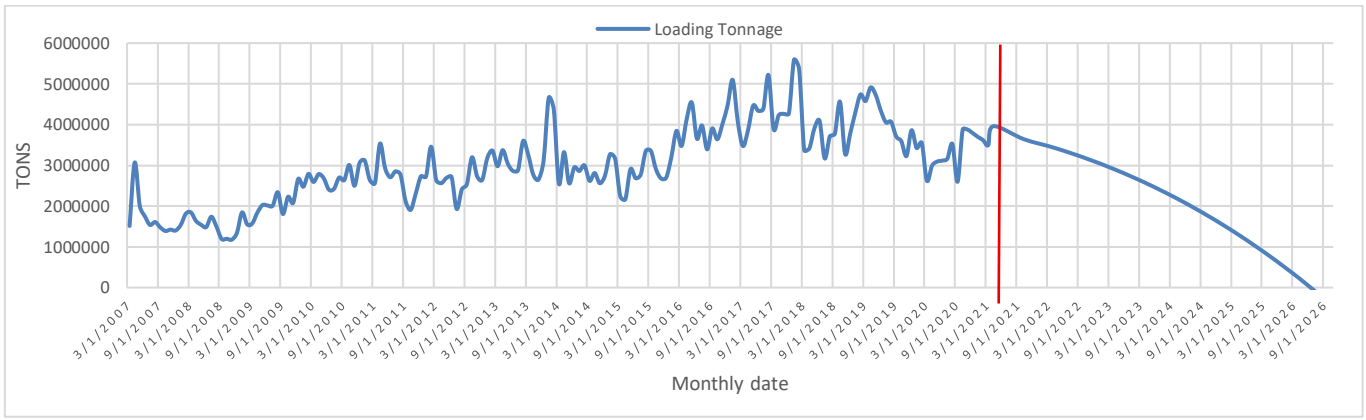


Figure 22. Forecast of Port Loading Tonnage (Values Are Reliable for Up to Three Years)

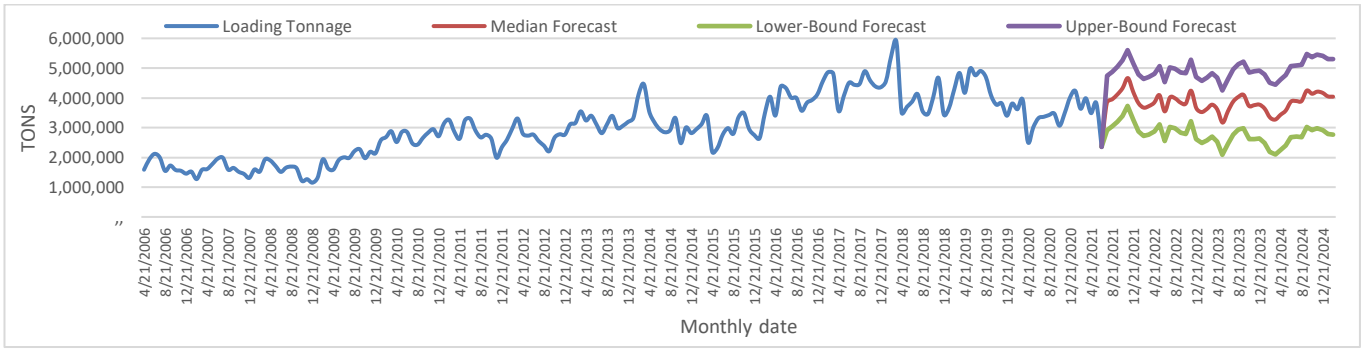


Figure 23. Three-Year Time-Series Forecast of Port Loading Tonnage

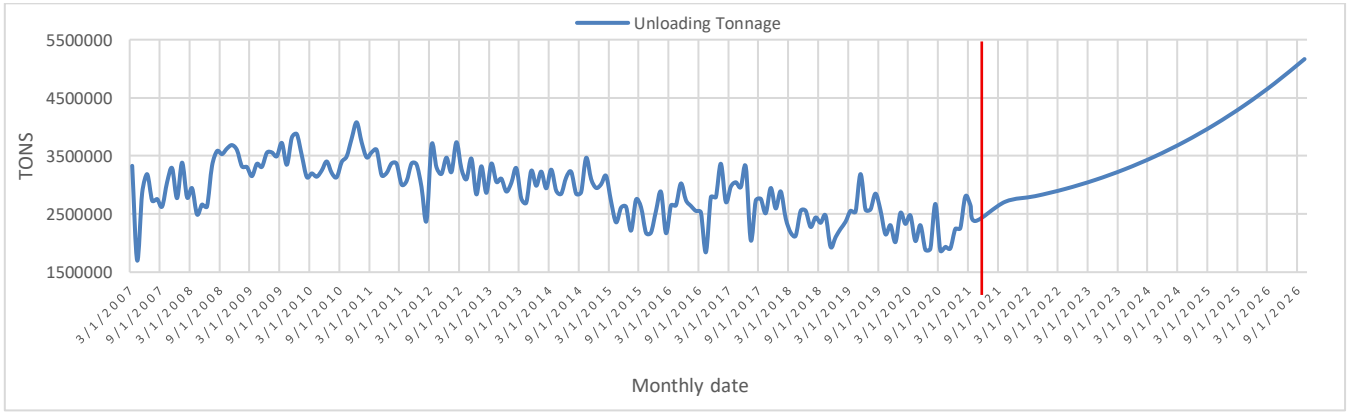


Figure 24. Forecast of Port Unloading Tonnage (Values Are Reliable for Up to Three Years)

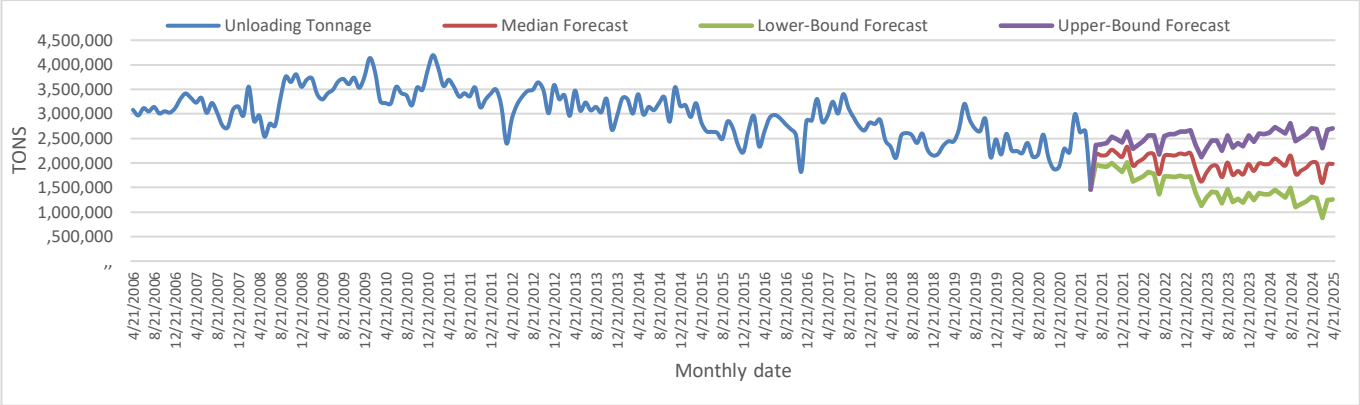


Figure 25. Three-Year Time-Series Forecast of Port Unloading Tonnage

6. Conclusion

This study provides a clear picture of the port's operational performance and demonstrates how operational fluctuations influence the efficiency of the maritime supply chain and the development of a marine-based economy. The findings offer a foundation for planning strategies aimed at enhancing productivity, reducing costs, and strengthening the port's role within a national sea economy.

a) Number of Vessels: The sharp decline in vessel calls at Terminal No. 1 following the 2013 sanctions indicates that external disruptions can significantly weaken trade flows. In contrast, Terminal No. 2 with its more modern equipment was able to retain a portion of the port's maritime trade capacity.

b) Vessel Dwell and Service Times: The increase in vessel dwell time at Terminal No. 1 after 2013, and at Terminal No. 2 after 2018, reflects higher operational costs and reduced productivity. The stability of service times (approximately 30 to 40 hours) in both terminals indicates a reliable level of operational efficiency within the maritime economy.

c) Incoming Trucks: The decline in warehouse-entry trucks since 2013 and the corresponding rise in direct (ship-side) operations signal a shift toward faster cargo circulation and improved alignment with optimized planning requirements.

d) Outgoing Trucks: The sharp reduction in outbound cargo from warehouses after 2015 followed by moderate recovery beginning in 2019 and subsequent stabilization suggests a restructuring of land-side distribution aimed at improving sea–land connectivity and reducing unnecessary delays.

e) Incoming and Outgoing Wagons: The significant decline in inbound wagons after 2018 and in outbound wagons after 2015 highlights reduced reliance on rail transport due to higher costs, operational complexity, and long transit times.

f) Cargo Tonnage via Trucks and Wagons: Cargo tonnage patterns are closely aligned with truck movement trends. The stable data observed from 2018 onward provide a reliable basis for future forecasting and maritime logistics planning.

g) Loading and Unloading Tonnage: The decline in unloading tonnage under economic pressures and sanctions, combined with the long-term upward trend in loading tonnage, reflects an increasing export-oriented role of the port within the broader marine-based economy.

7. References

[1] Joharianzadeh, M. (2012). *Cargo Forecasting and Berth Allocation in container ports.* (Master of Science (M.Sc.)). University of Tehran,

[2] Joharianzadeh, M., & Babazadeh, A. (2012). *Forecasting Port Cargo Demand: A Case Study of Kish Commercial Port*. Paper presented at the The 9th International Civil Engineering Congress. https://civilica.com/doc/166058

[3] Jugović, A., Hess, S., & Poletan Jugović, T. (2011). Traffic demand forecasting for port services. *Promet-Traffic&Transportation,23*(1),59–69. doi:https://doi.org/10.7307/ptt.v23i1.149

[4] Lättilä, L., & Hilmola, O.-P. (2012). Forecasting long-term demand of largest Finnish sea ports. *International Journal of Applied Management Science,4*(1),52–79. doi:https://doi.org/10.1504/IJAMS.2012.044871

[5] Miklius, W., & Wu, Y. (1988). Forecasting the demand for services of a New Port. *GeoJournal, 16*(3),295–300. doi:https://doi.org/10.1007/BF00270259

[6] Rafati, P. (1403). *Predicting required amount of port services: The case study of Shahid Rajaee port.* (Master of Science (M.Sc)). University of Tehran,

[7] Sadaghi, S. M., & Shivafar, I. (2024a). Optimization of Empty Container Operations through

Simulation (Case Study: Shahid Rajaee Port). *Science ROAD Journal,32*(118),61–74. doi:https://doi.org/10.22034/road.2023.423773.2217

[8] Sadaghi, S. M., & Shivafar, I. (2024b). Prediction of Empty Container Demand Using Deep Neural Networks (Case Study: Shahid Rajaee Port). *Journal fo Transportaion Research,21*(2),177–188. doi:https://doi.org/10.22034/tri.2024.417293.3194

[9] Sadaghi, S. M., Shivafar, I., & Rastad, M. (2024). Optimization of Empty Container Operations by Demand Prediction and Simulation (Case Study: Shahid Rajaee Port). *INTERNATIONAL JOURNAL OF COASTAL, OFFSHORE & ENVIRONMENTAL ENGINEERING,9*(2),38–52. doi:https://doi.org/10.22034/ijcoe.2024.467183.1089

[10] Tongzon, J. (1991). A model for forecasting future supply of shipping services at Australian ports. *Maritime Policy and Management, 18*(1), 55–68. doi:10.1080/03088839100000006

INTERNATIONAL JOURNAL OF
COASTAL, OFFSHORE & ENVIRONMENTAL ENGINEERING IJCOE Vol.11/No. 3/summer (69-85)

Available online at: www. Ijcoe.org

A Critical Review of Challenges and opportunities in Using Remote Sensing and Image Processing for Rip Current Studies

Azadeh Valipour[1*]

[1*] *Assistant Professor,Department of Marine Science and Technology, Jo.C., Islamic Azad University, Jouybar, Iran; azadeh.valipour@iau.ac.ir*

ARTICLE INFO

Article History:
Received: 31 March 2026
Accepted: 10 July 2026

Keywords:
Rip currents
Surf zone
Remote sensing
Machine learning
Artificial intelligence

ABSTRACT

Rip currents, often appearing as mushroom-shaped features within the surf zone, are a primary cause of swimmer drownings along beaches worldwide. Due to their transient nature, the application of advanced remote sensing and computer vision techniques for localized detection of these phenomena significantly mitigates the limitations traditionally associated with their study. In addition to these methods, the emergence of machine learning and artificial intelligence (AI) techniques provides powerful tools for a more precise investigation of rip currents, offering substantial support to remote sensing approaches and enhancing the efficiency of coastal lifeguard operations on larger scales. This study aims to present a comprehensive review of the relevant literature from 2014 to 2023, evaluating both traditional and modern approaches to analyzing the behavior of these coastal currents. Particular emphasis is placed on examining the conducted studies, including details on the categorization of research objectives, comparison of various tools, and exploration of associated opportunities and challenges.

1. Introduction

Rip currents are narrow, jet-like flows that move seaward from the vicinity of the shoreline, typically forming in the presence of irregular seabed topography, especially when incoming waves approach the coast nearly perpendicularly [1]. These currents constitute a significant component of the nearshore circulation system and can induce local bathymetric changes by carving flow channels [2]. Moreover, they play a vital role in coastal sedimentary and hydrodynamic processes, contributing to sediment transport and the dispersion of organisms and pollutants along the shoreline, thereby acting as influential agents in coastal dynamics [3].

On the other hand, due to their often rapid and transient nature, rip currents have become one of the most serious coastal hazards for swimmers in many parts of the world [4]. Consequently, understanding the dynamic behavior of rip currents is crucial for enhancing beach safety and, more broadly, for effective coastal zone management [5]. These currents are influenced by various factors such as wave height, wave direction, and shoreline morphology and are categorized into several types, including shear instability rips, flash rips, channel rips, focused rips, deflection rips, and shadow rips [6]. However, since the formation of rip currents is governed by complex hydrodynamic processes and the natural variability of the coastline, monitoring them is highly challenging—particularly given the wide range of rip types that may develop under diverse coastal hydrodynamic and morphological conditions during field observations. In addition, in-situ studies of rip currents are often time-consuming and costly due to their spatiotemporal variability and dynamic nature [7] .Therefore, there is a growing need for novel approaches (such as the integration of acoustic systems and satellite-derived data alongside traditional field measurements) to enhance our understanding of the behavior of these coastal currents [8].

Previous investigations have highlighted the application of various indicators and methods for studying rip currents, which, despite their individual limitations, function as effective tools and ultimately complement one another [2][9].

These research tools are generally classified into seven main categories: (i) numerical simulations, (ii) coastal video monitoring, (iii) laboratory analyses, (iv) field measurements, (v) analytical methods, (vi) remote sensing and coastal image processing techniques, and (vii) artificial intelligence techniques.

The first category—numerical simulations—has been widely utilized to explore a range of aspects, including the influence of coastal morphological features and seabed parameters on the characteristics of rip currents in a given region [1]. Other aspects addressed through numerical modeling include hydrodynamic properties, tidal variations, wave climate, rip current intensity and distribution, as well as morphodynamic changes and sediment transport mechanisms within rip channels [10] [11][12].

The second category, known as coastal video monitoring, has been deployed in various locations to investigate rip currents and their impacts on shoreline dynamics. These coastal monitoring techniques focus on the mechanisms of wave-induced currents, their behavior, and movement patterns while also addressing issues related to coastal erosion [13][14].

The third category, laboratory observations, serves as a valuable approach for analyzing the three-dimensional structure of rip currents [15][16], establishing causal relationships between hydrodynamic and morphodynamic variables, and understanding the dynamics of rip current systems in the nearshore region [17]. Primarily, laboratory investigations are employed to examine the formation and behavior of rip currents, the influence of various environmental factors on their development, and the conditions that affect their mobility [18]. Field observations play an indispensable role in complementing and validating rip current research. These studies provide valuable data on beach topography, bathymetry, shoreline changes, and the hydrodynamic characteristics governing the surf zone—such as incoming wave features—which are essential for understanding rip current generation mechanisms [19][20][21]. Field studies also assist in identifying spatial and temporal variations in shorelines and sediment bars, both of which are closely linked to rip current formation [22].

Additionally, field investigations facilitate the collection of sediment samples, enabling analysis of sediment transport patterns associated with rip currents [23][24].

Furthermore, field observations offer a critical opportunity to validate numerical models used to simulate rip currents [22][2][25] .Comparing numerical modeling results with field data yields a more comprehensive understanding of rip current events and their associated hazards, ultimately leading to improved safety measures for swimmers and more effective coastal management strategies [26] [6].

The fifth category, referred to as analytical models, encompasses the study of rip current formation patterns [27], wave–current interactions [28], and the prediction of various system characteristics such as current velocity [29] and rip spacing [30].These studies, in conjunction with laboratory and field observations, contribute to resolving existing uncertainties in nearshore hydrodynamic phenomena.

The sixth category, remote sensing and image processing techniques, provides valuable insights into the behavior of rip currents and assists in their identification and visualization [31][32].

In addition to these methods, the emergence of machine learning and artificial intelligence as the seventh category—either used independently or in combination with image processing techniques—represents a growing trend that facilitates automated rip current detection. These advanced approaches are capable of analyzing large volumes of imagery and detecting patterns and trends that may otherwise go unnoticed due to the transient nature of rip currents, which often hampers detection using conventional techniques [33][34].

In this context, over the past few decades, a considerable body of research within coastal engineering and management has focused on identifying the features and locations of rip currents using image processing, remote sensing, and AI techniques—an effort largely driven by the complex nature of these currents. Accordingly, the present study aims to examine the challenges and assess the strengths and limitations of various approaches based on image processing and remote sensing in rip current studies. As evident from the existing literature, despite the emergence of AI frameworks and their undeniable advantages, prior reviews remain limited in scope and lack in-depth analysis, which may hinder a comprehensive understanding of the associated limitations and research gaps. Thus, this study provides significant support for researchers in identifying suitable strategies tailored to the specific challenges of each approach and advancing the objectives of future investigations. The structure of this paper is as follows: Section 2 presents the materials and methods, including an overview of remote sensing and image processing tools, as well as the search strategy. Section 3 provides a comparative analysis of the extracted results, including literature synthesis, key findings, and thematic classifications. Finally, Section 4 concludes with a summary of the main outcomes of the study.

2. Data and Methods

2.1. Remote Sensing Tools

Remote sensing tools have long been recognized as complementary, highly efficient, and cost-effective means for investigating coastal phenomena, particularly in monitoring transient coastal events [35].

When selecting remote sensing data, it is essential to consider their classification based on spatial scale—namely, global, regional, and local.

Global-scale remote sensing data are used for large-scale applications. These include datasets derived from various meteorological satellites employed for weather analysis, forecasting, and disaster prevention. Regional-scale remote sensing data are typically obtained from medium-resolution imagery. Notable examples include data from MODIS and Landsat

satellites, which are commonly used for monitoring the surface features of seas and oceans. Regional data are also valuable for macroscopic assessments of environmental changes in coastal areas.

Local-scale satellites, on the other hand, are primarily utilized for monitoring smaller spatial extents where higher spatial and spectral resolutions are required. Among the most prominent local-scale remote sensing tools are the WorldView satellite series and Unmanned Aerial Vehicles (UAVs). Accordingly, the selection of appropriate remote sensing imagery depends on the specific characteristics of the coastal features under investigation. Given that rip currents are small-scale and short-lived phenomena, the use of high-resolution imagery is highly recommended for their detection and analysis [36][37] (Table 1)

Remote sensing tools used for the study and detection of rip currents can be categorized into several groups. The first category includes permanent stations and Surf Cam video imagery, which consists of video cameras installed along the shoreline. These systems are designed to provide and collect real-time visual information on coastal and ocean conditions for both coastal residents and researchers. Such remote monitoring tools offer broad spatial coverage of data and enable quantitative measurement of coastal morphodynamic phenomena, tracking of water movement, and analysis of current behavior over time [38][39]. The second category comprises Remotely Piloted Aircraft Systems (RPAS) and Unmanned Aerial Vehicles (UAVs). These technologies, known as Unmanned Aerial Vehicle Remote Sensing (UAVRS), have made monitoring of rip current systems more accessible, cost-effective, and scalable across most parts of the world using aerial photography and surface observation [40]. These video-based methods operate through advanced techniques such as optical flow estimation, offshore direction calculation, and temporal data fusion to analyze and interpret rip current dynamics [41][31].

The third category includes satellites and marine radar systems, which can also be employed for rip current analysis. Among these are X-band radar systems, which, through specialized algorithms, are capable of estimating the location, shape, size, and speed of rip currents, as well as their seasonal variations—factors that are often difficult to measure using traditional field-based observation tools [42][32]. In addition, High-Frequency (HF) radar systems are widely used for continuous monitoring of oceanic waves and currents under various environmental conditions [43]. HF radar systems, such as CODAR SeaSonde and WERA, can measure coastal ocean currents and wave patterns by providing radial current measurements and return signal variations across both spatial and temporal domains. Spaceborne Synthetic Aperture Radars (SARs), such as those on ENVISAT, RADARSAT-2, ALOS, COSMO-SkyMed, and TerraSAR-X, are capable of providing high-resolution Earth surface imagery and are highly effective for rip current studies. These satellites operate by transmitting microwave pulses, which allow them to function independently of daylight and cloud cover [44][45]. Each of these options has its specific advantages and disadvantages, which are thoroughly analyzed and evaluated in this study, along with the challenges and limitations of each method.

Table 1. Specifications of commonly used remote sensing satellites for studying rip currents

Satellite Type	Satellites and Sensors	Launch Date	Spatial Resolution (m)	Spectral Resolution Band	Temporal Resolution (Day)
Radar Satellites	Sentinel-1	1978.10	825	6	6
	RADARSAT-2	2007.12	1	1(X-band)	A few days to a few weeks
	TerraSAR-X	2007.6	Up to 1 meter and even better	1(C-band)	A few days to a few weeks
Optical Satellites	Landsat satellites (Landsat 7 ETM+, Landsat 4-5 TM)	1984-2020	30	5	16
	MODIS	1999/2	250-500-1000	9	0.5
	Landsat 8 OLI	2013.2	30	7	16
	Sentinel-2	2A-2015.6 2B-2017.3	10-60	13	5(combined)
Altimeter Satellites	Sentinel-3	3A-2016.2 3B-2018.4	300-1000	8	27

2.2. Field and In-situ Data

In-situ data used for monitoring rip currents are essential for measuring various factors, including current velocities, wave characteristics, wind, and the circulation of the nearshore tidal area. They also help in determining sediment characteristics and the morphodynamic conditions of the coast, such as measuring the slope of different sections of the shore and mapping the bathymetry of channels. These measurements are obtained through various methods, such as Acoustic Doppler Current Profilers (ADCPs), GPS drifters, buoys, wave gauges, and coastal monitoring systems [46][47][48].

These in-situ studies, while examining the behavior of water movement, also enable the detection of rip currents in situations where other methods may fail [32]. Moreover, these data serve as real-time information for the studied area at any specific time and are used to evaluate remote sensing data, as well as to assess the accuracy of the location of current channels [49]. In-situ data also provide general information about the current conditions of the coastal region,

including the state of the shore, substrate composition, and other physical water features, which are essential for predicting changes in the rip current system over time.

Furthermore, in-situ data collected from sources such as buoy records, tidal gauges, and backscatter profilers can be utilized to estimate coastal erosion patterns, wave-breaking patterns, and the stability of shoreline features [37]. It is worth noting that a combination of in-situ measurements and remote sensing data provides a more comprehensive understanding of rip current dynamics, enabling the identification of rip current systems and their behavioral changes under varying wave and substrate conditions that may not be captured by in-situ sensors [36].

2.3. Image Processing Methods

The general steps in image processing for rip current detection include Image Acquisition, Image Pre-processing, Feature Extraction, Detection and Classification, and Post-processing and Refinement (Figure 1). In the first step, Image Acquisition, rip current images are obtained from various sources using remote sensing tools. In this phase, special attention should be paid to imaging conditions (image quality, viewing angle, time of acquisition, and weather conditions).

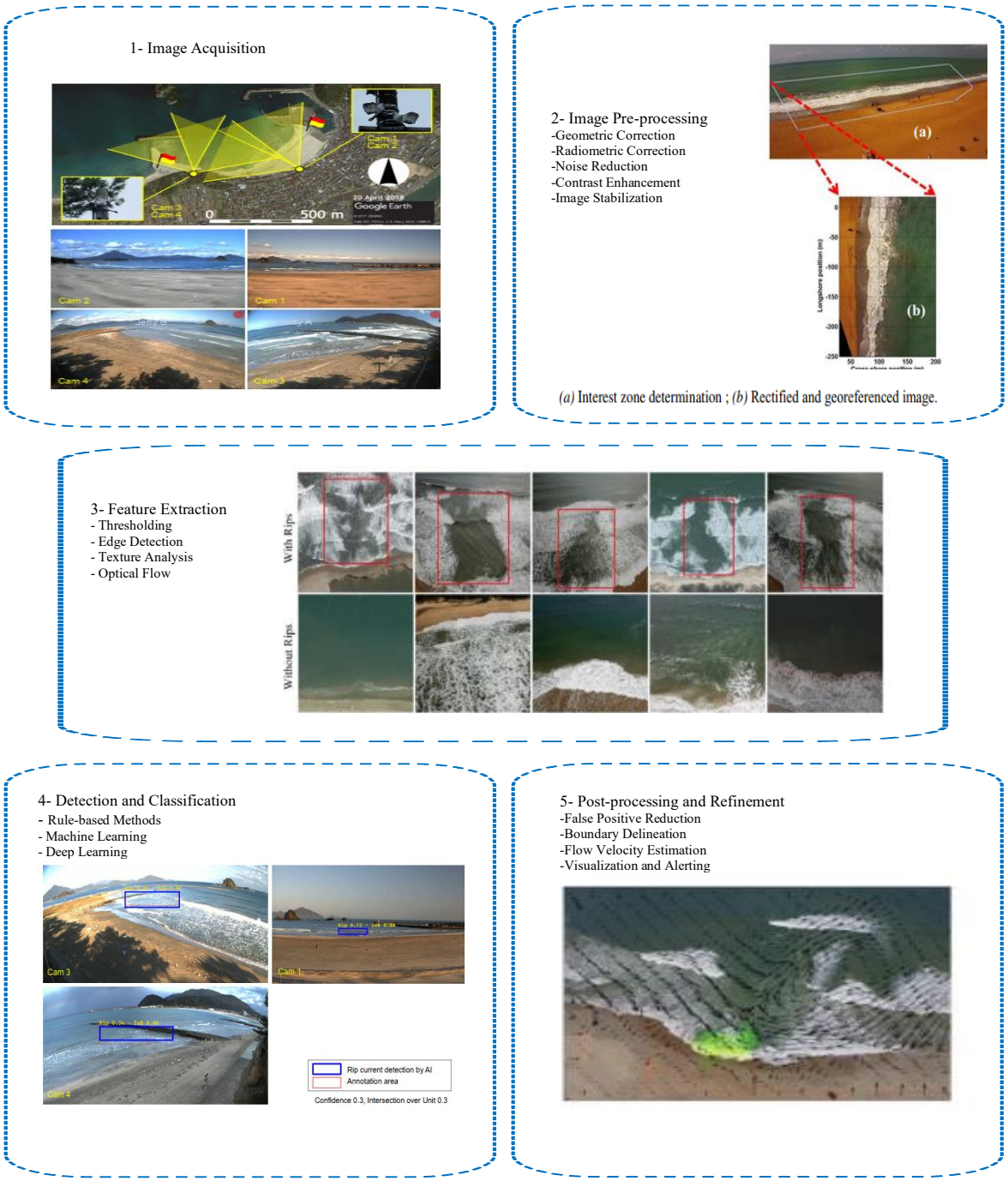


Figure 1. Image processing steps for ripping current studies [50]

In the Image Pre-processing stage, several operations are performed, including Geometric Correction, Radiometric Correction, Noise Reduction, Contrast Enhancement, and Image Stabilization to optimize results and improve the accuracy of the analysis. The next step, Feature Extraction, involves identifying rip current features in the form of visual patterns using suitable techniques such as Threshold (separating regions with specific brightness or color intensities), Edge Detection (identifying boundaries between regions with distinct visual features), Texture Analysis (examining patterns of intensity variations in a region to detect different water textures), Optical Flow Analysis (estimating the speed and direction of pixel motion in a video sequence), and finally, the use of Machine Learning algorithms plays a key role in automatic feature extraction and the development of rip current warning systems.

The following stage is Detection and Classification. Various methods are available for classifying rip currents, including Rule-based Methods, Machine Learning, and Deep Learning approaches. The detection of rip currents is based on the analysis of extracted features, where algorithms determine whether a rip current exists in the image and identify its location.

The final image processing step for rip current detection is Post-processing and Refinement. This stage includes False Positive Reduction, Boundary Delineation, Flow Velocity Estimation, and finally, Visualization and Alerting [51][52] .

A review of the available literature and scientific sources indicates that image processing methods for rip current detection are typically categorized into four groups: Traditional Image Processing, which involves classical image processing methods such as spatial filters, texture analysis, and visual feature extraction; Computer Vision, which includes the use of advanced computer vision algorithms; AI & Machine Learning, which involves employing Convolutional Neural Networks (CNNs), deep learning, and models such as YOLO and Grad-CAM for automatic rip current detection; and finally, Hybrid Models, which combine image processing methods with physical models or flow analysis.

2.4. Search Strategy

In this study, since the goal is to review the literature on research conducted on image processing and remote sensing techniques for the study of rip currents in recent years, including 41 articles (published between 2014 and 2023), both database search and snowball search methods were employed.

In the database search method, reputable databases were used to search for relevant articles from established scientific journals. In some cases, the snowball search method was utilized by referring to the sources of the identified articles. In the second approach, starting with a small set of related articles, the search was extended by examining their references and articles citing them.

This process enabled a comprehensive review of the literature and prior research in the field of study. Boolean operators were employed in the database search to refine the queries and obtain more relevant results. This allowed the search results to be narrowed down and the desired information to be presented more efficiently (Table 2).

Table 2. Selected Keywords in the Database Search Method

Search terms
(“rip currents detection” OR “rip currents monitoring” OR “rip current observation” OR “rip current forecasting”) AND (“image processing” OR “coastal remote sensing” OR “marine radar”) AND (“artificial intelligence” OR “machine learning” OR “deep learning” OR “convolutional neural network”)

3. Comparative Analysis/ Trends in Literature

Given the substantial number of studies in the reviewed literature, a concise summary of the main findings and applied techniques—categorized by author names and accompanied by specific methodological details—is provided in Table 3.

A brief examination of this table reveals that the most commonly utilized approach in image processing methods is the hybrid image processing technique, accounting for 78% (32 out of 41) of the reviewed studies. Among these hybrid approaches, several studies—such as that of Rampal et al. (2021)—focus on models integrating classical image processing techniques with artificial intelligence [53] .

Other studies, including those conducted by Mori et al. (2022) and de Silva et al. (2023), propose models that combine machine learning algorithms with flow analysis techniques [34][48]. Additionally, some research, such as the studies by Ishikawa et al. (2023) and Islam et al. (2022), explore hybrid models based on multi-source data integration—combining coastal surveillance camera data, satellite imagery, and drone images—to train machine learning models for rip current detection [52][50]. Furthermore, certain studies, such as the one by Haroon Rashid et al. (2023), fall into the category of models that integrate deep learning techniques with physical features, utilizing YOLO-V3 as an object detection framework [54].

Table 3. A summary of the main findings and applied techniques in various studies.

	Reference	Image processing	Used techniques	Type of study	Limitations of the study
1	Haller et al. (2014)	Hybrid method	- / Marine radar (X-band nautical)	Visualization and Tracking	- Limitation of generalizing the findings to other regions - Temporal limitations, with data being provided only as a 10-day average - Neglect of non-visual factors influencing current formation - Limitation of radar application in specific environmental conditions - Lack of investigation into the potential impacts of rip currents on swimmers - Absence of detailed information on the vertical structure currents - Spatial resolution limitations of marine radar
2	Sembiring et al. (2014)	Hybrid method	- / Coastal video imaging systems-Argus station (Argus video)	Bathymetry	- Limitation of generalizing the findings to other regions - Neglect of non-visual indicators and the potential uncertainties associated with video-based depth measurement technique - Accuracy of video-based measurements is dependent on environmental factors
3	. Hwang et al. (2014)	Traditional Image Processing	- / Traditional coastal video imaging systems -CCTV cameras (CCTV images)	Detection	- Inability to generalize the findings to other locations or beaches - Lack of suitable data quality due to the poor quality of CCTV images - Absence of discussion on potential challenges in practical beach management - Lack of further validation and testing of the developed method in diverse coastal environments
4	Bogle et al. (2014)	Traditional Image Processing	- / Traditional coastal video imaging systems (rectified image)	Observation and monitoring	- Inability to determine the exact location of sediment bars -Temporal and spatial limitations in recording current features
5	Yoon et al. (2014)	Hybrid method	- / Traditional coastal video imaging systems -CCTV cameras (CCTV images)	Tracking and locating	- Limitations in generalizing the findings - Limitations in video analysis and the potential for errors - A limited number of data points for velocity measurements - Limited information on the bathymetry of the underwater topography - Insufficient information regarding the characteristics and location of the drowning swimmers
6	Shin et al. (2014)	Hybrid method	Traditional coastal video imaging systems	Tracking and monitoring	-Limitation in estimating long-term morphological changes due to low resolution -Limitation in accurate measurement and the need for multi-image monitoring -Limitation in the generalizability of findings to other areas -Lack of investigation into the dynamic mechanisms of sediment transport
7	Wilson et al. (2014)	Hybrid method	electro-optical, infrared, and radar techniques (optical imagery, Argus time-exposed image, Infrared Particle Image)	Bathymetry	- Limitations in managing spurious long-range spatial correlations in the EnKF method - Limitation of the system's ability to generate long decorrelation lengths - Challenges in interpreting negative depths in specific locations
8	Hally-Rosendahl et al. (2015)	Hybrid method	- / A small plane (equipped with the multispectral camera system)	Tracking	-Lack of generalizability of findings to other coastal locations -Ignoring the long-term behavior trends of currents -Reliance on dye tracer measurements and lack of investigation into sediment transport processes -Uncertainty in estimating current velocities -Neglecting the impact of wave conditions on current dynamics
9	Sun et al. (2015)	Hybrid method	- / Coastal video imaging systems (UAV &Optical flow video-based technique)	Detection	-Lack of a detailed analysis of accuracy or false positive/negative rates -Potential limitations or considerations related to the use of drone technology -No discussion of the scalability of the proposed framework for large-scale implementation -Potential challenges in deploying drones for flow detection in various environments -Lack of comparison or evaluation of the proposed framework with other methods
10	Li et al. (2016)	Hybrid method	- / Remote sensing images (Not mentioned)	visually observe and analyze	-Inability to apply the study results to other regions -Limitations of the proposed method due to its reliance on the surf zone model -Failure to consider temporal variations in coastal hazards and rip current conditions -Lack of long-term observations to validate the proposed method
11	Scott et al. (2016)	Hybrid method	- / Remote sensing cameras was installed on the cliff top (plan-view timex images)	Tracking	-Limitation in generalizing the findings to other coastal areas -Lack of investigation of the effect of groin spacing and permeability on rip current dynamics -Lack of investigation of long-term changes in rip current behavior -Focus of the analysis on a specific range of wave conditions
12	Benassai et al. (2017)	Hybrid method	UAV (Unmanned aerial vehicle) & RPAS (Remotely Piloted Aircraft Systems)-Google earth images	Detection	-Inability to generalize the findings to other coastal areas -Uncertainties in accurately representing real-world conditions -Neglecting the impact of seasonal variations on rip current formation -Specific operational conditions (daylight, altitude limitations, etc.) in RPAS investigations -Neglecting the potential impact of human activities on current dynamic
13	Derian et al. (2017)	Hybrid method	- / UAV (Unmanned aerial vehicle) & optical flow	detection and monitoring	-Challenges in image quality and resolution in optical flow methods based on wavelets -Reduction in accuracy in videos due to raindrops or dust on the camera housing -Reduction in estimation accuracy due to the larger pixel size of images compared to the resolution of the modified grid -Limitations of comparison due to the limitations of comparing OF criteria with the results of acoustic Doppler velocimetry -Computational limitations of the proposed algorithm in real-time applications
14	Leatherman et al. (2017)	Hybrid method	- / Quadcopter drone	Detection	-Inability to generalize findings to coasts with different wave climatic -Lack of coverage of the impact of seasonal changes on the rip current system -Absence of discussion on specific human interventions
15	Radermacher et al. (2018)	Hybrid method	- / Coastal video imaging systems (UAV)	Bathymetry	-Limitations in generalizing findings to other locations and times -Inherent uncertainties in the depth inversion algorithm used for remote sensing bathymetry -Neglect of the dynamics of important near-shore processes or hydrodynamical processes -Limitations in the analysis due to camera resolution, georeferencing quality, and changes in wave climatic -Need for further validation and sensitivity analyses in diverse coastal settings
16	Gallop et al. (2018)	Hybrid method	- / Coastal video imaging systems-'Cam-Era' video system (time-exposure image, and Google Earth) & bathymetry observations (LiDAR)	Bathymetry	-Limitation of generalizations to other coasts -Neglect of the full complexity of coastal rip current zone dynamics and rip current behavior -Lack of investigation of wave variability at long time scales due to the limited study time -Neglect of the impact of human factors, such as beach user behavior or lifeguard interventions -Lack of consideration of the impact of seasonal changes or storm events on circulation patterns
17	Sridevi et al. (2019)	Hybrid method	- / High-resolution satellite imageries (ncluding Pleiades, Digital globe, Airbus, and Google Earth)	analyzing	-Limitation in generalizing results to other coastal areas -Recording rip current events over a limited time period rather than a long-term period -Insufficient information regarding the demographic characteristics of drowning victims or the exact circumstances surrounding each drowning event. -Lack of discuss the potential impact of human factors or safety measures on beaches and their influence on the results. -High cost of high-resolution satellite imagery -Dependence on weather, cloud cover conditions, solar radiance, and other meteorological conditions and their impact on the quality of remote sensing images.
18	Pujianiki et al. (2020)	Hybrid method	- / Coastal video imaging systems (UAV)	Visualization and Tracking	–Limitation in generalizing the findings to other rip current-prone areas due to the focus on a specific location. -Lack of use of complementary techniques such as in-situ measurements or numerical modeling for analysis, and reliance solely on aerial and drone imagery. -Lack of discussion of the effectiveness and practical implementation of these beach rip current warning strategies. -Lack of consideration of potential errors associated with placing ground control points (GCPs), measurement accuracy, or data integration.

					-Lack of assessing the feasibility of using drones in broader coastal safety initiatives in future research endeavors.
19	McGill et al. (2021)	Hybrid method	- / Coastal video imaging systems (UAV)	detection	-The accuracy of rip current detection and the reduction of backwash detection with false positives are influenced by changes in the surfcam camera angles -Challenges related to camera placement and limitations in controlling the placement of surfcam cameras -False detections (false positives), particularly including swimmers, surfers, as common sources of error in rip current identification -Limitations in image correction and the use of uncorrected images -Limitations in calibration methods due to the subjective nature of visual observations for calibration and validation, instead of in-situ instruments
20	Carpi et al. (2021)	Hybrid method	- / Coastal video imaging systems (UAV)	monitoring	-Limitation of high-resolution bathymetry data -Influence of rip current erosive capacity on near-shore bed grain size and bathymetry, and its impact on the accuracy of findings -Limitation of rip current visibility in the visual monitoring system due to boundary conditions such as seabed, waves, and sunlight -Limitation of collecting field data for rip currents due to the dynamic nature of the surf zone
21	Kim et al. (2021)	Hybrid method	- / Landsat satellites (Google Earth images), Drone	Tracking	-Limitations of GPS drifters due to low accuracy and being trapped in the surf zone -Limitation of the study scope and available resources for data collection and analysis -Limitation of generalizing the findings to other coastal areas with different characteristics -Decrease in the accuracy of the dye-tracking method under the influence of environmental factors such as wind speed, water turbidity, and dye dispersion -Lack of discussion on potential discrepancies or error sources between the two methods of dye tracking and numerical simulations
22	Fatchurohman et al. (2021)	Hybrid method	- / Coastal video imaging systems (UAV)	Tracking & monitoring	-Limitation of generalizing the findings to other coastal areas -Lack of a comprehensive investigation into the complexity of rip current dynamics due to the reliance on fluorescent dye and drone technology -Neglecting additional factors influencing rip current formation, such as seasonal variations, wave patterns, and coastal morphology -Limitations of the fluorescent dye method, including dilution and dispersion in natural waters -Lack of investigation into the impact of human factors influencing rip current incidents, such as beachgoer behavior and safety awareness levels
23	Zhang et al. (2021)	Hybrid method	- / UAV (Unmanned aerial vehicle) & Aerial and shore-based optical cameras -Google earth images	Tracking & bathymetry & Identificatio n	-Limitations in accurately predicting the timing and location of rip currents due to the highly variable spatiotemporal nature of these phenomena -Limitations in considering the full extent of rip currents in field studies -Limitations in the effectiveness of remote sensing tools, such as optical cameras and LiDAR, in accurately capturing the dynamics of rip current
24	Marchesiello et al. (2021)	Hybrid method	- / Coastal video imaging systems (UAV)	Tracking & monitoring	-Limitation of generalizing the findings to other coastal areas -Limitation of computational resources required for 3D wave-resolving models -Creation of a level of uncertainty in model results due to model simplifications and assumptions -Potential sensitivity to specific model settings and their impact on results -Necessity for further validation of findings against real-world data and scenarios
25	Hong et al. (2021)	Hybrid method	- / Coastal video imaging systems (UAV)	Tracking	-Focus on short-term simulations and neglect factors such as the long-term evolution of sedimentary barriers, irregular waves, and tides -Neglecting sediment transport in modeling to provide a more comprehensive understanding of rip current dynamics -Limitations arising from not considering the impact of long-term observations on specific sections of the coastline to provide more statistical data -Limitation arising from not examining the combination of empirical formulas or probabilistic models
26	Xue et al. (2021)	Traditional Image Processing	- / HISEA-1, the first C-band SAR small satellite	Observation and monitoring	-Incomplete calibration due to the HISEA-1 being in the startup phase and the image processing plugin of HISEA-1 still under development. -Lack of a comprehensive analysis of all the features that can be identified using SAR images
27	Rodríguez-Padilla et al. (2021)	Hybrid method	- / Coastal video imaging systems (Optical flow video-based technique)	detection	-Limitations in the accuracy of flow velocity estimation using the optical flow technique -Limitations arising from the fixed position of the camera on the coast and the lack of consideration of the variability of the coastal rip current circulation -The inability to generalize the findings due to the study's focus on high-energy wave conditions and the lack of consideration of the optical flow method under different wave energy regimes -Potential limitations in the accuracy and uncertainty of in-situ drifter results
28	Anderson et al. (2021)	Hybrid method	- / Coastal video imaging systems -Argus station (Argus image- high-resolution optical cameras- Optical flow video-based technique)	Detection & Identificatio n - Tracking & monitoring	-The need to develop and improve filtering techniques presented with in-situ observations -Optimization of selected parameters in the WAMFlow technique based on field measurements -Limitations in the selected optical tracking algorithm in WAMFlow, for example, the inability to identify sharp edges -The challenging nature of directly comparing velocities provided by drifters with remotely sensed or in-situ fixed current meters -Limitations arising from changes in environmental conditions, such as tidal level and offshore waves, for longer deployment periods of drifters compared to image recordings
29	Borra et al. (2022)	Hybrid method	- / Coastal video imaging systems (marine radar-timex image- GNSS drifters)	Identificatio n & monitorizati on	-Lack of continuous or sufficient video image data -Limited generalizability of the findings to other coastal regions -No discussion of the specific remote sensing tool used for satellite image analysis, and its impact on the reproducibility and comparison of the study with other research efforts -Lack of providing consistent and reliable data over long periods due to the temporary nature of the video camera setup -Failure to examine the potential effects of human interventions or coastal structures on rip current dynamics
30	Pitman et al. (2016)	Traditional Image Processing	- / Coastal video imaging systems (marine radar-timex image)	Detection	-Limitations in accurately identifying rip currents due to significant differences in detections based on original and synthetic images -Insufficient prediction of rip channel occurrence due to oversimplification of morphology in images in the proposed method -Limitations in the accuracy of results due to significant noise in the original image
31	Maryan et al. (2019)	AI & Machine Learning	Machin learning -SVM, CNN / -	Detection	-Limitation of generalizations to other types of tasks Object detection due to focusing on rip channel detection -The need to train convolutional neural networks on a large dataset for suitable results -Oversimplification of the model selection process due to comparing datasets to determine the most effective input type for each model -Lack of comprehensive analysis of all potential factors affecting algorithm performance -Lack of in-depth discussion of practical concepts, applications, or challenges of deployment in the real world
32	Ellenson et al. (2020)	AI & Machine Learning	Machin learning (CNN) / coastal video imaging systems (marine radar-Argus daytimexposure imagery)	Visualizatio n & detection	-Limitation of generalizing results directly to other locations -Lack of investigation into the impact of different image pre-processing techniques on the performance of the CNN model -Limitation of the CNN model's performance under the influence of the quality and resolution of daily Argos exposure images as input -Lack of investigation into the potential impact of environmental factors, such as weather conditions or seasonal variations, on the model's classification accuracy -Lack of comparison of the CNN model's performance with other machine learning algorithms or traditional image processing techniques -Lack of attention to the computational requirements and scalability of the CNN model for large-scale applications

					-Lack of a comprehensive analysis of limitations and potential sources of error in the process of classifying coastal states using CNN
33	de Silva et al. (2021)	AI & Machine Learning	Faster R-CNN / ground-based imaging (stationary cameras such as CCTV or web cameras) & Google EarthTM	Detection	-Limitation of the dataset used for training and testing the model and overestimation of results in real-world scenarios -Need to collect more diverse samples of visual representations of rip currents in future work -Need to evaluate and explore metrics that incorporate a temporal dimension to improve model training and performance -Creating a challenge in comparing model performance with previous works due to the lack of public datasets to validate results -Lack of using transfer learning due to the unavailability of pre-trained deep learning models in similar domains to improve model performance
34	Rampal et al. (2022)	Hybrid method	Deep learning (technique Grad-CAM) / High-resolution aerial imagery from Google Earth	detection and localization	-Limitation of generalizing the model to diverse coastal environments and marine conditions -Limitation of the complexity of resolving the amorphous structure with artificial intelligence -Limitation in terms of robustness and applicability in the real world -Limitation of the algorithm's applicability to other types of data sources or monitoring systems
35	Mori et al. (2022)	Hybrid method	Machine learning method - Timex (Time-exposure images) and Faster RCNN / Coastal video imaging systems(surfcams)	Detection	-Ignoring other detection techniques or factors affecting rip currents and focusing on flow visualization methods - Limitations of the direct application of flow visualization methods -Limitations of the applicability of methods for specific video metrics due to the data required for analysis, including video quality, stability, and duration -The challenging nature of detecting weak rip currents due to low flow velocity -The inherent limitations of rip current detection methods due to the complexity of defining clear boundaries and temporal bounds
36	Zhu et al. (2022)	AI & Machine Learning	(YOLO-Rip)-Deep learning(joint dilated convolutional) / -	Detection	-Limitation of generalizing the model to various rip current features due to the focus on improving the accuracy of rip current detection using the YOLO-Rip model -Lack of discussion of potential limitations in real-world deployment scenarios, such as different environmental conditions or complex backgrounds -Lack of comparison of the YOLO-Rip model with a wider range of existing advanced models for rip current detection -Failure to address the computational resources required for training and deploying the model -Lack of attention to potential challenges related to data collection, preprocessing, or interpretability of the YOLO-Rip model for real-world implementation
37	Islam et al. (2022)	Hybrid method	Deep learning and Machine Learning-- Machin learning (CNN) / Drone-shot images, bathymetric images, Google earth images	Detection	-Failure of the proposed approach (CNN and MLA) for images that do not match the training dataset -Lack of extensive investigation of various factors due to the focus on beach images, bathymetry images, and beach parameters -Limitation of the generalizability of results to different coastal conditions -Challenges in real-world scenarios when implementing data collection methods -Lack of a comprehensive analysis of the limitations and potential uncertainties of the proposed models and their practical application in coastal management -Lack of a comprehensive analysis of false positive and false negative rates of detection models and their impact on real-world practical application
38	Qi et al. (2023)	Hybrid method	(YOLOv5s model)-Deep learning(joint dilated convolutional) -Deep learning (joint expansion convolution JDC) /-	Detection	-Limitation of the applicability of the findings in scenarios with multiple scattered flow targets in a single image -Limitation in addressing real-world environmental interferences that affect detection accuracy -Limitation of generalizing the model to different coastal environments or different rip current conditions -Limitation of the real-time application of the improved model in coastal management scenarios in real-world rip current detection and warning systems
39	de Silva et al. (2023)	Hybrid method	(RipViz)-Deep learning-LSTM (Long Short-Term Memory) /-	analyzing and visualizing	-Challenges related to the difficulty of learning the behavior of machine learning algorithms, especially LSTM autoencoders, to detect abnormal trajectory sequences -Lack of information regarding the performance or accuracy of the RipViz method in detecting and visualizing rip current
40	Haroon Rashid et al. (2023)	AI & Machine Learning	(RipDet+) -Deep learning & Deep neural network /-	Detection	-Challenge of dealing with small training sample size and the unavailability of pre-trained models -Failure to increase performance with an increase in the number of warm-up epochs or the use of a relatively high fixed learning rate during training -Lack of investigation of ensemble techniques for RipDet -Limitations of using SGD and SGD with momentum instead of Adam for Rip current detection
41	Ishikawa et al. (2023)	Hybrid method	deep learning techniques (Tiny YOLO algorithm as the object detected) / web cameras placed strategically on the beach	Detection	-Limitation in detecting fully and accurately (with an AI model accuracy of 48%) rip currents by the AI model -Challenges related to changes in wave conditions and obstacles such as water droplets on the camera for accurate rip current detection -Limitation related to the need for new training data to improve the overall goal of the AI model and improve rip current detection

The results of this study, as illustrated in Figure 2, indicate that among the remote sensing techniques employed, aerial imaging accounts for the highest proportion of use (38.77%) and is regarded as one of the main and most widely applied methods in rip current studies. Satellite imagery ranks second, with a usage share of 24.48%. A review of relevant studies shows that one of the main reasons for the widespread application of aerial imaging in these studies is the higher spatial resolution of images captured using drones compared to satellite imagery [55][3]. This characteristic enables researchers to observe more detailed features of rip currents, such as wave patterns, breaking zones, and water level variations [1][56]. Moreover, operating aircraft or drones to capture aerial images offers significantly greater flexibility than other techniques [57], allowing for easy acquisition of images at various times and specific locations [58]. In addition, some aerial cameras are capable of collecting multispectral data, which can be used to extract further information about water properties. Compared to other methods such as LiDAR, aerial imaging is generally less expensive and more cost-effective [59]. Furthermore, findings from various studies demonstrate that aerial imagery can be integrated with data obtained from other sensors—such as radar and sonar—to generate a more comprehensive understanding of coastal environments where rip currents occur [60]. It is important to note, however, that the selection of an appropriate method for studying rip currents depends on various factors, including the research objective, available budget, access to equipment, and environmental conditions. Nonetheless, due to the aforementioned advantages,

aerial imaging is recognized as one of the principals and most commonly used techniques in this field, with a usage share of 38.77%.

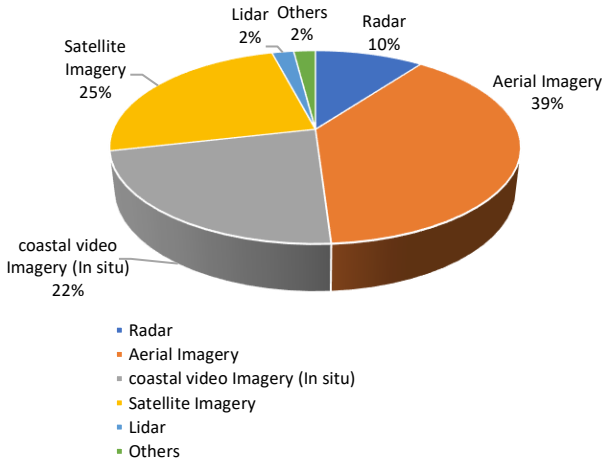


Figure 2. Categorization of percentage of used remote sensing technique for rip current studies.

A review of various studies on rip current research, as illustrated in Figure 3, reveals that Convolutional Neural Networks (CNNs), with a usage share of 33.33%, are the most widely used artificial intelligence method for image processing in rip current detection. There are several reasons for the widespread adoption of CNNs in this context, primarily related to the unique characteristics of these networks and the nature of rip current-related data. CNNs are specifically designed for image data processing, and in rip current studies, visual data—such as aerial imagery, satellite images, and marine videos—serve as the primary source of information. A review of relevant literature demonstrates that CNNs are highly capable of recognizing complex visual patterns, textures, and features present in such imagery [33][61][52].

One of the key advantages of CNNs lies in their ability to automatically extract significant features from data. This capability stems from their deep architecture, which allows them to learn multiple levels of feature abstraction. As a result, CNNs can identify more intricate patterns compared to other methods. Moreover, images of rip currents often contain noise and environmental variability, and CNNs, due to their strong generalization capabilities, are more robust to such noise and can detect rip currents with greater accuracy [33]. In addition, recent years have witnessed significant advancements in CNN technologies, along with the development of powerful software libraries such as TensorFlow and PyTorch, which have made their implementation more accessible for researchers. Following CNNs, the next most commonly used AI tools in rip current studies are Faster R-CNN and Tiny-YOLOv3 & RipDet^{+}, each accounting for 16.66% of usage. These models are designed for object detection in images and have been adapted for rip current detection as well [62][54][50]. Nevertheless, due to their greater flexibility and superior ability to learn complex features, CNNs remain the most popular choice among researchers [63].

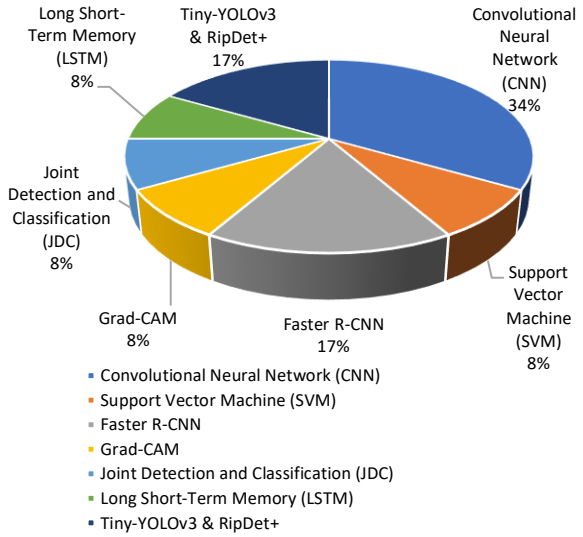


Figure 3. Categorization of percentage of used AI technique for rip current studies.

The results also indicate that among various imaging techniques—namely Radar Imagery, Optical Imagery, Lidar Imagery, and Thermal Imagery—optical imagery holds the highest share of application (39.81%) in remote sensing studies of rip currents (Figure 4). This widespread use can be attributed to several advantages of optical imagery, including high spatial resolution for capturing fine details of the water surface, waves, and flow patterns; relatively low cost; ease of interpretation; and accessibility of the imagery [64][65].

Moreover, the limitations of other imaging methods further reinforce the preference for optical imagery. For instance, although radar imaging, with a usage share of 13.95%, is capable of capturing data in adverse weather conditions and at night, literature reviews indicate that its resolution is generally lower than that of optical imagery. Additionally, radar image interpretation is more complex due to the influence of factors such as incidence angle, polarization, and surface roughness [36][31]. Lidar imagery, representing 2.32% of usage, enables precise measurement of water surface elevation, yet its application is limited due to high equipment and data processing costs [32][66][67] .

Moreover, the limited penetration of laser signals in water restricts its ability to study subsurface layers. Similarly, thermal imagery, with a comparable share to Lidar, is useful for detecting temperature differences on the water surface but is less suitable for high-resolution surface current analysis.

As illustrated in Figure 4, within the optical imagery category, visible imagery accounts for a significantly larger share compared to near-infrared (NIR) imagery. This preference is due to the considerable advantages of visible imaging. Since 2014, advancements in digital

camera technology have led to increased image resolution, reduced noise, and improved performance under various coastal environmental conditions [68].

Furthermore, the development of image processing software has enabled the extraction of quantitative information such as current velocity, flow direction, and wave height. The more limited use of near-infrared imagery stems from several drawbacks, including restricted water penetration, the need for specialized equipment, and the complexity of interpreting NIR images due to the influence of variables such as temperature, humidity, and surface material composition. These factors have led to the broader use of visible imagery in rip current studies.

It is also worth noting that the selection of X-band radar imagery over other radar technologies, such as Synthetic Aperture Radar (SAR) in rip current studies, is due to several key advantages. X-band radar provides higher spatial resolution because of its shorter wavelength, which enables the capture of more detailed images of water surfaces and flow patterns. Additionally, X-band radar is highly sensitive to small changes on the water surface, making it especially suitable for detecting phenomena such as small waves, foam, and rip current-induced surface variations. Its limited penetration into water confines the imagery to surface-level features, which is beneficial for studying surface currents. Moreover, X-band radars are generally more cost-effective than SAR systems, making them more accessible for widespread research applications [32]. Given these benefits and the limitations of SAR, the use of X-band radar in rip current studies has significantly increased since 2014.

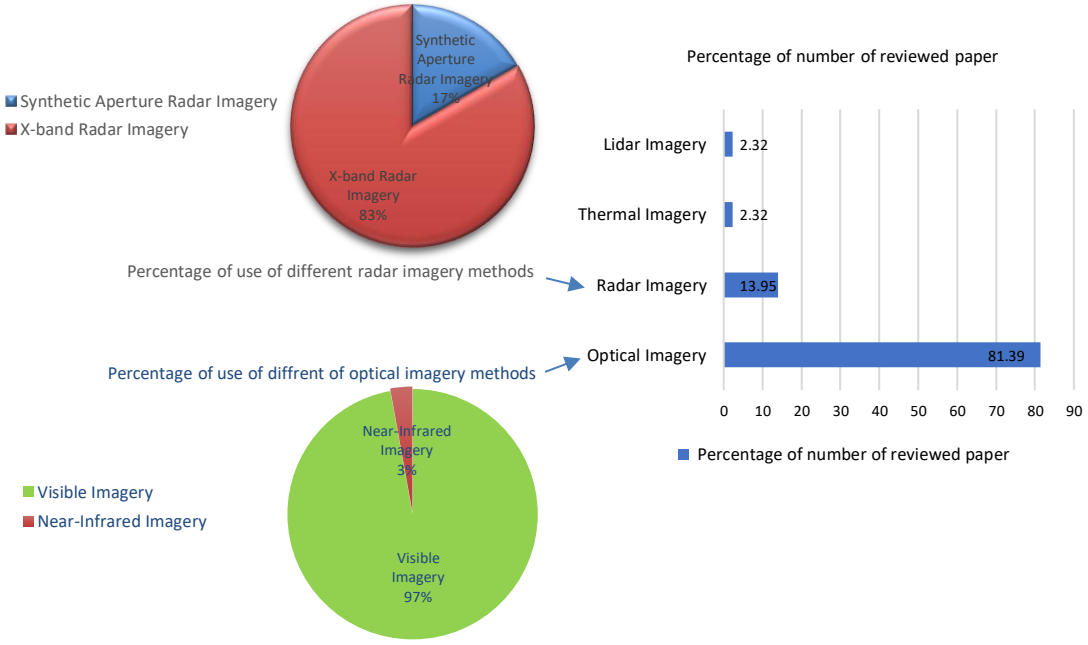


Figure 4. Categorization of Percentage of number of reviewed papers, based on Remote sensing imaging methods used for rip current studies.

The analysis of various sources, as illustrated in Figure 5, reveals that although rip current detection (38%) plays a crucial role as the first step in managing the risks associated with this phenomenon, tracking and continuous monitoring of rip currents are also of significant importance. However, there are several reasons why tracking and monitoring have received less attention than detection in recent years [69]. Other research objectives, including depth estimation, visual representation, and data analysis, are also pursued to enhance understanding and promote the practical application of research findings [70][71][13]. One of the main reasons for the predominant focus on rip current detection (with a 38% share) is the fact that rip currents are among the most hazardous marine phenomena, claiming numerous lives each year. Early detection of these currents can greatly contribute to saving the lives of swimmers and boaters [40]. Moreover, rip currents are often not visually apparent and may be hidden beneath the surface or obscured by strong wave activity, rendering traditional shoreline surveillance methods insufficient for preventing accidents [72][14][73].

As a result, recent advancements in remote sensing—particularly high-resolution satellite imagery and radar data—have facilitated more accurate and timely detection of rip currents. Furthermore, machine learning and artificial intelligence algorithms are capable of analyzing vast amounts of data and identifying complex patterns within satellite images. Consequently, accurate and timely detection of rip currents supports the enhancement of early warning systems and coastal safety management [74] .In addition, information obtained through detection efforts can be utilized in numerical modeling of coastal currents, designing coastal structures, and planning

recreational activities along the shore [75][53]. In contrast, the relatively lower focus on rip current tracking (22%) and monitoring (18%) can be attributed to the technical and operational challenges associated with these systems. Rip currents are highly dynamic and variable phenomena, influenced by multiple factors such as tides, winds, and coastal morphology. Accurately and continuously tracking these currents requires advanced monitoring systems and sophisticated algorithms [76][25]. Moreover, establishing and maintaining extensive monitoring systems along long and dispersed coastlines is highly costly. Remote sensing data and other observation methods may not always provide the resolution and accuracy necessary for precise rip current tracking. Additionally, rip currents can change direction and intensity rapidly, requiring monitoring systems to be capable of detecting these swift variations. All these factors—combined with the fact that evaluating the effectiveness of tracking and monitoring methods requires long-term, high-quality datasets—have resulted in comparatively less attention being paid to tracking and monitoring in rip current research compared to detection efforts [39].

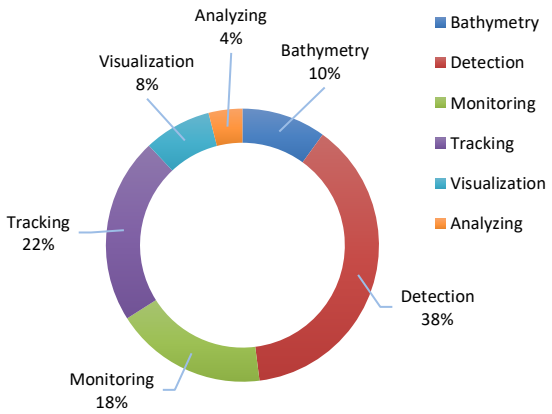


Figure 5. Categorization of percentage of study type for rip current studies.

4. Research Gaps and Future Directions

In examining the challenges, the reviewed studies were categorized into two main groups: those employing traditional methods and computer vision techniques, and those utilizing artificial intelligence (AI) and computer vision for image processing. As illustrated in Figure 6, the analysis of studies based on traditional methods and computer vision indicates that calibration and validation have been identified more frequently than other limitations in this category of research. In other words, to ensure the accuracy of the results, continuous calibration and validation of models and image processing algorithms are necessary, which poses a significant constraint in most studies. Another major limitation in this group is the exclusion of non-visual indicators (e.g., water depth). Since various traditional and computer vision-based image processing techniques rely primarily on visual information analysis, critical factors such as water depth and bathymetry (underwater topography), which significantly influence rip currents, may not be directly detectable. These limitations can directly affect the accuracy of the obtained results.

Another frequently reported challenge is the limitation related to spatial resolution. Although high-resolution images obtained through remote sensing techniques are often available, in some cases, the resolution may still be insufficient for analyzing fine-scale features of rip currents. This issue becomes particularly pronounced in areas with dense vegetation or turbid waters, where detecting and tracking rip currents becomes problematic.

Other reported challenges and limitations, in order of frequency, include the influence of tides and waves, atmospheric conditions, rapid variability of currents, precise boundary delineation of currents, seasonal and annual variations, surface cover effects, and various environmental factors.

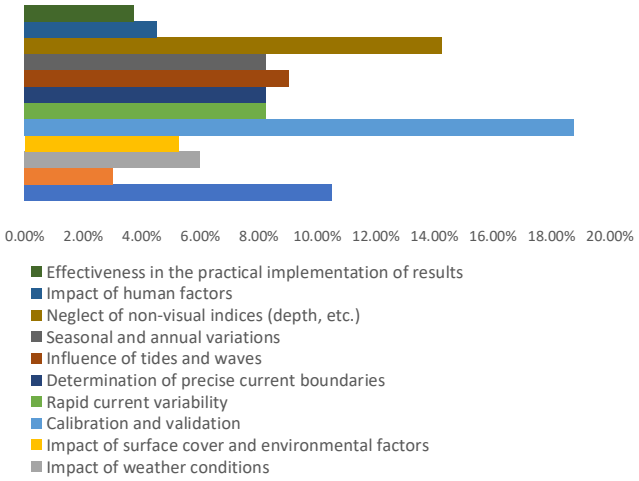


Figure 6. Percentage of challenges in image processing based on traditional methods and computer vision.

Figure 7 presents a comparison of the challenges identified in studies that utilize artificial intelligence (AI) and computer vision for image processing. Among the various limitations, spatial and temporal constraints are among the most frequently reported challenges in this group of studies. In other words, the results obtained in each study often face significant difficulties in terms of model generalization. This is primarily due to the fact that most AI models are trained on specific datasets and may not perform well under different conditions or in other geographical locations.

Challenges related to insufficient and noisy data, limitations in defining different flow classes, uncertainty in input data, and the “black-box” nature of AI models (i.e., the lack of transparency in how results are derived) have been reported with similar frequency across the literature. Other notable challenges, in descending order of occurrence, include the unavailability of trained models for benchmarking,

rapid and nonlinear flow variations, high computational costs, and inadequate labeling of the datasets used.

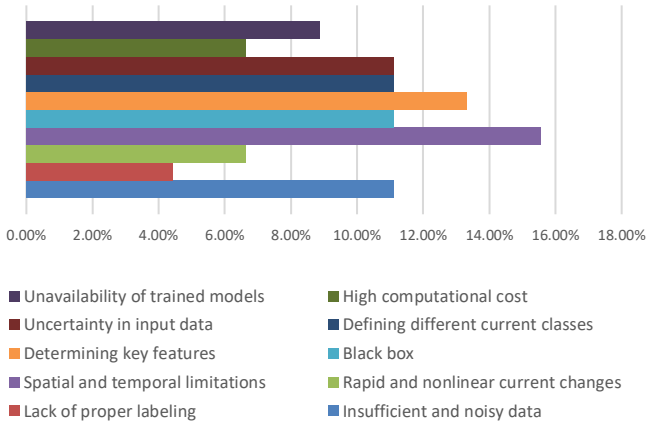


Figure 7. Percentage of challenges in image processing based on artificial intelligence tools and computer vision.

In this study, heatmap analysis of the challenges and limitations in various studies has been employed as a powerful approach to better understand these areas and guide future research. By identifying the challenges and weaknesses of each specific technique, innovative solutions can be proposed to advance remote sensing and artificial intelligence studies, ultimately unlocking the full potential of these technologies.

Figure 8 presents a heatmap of different remote sensing tools (such as Radar, Aerial Imagery, etc.) along the horizontal axis and various challenges and limitations of remote sensing (such as Temporal resolution, Spatial resolution, etc.) along the vertical axis. Each cell in this heatmap indicates the intensity of the relationship between a specific challenge and a particular tool. Warmer colors denote stronger correlations, while cooler colors indicate weaker correlations.

The heatmap in Figure 8 highlights various aspects, including general challenges common to all remote sensing tools, such as seasonal and annual variations and the lack of non-visual indicators (e.g., depth) in the use of different remote sensing tools. These challenges are present in almost all remote sensing tools, with none of them being entirely unaffected (absence of red, or completely cold colors). The primary reason for the commonality of the seasonal and annual variation challenge across all remote sensing tools is the changes in vegetation cover across different seasons, which affect the reflection of light from the Earth's surface and, consequently, the pixels in satellite images. Changes in water resources, such as rainfall, evaporation, and transpiration throughout the year, influence the amount of water on the Earth's surface, soil moisture, and the depth of surface waters, all of which are visible in satellite imagery. Additionally, changes in atmospheric phenomena, in line with seasonal variations, impact the quality of satellite images, complicating their interpretation. The shared challenge of the lack of non-visual indicators in all remote sensing tools is attributed to the limitations of the remote sensing sensors. Most remote sensing sensors are sensitive to visible, near-infrared, and thermal infrared spectra. These sensors provide information on light reflection from the Earth's surface but do not offer details about subsurface features such as depth, temperature, etc. The complexity of natural phenomena, such as rip currents, also contributes to the shared challenge of not accounting for non-visual indicators in all remote sensing tools for rip current detection.

Moreover, Figure 8 significantly aids in identifying the major challenges associated with each remote sensing tool. For instance, due to the widespread use of aerial imagery as the most common remote sensing technique, the challenge of calibration and validation is shown as the most frequently encountered challenge (represented by dark green) in this technique. This challenge is also depicted as the most influential (dark green) in satellite imagery techniques. This indicates that calibration and validation can impact the accuracy of both aerial and satellite imagery techniques. Thus, the strengths and weaknesses of each remote sensing technique in dealing with various challenges can be identified. It is also noteworthy that in both aerial and satellite imagery techniques, the impact of surface cover and environmental factors and impact of weather conditions on the accuracy of the techniques are significant. However, in these two remote sensing techniques, temporal resolution (the time interval between two consecutive images) is not a major challenge. This is because aerial imagery allows for more flexibility in the timing of flight missions, making it much easier to capture aerial images at different times and locations. On the other hand, in rip current studies, parameters such as flow speed, flow direction, wave height, and wave breaking patterns are much more critical and challenging than temporal resolution. These parameters can be extracted using satellite images with appropriate spatial resolution and image processing techniques.

According to Figure 8, spatial resolution (the smallest detail that can be distinguished in an image) is another challenge that is particularly notable in radar imagery from various remote sensing tools. According to the findings from related studies, one of the main reasons for the limitation of achieving very high spatial resolution in radar images is the technical constraints of radar systems. In other words, the spatial resolution of radar systems depends on various factors, such as operating frequency, antenna size, and distance to the target. Given the specific characteristics of rip currents—such as their small size and rapid changes—the spatial resolution limitation in radar imaging is a major challenge in rip current studies. However, this challenge can be partially addressed through the use of various techniques and the development of new technologies.

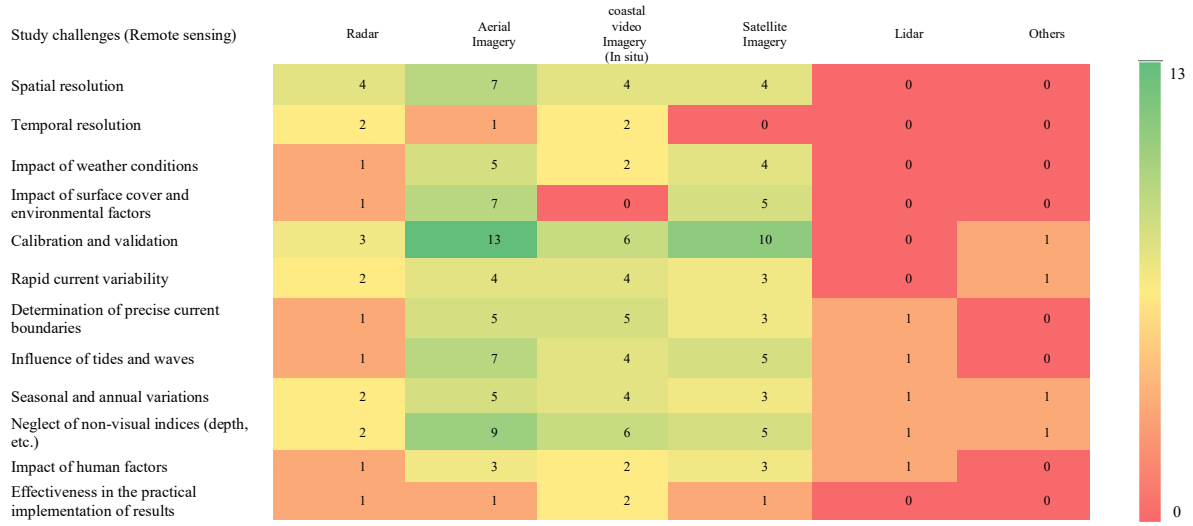


Figure 8. Heat map showing the study challenges against a variety of RS techniques.

Figure 9 presents a heatmap of various techniques and hybrid tools in artificial intelligence (e.g., Machine Learning (SVM), Machine Learning (CNN), Deep Learning (Faster R-CNN), etc.) along the horizontal axis, and various challenges encountered in employing these methods (e.g., Lack of proper labeling, Insufficient and noisy data, Rapid and nonlinear current changes, etc.) along the vertical axis. Each cell in the heatmap indicates the intensity of the relationship between a specific challenge and a particular technique. Warmer colors denote stronger correlations, while cooler colors indicate weaker correlations.

The heatmap in Figure 9 illustrates the challenges encountered with each specific AI technique. The results show that, in machine learning methods such as CNN and SVM, the primary challenges are related to model generalization (spatial and temporal limitations), challenges in interpreting results (black-box nature), and specific challenges in studying rip currents (identifying key features).

In other deep learning techniques and hybrid methods, including LSTM, JDC, Grad-CAM, Faster R-CNN, and Tiny-YOLOv3 & RipDet+, no specific recurring challenge is observed. However, in the two deep learning techniques, Faster R-CNN and Tiny-YOLOv3 & RipDet+, the challenge of insufficient and noisy data, which pertains to the quality of input data, is identified as the most impactful limitation in rip current studies. As noted, both of these techniques are object detection models widely used in the field of computer vision, with Faster R-CNN known for its high accuracy and Tiny-YOLOv3 for its high speed. Consequently, both models require high-quality and large volumes of training data, and insufficient training data may lead to problems such as overfitting or underfitting. Additionally, noise in the data can reduce the model's accuracy. Since RipDet+ is specifically designed for rip current detection, it requires training data with accurate and domain-specific labeling.

On the other hand, aside from the high cost and time involved in collecting and labeling rip current data, the complexity and variable nature of rip currents make it highly challenging to gather diverse and representative data for this phenomenon. All these factors make the challenge of insufficient and noisy data the most prominent limitation in rip current studies for the two aforementioned techniques.

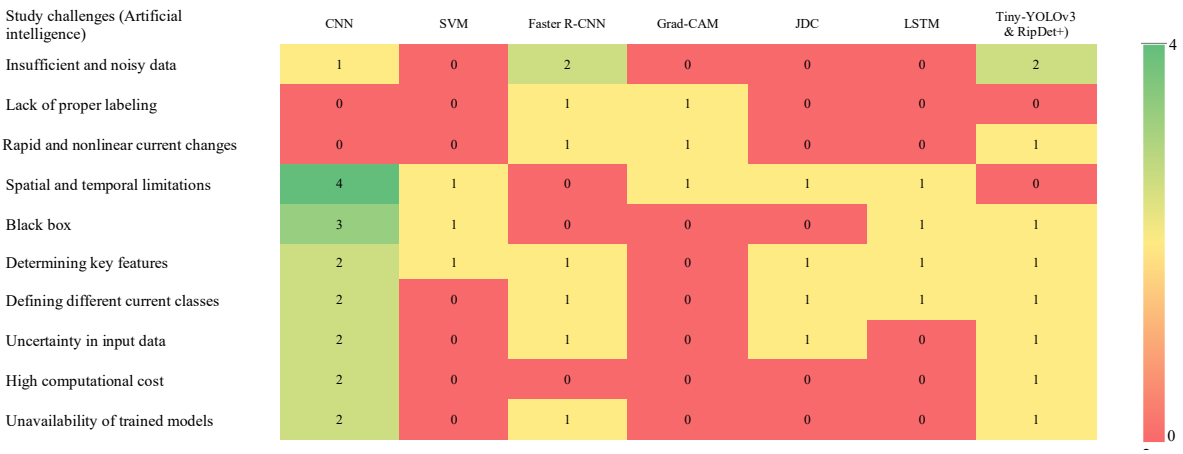


Figure 9. Heat map showing the study challenges against a variety of AI techniques.

5. Conclusions

This study provides a comprehensive review of the application of various image processing and remote sensing techniques in rip current studies. The findings revealed that combined processing methods, particularly those utilizing multi-source data (coastal surveillance cameras, satellite imagery, and drones), were the most widely used (approximately 78% of the studies). Additionally, studies combining classical image processing with machine learning and flow analysis have been more successful in accurately detecting rip currents.

Among remote sensing imaging methods, optical imagery, with a share of 81.39%, has been the most commonly used due to its high resolution, lower cost, and ease of interpretation. It is worth noting that while aerial imagery, with a share of 38.77%, has been one of the most widely used methods in rip current studies due to its higher spatial resolution and flexibility in data collection, satellite imagery, with a share of 24.48%, has also held a significant position. However, the combination of these images with other data, such as radar and sonar, can provide more comprehensive information about coastal environments.

Regarding the use of artificial intelligence tools, Convolutional Neural Networks (CNN), with a share of 33.33%, have been identified as the most widely used method in rip current image processing due to their ability to automatically extract complex visual features and their resilience to noise. Other AI models, such as Faster R-CNN and Tiny-YOLOv3, have also been used for object detection in images, but CNNs are more popular due to their greater flexibility and ability to learn more complex features.

The results indicated that the main focus of studies has been on the detection of rip currents (38%), while tracking (22%) and continuous monitoring (18%) of these currents have received less attention. One of the reasons for this is the technical challenges and high costs associated with establishing and maintaining monitoring systems. Additionally, the rapid changes in rip currents and the need for long-term, high-quality data to assess the effectiveness of monitoring and tracking methods have been other significant barriers.

The review of challenges in the studies revealed that limitations related to model calibration and validation, the failure to consider non-visual indicators (such as depth and underwater topography), inappropriate spatial resolution, and the impact of weather conditions were among the common problems in traditional image processing and computer vision methods. In AI-based studies, challenges related to the generalization of models, insufficient and noisy data, and uncertainty in defining the classes of rip currents were considered major obstacles. Overall, the results of this study indicate that combining image processing, remote sensing, and artificial intelligence techniques can enhance the detection, tracking, and monitoring of rip currents. Furthermore, the development of AI models with high generalization capability and the integration of multi-source data can pave the way for future research in this field.

6. References

1. Hong, X., Zhang, Y., Wang, B., Zhou, S., Yu, S., & Zhang, J. (2021). Numerical study of rip currents interlaced with multichannel sandbars. *Natural Hazards, 108*(1), 593–605. https://doi.org/10.1007/s11069-021-04696-8

2. Dudkowska, A., Boruń, A., Malicki, J., Schönhofer, J., & Gic-Grusza, G. (2020). Rip currents in the non-tidal surf zone with sandbars: Numerical analysis versus field measurements. *Oceanologia, 62*(3), 291–308. https://doi.org/10.1016/j.oceano.2020.02.001

3. Carpi, L., Mucerino, L., Bonello, G., Besio, G., & Ferrari, M. (2021). Rip currents investigation on a Ligurian pocket beach, NW Mediterranean. *Estuarine, Coastal and Shelf Science, 262*, 107579. https://doi.org/10.1016/j.ecss.2021.107579

4. Johnson, D., & Pattiaratchi, C. (2004). Transient rip currents and nearshore circulation on a swell-dominated beach. *Journal of Geophysical Research: Oceans, 109*(C2), C02026. https://doi.org/10.1029/2003JC001798

5. MacMahan, J. H., Thornton, E. B., & Reniers, A. J. H. M. (2006). Rip current review. *Coastal Engineering, 53*(2–3), 191–208. https://doi.org/10.1016/j.coastaleng.2005.10.009

6. Castelle, B., Scott, T., Brander, R. W., & McCarroll, R. J. (2016). Rip current types, circulation and hazard. *Earth-Science Reviews, 163*, 1–21. https://doi.org/10.1016/j.earscirev.2016.09.008

7. Dalrymple, R. A. (1975). A mechanism for rip current generation on an open coast. *Journal of Geophysical Research, 80*(24), 3485–3487. https://doi.org/10.1029/JC080i024p03485

8. Thornton, E. B., MacMahan, J., & Sallenger, A. H. (2007). Rip currents, mega-cusps, and eroding dunes. *Marine Geology, 240*(1–4), 151–167. https://doi.org/10.1016/j.margeo.2007.02.018

9. Winter, G., Van Dongeren, A., De Schipper, M., & Van Thiel De Vries, J. (2012). A field and numerical study into rip currents in wind-sea dominated environments. *Proceedings of the Coastal Engineering Conference*, 33, currents.36. https://doi.org/10.9753/icce.v33.currents.36

10. Valipour, A., Khaniki, A., & Bidokhti, A. (2014). Investigating the reactions of rip current pattern and sediment transport in rip channel against changes of bed parameters using numerical simulations. *Indian Journal of Geo-Marine Sciences, 43*(May), 831–840. http://nopr.niscair.res.in/handle/123456789/28776

11. Damgaard, J., Dodd, N., Hall, L., & Chesher, T. (2000). Morphodynamic modelling of rip channels. In *Coastal Engineering 2000: Proceedings of the 27th International Conference on Coastal Engineering* (Vol. 276, pp. 441–453). https://doi.org/10.1061/40549(276)35
12. Castelle, B., & Coco, G. (2012). The morphodynamics of rip channels on embayed beaches. *Continental Shelf Research, 43*, 10–23. https://doi.org/10.1016/j.csr.2012.04.010
13. Bogle, J. A., Bryan, K. R., Black, K. P., Hume, T. M., & Healy, T. (2000). Video observations of rip formation and evolution. *Journal of Coastal Research, Special Issue* (No. 34).
14. Kim, B. S. S. K. H. (2014). Rip current monitoring using video analysis. *Journal of Coastal Research, 72*, 28–32.
15. Haas, K. A., & Svendsen, I. A. (2002). Laboratory measurements of the vertical structure of rip currents. *Journal of Geophysical Research: Oceans, 107*(C5), 1–19. https://doi.org/10.1029/2001JC000911
16. Drønen, N., Karunarathna, H., Fredsøe, J., Mutlu Sumer, B., & Deigaard, R. (2002). An experimental study of rip channel flow. *Coastal Engineering, 45*(3–4), 223–238. https://doi.org/10.1016/S0378-3839(02)00035-2
17. Haller, M. C., Dalrymple, R. A., & Svendsen, I. A. (2002). Experimental study of nearshore dynamics on a barred beach with rip channels. *Journal of Geophysical Research: Oceans, 107*(C6), 1–21. https://doi.org/10.1029/2001JC000955
18. Castelle, B., Bonneton, P., Dupuis, H., & Sénéchal, N. (2010). Laboratory experiment on rip current circulations over a moveable bed: Drifter measurements. *Journal of Geophysical Research: Oceans, 115*(C12), 1–17. https://doi.org/10.1029/2010JC006343
19. Van Dongeren, A., Van Ormondt, M., Sembiring, L., Sasso, R., Austin, M., Briere, C., Swinkels, C., Reniers, A. J. H. M., & Roelvink, D. (2013). Rip current predictions through model-data assimilation on two distinct beaches. In *Coastal Dynamics 2013* (pp. 1775–1786). https://www.slideshare.net/ALBICEE/lembar-observasi-siswa-50178674
20. MacMahan, J., Reniers, A. J. H. M., Thornton, E. B., Stanton, T. P., Brown, J., Henriquez, M., Gallagher, E., Morrison, J., & Austin, M. (2010). Mean Lagrangian flow behavior on an open coast rip-channeled beach: A new perspective. *Marine Geology, 268*(1–4), 1–15. https://doi.org/10.1016/j.margeo.2009.09.011
21. Smith, J. A., & Largier, J. L. (1995). Observations of nearshore circulation: Rip currents. *Journal of Geophysical Research: Oceans, 100*(C6). https://doi.org/10.1029/95JC00751
22. Shin, S., Nam, J., Son, S., Kim, I. H., & Jung, T. H. (2017). Field observation and numerical modelling of rip currents within a pocket beach. *Journal of Coastal Research, 33*(Special Issue 79), 229–233. https://doi.org/10.2112/SI79-047.1
23. Brander, R. W. (1999). Sediment transport in low-energy rip current systems. *Journal of Coastal Research, 15*(3), 839–849.
24. Aagaard, T., Greenwood, B., & Nielsen, J. (1997). Mean currents and sediment transport in a rip channel. *Marine Geology, 140*(1–2), 25–45. https://doi.org/10.1016/S0025-3227(97)00025-X
25. Kim, H. D., & Kim, K. H. (2021). Analysis of rip current characteristics using dye tracking method. *Atmosphere, 12*(6), 1–12. https://doi.org/10.3390/atmos12060719
26. McCarroll, R. J., Castelle, B., Brander, R. W., & Scott, T. (2015). Modelling rip current flow and bather escape strategies across a transverse bar and rip channel morphology. *Geomorphology, 246*, 502–518. https://doi.org/10.1016/j.geomorph.2015.06.041
27. Bowen, J. (1969). Rip currents: 1. Theoretical investigations. *Journal of Geophysical Research, 74*(23), 5467–5478.
28. Osaisai, E. F. (2013). An analytical model of the rip current flow. *International Journal of Computational Engineering Research*, 3(8), 1–12. Retrieved from http://www.ijceronline.com
29. Barthélemy, E. (2017). Rip currents vorticity scaling. In *Coastal Dynamics 2017* (pp. 399–408).
30. Valipour, A., & Bidokhti, A. A. (2018). An analytical model for the prediction of rip spacing in intermediate beaches. *Journal of Earth System Science, 127*(8), 1–11. https://doi.org/10.1007/s12040-018-1013-5
31. Pitman, S., Gallop, S. L., Haigh, I. D., Mahmoodi, S., Masselink, G., & Ranasinghe, R. (2016). Synthetic imagery for the automated detection of rip currents. *Journal of Coastal Research, 1*(75), 912–916. https://doi.org/10.2112/SI75-183.1
32. Haller, M. C., Honegger, D., & Catalan, P. A. (2014). Rip current observations via marine radar. *Journal of Waterway, Port, Coastal, and Ocean Engineering, 140*(2), 115–124. https://doi.org/10.1061/(ASCE)WW.1943-5460.0000229
33. Maryan, C., Hoque, M. T., Michael, C., Ioup, E., & Abdelguerfi, M. (2019). Machine learning applications in detecting rip channels from images. *Applied Soft Computing Journal, 78*, 84–93. https://doi.org/10.1016/j.asoc.2019.02.017
34. de Silva, A., et al. (2023). RipViz: Finding rip currents by learning pathline behavior. *IEEE Transactions on Visualization and Computer Graphics, PP*(ML), 1–13. https://doi.org/10.1109/TVCG.2023.3243834
35. Devi, G. K., Ganasri, B. P., & Dwarakish, G. S. (2015). Applications of remote sensing in satellite oceanography: A review. *Aquatic Procedia,*

4(ICWRCOE), 579–584. https://doi.org/10.1016/j.aqpro.2015.02.075
36. Borra, S., et al. (2022). Identifying rip channels along RK Beach, Visakhapatnam using video and satellite imagery analysis. *Journal of the Indian Society of Remote Sensing, 50*(8), 1585–1602. https://doi.org/10.1007/s12524-022-01539-2
37. Jiang, D., Hao, M., & Fu, J. (2016). Monitoring the coastal environment using remote sensing and GIS techniques. In *Applied Studies in Coastal and Marine Environment* (No. 2). https://doi.org/10.5772/62242
38. Andriolo, U., Sánchez-García, E., & Taborda, R. (2019). Operational use of surfcam online streaming images for coastal morphodynamic studies. *Remote Sensing, 11*(1), 1–21. https://doi.org/10.3390/rs11010078
39. McGill, S. (2022). Rip current and channel detection using surfcams and optical flow. *Shore & Beach*, August, 50–58. https://doi.org/10.34237/1009015
40. Benassai, G., et al. (2017). Rip current evidence by hydrodynamic simulations, bathymetric surveys and UAV observation. *Natural Hazards and Earth System Sciences, 17*(9), 1493–1503. https://doi.org/10.5194/nhess-17-1493-2017
41. Sun, A. (2023). UAV-video-based rip current detection in nearshore areas. *arXiv*. http://arxiv.org/abs/2304.11783
42. Trizna, D. B. (2019). Coherent marine radar observations of rip current features with high temporal resolution. In *OCEANS 2018 MTS/IEEE Charleston* (pp. 1–5). https://doi.org/10.1109/OCEANS.2018.8604640
43. Lipa, B., Nyden, B., Barrick, D., & Kohut, J. (2008). HF radar sea-echo from shallow water. *Sensors, 8*(8), 4611–4635. https://doi.org/10.3390/s8084611
44. Paz-Delgado, M. V., Payo, A., Gómez-Pazo, A., Beck, A. L., & Savastano, S. (2022). Shoreline change from optical and SAR satellite imagery at macro-tidal estuarine, cliffed open-coast and gravel pocket-beach environments. *Journal of Marine Science and Engineering, 10*(5). https://doi.org/10.3390/jmse10050561
45. Yang, X., Zhao, J., Wei, Z., Wang, N., & Gao, X. (2022). SAR-to-optical image translation based on improved CGAN. *Pattern Recognition, 121*, 108208. https://doi.org/10.1016/j.patcog.2021.108208
46. Mouragues, A., et al. (2021). Field observations of wave-induced headland rips. *Coastal Dynamics*. https://doi.org/10.2112/SI95-0XX.1
47. Song, D. S., & Bae, H. K. (2011). Observation and forecasting of rip current generation in Haeundae Beach, Korea plan and experiment. *Journal of Coastal Research*, Special Issue 64, 946–950.
48. Mori, I., De Silva, A., Dusek, G., Davis, J., & Pang, A. (2022). Flow-based rip current detection and visualization. *IEEE Access, 10*, 6483–6495. https://doi.org/10.1109/ACCESS.2022.3140340
49. Radermacher, A. J. H. M. R. M., & de Schipper, M. A. (2018). Sensitivity of rip current forecasts to errors in remotely-sensed bathymetry. *Coastal Engineering, 135*, 66–76. https://doi.org/10.1016/j.coastaleng.2018.01.007
50. Ishikawa, T., Shimada, R., & Komine, T. (2023). Rip current detection in an open area and along jetty using AI. *Coastal Engineering Proceedings, 37*, 7. https://doi.org/10.9753/icce.v37.papers.7
51. Melet, A., et al. (2020). Earth observations for monitoring marine coastal hazards and their drivers. *Surveys in Geophysics, 41*(6). https://doi.org/10.1007/s10712-020-09594-5
52. Islam, M. A., & Shampa, M. T. A. (2022). Rip current: A potential hazard zones detection in Saint Martin's Island using deep learning and machine learning approach. *Electronic Letters on Computer Vision and Image Analysis, 21*(2), 63–81. https://doi.org/10.5565/REV/ELCVIA.1604
53. Rampal, N., Shand, T., Wooler, A., & Rautenbach, C. (2022). Interpretable deep learning applied to rip current detection and localization. *Remote Sensing, 14*(23). https://doi.org/10.3390/rs14236048
54. Rashid, A. H., Razzak, I., Tanveer, M., & Hobbs, M. (2023). Reducing rip current drowning: An improved residual based lightweight deep architecture for rip detection. *ISA Transactions, 132*, 199–207. https://doi.org/10.1016/j.isatra.2022.05.015
55. Fatchurohman, H., Khasanah, A. N., & Cahyadi, A. (2021). Identification of rip current hazards using fluorescent dye and unmanned aerial vehicle (A case study of Drini Beach, Gunungkidul, Indonesia). *Natural Hazards and Earth System Sciences*. https://doi.org/10.5194/nhess-2021-221
56. Marchesiello, P., et al. (2021). Tridimensional nonhydrostatic transient rip currents in a wave-resolving model. *Ocean Modelling, 163*. https://doi.org/10.1016/j.ocemod.2021.101816
57. Zhang, Y., Huang, W., Liu, X., Zhang, C., Xu, G., & Wang, B. (2021). Rip current hazard at coastal recreational beaches in China. *Ocean & Coastal Management, 210*, 105734. https://doi.org/10.1016/j.ocecoaman.2021.105734
58. Hally-Rosendahl, K., Feddersen, F., & Clark, D. B. (2015). Surfzone to inner-shelf exchange estimated from dye tracer balances. *Journal of Geophysical Research: Oceans*, 2121–2128. https://doi.org/10.1002/jgrc.20224
59. Gallop, S. L., Bryan, K. R., Pitman, S. J., Ranasinghe, R., Sandwell, D. R., & Harrison, S. R. (2018). Rip current circulation and surf zone retention on a double barred beach. *Marine Geology, 405*, 12–22. https://doi.org/10.1016/j.margeo.2018.07.015
60. Ellenson, A. N., Simmons, J. A., Wilson, G. W., Hesser, T. J., & Splinter, K. D. (2020). Beach state recognition using ARGUS imagery and convolutional neural networks. *Remote Sensing, 12*(23), 3953. https://doi.org/10.3390/rs12233953

61. de Silva, A., Mori, I., Dusek, G., Davis, J., & Pang, A. (2021). Automated rip current detection with region based convolutional neural networks. *Coastal Engineering, 166*, 103859. https://doi.org/10.1016/j.coastaleng.2021.103859
62. Rui Qi, R., & Dao-Heng Zhu, X. Q. (2023). Research on rip currents detection method based on improved YOLOv5s [電腦學刊]. *Journal of Computer Science*, 34(2), 113–127. https://doi.org/10.53106/199115992023043402009
63. Zhu, D., Qi, R., Hu, P., Su, Q., Qin, X., & Li, Z. (2022). YOLO-Rip: A modified lightweight network for rip currents detection. *Frontiers in Marine Science, 9*, Article 930478. https://doi.org/10.3389/fmars.2022.930478
64. Rodríguez-Padilla, I., et al. (2021). Wave-filtered surf zone circulation under high-energy waves derived from video-based optical systems. *Remote Sensing, 13*(10), Article 1874. https://doi.org/10.3390/rs13101874
65. Anderson, D., Spicer Bak, A., Brodie, K. L., Cohn, N., Holman, R. A., & Stanley, J. (2021). Quantifying optically derived two-dimensional wave-averaged currents in the surf zone. *Remote Sensing, 13*(4), Article 690. https://doi.org/10.3390/rs13040690
66. Xue, S., Geng, X., Meng, L., Xie, T., Huang, L., & Yan, X. H. (2021). HISEA-1: The first C-band SAR miniaturized satellite for ocean and coastal observation. *Remote Sensing, 13*(11), Article 2076. https://doi.org/10.3390/rs13112076
67. Wilson, C. C. C. G. W., Ozkan-Haller, H. T., Holman, R. A., Haller, M. C., & Honegger, D. A. (2014). Surf zone bathymetry and circulation predictions via data assimilation of remote sensing observations. *Journal of Geophysical Research: Oceans, 119*, 3868–3882. https://doi.org/10.1002/2013JC009213
68. Dérian, P., & Almar, R. (2017). Wavelet-based optical flow estimation of instant surface currents from shore-based and UAV videos. *IEEE Transactions on Geoscience and Remote Sensing, 55*(10), 5790–5797. https://doi.org/10.1109/TGRS.2017.2714202
69. Scott, T., Austin, M., Masselink, G., & Russell, P. (2016). Dynamics of rip currents associated with groynes: Field measurements, modelling and implications for beach safety. *Coastal Engineering, 107*, 53–69. https://doi.org/10.1016/j.coastaleng.2015.09.013
70. Sridevi, T., Kumar, R., Sridevi, T., & Arun Kumar, S. V. V. (2019). Seasonal variability of rip current probability along a wave-dominated coast using high resolution satellites and wave data NASA-ISRO L&S band SweepSAR (NISAR) mission. *Journal of Geomatics, 13*(1), 149–155. Retrieved from https://www.researchgate.net/publication/336103693
71. Sembiring, L., Van Dongeren, A., Winter, G., Van Ormondt, M., Briere, C., & Roelvink, D. (2014). Nearshore bathymetry from video and the application to rip current predictions for the Dutch coast. *Journal of Coastal Research, 70*, 354–359. https://doi.org/10.2112/SI70-060.1
72. Yoon, J. C. S. B., & Park, W. K. (2014). Observation of rip current velocity at an accidental event by using video image analysis. *Journal of Coastal Research, 72*, 16–21.
73. Li, Z. (2016). Rip current hazards in South China headland beaches. *Ocean & Coastal Management, 121*, 23–32. https://doi.org/10.1016/j.ocecoaman.2015.12.005
74. Hwang, J. S., Yun, H. S., Suh, Y. C., Lee, J., & Kang, S. C. (2016). Rip current research using a CCTV image analysis including swimmer detecting techniques at Haeundae Beach, Korea. *Journal of Coastal Research, Special Issue*. [Details not fully provided for volume/pages]
75. Leatherman, S. B. (2017). Rip current measurements at three south Florida beaches. *Journal of Coastal Research, 33*(5), 1228–1234. https://doi.org/10.2112/JCOASTRES-D-16-00124.1
76. Pujianiki, N. N., Antara, I. N. G., Temaja, I. G. R. M., Partama, I. G. D. Y., & Osawa, T. (2020). Application of UAV in rip current investigations. *International Journal of Advanced Science, Engineering and Information Technology, 10*(6), 2337–2343. https://doi.org/10.18517/ijaseit.10.6.12620

INTERNATIONAL JOURNAL OF
COASTAL, OFFSHORE & ENVIRONMENTAL ENGINEERING IJCOE Vol.11/No. 3/Summer 2026 (86-97)

Available online at: www. Ijcoe.org

The failure probability of reinforced concrete marine structures and cost optimization of maintenance

Abdolhossein Mohammadrahimi[1*], Afshin Ghasri[2], Mesbah Sayebani[3], Akbar Esfandiari[4]

[1] Assistant Professor,Department of Marine Engineering, Chabahar maritime university, Shahid Rigi Ave, Chabahar, Iran; rahimi@cmu.ac.ir*
[2] Department of Maritime Engineering, Amirkabir University of Technology, Hafez Ave, Tehran, Iran; afshin;ghasri@gmail.com
[3] Assistant Professor, Department of Maritime Engineering, Amirkabir University of Technology, Hafez Ave, Tehran, Iran; msaybani@aut.ac.ir
[4] Assistant Professor,Department of Maritime Engineering, Amirkabir University of Technology, Hafez Ave, Tehran, Iran; a_esfandiari@aut.ac.ir

ARTICLE INFO

Article History:
Received 2 Apr 2026
Accepted 15 July 2026
Available online ….

Keywords:
Corrosion, Crack width, symptom-based Reliability, Maintenance and repair, Cost Optimization

ABSTRACT

Due to the increased life of marine structures in the world, repair and maintenance of low cost and high reliability are of concern in this industry. In this paper, the corrosion-induced crack width of reinforced concrete (RC) structure in the marine environment is estimated according to the experimental data, laboratory results, and numerical formulas. Symptom-based Weibull function distribution and Bayesian theory have been used to predict the structural reliability in different modes (without repair and maintenance, with maintenance, and with repair and maintenance) and the probability of failure was assessed before and after maintenance to predict the appropriate time for its implementation using Bayesian theory. Bi-objective optimization was utilized to provide the client with optimal decisions regarding the probability of structural failure as well as the type of repair and maintenance strategies. The results showed the effectiveness of the proposed method in predicting performance, improving life service, and optimizing repair and maintenance costs of the marine structure.

1. Introduction

Improving marine structure lifetime is a recent concern for maritime industry in the word. Marine structures are being under serious damage or even severe failure as they are subjected to the environmental forces of aggressive marine environment including corrosion, waves, floats, etc. The evident need for effective repair and maintenance strategies is felt by all concerned in maritime industry including owners, classification society, and officials. Repair and maintenance are more cost-effective, less risky, and simpler than the design and construction of marine structures. This need is more evidently felt when the structure service age is increased [1].

Structural health monitoring is one of the ways to identify fatigue damage to the structure. Its ultimate goal is to detect the existence, location, and extent of structural damage. Additional to structural health monitoring and its data, reliability and probabilistic analysis can be utilized to predict future performance and service life of the structure. The durability of the structure is enhanced using repair and maintenance strategies to improve structural performance and lifetime. A targeted program can provide information on the present condition, repair and maintenance regularities, and the future performance of the structure.

Full inspection and assessment are requisites to ensure the sustainability of structure and reduce costs (proper repair and maintenance implementation). Structural health monitoring strategy is integrated with life cycle management to predict the structure performance, estimate optimal maintenance strategy, and thus use the structure beyond its design life span. RC structures as

a type of marine structures may change from the initial design to the state that threatens their safety and usability due to corrosion, service aging, or changes in their resistance to toughness. Therefore, damage prediction is essential to estimate the structure remnant life and implement maintenance and repairs. In fact, the structural reliability and serviceability are predictable from probabilistic functions using specific information of structures (crack width in RC structures). The prediction of future state from observation of present state via probabilistic functions determines a set of actions to optimize repair and maintenance strategies based on the structural reliability and costs.

.

In this paper, data from various experimental resources and results from computational relations on crack width estimation in the marine environment are used to predict the probability of failure and the remaining life of RC structures by the use of Weibull function distribution. Assuming that repair and maintenance service has been done, the structure information is updated and the probabilistic functions are analyzed by means of Bayesian theory. Finally, the information obtained from probability functions in different modes is used to estimate the optimal choice based on time and cost for repair and maintenance of the structure.

There have been various assessments of cracking and its impact upon structural fracture. Recent research shows that life expectancy of RC structures is highly dependent on environmental conditions. The corrosive atmosphere is a determinant of corrosion and cracking in RC structures [2,3]. There is sample research on the problem of concrete corrosion and surface cracking that predict theoretical models for its developing time [4–7]. Some researchers have modeled fatigue behavior adapting the finite element method to contrast the laboratory with model data for the structure [8–10]. In addition, various mathematical models have been proposed to predict concrete cracking time [11]. In the past, some research has been done on crack development in RC structures. Liu and Weyers first modeled the time to steel corrosion-induced cracking on cover concrete in a round of experiments. They made 5-year observations on the distribution of model cracks to examine the impact of corrosion on reliability. They found that cracking time acts as a symptom of the time-based prediction model [5].

The science of reliability is willingly introduced in the 1960s. Some probabilistic methods have been used to predict the structure's lifetime. These methods can predict a more accurate and realistic life span and time to corrosion at cracked surfaces [12–15]. In 1968, Benjamin proposed the concept of probabilistic design and structural reliability [16]. In 1987, Frangopol et al. examined the effect of structural damage on time-based reliability [17]. In 1998, Sarma and Adeli conducted a study on RC structures suggesting that the focus of research must shift from the initial optimization cost to the repair and maintenance costs [16].

In 1983, Surahman and Rojiani developed reliability-based optimizations for RC structures [16]. In 2000, Cempel et al. introduced a new concept of reliability based on symptoms (physical properties) to assess system conditions. This reliability has priority over time-based reliability in updating useful data (physical properties) to assess the structure's current and future conditions. Later, this concept of reliability was applied to measurable data such as geometry, material properties, static and dynamic behavior, structural damage and loading [18]. In 2011, Straub designed a new method to estimate the reliability of RC structures using Bayesian theory [19].

In 2012, Chen and Alani evaluated reliability to calculate offshore structure deterioration over time, providing an optimal repair program for the structure service life [20]. In 2015, Chen investigated the effect of corrosion on RC structures in an experimental research based on physical properties. The crack width of steel-concrete bond corrosion was studied using reliability based on physical properties on which the data were collected. Weibull probability distribution and Bayesian updating functions were used to assess reliability and predict the best repair and maintenance time to extend service life of the structure [21].

In 2017, Yu Bo et al. investigated the impact of sea environment on the reliability and probability of failure in offshore RC structures. They also examined environmental conditions, material properties, parameters influencing RC structures, and their implementation in the marine environment [21].

2. Corrosion in the Marine Environment

2.1. Initiation and Propagation of Cracks

corrosion cracking that leads to the failure of marine structures containing high-strength steel occurs in three different phases.

1) Crack initiation , 2) Crack propagation at a slow rate, 3) Fully cracked cover at a high propagation rate approaching the critical condition and leading to the final fracture [22].

The crack width on the concrete cover surface as an on-site measurable parameter follows analytical models. Experimental research shows that the bond strength of corroded steel is highly correlated with the crack width of concrete. The bond strength can be expressed as a function of crack width over time [23]. Figure 1 shows the predicted bond strength of intact normalized steel [24] and the experimental result of Law et al. [25].

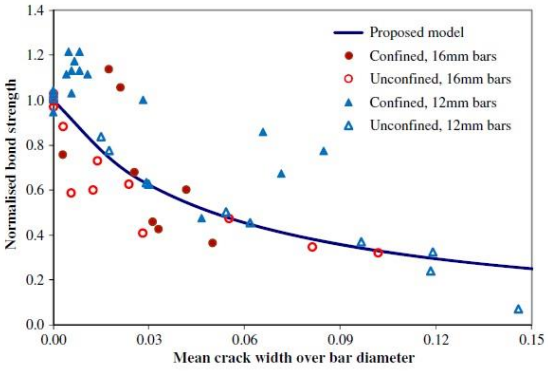


Figure 1. Normalized bond strength as a function of the ratio of mean crack width over the steel bar diameter, analytical predictions and experimental results of Law et al. [26]

As the bond strength of corroded steel decreases, the structure load-bearing capacity like bending strength is decreased. The results indicate that crack width is a predictor of steel bond strength. The reduction in bond strength begins with the initiation of concrete cover cracking. Therefore, crack width can be considered as a proper symptom in assessing the probability of failure and the reliability of the structure. The data on crack width can be used to estimate the structure remaining life.

2.2 Corrosion-induced Cracking Model

Steel corrosion-induced concrete cracking can be modeled as a walled cylinder, as shown in Figure 2 [26]. In this model, rebar with an internal radius of D_b is located in a clear concrete cover C. The first damage occurs on the concrete surface [27].

Diagrams must be also represented with clear axes, fonts, without background, with distinguishable lines in a black and white version.

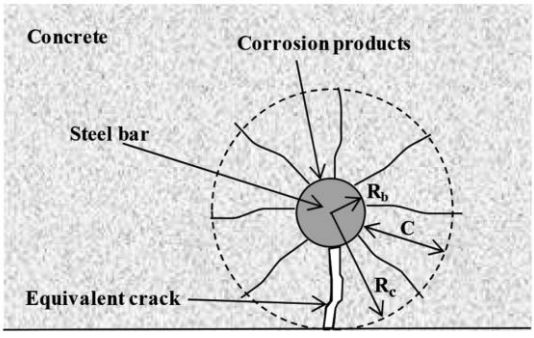


Figure 2. Schematic of steel-concrete bond corrosion [27]

The mass of rust (M_r) produced (Kg/m) per unit time is expressed as Eq.(1) [28]. Using this equation, the rate of corrosion rust in a period of time can be easily calculated.

$$M_r = \left(m_c \int_0^t \pi D_b i_{corr}(\tau) d\tau\right)^{1/2} \quad (1)$$

In this equation, t is the duration of corrosion per year, m_c is an empirical coefficient taken as 2.1×10^{-2}, i_{corr} represents the mean annual corrosion current per unit length at the surface area of the rebar [28].

2.2.1. Crack Initiation

The mass of rust produced at the beginning of cracking is calculated by Eq.(2) [28]:

$$M_r(T_p) = \frac{\pi}{\alpha_m} D_b d_0 \quad (2)$$

T_p is the time required for corrosion products to fill a porous zone of thickness d_0.

The parameter α_m is an empirical coefficient taken as $\alpha_m = 2.05 * 10^{-4}$ [28]. In other words, the time required to fill the entire porous zone (T_p) can be estimated using Eq.(1). It is also worth noting that rust propagation causes stress in rebar surroundings. Therefore, when the hoop stress at the rebar surface equals the tensile strength, the concrete initiates to crack at the rebar surface. The required mass of rust is obtained by Eq.(3) [28]:

$$M_r(T_i - T_p) = \frac{(1-\upsilon)R_b^2 + (1+\upsilon)R_c^2}{R_b^2 + R_c^2} \times R_b \times \frac{f_t}{E} \times \frac{\pi D_b}{\alpha_m} \quad (3)$$

R_b represents the radius of the reinforcement, R_c represents the corrosion radius of the concrete surface, υ is the Poisson's coefficient, E is Young's modulus, f_t corresponds to the tensile strength and T_i is the time required for corrosion to be started.

Similarly, the required time for crack initiation at the rebar surface is calculated from the time through which the porous zone is filled to the time through which hoop stress approaches the tensile strength (Eq.(1)). In these equations, corrosion time and rate in marine environment are calculated based on the structure geometric properties until crack propagation.

2.2.2. Crack Propagation

Numerous studies have been carried out on concrete cracking models that indicate no significant change in concrete deterioration under different conditions [29]. On the other hand, a significant increase in the crack width is associated with an insignificant tensile strength of cracked concrete.

The normalized actual crack width in $W(r)$ is defined as follows [28]:

$$W = \frac{f_t}{G_F} w(r) \quad (4)$$

where G_F is the fracture energy of concrete.

The normalized crack width is revised as follows [28]:

$$W = \frac{\delta_{bc}(R_c.r)}{\delta_{bc}(R_c.R_b)} W_b \quad (5)$$

In this equation, the crack width coefficient $\delta_{bc}(R_c.r)$ is expressed as follows and the coefficient $\delta_{bc}(R_c.R_b)$ is obtained from $\delta_{bc}(R_c.r)$ when $r = R_b$.

$$\delta_{bc}(R_c.r) = \frac{(R_c - r)}{l_0(l_0 - R_c)(l_0 - r)} + \frac{1}{l_0^2} ln \frac{R_c|l_0 - r|}{r|l_0 - R_c|} \quad (6)$$

where $l_0 = \frac{n_c W_{cr}}{2\pi} l_{ch}$ and $l_{ch} = \frac{E G_F}{f_t^2}$, $n_c = \frac{2\pi R_c}{L_c}$.

l_{ch} is the length of property introduced by Hillerborg et al. [30] and L_c is the spacing of crack bands [28].

Therefore, the normalized crack width at rebar surface W_b is expressed as follows:

$$W_b = ((1 + \nu)R_c(l_0 - R_c)\delta_{bc}(R_c.R_b) \times W_{cr}) \quad (7)$$

The mass of rust required for the crack propagation on the concrete surface at the time of crack initiation is obtained by Eq.(8):

$$M_r(T_c - T_p) = [1 + \frac{l_0 - R_b}{R_b}\frac{W_b}{W_{cr}}] \times R_b \times \frac{f_t}{E} \times \frac{\pi D_b}{\alpha_m} \quad (8)$$

As a result, the time for the crack to propagate on the concrete surface T_c is estimated using Eq.(1).

2.2.3. Fully Cracked Cover

As soon as cracking reaches the surface of free concrete, the cover is completely cracked. The normalized crack width at this stage of corrosion is expressed as bellow [28]:

$$W = W_c + \frac{\delta_{bc}(R_c.r)}{\delta_{bc}(R_c.R_b)}(W_b - W_c) \quad (9)$$

The normalized crack width at the rebar surface W_b within the time period of this stage is also expressed as bellow [28]:

$$W_b = \left(\frac{E}{f_t} \times \frac{\alpha_m M_r(t)}{\pi D_b} - R_b\right) \times \frac{W_{cr}}{l_0 - R_b} \quad (10)$$

Therefore, the crack width at the concrete surface W_c can be calculated as a function of time. The time to reach the critical value for concrete T_{cr} can be estimated by Eq.(10) assuming that $W_b = W_{cr}$. Also, the critical mass of rust (concrete surface cracking) can be calculated by Eq.(11):

$$M_r(t_{cr}) = \frac{l_0 f_t D_b \pi}{E \alpha_m} \quad (11)$$

Finally, if i_{corr} is kept constant during the cracking process, the total crack width per time t is the sum of all concrete surface crack widths [31]. Therefore, the crack width is considered as a function of time as follows [28]:

$$\begin{array}{ll} \tilde{w}(t) = 0 & for\ 0 \le t \le T_c \\ \tilde{w}(t) = a^c t^{1/2} - b^c & for\ T_c \le t \le T_{cr} \\ \tilde{w}(t) = a^d t^{1/2} - b^d & for\ t > T_{cr} \end{array} \quad (12)$$

The values of a^c and b^c can be represented as below:

$$a^c = 0.145\ \alpha_m \frac{E}{f_t}\sqrt{\frac{i_{corr}}{\pi D_b}} \times \frac{1}{(l_0 - R_b)[1 - R_c(l_0 - R_c)\delta_{bc}(R_c.R_b)]} \times n_c W_{cr} \quad (13)$$

$$b^c = \frac{\frac{R_b}{(l_0 - R_b)} + R_c(l_0 - R_c)\delta_{bc}(R_c.R_b)}{1 - R_c(l_0 - R_c)\delta_{bc}(R_c.R_b)} \times n_c W_{cr} \quad (14)$$

Also, the values of a^d and b^d can be represented as below:

$$a^d = 0.145\ \alpha_m \frac{\sqrt{\pi D_b i_{corr}}}{R_{cr}} \quad (15)$$

$$a^d = \pi D_b\left(1 - \frac{R_b}{R_{cr}}\right) - n_c W_{cr} \quad (16)$$

Therefore, it can be concluded that if the mean corrosion rate of rebar remains constant during the process, the crack propagation induced by steel corrosion follows square–root–of–time rule.

2.3. Sample Beam

A concrete beam in the marine environment is considered as the study structure in this paper. The beam includes a rebar of 16 mm diameter with a clear concrete cover of 40 mm. The mean compressive strength of concrete is taken f_c = 45 MPa. This value is also considered to estimate other properties of concrete. Therefore, the required parameters are estimated as follows:

The tensile strength of concrete is equal to $f_t = 0.69\sqrt{f_c} = 4.63\ MPa$

The modulus of elasticity is equal to $E = 4400 f_c^{0.516} = 31.4\ GPa$

Poisson's coefficient is taken as ν = 0.18

According to laboratory data, the fracture energy of concrete and the ultimate cohesive crack width are respectively considered $G_F = 96\ N/m$ and $w_u =$

0.15 mm in the structure. According to previously used data [28,31], the allowable crack width is assumed to be $w_l = 1\,mm$ for the RC structure in the marine environment. Also, the maximum aggregate size is considered to be 25 mm. The total crack number is obtained from the formula $n_c = 2\,\pi\ R_c/L_c \approx 4$. The structure designed service life is 60 years. Also, the baseline of the corrosion penetration rate is $i_{corr} = 5\ \mu A/cm^2$.

The crack width per unit time has been calculated by some methods and the crack growth in RC structures has been formulated by some researchers. Alongside crack growth prediction, different laboratory data [27,32–34] have been collected by Chen [24]. In the following, the Eq.(12) is used to predict the cracked structure width (with studied specification). As shown in Figure 3, there is no significant difference between predicted data by Eq.(12) and predicted data by Chen in the corrosion-induced crack width. These results are taken as the presumptions for the crack growth in the offshore environment and used for the following predictions.

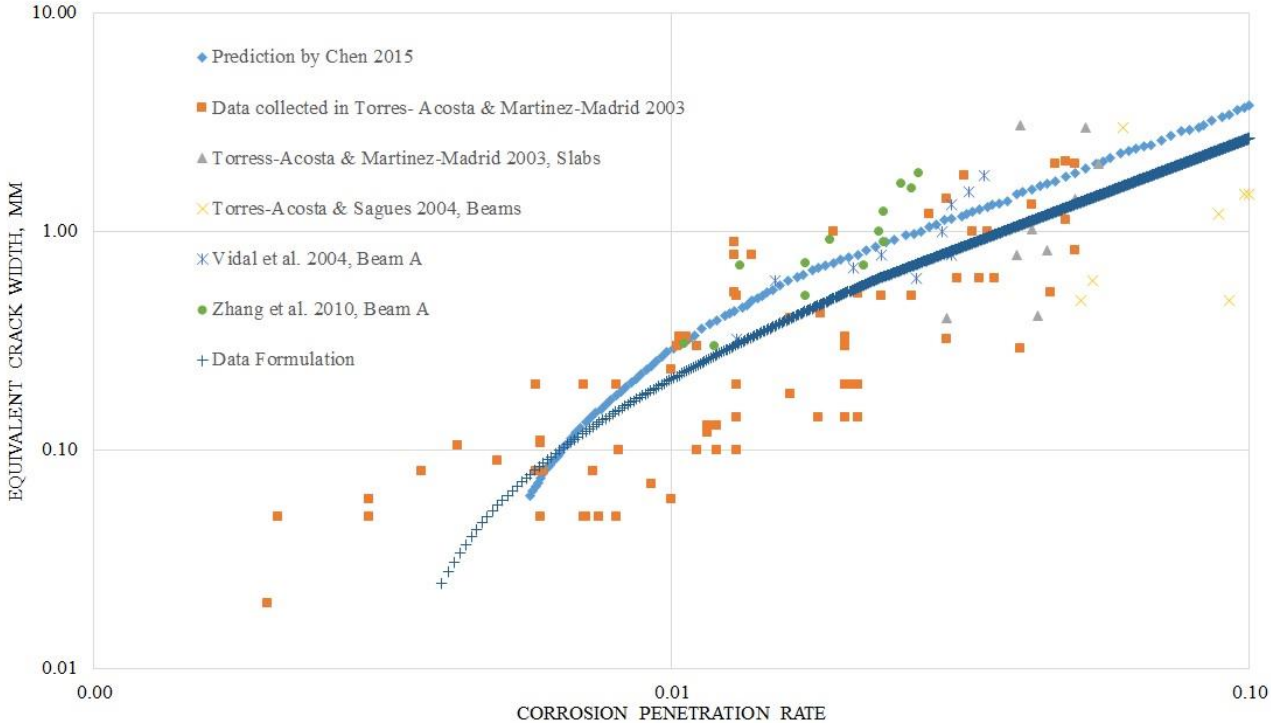


Figure 3. Crack width values under the function of mean corrosion penetration rate (laboratory data and presumed results)

3. Symptom-based Reliability and Weibull Function Distribution

Time-based reliability is an old method that has given way to symptom-based reliability due to some limitations including ignorance of extra information available to the structure. Since environmental forces are constantly changing in the specific maritime environment, symptom-based reliability has priority over time-based reliability for marine structures. The health monitoring process can formulate useful symptoms to evaluate the current state and predict the future condition for developing optimal maintenance strategies. In symptom-based systems, reliability depends on measurable data. When a symptom exceeds its critical value, the failure of system or its components will take place [18]. Weibull model as a well-known and flexible model for service life distribution can be used for symptom-based reliability. Therefore, in Weibull Life Distribution Model based on the symptom Y (e.g. crack width) caused by the damage parameter X (e.g. average corrosion penetration rate), its probability density function (PDF) is defined as [35]:

$$f(Y) = \left(\frac{\alpha}{Y}\right)\left(\frac{Y}{Y_b}\right)^{\alpha} \exp\left(-\left(\frac{Y}{Y_b}\right)^{\alpha}\right) \qquad (17)$$

Where $Y_b = \gamma Y_L$ and γ is the scale factor, calculated from the design requirements and the limit value of Y_L. The value of the shape factor (0 <α) is calculated by the following formula [35]:

$$\alpha = \frac{\sum_i \{\ln\left[-\ln\left(1-\frac{x_i}{x_b}\right)\right]\}^2}{\sum_i \left\{\ln\left[-\ln\left(1-\frac{x_i}{x_b}\right)\right]\right\} \ln\left(\frac{Y_i}{Y_b}\right)} \qquad (18)$$

The damage parameter x_b corresponds to Y_b. The probability of failure (cumulative distribution function CDF) is expressed as a function of damage parameter $x_{(t)}$ with respect to time t as follows [35].

$$P_f\big(Y(t)\big) = 1 - \exp[-\left(\frac{Y(t)}{Y_b}\right)^{\alpha}] \quad (19)$$

By calculating probability of failure, the reliability based on symptom (survival function) for the symptom Y is expressed as a function of damage parameter $x_{(t)}$ as follows [35]:

$$R\big(Y(t)\big) = \int_{Y(t)}^{\infty} f(y)dy = \exp[-\left(\frac{Y(t)}{Y_b}\right)^{\alpha}] \quad (20)$$

3.1. Bayesian Theory and Reliability

In 1958, Bayesian theory was first developed by Thomas Bayes. This method is used for adjusting previous information to new evidence in order to update or modify studied parameters. In maintenance studies,
routine inspections, maintenance and repairs are
conducted to update information on the structures and make decisions about their future. This information should be considered in probabilistic functions and service life.
Under such conditions, when the structure is monitored, inspected, or repaired at the specific crack width $\widetilde{w} = \widetilde{w}^a$, the entire structure undergoes some changes in reliability and probability of failure. Therefore, the crack width information must be updated. The function $g(\widetilde{w}.\widetilde{w}^a)$ is defined as a likelihood function to simulate up-to-date values [35]:

$$g(\widetilde{w}.\widetilde{w}^a) = f(\widetilde{w} - \widetilde{w}^a) = \frac{\alpha}{\widetilde{w} - \widetilde{w}^a}(\frac{\widetilde{w} - \widetilde{w}^a}{\lambda' w_l})^{\alpha}\exp[-\left(\frac{\widetilde{w} - \widetilde{w}^a}{\lambda' w_l}\right)^{\alpha}] \quad (21)$$

In this equation, λ' is the scale factor updated and represented as follows [35]:

$$\lambda' = \frac{w^a}{w_l}[-\ln\left(1 - \frac{\bar{x}^a}{\bar{x}_b}\right)]^{-1/\alpha} \quad (22)$$

In this equation, $\bar{x}^a$ is the average corrosion penetration rate at the crack width $\widetilde{w}^a$. Having been updated, probability density function must be multiplied by the reliability symptom $\widetilde{w} = \widetilde{w}^a$, $R(\widetilde{w}^a)$ to keep the unity of cumulative distribution function. Accordingly, at different crack widths $\widetilde{w} = \widetilde{w}_i^a$, the probability density function is expressed as [36]:

$$f_{i+1}^a(\widetilde{w}) = \frac{g_i(\widetilde{w}.\widetilde{w}_i^a)f_i(\widetilde{w})}{\int_0^{\infty} g_i(\widetilde{w}.\widetilde{w}_i^a)f_i(\widetilde{w})d\widetilde{w}}R_i(\widetilde{w}_i^a) \quad (23)$$

The $g_i(\widetilde{w}.\widetilde{w}_i^a)$ is the likelihood function of i-th structure assessment program at the crack width $\widetilde{w} = \widetilde{w}_i^a$ and $f_i(\widetilde{w})$ is the initial probability density function for structure assessment. $R_i(\widetilde{w}_i^a)$ shows the structural reliability of i-th structure assessment program [36].
Therefore, the reliability is obtained via integration of updated probability density function over the desired point [36]:

$$R^a(\widetilde{w}) = \int_{\widetilde{w}}^{\infty} f^a(\theta)d\theta \quad (24)$$

In general, repairs are necessary for structure safety improving its strength and reliability. After repairs, the symptom-based reliability profile is changed. The probability density function in the crack width $\widetilde{w} = \widetilde{w}_j^r$ after repairs is modified as [37]:

$$f_{j+1}^r(\widetilde{w}) = f(\widetilde{w}) \quad for\ \widetilde{w} < \widetilde{w}_j^r$$
$$f_{j+1}^r(\widetilde{w}) = f_j\big(\widetilde{w} - \widetilde{w}_j^r\big)R_j\big(\widetilde{w}_j^r\big)\ for\ \widetilde{w}_j^r \le \widetilde{w} < \widetilde{w}_{j+1}^r \quad (25)$$

3.2. Sample Modeling

A sample beam is tested in the marine environment. The beam profile specifications are described in Section 2.3. The predicted data on crack growth are analyzed in three different modes to model the sample beam in the probability distribution function. In the first step, the structure is inspected without repair and maintenance. The structure surface is then inspected at a crack width of 0.8 mm. In the third step, beam repairs are made at a crack width of 1.2 mm. In the fourth step, the beam surface is inspected at a crack width of 0.8 mm and the structure is repaired at a crack width of 1.2. Finally, the probability of failure and the reliability of structure are examined. In fact, the structure is inspected after observing 0.8 mm wide cracks on the concrete surface. This inspection leads to structural modification. Later, at another time in the structure life cycle, repairs are made at a 1.2 mm width of cracks. The state (remaining life) of the structure changes after

making repairs and inspections. Providing updates and information on the structure is thus necessary to re-predict the remnant life of the structure. In this case, the structure is updated using Bayesian theory.

Figure 4 shows the structure probability density as a function of crack width. According to the initial state of the structure without maintenance and repairs, there is 50% probability of failure at the crack width of 1 mm. This state represents a structure working on all the basic engineering assumptions of 60-year life expectancy. After conducting inspection and updating information on the structure state, a tangible change occurs in the density function. According to the cumulative distribution function shown as a function of crack width (Figure 5), the structure operates on less than 40% probability of failure at the crack width of 1 mm. When the structure is inspected at the crack width of 0.8 mm, there is a sudden fall in the structural deterioration process continuing on a slower rate.

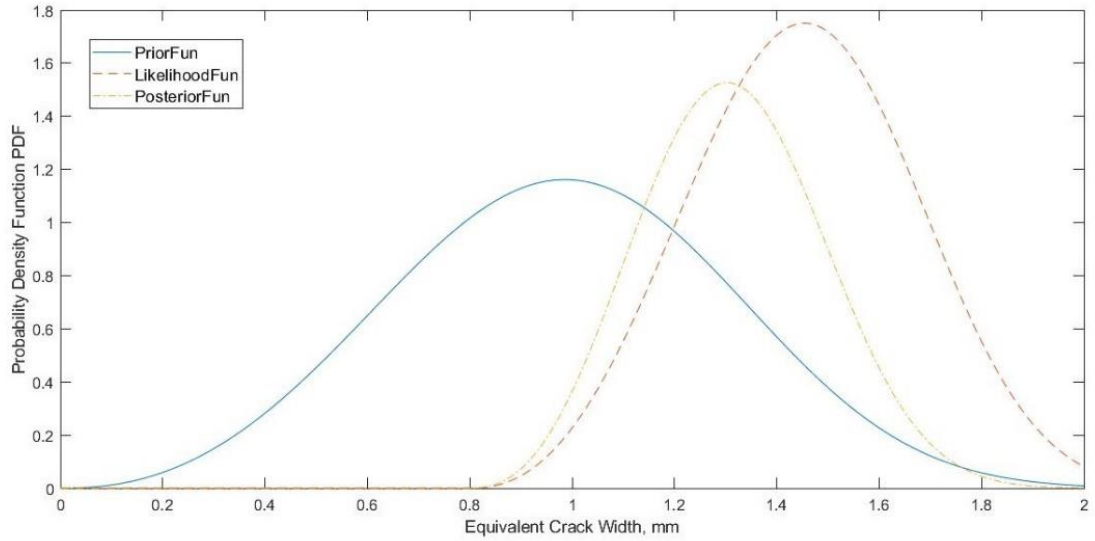


Figure 4. The initial, likelihood, and future probability density functions at 0.8 crack width inspection

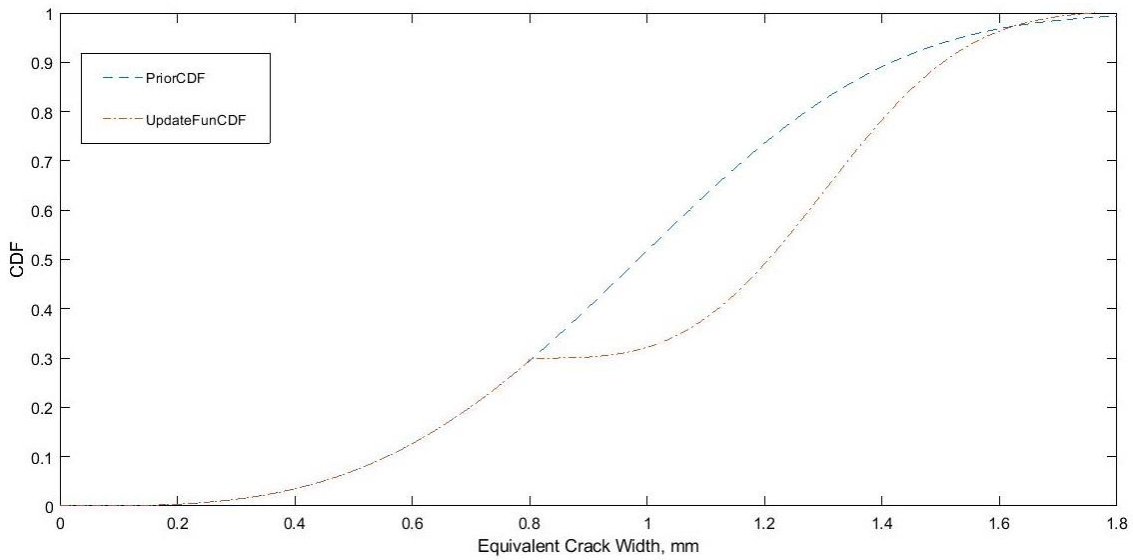


Figure 5. The diagram of cumulative distribution function for the structure both without and with inspection at the crack width of 0.8 mm

In the third step, the structure is modeled in such a way that repairs are conducted on the structure only at a crack width of 1.2 mm. There is more than 50 % probability of failure at the crack width of 1.2 before repairs, which is sharply reduced afterward. By making repairs, the probability density function and the probability of failure reach near zero at a crack width of 0.3 mm (shown in Figures 6 and 7). Therefore, repairs affect the process of structural deterioration. The probability of failure is procrastinated from 2 mm to more than 2.5 mm crack width in the structure.

In the fourth step of modeling, the structure is inspected at 0.8 mm and repaired at 1.2 mm crack width. In this mode, there are significant changes in the lifespan of the structure (Figure 6). The results on the probability density function from Figure 6 and the results on the probability of structural failure from Figure 7 show significant improvement in the structural reliability. In

this step, there is an increase up to 2.5 mm in the structure lifespan alongside a 50% probability of failure at 1.5 mm crack width.

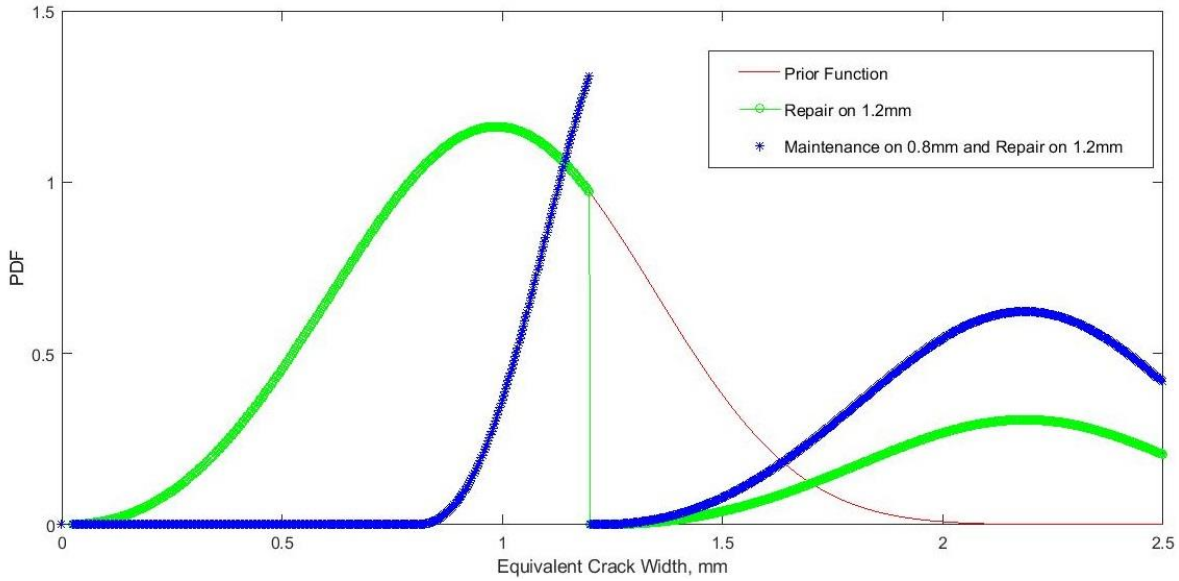


Figure 6. The probability density function under different conditions (without inspection and repairs, repairs at 1.2, inspection at 0.8, and repairs at 1.2 mm crack width)

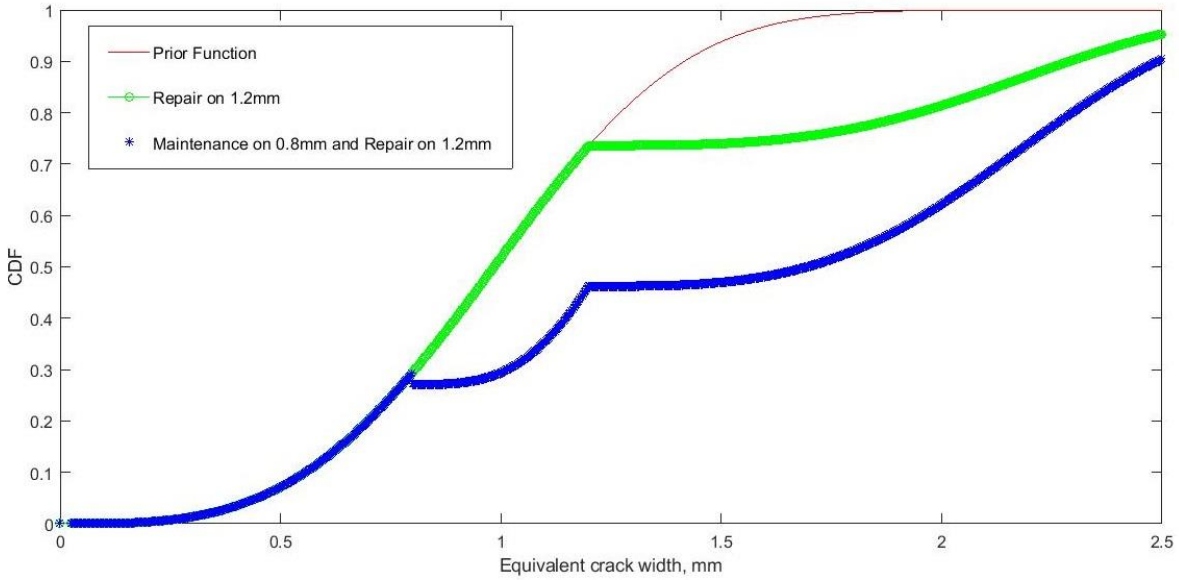


Figure 7. The probability of failure under different conditions (without inspection and repairs, repairs at 1.2, inspection at 0.8, and repairs at 1.2 mm crack width)

As expected, conducted inspections and repairs increased reliability and decreased probability of failure in the structure. As a consequence, the structure design life and durability are enhanced. Inspection, maintenance, and repair routines demand high costs. Whether maintenance implementation is a more cost-effective way than structural reconstruction is the key question. To what extent and when maintenance strategies are worth implementing and budgeting are discussed in the following.

4. Maintenance Strategy

The reliability assessment and cost analysis of the structures provide vital information for decision-making on rational management [35]. The optimal planning for making inspection, maintenance and repairs on engineering structures is conditional to cost analysis of the structure life cycle. This optimization entails minimizing the total cost of life expectancy including inspection, monitoring, maintenance, and repairs [35]. All the expected costs for the structure remaining life are expressed as [35,36]:

$$C_{total} = C_{insp} + C_{main} + C_{rep} + C_{fail} + C_{mon} \quad (26)$$

In this equation, C_{insp} expresses the inspection cost, C_{main} denotes the maintenance cost, C_{req} implies the cost of repairs, C_{fail} corresponds to the probability of failure cost, C_{mon} is the cost of monitoring the structure. The expected C_{insp} inspection costs for N_i number of inspections within the structure remaining service life of T can be calculated by Eq.(27). [35,36]:

$$C_{insp}(T) = \sum_{i=1}^{N_i} \frac{C_{insp.i}}{(1+d_r)^{t_i}} \quad (27)$$

In this equation, C_{insp} implies the cost of i-th inspection of the structure at the time t_i and d_r is the annual discount rate.

The expected maintenance cost of C_{main}, including the cost of preventive and routine maintenance over the remaining service life of T, depends on the relevant planning. The expected repair cost of C_{req} for the N_j number of repairs over the remaining service life of T is defined as [35,36]:

$$C_{rep}(T) = \sum_{j=1}^{N_j} \frac{C_{rep.j}}{(1+d_r)^{t_j}} \quad (28)$$

Where $C_{rep,j}$ is the cost of j-th repair of the structure at the time t_j.

The maintenance strategy, including inspection and repairs on the structure, may change the probability of structural failure. The cost of expected failure C_{fail} for the remaining service life of T is defined as [35,36]:

$$C_{fail}(T) = C_f P_f(0) + \sum_{t=1}^{T} \frac{C_f(P_f(t) - P_f(t-1))}{(1+d_r)^t} \quad (29)$$

Where C_f is the cost of structural failure at the present time, and $P_f(0)$ and $P_f(t)$ are the probability of failure in recent and t years, respectively.

In the case of no structural health monitoring, optimal planning is obtained from the minimization of both inspection and structural failure cost functions at the end of the structure service life T. Based on these two objective functions, minimization should be done as follows [35,36]:

$$Min\ C_{insp}(T)\ and\ Min\ C_{fail}(T) \quad (30)$$

In the case of inspection and repairs, structural information as well as reliability is updated. The repair and monitoring costs are also included in the total cost at the end of service life T. The minimization is obtained from the following objective functions [35,36]:

$$Min\left[C_{rep}(T) + C_{insp}(T)\right] and\ Min\ C_{fail} \quad (31)$$

Due to lack of information, the maintenance cost of the studied structure in the sea environment is assumed to be similar to that of the real structure in the corrosive environment of Orcesi and Frangopol's study [36]. Accordingly, the inspection and repair costs in different conditions are as follows.

First of all, no repair is conducted and the structure remains unchanged to the end of service life. In this step, there is no charge of maintenance. In the second step, a charge of $ 225,600 is assumed depending on the maintenance work. The charges of $229,200, $341,800, and $487,100 are considered for maintenance in the third, fourth, and fifth steps proportionate to the required repairs.

Given the definition of multi-objective optimization, inspection, repair, and failure cost functions constitute objective functions in this problem. The objective functions are identified by equations 30 and 31. The Non-dominated Sorting Genetic Algorithm (NSGA II) is used to find the best solution to the problem while optimizing the two objective functions. The design parameters of this problem include the time of maintenance and the type of selective reaction. In the first step, it is assumed that the structure is inspected at a crack width of 0.8 mm. The two objective functions are changing. The first is the inspection cost function with a different condition in the structure. The second objective function is the probability of structural failure for inspection at the crack width of 0.8 mm (Figure 5). Among various conditions, the optimal costs concerning structural failure and inspection cost functions are represented in Figure 8. According to the available budget, risk-taking potential is determined by making the best decision among the proposed selections.

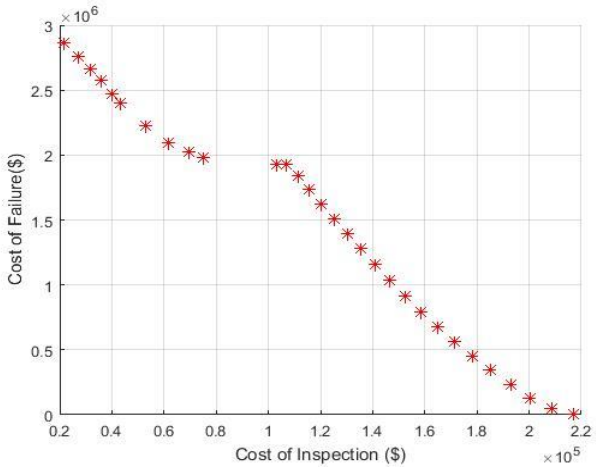


Figure 8. Pareto front diagram of the inspection cost function versus the failure cost function (with the assumption of 0.8 mm crack width)

It is further assumed that the structure is not inspected and only repaired at the crack width of 1.2 mm. In this step, the objective functions include the cost of structural failure at the crack width of 1.2 mm (Figure 7) and the cost of repairs in different modes. The best possible time and the lowest probable cost are found regarding the reliability of the structure. Figure 9 represents the resulting Pareto front including the best options for implementing structural repairs based on the crack width and the repair cost.

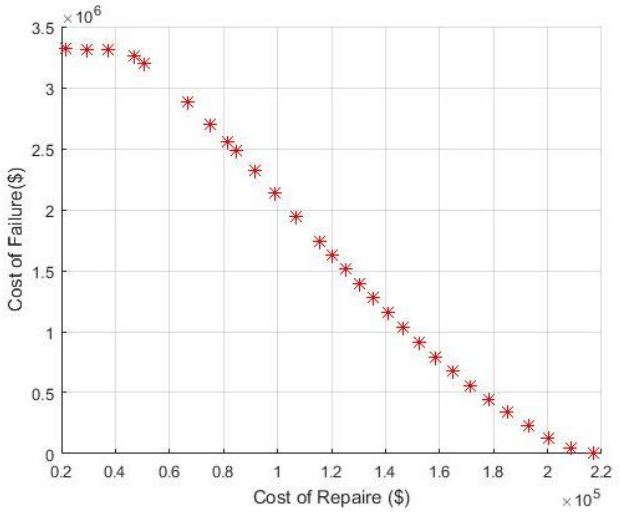


Figure 9. Pareto front diagram of repair cost function versus failure cost function (with the assumption of 1.2 mm crack width)

As seen in Figure 6, making repairs on the structure is much more effective than carrying out inspections. In fact, the reliability of the structure is increased by 0.8 mm after repairs. Assuming that a failure cost of $ 2 million is decided and comparing diagrams 9 and 10, a difference of $ 40,000 is obtained between inspection and repair costs. Making decisions on the time and the type of inspections is subject to the project budget and the employer's selection.

In the third step, the structure goes under inspection and repairs. Compared to previous steps, the probability of structural failure undergoes dramatic changes, making it extremely difficult to decide on the exact time and cost. In this case, the first function is the cost of repair and maintenance and the second function is the probability of failure considering crack width of 0.8 mm for inspection and crack width of 1.2 mm for repair (Figure 7). The best decisions are proposed using the genetic algorithm (NSGA II method) (Figure 10). The employer is provided with options relative to the potential for taking risks and the budget available.

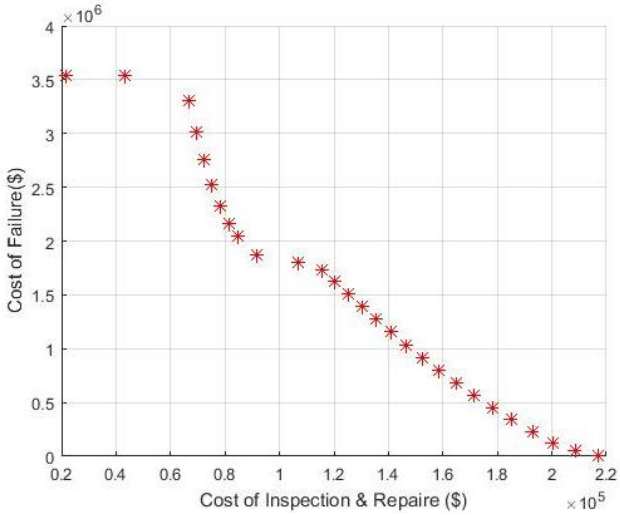


Figure 10. Pareto front diagram of inspection and repair cost function versus failure cost function (with the assumption of 0.8 mm crack width for inspection and 1.2 mm crack width for repair)

This diagram indicates that the difference between inspection and repair costs is not significant assuming that the failure cost of $ 2 million is accepted. Hence, the employer's decision on the inspection, maintenance, and repair costs is vital to take risks of structural failure.

5. Conclusions

In this paper, the propagation of crack width for a RC structure in the marine environment was investigated using Weibull probability function. The probability of failure was assessed before and after maintenance to predict the appropriate time for its implementation using Bayesian theory. The optimal condition for the structure was estimated by two functions of probability of failure and maintenance strategy. The following results are obtained:

1- Crack width was a good symptom for reliability assessment in the structure. Weibull distribution function was used to predict structural performance on the base of crack width propagation.

2- Bayesian theory and maintenance strategy were applied to update the structure information and improve its life service. The reliability and probability of failure were strongly influenced by maintenance implementation.
3- Repair and maintenance planning provided updates on the structure life expectancy and caused effects on the probability of failure and the probability density functions. The genetic algorithm (NSGA II) was used to propose the optimum strategy for repair and maintenance regarding two objective functions (probability of failure and varied strategies). It was concluded that the time and type of maintenance strategy depend on the risk-taking and financial potentials.
4- In this work, crack width propagation was the mere factor considered as a symptom. Not only may other factors affect the probability of structural failure, but also the cost of maintenance and repairs.
5- The maintenance and repairs were conducted on a fractured structure in this study. Preventive maintenance services can be investigated in future studies.

6. References

[1] Frangopol DM, Okasha NM. Life-cycle framework for maintenance , monitoring , and reliability of naval ship structures. Integration The Vlsi Journal 2010:69–76.
[2] Torres-Acosta AA, Navarro-Gutierrez S, Terán-Guillén J. Residual flexure capacity of corroded reinforced concrete beams. Engineering Structures 2007;29:1145–52. doi:10.1016/j.engstruct.2006.07.018.
[3] Li C-Q, Zheng J-J. Analytical Model for Corrosion-Induced Crack Width in Reinforced Concrete Structures. Structural Journal 2006;103:479–87. doi:10.14359/16423.
[4] Alonso C, Andrade C, Rodriguez J, Diez JM. Factors controlling cracking of concrete affected by reinforcement corrosion. Materials and Structures 1998;31:435–41. doi:10.1007/BF02480466.
[5] Y. Liu, R. E. Weyers. Modeling the Time to Corrosion Cracking in Chloride contaminated Reinforced Concrete Structures. ACI Materials Journal 1998;95:675–80. doi:10.1016/S0008-8846(98)00259-2.
[6] Andrade C, Alonso C, Molina FJ. Cover cracking as a function of bar corrosion: Part I-Experimental test. Materials and Structures 1993;26:453–64. doi:10.1007/BF02472805.
[7] Oh BH, Kim KH, Jang BS. Critical corrosion amount to cause cracking of reinforced concrete structures. ACI Materials Journal 2009;106:333.
[8] Uddin F, Maalej M, Mihashi H. Cover Cracking of Reinforced Concrete Beams Due to Corrosion of Steel 2008:2008.
[9] Chen D, Mahadevan S. Chloride-induced reinforcement corrosion and concrete cracking simulation 2008;30:227–38. doi:10.1016/j.cemconcomp.2006.10.007
[10] Barlowt P, Bartht F, Bishara AG, Boggs HL, Brandee ME, Darwin D, et al. Causes, Evaluation and Repair of Cracks in Concrete Structures 1998;93:1–22.
[11] Jayasuriya A, Pheeraphan T, Stage APS. Prediction of Time to Crack Reinforced Concrete by Chloride Induced Corrosion 2017;11:1197–203.
[12] Kirkpatrick TJ, Weyers RE, Anderson-cook CM, Sprinkel MM. Probabilistic model for the chloride-induced corrosion service life of bridge decks 2002;32:1943–60.
[13] Suo Q, Stewart MG. Corrosion cracking prediction updating of deteriorating RC structures using inspection information. Reliability Engineering and System Safety 2009;94:1340–8. doi:10.1016/j.ress.2009.02.011.
[14] Thoft-christensen P. Aalborg Universitet Papers, volume 5 - 1997-2000 Thoft-Christensen, Palle 2006;5.
[15] Ã DVV, Trapper PA. Probabilistic evaluation of initiation time of chloride-induced corrosion 2008;93:364–72. doi:10.1016/j.ress.2006.12.010.
[16] Adeli H, Sarma KC. Cost optimization of structures: fuzzy logic, genetic algorithms, and parallel computing. John Wiley & Sons; 2006.
[17] Frangopol DM, m. ASCE, Curley JP. EFFECTS OF DAMAGE AND REDUNDANCY ON STRUCTURAL RELIABILITY 3 By Dan M, Frangopol, 1 M. ASCE, and James P. Curley 2 1987;113:1533–49.
[18] CEMPEL C, NATKE HG, YAO JTP. Symptom Reliability and Hazard for Systems Condition Monitoring. Mechanical Systems and Signal Processing 2000;14:495–505. doi:10.1006/mssp.1999.1246.
[19] Straub D. Reliability updating with inspection and monitoring data in deteriorating reinforced concrete slabs. Applications of Statistics and Probability in Civil Engineering -Proceedings of the 11th International Conference on Applications of Statistics and Probability in Civil Engineering 2011:2309–16.
[20] Alani AM, Chen H-P. Reliability and optimised maintenance for sea defences. Proceedings of the ICE - Maritime Engineering 2012;165:51–64. doi:10.1680/maen.2010.37.
[21] Yu B, Ning C, Li B. Probabilistic durability assessment of concrete structures in marine environments: Reliability and sensitivity analysis. China Ocean Engineering 2017;31:63–73.
[22] Pedeferri P, Bertolini L, Elsener B, Redaelli E, Polder RB, Pedeferri P, et al. Corrosion of Steel in Concrete - Prevention, Diagnosis, Repair. 2013. doi:10.1002/3527603379.
[23] Nepal J, Chen H-P. Risk-based optimum repair planning of corroded reinforced concrete structures. Structural Monitoring and Maintenance 2015;2:133–43. doi:10.12989/smm.2015.2.2.133.
[24] Chen H. Monitoring-Based Reliability Analysis of Aging Concrete Structures by Bayesian Updating 2015:1–8. doi:10.1061/(ASCE)AS.1943-5525.
[25] Law DW, Tang D, Molyneaux TKC, Gravina R. Impact of crack width on bond: Confined and

unconfined rebar. Materials and Structures/Materiaux et Constructions 2011;44:1287–96. doi:10.1617/s11527-010-9700-y.
[26] Nepal J, Chen H. Risk-based optimum repair planning of corroded reinforced concrete structures. Structural Monitoring and Maintenance 2015;2:133–43. doi:10.12989/smm.2015.2.2.133.
[27] Zhang R, Castel A, François R. Concrete cover cracking with reinforcement corrosion of RC beam during chloride-induced corrosion process. Cement and Concrete Research 2010;40:415–25. doi:10.1016/j.cemconres.2009.09.026.
[28] Chen H, Alani AM. Optimized maintenance strategy for concrete structures affected by cracking due to reinforcement corrosion. ACI Structural Journal 2013;110:229–38.
[29] Bazant ZP, Planas J. Fracture and size effect in concrete and other quasibrittle materials. vol. 16. CRC press; 1997.
[30] Hillerborg A, Modéer M, Petersson PE. Analysis of crack formation and crack growth in concrete by means of fracture mechanics and finite elements. Cement and Concrete Research 1976;6:773–81. doi:10.1016/0008-8846(76)90007-7.
[31] Zhang R, Castel a., François R. Serviceability Limit State criteria based on steel–concrete bond loss for corroded reinforced concrete in chloride environment. Materials and Structures 2009;42:1407–21. doi:10.1617/s11527-008-9460-0.
[32] Torres-Acosta AA, Sagues AA. Concrete cracking by localized steel corrosion--Geometric effects. Materials Journal 2004;101:501–7.
[33] Torres-Acosta A a., Mart nez-Madrid M. Residual Life of Corroding Reinforced Concrete Structures in Marine Environment. Journal of Materials in Civil Engineering 2003;15:344–53. doi:10.1061/(ASCE)0899-1561(2003)15:4(344).
[34] Vidal T, Castel A, François R. Analyzing crack width to predict corrosion in reinforced concrete. Cement and Concrete Research 2004;34:165–74. doi:10.1016/S0008-8846(03)00246-1.
[35] Chen H-P, Ni Y-Q. Structural Health Monitoring of Large Civil Engineering Structures. 2018. doi:10.1002/9781119166641.
[36] Orcesi AD, Frangopol DM. Optimization of bridge maintenance strategies based on structural health monitoring information. Structural Safety 2011;33:26–41. doi:10.1016/j.strusafe.2010.05.002.
[37] Okasha NM, Frangopol DM. Lifetime-oriented multi-objective optimization of structural maintenance considering system reliability, redundancy and life-cycle cost using GA. Structural Safety 2009;31:460–74. doi:10.1016/j.strusafe.2009.06.005.

Available online at: www. Ijcoe.org

The Role of Standards in Maritime-Based Development: An Analysis of Challenges in Iran's Maritime Industry

Amir Nezam Barati[1]* Ali Sheikh Bahai[2], Meysam Bali[3] ,Ali Alimohamadpour [4]

[1] Assistant Professor of Law, Department of Law, Imam Khomeini Maritime Science University, Mazandaran, Iran nezambarati@gmail.com*
[2] PhD Candidate in Marine Physics, University of Hormozgan, Bandar Abbas, Iran, meysam.bali@aut.ac.ir
[3]Meysam Bali, Assistant Professor, Faculty of Marine Engineering, Amirkabir University of Technology, Tehran, Iran, meysam.bali@aut.ac.ir
[4] Assistant Professor, Department of Economic and Accounting, Imam Khomeini Maritime Science University, Mazandaran, Iran, alimohamadpoor.ali@gmail.com

ARTICLE INFO

Article History:
Received 13 Apr 2026
Accepted 24 July 2026
Available online ….

Keywords: **Maritime standards,Blue Economy,Sustainable development.**

ABSTRACT

Maritime-based development has emerged as a critical pathway for achieving sustainable economic growth, particularly for coastal states whose industries depend on safe, efficient, and environmentally responsible maritime operations. Despite its strategic maritime position, Iran faces significant challenges in aligning its maritime sector with international standards. This study examines the role of technical, legal, and operational standards in shaping maritime-based development, with a focus on identifying structural barriers within Iran's maritime industry. Employing a comparative qualitative methodology, the research analyzes international benchmarks—including key IMO conventions such as SOLAS, MARPOL, and STCW—and compares them with Iran's existing regulatory framework, institutional capacities, and enforcement practices.

The findings reveal several critical gaps, including outdated regulatory instruments, weak and fragmented inspection mechanisms, insufficient adherence to IMO-mandated safety and environmental standards, and limited integration of global best practices in maritime education and training. Additionally, the study identifies institutional overlap and lack of inter-agency coordination as major obstacles to effective implementation.The research concludes that Iran can significantly enhance its maritime competitiveness by updating national regulations, strengthening port and vessel inspection systems, adopting a unified maritime governance structure, and fully harmonizing its educational programs with STCW requirements. These reforms are essential for enabling Iran to transition toward a modern, safe, and globally competitive maritime economy, thereby leveraging its maritime geography for sustainable national development.

Introduction

Maritime industries play a vital role in supporting global trade, energy security, and sustainable economic growth. Over 80 percent of the world's goods are transported by sea, making maritime safety, efficiency, and environmental protection critical to international development [1]. In this context, technical and regulatory standards serve as the backbone of maritime operations, ensuring compliance, safety, and interoperability across borders. The International Maritime Organization (IMO) and other classification societies such as DNV, ABS, and ClassNK have developed a complex

framework of conventions and technical standards[15]including SOLAS, MARPOL, and STCW that define the parameters of modern maritime governance [2] , [3] [11].

In Iran, the maritime sector has immense potential due to its geographical position along the Persian Gulf, the Gulf of Oman, and the Caspian Sea. However, despite this strategic advantage, Iran's maritime industry faces persistent challenges in achieving global competitiveness. Several studies have identified issues such as outdated technical regulations, limited compliance with IMO conventions, weak inspection mechanisms, and inadequate integration of international standards into domestic law [4]. These shortcomings hinder the effective modernization of Iran's maritime infrastructure and reduce its ability to participate in the global blue economy.

This paper argues that updating and harmonizing Iran's maritime standards with international norms is essential for advancing maritime-based development. Through a comparative analysis of international practices and Iran's existing regulatory system, the study explores how standards can act as instruments for improving safety, sustainability, and economic growth. Ultimately, it aims to provide practical recommendations for aligning Iran's maritime framework with global technical and legal standards, thereby fostering a stronger, safer, and more sustainable maritime sector.

2. Conceptual Framework and Literature Review of Maritime Standards

1.2. Definition of Maritime Standards

Maritime standards are formalized criteria and specifications designed to ensure the safety, efficiency, and sustainability of maritime operations. These standards encompass technical, operational, safety, and environmental dimensions, guiding ship design, navigation, port operations, and pollution prevention. Technical standards specify the structural and mechanical requirements for vessels, including hull integrity, machinery, and onboard equipment, whereas operational standards define protocols for crew management, navigation, and emergency response [1].

Safety standards focus on reducing accidents and protecting life at sea, as codified in conventions such as SOLAS, while environmental standards, exemplified by MARPOL, aim to prevent marine pollution and promote sustainable shipping practices [2],[5].

2.2. Types of Maritime Standards

Maritime standards can be categorized into four main types:

1. Technical Standards: Cover vessel construction, materials, machinery, classification rules, and equipment certification [3], [6].
2. Safety Standards: Include navigation rules, life-saving appliances, firefighting systems, and emergency preparedness as defined in STCW and SOLAS [2], [10].
3. Environmental Standards: Regulate emissions, ballast water management, oil discharge, and waste handling to comply with MARPOL and ISO environmental standards [11].
4. Operational Standards: Address crew training, watchkeeping, port procedures, and ship management practices, ensuring that both personnel and organizational processes meet international benchmarks [1].

3.2. International Standardization Organizations

Several international organizations play a central role in developing and harmonizing maritime standards:

International Maritime Organization (IMO): A specialized UN agency responsible for creating conventions, codes, and guidelines to ensure maritime safety and environmental protection [2].

International Organization for Standardization (ISO): Develops technical standards applicable to shipbuilding, port operations, and maritime management systems [11].

International Association of Classification Societies (IACS): Provides unified technical requirements and classification rules adopted by major classification societies worldwide, bridging the gap between legal conventions and practical ship inspection [9].

These organizations collectively provide a structured framework that ensures global interoperability, safety, and environmental compliance in maritime operations.

4.2. Literature Review

The literature on maritime development highlights the central role of technical and legal standards in ensuring maritime safety, operational efficiency, and environmental protection. According to Chircop, Coffen-Smout, and McConnell [1], maritime law and governance have evolved through the codification of international conventions under the

International Maritime Organization (IMO), particularly the Safety of Life at Sea (SOLAS), Marine Pollution (MARPOL), and Standards of Training, Certification and Watch-keeping (STCW) conventions. These conventions establish the global framework for ship construction, pollution control, and crew training—forming the core of modern maritime regulation.

Classification societies, including the American Bureau of Shipping (ABS), Det Norske Veritas (DNV), Lloyd's Register, and ClassNK, have complemented these conventions by developing detailed technical standards for ship design, materials, machinery, and safety inspections [3], [15]. As Goulielmos argues, the work of classification societies bridges the gap between legal requirements and practical implementation, thereby promoting reliability and accountability within the maritime sector [8]. The International Association of Classification Societies (IACS) further enhances standardization by coordinating unified requirements among its members to ensure consistency and interoperability in global shipping [9].

Several studies emphasize that the adoption of international standards contributes directly to sustainable maritime development. Bateman notes that standardization improves not only ship safety and environmental protection but also trade competitiveness by ensuring compliance with global insurance and port state control systems[7].

In this sense, standards serve as both a technical instrument and a policy tool for achieving maritime-based economic growth. Countries such as Norway, Japan, and South Korea have successfully aligned their national frameworks with IMO and ISO standards, resulting in advanced maritime clusters and resilient marine economies [4] [14].

In contrast, research on Iran's maritime system suggests persistent gaps between national regulations and international norms [4]. Although Iran has ratified major IMO conventions, challenges remain in the areas of technical supervision, port state control, and the integration of updated standards into domestic law. The Iranian Ports and Maritime Organization [13] has made progress in establishing safety guidelines, yet the lack of an independent classification authority and limited training consistent with STCW requirements have hindered full compliance. As a result, Iran's maritime industry operates below its potential capacity in contributing to blue economy development.

Overall, the literature underscores that maritime standards are not merely regulatory obligations but strategic drivers of sustainable development. Modernizing these standards and ensuring their effective implementation can significantly enhance national competitiveness, safety, and environmental stewardship within the maritime domain.

3. Comparative Analysis of Maritime Standards in Selected Countries

1.3. Overview

A comparative examination of maritime standards across advanced maritime nations reveals significant differences in regulatory frameworks, institutional structures, and approaches to safety and sustainability. Countries such as Singapore, Norway, and Japan have developed comprehensive systems that integrate international norms with domestic innovation. This chapter explores how these countries have institutionalized maritime standards and what lessons can be drawn for Iran's maritime industry.

2.3. Singapore: A Model of Integrated Maritime Governance

Singapore is widely regarded as a global leader in maritime management. Its success stems from the Maritime and Port Authority of Singapore (MPA), which harmonizes international standards set by the International Maritime Organization (IMO) with local regulations. The MPA enforces high-level technical and safety standards, regularly updating them in line with IMO conventions such as SOLAS, MARPOL, and STCW.

Moreover, Singapore's emphasis on digitalization and sustainability, for example, through the Smart Port and Green Port initiatives shows how standards can promote innovation. The coordinated application of technical, environmental, and operational benchmarks has turned Singapore into a maritime hub that balances economic efficiency with environmental protection.

3.3. Norway: Leadership in Safety and Environmental Standards

Norway's maritime governance is deeply rooted in its commitment to safety culture and environmental stewardship. The Norwegian Maritime Authority

(NMA) plays a central role in implementing national standards aligned with IMO and European Maritime Safety Agency (EMSA) directives. Norway was among the first to adopt advanced ballast water management systems and low-emission vessel technologies.

The country's investment in research, especially through the SINTEF Ocean Research Institute, has led to continuous updates of safety codes and ship design standards. Norwegian maritime education institutions also play a key role in standard dissemination by training professionals in compliance with both national and international frameworks.

4.3. Japan: Tradition and Technology Combined

Japan represents a unique blend of maritime tradition and high technology. The Japanese Ministry of Land, Infrastructure, Transport, and Tourism (MLIT) oversees a robust framework of safety and environmental standards. Japan's shipbuilding industry adheres closely to International Association of Classification Societies (IACS) regulations while also developing domestic innovations to improve ship efficiency and safety [9].

Japan's Maritime Bureau has also been instrumental in advancing research on autonomous ships and decarbonization technologies. This dual focus on technological modernization and strict compliance has strengthened Japan's maritime competitiveness on the global stage.

5.3. Lessons for Iran

A comparison with these leading maritime nations suggests several key insights for Iran:

1. Institutional Integration: A unified authority—similar to Singapore's MPA—could help streamline Iran's maritime governance system.

2. Safety and Research Orientation: Following Norway's model, Iran should enhance investment in maritime safety research and education.

3. Technology and Innovation: Inspired by Japan, Iran could adopt new technologies such as smart navigation and green shipping solutions.

4. Alignment with IMO Conventions: Regular harmonization of domestic regulations with IMO standards would improve international cooperation and trade credibility.

By learning from these experiences, Iran can build a more resilient and internationally compliant maritime system that supports marine-based economic growth.

4. The Current Status of Maritime Standards in Iran

1.4. Institutional and Legal Framework

Iran's maritime sector is governed primarily by the Ports and Maritime Organization (PMO), under the supervision of the Ministry of Roads and Urban Development. The PMO is responsible for regulating ship safety, port operations, and maritime inspections in accordance with both national law and international conventions ratified by Iran [4]. Iran has officially ratified key IMO conventions, including SOLAS, MARPOL, and STCW, which provide the foundational framework for ship safety, environmental protection, and crew training [5].

Despite this formal compliance, several studies indicate that Iran's maritime standards face challenges in practical implementation. These challenges include gaps in inspection mechanisms, outdated technical regulations, and insufficient alignment with the latest IMO updates [14].

For instance, the enforcement of technical classifications for ship hulls and machinery remains inconsistent across ports, limiting the overall safety and operational reliability of the fleet.

2.4. Technical and Safety Standards

Iran has developed domestic guidelines for ship construction, classification, and safety procedures, primarily outlined in the Guide to Implementation of Maritime Safety and Technical Regulations[4]. However, compared to international best practices, these guidelines often lag behind in terms of technological updates and standard harmonization. Safety standards such as life-saving equipment, firefighting systems, and navigational aids are generally compliant but suffer from limited inspection frequency and inconsistent documentation.

Moreover, training of maritime personnel, though mandated by STCW standards, shows gaps in practical implementation. Many seafarers report insufficient hands-on training for emergency procedures and operational compliance, which can affect overall safety levels on board [4].

3.4. Environmental Standards

Environmental regulation in Iran aligns formally with MARPOL conventions, including oil spill prevention, ballast water management, and emission control [5]. However, the monitoring and enforcement of these standards are uneven, particularly in southern ports along the Persian Gulf. While national legislation exists, inadequate technical equipment for environmental surveillance and limited reporting mechanisms reduce the effectiveness of these environmental protections [14].

3.4. Challenges and Gaps

Based on current research, the main challenges for Iran's maritime standards include:

1. Outdated Technical Regulations: Delays in updating domestic codes in line with IMO revisions.

2. Weak Inspection and Enforcement: Inconsistent application of classification rules and safety inspections.

3. Insufficient Integration with International Standards: Limited harmonization with ISO and IACS standards.

4. Training Gaps: Crew and personnel training not fully aligned with modern STCW requirements.

5. Coordination Deficiencies: Lack of centralized oversight between PMO, Navy, and port authorities.

Addressing these gaps is essential to enhance maritime safety, international compliance, and the potential for marine-based economic growth.

5. The Role of Maritime Standards in Marine-Based Development

1.5. Standards as Drivers of Marine-Based Development

Maritime standards play a critical role in promoting marine-based economic growth by ensuring safety, operational efficiency, and environmental sustainability. The adoption of international standards—covering ship construction, navigation, pollution control, and crew competency—provides a foundation for developing a competitive and resilient maritime sector [7]; Chircop, Coffen-Smout, & McConnell, 2020) [1]. By aligning domestic regulations with IMO conventions, ISO guidelines, and IACS classification rules, countries can enhance trade credibility, attract foreign investment, and support the expansion of port and shipping infrastructure.

2.5. Economic Impacts of Standardization

Standardized maritime practices directly contribute to economic development by:

1. Reducing Operational Risks: Minimizing accidents and technical failures lowers costs for shipping companies and insurers [3].
2. Facilitating International Trade: Compliance with international standards enables easier port access and strengthens participation in global supply chains [14].

3. Encouraging Innovation: Standardization encourages adoption of green technologies, digital navigation systems, and efficient vessel designs, which in turn boost productivity and competitiveness [12].

In Iran, insufficient standardization has historically limited the growth of marine-based industries, reducing the country's potential to fully exploit its strategic maritime position in the Persian Gulf, the Gulf of Oman, and the Caspian Sea [4]. Improving standards could significantly enhance ship safety, port efficiency, and the overall maritime value chain, thereby supporting a sustainable blue economy.

3.5. Environmental and Sustainability Benefits

Maritime standards also provide a framework for environmental protection, a key factor for sustainable marine-based development. Adoption of MARPOL and ISO environmental standards ensures reduced oil spills, emissions, and ballast water contamination [5], [11]. Countries with strong environmental compliance, such as Norway and Japan, demonstrate that harmonized standards can simultaneously protect marine ecosystems and support long-term economic growth.

4.5. Policy Recommendations for Iran

Based on international experiences and current gaps in Iran's maritime system, the following strategies are recommended:

2. Update Technical Regulations: Ensure that shipbuilding, machinery, and classification rules are consistent with the latest IMO and IACS standards.

2. Strengthen Inspection Mechanisms: Improve port state control, vessel classification, and compliance audits to enhance safety and reliability.

3. Enhance Training Programs: Align seafarer education with STCW standards and practical operational training.

4. Promote Innovation and Green Shipping: Encourage adoption of digital navigation, emission reduction technologies, and energy-efficient vessel designs.

5. Institutional Coordination: Establish a centralized maritime authority to coordinate enforcement, regulation, and education across agencies.

By implementing these measures, Iran can leverage standards as a key driver of marine-based economic development, fostering international competitiveness and sustainable growth.

6. Comparative Analysis and Lessons for Iran

1.6. Comparative Overview

A comparative analysis of maritime standards in leading maritime nations—such as Singapore, Norway, and Japan—highlights key factors that contribute to a safe, efficient, and sustainable maritime sector. Singapore integrates international conventions with national regulations through the Maritime and Port Authority (MPA), ensuring seamless compliance with SOLAS, MARPOL, and STCW standards while promoting technological innovation [14]. Norway emphasizes a strong safety culture and environmental stewardship, enforced by the Norwegian Maritime Authority (NMA), and invests heavily in maritime research and education [8]. Japan combines advanced shipbuilding technology with rigorous regulatory compliance, aligning domestic standards with IACS classification rules while promoting innovation in digital navigation and green shipping [12]

2.6. Lessons Learned

From these examples, several critical lessons emerge for Iran:

1. Centralized Governance: Establishing a unified maritime authority, similar to Singapore's MPA, can streamline regulatory enforcement and coordination.

2. Safety and Environmental Culture: Adopting Norway's emphasis on safety culture and environmental monitoring will enhance operational reliability and sustainability.

3. Technological Modernization: Following Japan's approach, Iran can integrate digital navigation, energy-efficient vessels, and emission reduction technologies to boost competitiveness.

4. Education and Training: Aligning maritime education programs with STCW requirements ensures highly skilled seafarers and effective operational compliance.

5. International Alignment: Continuous harmonization of national regulations with IMO, ISO, and IACS standards strengthens trade credibility and fosters global cooperation.

3.6. Implications for Iran's Maritime Development

The comparative analysis indicates that Iran's current maritime framework can benefit significantly from adopting international best practices. Specifically:

Updating technical and safety regulations to match global standards will reduce operational risks and improve fleet reliability.

Strengthening inspection, classification, and port state control mechanisms will enhance compliance and safety.

Encouraging innovation and adoption of green technologies will support a sustainable blue economy.

Effective institutional coordination across PMO, naval authorities, and educational institutions will ensure consistency and regulatory efficiency.

By applying these lessons, Iran can transform its maritime industry into a globally competitive, sustainable, and safe sector capable of supporting marine-based economic growth.

7. Conclusions and Policy Recommendations

1.7. Conclusions

This study highlights the pivotal role of maritime standards in promoting safe, efficient, and sustainable marine-based development. The analysis demonstrates that standards covering technical, operational, safety, and environmental aspects—are not merely regulatory obligations

but strategic instruments for economic growth. Iran's maritime sector, while formally aligned with major IMO conventions such as SOLAS, MARPOL, and STCW, faces challenges in practical implementation, including gaps in inspection, training, technical regulations, and environmental monitoring [4]; [14].

Comparative lessons from leading maritime nations—Singapore, Norway, and Japan—underscore the benefits of centralized governance, rigorous safety culture, technological innovation, and international alignment. These experiences suggest that Iran can significantly enhance its maritime sector by modernizing standards, strengthening enforcement, and promoting training and innovation.

2.7. Policy Recommendations

Based on the analysis, the following policy recommendations are proposed for Iran:

1. Update and Harmonize Regulations: Regularly revise domestic technical, safety, and environmental standards to align with the latest IMO, ISO, and IACS requirements.

2. Strengthen Inspection and Enforcement: Enhance port state control, ship classification, and safety audits to ensure compliance and operational reliability.

3. Enhance Training Programs: Align maritime education and professional training with STCW standards, emphasizing practical skills and emergency preparedness.

4. Promote Technological Innovation: Encourage adoption of digital navigation systems, energy-efficient vessels, emission reduction technologies, and green shipping solutions.

5. Institutional Coordination: Establish a centralized maritime authority to improve coordination among PMO, naval, port, and educational institutions.

6. Support Research and Development: Invest in maritime research centers and partnerships with international institutions to develop domestic expertise in shipbuilding, port management, and environmental protection.

Implementing these recommendations can transform Iran's maritime sector into a globally competitive, safe, and sustainable system, capable of supporting a thriving marine-based economy and enhancing international trade.

Maritime standards serve as a strategic link between regulatory compliance, safety, environmental protection, and economic development. For Iran, updating standards, strengthening enforcement mechanisms, and fostering innovation are critical steps toward achieving sustainable marine-based growth. By learning from international best practices and integrating them with domestic capabilities, Iran can maximize the economic potential of its strategic waterways and ports while ensuring long-term environmental and operational sustainability.

References

[1] Chircop, A., Coffen-Smout, S., & McConnell, M. (2020). Maritime law and practice. Routledge.
[2] International Maritime Organization (IMO). (2020). SOLAS: Consolidated edition. IMO Publications.
[3] Det Norske Veritas (DNV). (2022). Rules for classification of ships. DNV Publications.
[4] Seyed Nezam, A. (2021). Legal and technical framework of maritime safety in Iran. Tehran: Law Publications.
[5] International Maritime Organization (IMO). (2021). MARPOL: Pollution prevention. IMO Publications.
[6] American Bureau of Shipping (ABS). (2022). Rules for building and classing marine vessels. ABS Publications.
[7] Bateman, S. (2018). Sea change: The evolving maritime regulatory framework. Routledge.
[8] Goulielmos, A. M. (2019). Marine safety and the role of classification societies. Journal of Maritime Affairs, 18(2), 147–161.
[9] International Association of Classification Societies (IACS). (2022). Unified requirements. Retrieved from https://www.iacs.org.uk
[10] International Maritime Organization (IMO). (2019). STCW: Standards of training, certification and watch keeping. IMO Publications.
[11] ISO. (2021). Maritime standards overview. International Organization for Standardization.

[12] Lloyd, J. (2018). International regulatory framework of maritime transport. Maritime Policy & Management, 45(3), 321–335.
[13] Ports and Maritime Organization (PMO). (2023). Guide to implementation of maritime safety and technical regulations. Tehran: PMO Publications.
[14] Tan, A. (2021). Challenges in global maritime standardization. Ocean Development & International Law, 52(1), 45–60.
[15] ClassNK. (2022). Technical rules and guidelines. ClassNK Publications.